

MANIPULATING THE ARCHITECTURE OF BIMETALLIC
NANOSTRUCTURES AND THEIR PLASMONIC
PROPERTIES

Christopher John DeSantis

Submitted to the faculty of the University Graduate School

in partial fulfillment of the requirements

for the degree

Doctor of Philosophy

in the Department of Chemistry

Indiana University

November 2014

UMI Number: 3665584

All rights reserved

INFORMATION TO ALL USERS

The quality of this reproduction is dependent upon the quality of the copy submitted.

In the unlikely event that the author did not send a complete manuscript and there are missing pages, these will be noted. Also, if material had to be removed, a note will indicate the deletion.



UMI 3665584

Published by ProQuest LLC (2014). Copyright in the Dissertation held by the Author.

Microform Edition © ProQuest LLC.

All rights reserved. This work is protected against unauthorized copying under Title 17, United States Code



ProQuest LLC.
789 East Eisenhower Parkway
P.O. Box 1346
Ann Arbor, MI 48106 - 1346

Accepted by the Graduate Faculty, Indiana University, in partial fulfillment of the requirements for the degree of Doctor of Philosophy.

Doctoral Committee

Sara E. Skrabalak, Ph.D

Trevor Douglas, Ph.D

Amar H. Flood, Ph.D

Liang-Shi Li, Ph.D

November 27, 2014

Copyright © 2014
Christopher John DeSantis

Dedicated to my mother Darla K DeSantis and my father Anthony John DeSantis

Acknowledgement

This thesis was prepared thanks to the generosity, work ethic, and—most of all—patience of my advisor Dr. Sara Skrabalak. It has been a pleasure to work with someone so talented and dedicated, someone who will surely become one of the great superstars of the field. I also thank the three undergraduate students I have had the honor to work with, Aaron Sue, Matthew Bower, and Andjela Radmilovic, as well as the exchange student from Tsinghua in China Haoming Liu. All four are incredibly talented and driven. I believe they have bright futures.

Two other Skrabalak Laboratory graduate students have aided me on projects. Alison Smith has been a great resource for the physical properties—in particular plasmonic properties—of branched nanostructures. Rebecca Wiener has been an invaluable co-worker and for whom I have collaborated with repeatedly. Her work has already expanded upon the understanding of nanoparticle growth of bimetallic nanostructures published here. I also thank the rest of the Skrabalak group members I have worked with: Moitree Laskaar, Dr. Nathan Motyl, Dr. Amanda K. P. Mann, Dennis Chen, Jie Fu, Samantha Harvey, Mariana B. T. Cardoso, Dr. Nancy Ortiz, Dr. Hamed Ataee-Esfahani, Ethan Harak, Corinne Weinel, William Bowers, Craig Girten, Kun ha Park, Susanne Wicker, Lin Xu, and Dr. Ellen Steinmiller.

Dr. Dennis Peters and Dr. Angela Pevery aided me in electrochemical experiments published in this thesis. I also thank the Flood Laboratory for allowing me to perform many optical measurements. In particular, I thank Dr. Edward Witliki for his wealth of knowledge on Raman as well as Chris Benson and Craig Marlatt for general

assistance. Tetrahedral Pd seeds were provided by Yan Dai of Dr. Nenfang Zhang's group at Xiamen University, China.

Dr. David Morgan has been an outstanding resource for transmission electron microscopy. I thank him for a vast amount of assistance and giving me a strong fascination for all things electron microscopy. I also thank Dr. Barry Stein, Dr. John Perry, Dr. Maren Pink and Yaroslav Losovyj. Finally, I thank the many professors who have given me important insight that has led me to better understand the work I have done. In particular, I thank Dr. Amar Flood, Dr. Emilie Ringe, Dr. Liang-Shi Li, Dr. Bogdan Dragnea, Dr. Donghwan Li, Dr. Jeffery Zaleski, and Dr. Trevor Douglas.

Funding for the research in thesis was provided by the NSF Award CHE-1306853, the Cottrell Scholar Program, the Raymond Siedle Fellowship in Materials Chemistry, the Chester Davis Fellowship in Inorganic Chemistry, and Indiana University.

Christopher John DeSantis

Manipulating the Architecture of Bimetallic Nanostructures and their Plasmonic Properties

There has been much interest in colloidal noble metal nanoparticles due to their fascinating plasmonic and catalytic properties. These properties make noble metal nanoparticles potentially useful for applications such as targeted drug delivery agents and hydrogen storage devices. Historically, shape-controlled noble metal nanoparticles have been predominantly monometallic. Recent synthetic advances provide access to bimetallic noble metal nanoparticles wherein their inherent multifunctionality and ability to fine tune or expand their surface chemistry and light scattering properties of metal nanoparticles make them popular candidates for many applications. Even so, there are currently few synthetic strategies to rationally design shape-controlled bimetallic nanocrystals; for this reason, few architectures are accessible. For example, the “seed-mediated method” is a popular means of achieving monodisperse shape-controlled bimetallic nanocrystals. In this process, small metal seeds are used as platforms for additional metal addition, allowing for conformal core@shell nanostructures. However, this method has only been applied to single metal core/single metal shell structures; therefore, the surface compositions and architectures achievable are limited. This thesis expands upon the seed-mediated method by coupling it with co-reduction. In short, two metal precursors are simultaneously reduced to deposit metal onto pre-formed seeds in hopes that the interplay between two metal species facilitates bimetallic shell nanocrystals. Au/Pd was used as a test system due to favorable reduction potentials of

metal precursors and good lattice match between Au and Pd. Alloyed shelled Au@Au/Pd nanocrystals were achieved using this “seed-mediated co-reduction” approach. Symmetric eight-branched Au/Pd nanocrystals (octopods) are also prepared using this method. This thesis investigates many synthetic parameters that determine the shape outcome in Au/Pd nanocrystals during seed-mediated co-reduction. Plasmonic, catalytic, and assembly properties are also investigated in relation to nanocrystal shape and architecture. This work provides a foundation for the rational design of architecturally defined bimetallic nanostructures.

Sara E. Skrabalak, Ph.D

Trevor Douglas, Ph.D

Amar H. Flood, Ph.D

Liang-Shi Li, Ph.D

Table of Contents	
Acceptance	ii
Acknowledgements	v
Abstract	vii
Chapter 1: An Introduction to Bimetallic Noble Metal Nanocrystals and their Properties	1
1.1 Introduction	2
1.2 Synthetic Strategies toward Controlling the Shape of Noble Metal Nanoparticles	3
1.3 Plasmonic Properties of Single Metal Nanoparticles	9
1.4 Multifunctional Properties of Bimetallic Nanoparticles	11
1.5 Thesis Overview: Au/Pd Nanostructures as a Model System for Examining Seed-Mediated Co-reduction	23
1.6 References	24
Chapter 2: The Shape-controlled Synthesis of Au/Pd Nanocrystals using Seed- Mediated Co-reduction	36
2.1 Introduction	37
2.2 Synthesis of Au/Pd Octopods and Concave Nanocrystals	38
2.3 Investigation of Synthetic Conditions that Control Architecture of Au/Pd Nanostructures Prepared by Seed-Mediated Co- Reduction	51
2.4 Synthetic Control of Au/Pd Nanostructures	53
2.5 Evaluation of Capping Agents	64

2.6 Optical Properties of Au/Pd Nanocrystals	70
2.7 Conclusions	73
2.8 References	74
Chapter 3: Elucidating the Role of Seed Structure in the Synthesis of Symmetrically Branched Nanocrystals	86
3.1 Introduction	87
3.2 Results and Discussion	89
3.3 Conclusions	101
3.4 References	101
Chapter 4: Optical Properties of Au/Pd Nanoparticles with Defined Architectures	107
4.1 Introduction	108
4.2 Size-Dependent Optical Properties of Au/Pd Octopods	109
4.3 Synthesis of Au/Pd Octopods and the Influence of Particle Size on LSPR Position	112
4.4 Refractive Index Sensitivities of Au/Pd Octopods	117
4.5 SERS Activities of Au/Pd Octopods	121
4.6 Summary of Findings from the LSPR Properties of Size-Controlled Au/Pd Octopods	123
4.7 Manipulating the Optical Properties of Symmetrically Branched Au/Pd Nanocrystals through Interior Design	124
4.8 Interior Design of Au/Pd Octopods through Selective Etching	126

4.9 LSPR Properties of Au/Pd Octopods with Compositionally Controlled Interiors	130
4.10 Summary of the Findings from the Synthesis and Optical Properties of Au/Pd Octopods with Compositionally Controlled Interiors	132
4.11 Overall Conclusions	133
4.12 Notes and References	133
Chapter 5: Shaping the Synthesis and Assembly of Symmetrically Stellated Au/Pd Nanocrystals with Aromatic Additives	142
5.1 Introduction	143
5.2 Results and Discussion	145
5.3 Conclusions	159
5.4 References	159
Chapter 6: Summary and Outlook	163
6.1 Summary of Chapters 2-5	164
6.2 Outlook	166
6.3 References	171
Appendix A: Experimental	175
Appendix B: Supplemental Figures	197
Appendix C: Octopod Volume Proof	247
Curriculum Vitae	

**Chapter 1: An Introduction to Bimetallic Noble Metal Nanocrystals and their
Properties**

1.1 Introduction

Inorganic materials, when confined on the nanoscale, can exhibit properties unique to their bulk-scale and molecular scale analogues. These properties are inherent to their size, shape, and composition.¹ Noble metal (Pd, Pt, Au, Ag) nanoparticles have garnered much attention due to their relative low resistance to oxidation compared to base metals and high electron densities. These two factors allow for two important properties. First, noble metal nanoparticle surfaces have low-coordination sites which can be altered for desirable surface affinities. Second, the electrons in the conduction band of noble metal nanoparticles can oscillate upon irradiation by an incident light source, allowing for a property known as localized surface plasmon resonance (LSPR). These fascinating properties enable noble metal nanoparticles to be employed in a diverse range of applications that include contrast enhancement agents in biomedical imaging platforms, vectors for cancer therapies, adsorbents for environmental remediation, and as heterogeneous catalysts.²⁻⁵ This chapter discusses recent uses of noble metal nanoparticles and their relevant plasmonic features as well as synthetic strategies to design bimetallic noble metal nanoparticles using the seed-mediated method. The goal of the experiments in this thesis is to establish new synthetic strategies for the design of bimetallic noble metal nanoparticles toward a wider range of morphologies, compositions, and, in turn, plasmonic properties.

1.2 The Synthetic Strategies toward Controlling the Shape of Noble Metal Nanoparticles⁶

Noble metal nanostructures can be hosts to a wide range of plasmonic applications, ranging from photothermal therapy to *in vivo* imaging and diagnostics. Still, the ability to manipulate the optical properties of quasi-spherical metal colloids through particle size and composition is limited, particularly when trying to extend the LSPR maximum into the near-infrared for applications in nanomedicine and solar energy utilization. This limitation is addressed by considering the shape of nanocrystals as an important parameter in the design of plasmonic colloids, as non-spherical nanoparticles can exhibit multiple LSPRs on account of lowering shape symmetry. Au nanorods, for example, exhibit longitudinal and transverse LSPRs corresponding to the long and short axes of their structure, respectively.⁷ Lowering of shape symmetry can also provide locations where electric field intensity can concentrate, colloquially known as “hot spots.”⁸ These hot spots facilitate detection of molecules, most popularly *via* surface-enhanced Raman spectroscopy (SERS) at remarkably low concentrations.⁹ Additionally, for non-spherical nanoparticles, changes in the polarization of the irradiating light can turn on and off specific hot-spots.¹⁰

Much of what is known about the optical properties of shape-controlled metal nanostructure has been enabled by the advances in synthesis, which now provide a range of shape-controlled nanostructures as high-quality samples.¹ Shapes range from Platonic solids, such as cubes and octahedra, to Archimedean solids, such as cuboctahedra, to Catalan solids, such as tetrahexahedra and rhombic dodecahedra.^{1, 11-15} Surfaces can be modified to have high-energy high-index facets, high angle vertices, and concavities.¹⁶

These structures can also be tailored in their size and composition. Three synthetic parameters have been emphasized when approaching the synthesis of shape-controlled nanocrystals: seed shape, capping agents present, and growth kinetics.

Many of the final structural characteristics of a nanoparticle are determined in the earliest stages of a nanomaterial synthesis. For example, *in situ* TEM studies of metal nanoparticle formation reveal that both monomer overgrowth and particle-particle cohesion can occur simultaneously, the latter which has been rationalized for the appearance of crystal defects in nanoparticles.¹⁷ Such crystal defects (*e.g.*, twin planes and stacking faults) direct which nanocrystal shapes are then synthetically accessible.^{1, 18} For example, single-crystalline nanocubes and octahedra generally form from single-crystalline seeds, whereas multiply-twinned nanorods form from pentagonally-twinned seeds.^{1, 7} In general, the use of a seed with a specific symmetry can facilitate the synthesis of a larger particle with the same or similar symmetry. The role of seed shape on final nanocrystal structure has been reviewed in the works of Xia and co-workers and the general principle is highlighted in **Figure 1.1**.^{1, 19} Significantly, the recognition that initial seed structures direct the shapes of the final nanostructures has led to the separation of the primary nucleation step from the subsequent overgrowth phase to improve the quality and structural complexity of shape-controlled nanocrystals. Such “seeded” methods are now premier means to shape-controlled nanocrystals given the continued challenges in predicting and controlling the earliest stages of nanomaterial syntheses.²⁰

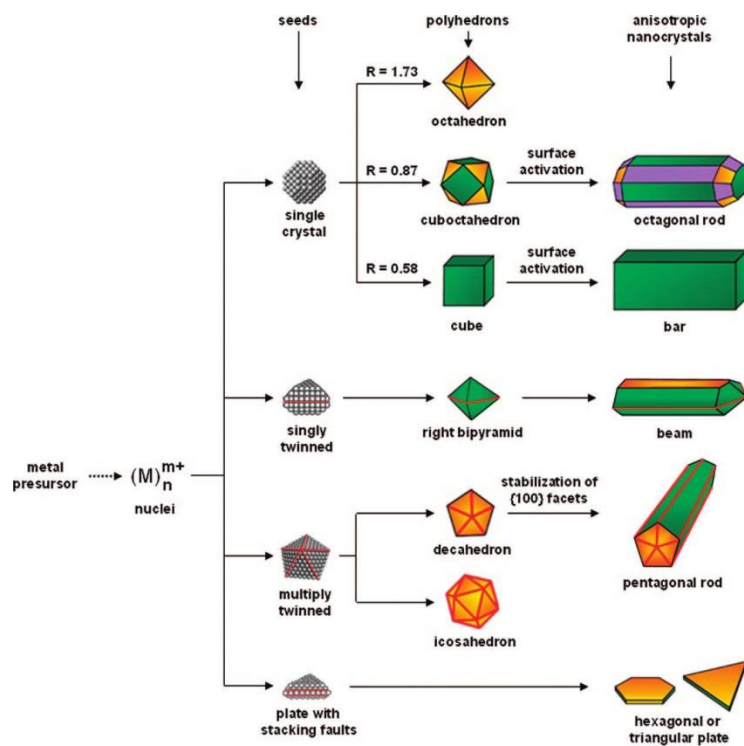


Figure 1.1. Schematic illustrating the importance of the initial seed structures in the role of the final particle shape. Reproduced from ref 19.

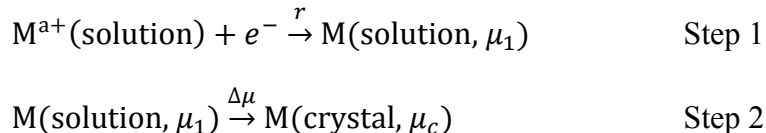
Capping agents (*e.g.*, ligands, polymers, anions, surfactants) also contribute to the final outcome from a nanomaterial synthesis. Aside from providing colloidal stability, capping agents can facilitate the preferential growth of specific facets and the adoption of a final nanocrystal shape.¹ Several factors have been postulated to explain the dynamic role capping agents have in controlling shape, ranging from preferential adsorption onto specific facets to kinetic control of adatom addition and diffusion.^{1, 21} As “facet blockers,” capping agents are thought to preferentially adsorb onto specific facets of seeds. This adsorption process provides a means of thermodynamic stabilization, inhibiting deposition at those sites and facilitating their expression in the final shape of the nanocrystals.^{22, 23} One illustration of the structure-directing effect of capping agents is from the synthesis of {111}-terminated Ag octahedra and {100}-terminated Ag

nanocubes from quasi-spherical Ag seeds in the presence of trisodium citrate or poly(vinylpyrrolidone) (PVP), respectively.²² In this example, all other synthetic parameters were held constant. The emergence of octahedra in the presence of citrate was consistent with density functional theory (DFT) calculations which found that citrate has a binding constant that is six orders of magnitude greater in adsorption to Ag(111) compared to Ag(100) on account of the favorable match of symmetry between the functional groups of citrate and the Ag(111) surface. In contrast, PVP preferentially adsorbs to {100} surfaces and {100}-terminated Ag nanocubes form.²²

In general, capping agents have been identified that can facilitate the preferential expression of low index facets in the colloidal synthesis of noble metals, but there is still a need to identify new capping agents which can stabilize higher index surfaces in order to facilitate the synthesis of completely new nanocrystals shapes. One promising development involves the use of phage display techniques to identify tailored peptides for use as capping agents.²³ In this approach, a library of peptide sequences are screened for their binding affinity at model surfaces and those with the greatest binding affinities can then be applied as capping agents to nanoparticle syntheses. For example, the T7 (TLTTLTN) peptide preferentially binds to Pt {100} surfaces, and {100}-terminated Pt nanocubes were formed when this peptide was used as a capping agent in the synthesis of Pt nanostructures. Importantly, the structural control of peptide sequences goes beyond stabilizing low-index metal surfaces. Nanostructures with complex morphologies, such as Pt multipods or Ag nanowires with a spiral structure, have been achieved with peptides that preferentially bind to higher energy surfaces or induce multiple nucleation events,

respectively. These findings hint toward a possibility of greater structural control through designer capping agents.

In conjunction with these “facet blocking” effects, capping agents as well as other additives to a synthesis can manipulate the kinetics of nanoparticle growth, which in turn can alter their shape towards higher energy surfaces and morphologies not predicted by capping agent selection. Shown in **Scheme 1.1** are two steps typically found in the growth of metal nanocrystals, where μ_1 is the chemical potential of metal atoms reduced in solution, μ_c is the chemical potential of metal atoms of the solid phase, and their difference $\Delta\mu$ is the thermodynamic driving force for crystallization (*i.e.*, the solution supersaturation).²¹ In Step 1, metal precursor M^{a+} is reduced and metal M attaches to the crystal in Step 2.



Scheme 1.1

In accordance with the Thompson-Gibbs equation, excess energy from a crystallization process contributes to the surface energy of crystallites at constant pressure and temperature. Recent work by Lin *et al.* illustrated that in seeded growth of Au nanocrystals, an increase in supersaturation results likewise in nanocrystals with higher energy facets expressed.²¹ This control was achieved chemically in accordance with **Scheme 1.1** by varying either the concentration of Au precursor or the reaction pH. In the case of precursor concentration, the nanocrystals adopted {111}-terminated octahedral, {111}/{100} cuboctahedral, and {100} cubic profiles with increasing supersaturation achieved by the increase in precursor. This trend is consistent with the

relative surface energies, γ , of low index facets for Au (*i.e.*, $\gamma_{[111]} < \gamma_{[100]} < \gamma_{[100]}$). In the case of reaction pH, ascorbic acid was used as a reducing agent for HAuCl₄ in aqueous solutions containing CTAB and the reduction rate is increased at high pH. Thus, Au nanocrystals adopt a cubic shape at low pH and trisoctahedral and rhombic dodecahedral shapes, with {331} and {110} facets, respectively, at higher pH. By surveying recent manuscripts on shape-controlled nanocrystals synthesis, Lin *et al.* concluded that manipulation of synthetic parameters that adjust solution supersaturation represents a general means of morphology control.²¹ However, we note that this control is likely to be most easily applied to seeded methods as the primary nucleation step results in a dramatic reduction in supersaturation. We also note that the interplay of different components in a synthesis can alter reduction processes, and thus supersaturation, in seemingly unpredictable ways. Deconvoluting these interactions is at the forefront of research in the area of nanomaterial synthesis.

In fact, Mirkin and co-workers recently outlined the rules governing Au nanocrystal formation in an aqueous, seed-mediated approach by decoupling the intertwined roles of seed morphology, capping agent, and growth kinetics.^{24, 25} These principles can be applied to the shape-controlled synthesis of metal nanocrystals with other compositions, which in turn will reveal new optical properties. For example, Pd nanocrystals typically have LSPRs in the UV region. However, under kinetically controlled growth conditions, Pd nanoplates can be prepared that have LSPRs that extend as far as 500 nm.²⁶ On account of their LSPRs extending into the visible region, these structures may be useful for LSPR-sensing and storage of hydrogen simultaneously. As

these synthetic strategies are applied to new compositions, it is envisioned that novel nanoparticles will be designed for new applications in colloidal plasmonics.

1.3 Plasmonic Properties of Single Metal Nanoparticles²⁷

Attention to synthetic details and improved characterization of nanoscale materials are providing general guidelines toward the design and synthesis of new nanostructures with unprecedented control over crystallite size, shape, and composition.^{1, 28, 29} These advances are increasing interest in plasmonic colloids, where it is now possible to correlate nanocrystal structure to optical properties such as localized surface plasmon resonance (LSPR).³⁰ This intrigue in colloidal plasmonics is based upon the ability to manipulate the light scattering and absorption properties of metal nanostructures as well as to concentrate light at their sharp features.²⁹ These abilities enable high sensitivity in plasmon-enhanced spectroscopic techniques such as surface-enhanced Raman spectroscopy (SERS).³¹ Additionally, high sensitivity to changes in refractive index (RI) has also been observed. In turn, metal nanostructures are being explored for sensor applications that include the selective detection of antigen-antibody binding events, volatile organic compounds, and even intermediates in catalytic processes.³² The plasmonic properties of metal nanostructures are also being exploited to provide contrast enhancement in biomedical imaging modalities as well as a platform for photothermal cancer treatment.³³ New directions that use plasmonic colloids as light-harvesting antennae for solar water splitting and other catalytic and energy applications are underway.³⁴

Much research in the field of colloidal plasmonics focuses on Au or Ag as monometallic size- and shape-controlled nanoparticles.^{28, 35, 36} This focus arises from the extinction (absorption + scattering) properties of Au and Ag nanoparticles occurring in the visible region along with the relative ease with which high-quality nanostructures can be achieved compared to other metals that could support a LSPR in the visible region. Gold nanorods arguably garner the most interest on account of the large range of the electromagnetic spectrum that is accessible by their longitudinal LSPR (from 600 to 1800 nm to date).^{7, 36} That is, Au nanorods with aspect ratios of 2 or greater (defined as the longitudinal axis (length) divided by the transverse axis (width) of the rods) display two LSPR peaks, corresponding to polarization along each axis of the nanorod. The longitudinal feature shifts linearly to longer wavelengths with increasing aspect ratio and demonstrates the ability to manipulate the extinction properties of metal colloids through shape-controlled syntheses for use in applications.⁷ For example, nanostructures with LSPRs in the near-infrared are of interest for biological applications as this region corresponds with where the attenuation of light by blood and soft tissue is minimal.⁴ Thus, drugs and targeting molecules can be loaded onto the surfaces of Au nanorods. These bioconjugated Au nanorods can then be injected in vivo, tracked as they move through a body by techniques such as photothermal or photoacoustic imaging, and the drugs can be released through irradiation of the nanorods at the corresponding LSPR. Gold nanoshells, nanocages, and nanostars also show promising optical properties of many applications, including those in the biomedical field.^{37, 38}

1.4 Multifunctional Properties of Bimetallic Nanoparticles²⁷

Given the excitement surrounding monometallic colloidal plasmonics, the recent interest in incorporating a second metal into colloidal platforms to achieve greater plasmonic modifiability or multifunctionality is not surprising.³⁹ The theoretical frequency of a surface plasmon localized to a spherical nanoparticle in vacuum is $\frac{\omega_p}{\sqrt{3}}$ where ω_p is the bulk plasmon frequency.⁴⁰ As **Equation 1.1** indicates, ω_p depends on the dielectric constant of the metal nanoparticle where $\epsilon_{bulk}(\omega)$ is the wavelength-dependent bulk dielectric constant, γ is the mean collision frequency of the conduction electrons, v_F is the Fermi velocity of the bulk metal, and R is the radius of the nanoparticle.^{41, 42} In the case of bimetallic *alloyed* colloids, the dielectric constant will be distinct from either of the individual metals. Thus, composition provides a synthetic lever to manipulate the plasmonic properties of colloids. However, achieving sample monodispersity and shape control for alloyed nanostructures is synthetically challenging, but these features are required for bimetallic colloids to be used in many applications. To address this limitation, contemporary synthetic protocols for bimetallic nanostructures often use a seed-mediated method to ensure structural homogeneity, wherein presynthesized nanoparticle “seeds” are used as a structurally defined platform for deposition of the second metal.^{43, 44} As shown in the center of **Figure 1.2**, the seed-mediated method can provide access to a variety of bimetallic architectures, ranging from conformal core@shell nanocrystals to structures with regionally localized compositions or alloyed shells. Each of these bimetallic architectures displayed optical properties different from those of its monometallic analogue.

$$\varepsilon(R, \omega) = \varepsilon_{bulk}(\omega) + \frac{\omega_p^2}{\omega^2 + i\omega\gamma} - \frac{\omega_p^2}{\omega^2 + i\omega\left(\gamma + \frac{v_F}{R}\right)}$$

Equation 1.1

Historically, interest in the plasmonic properties of bimetallic colloids focused on those composed of Au interiors and Ag exteriors.⁴⁵⁻⁴⁷ This focus arises not only from the ability of each metal to independently support a LSPR in the visible region but also from the diversity of shape-controlled Au nanocrystals available for use as seeds, which are resistant to galvanic replacement. For example, Xiang et al. deposited Ag shells onto Au nanorods via the seed-mediated method to achieve Au@Ag nanorods, controlling the thickness of the Ag shells through the deposition process.⁴⁸ Even thin coatings (less than 2 nm) of Ag result in a blue shift of the longitudinal LSPR by over 50 nm, and this observation can be attributed to the change in polarizability and restoring force for the oscillatory electrons that arise from the core@shell architecture.^{42, 49} The ability to modify the resonant wavelength of Au@Ag nanorods allows for the intensity of SERS features to be maximized by ensuring overlap between the LSPR and incident laser wavelength.⁵⁰ Two transverse LSPRs appear at shorter wavelengths (compared to only one resonance in the Au-only case) and have been ascribed to the outer Ag shell and the interface between the Au core and Ag shell. These transverse LSPRs do not shift in position appreciably as the shell thickness increases. Ultrafast transient absorption spectroscopy experiments by Yu et al. demonstrated that the longitudinal feature consists of two overlapping resonances, likewise corresponding to the Ag shell and Au interior.⁵¹ Interestingly, Au@Ag nanorods display narrower ensemble linewidths compared to Au nanorods at the same resonant wavelength, and this feature is referred to as plasmon

focusing, which was studied by Becker et al. (**Figure 1.2A**).⁵² The addition of Ag layers to Au nanocrystals to form Au@Ag nanocubes via a seed-mediated method also leads to reduced broadening of the most intense LSPR peak.^{53, 54} It was noted by Ma et al. that the optical properties of the Au core could be completely screened by the Ag shell when sufficiently thick. For example, Au@Ag nanocubes with a core diameter of 11 nm exhibit properties similar to Ag nanocubes when the Ag shell is greater than 2 nm, whereas two LSPRs are observed when the Ag shell thickness is between 1 and 2 nm (**Figure 1.2B**). These results are consistent with computations using discrete dipole approximation (DDA) method.⁵³

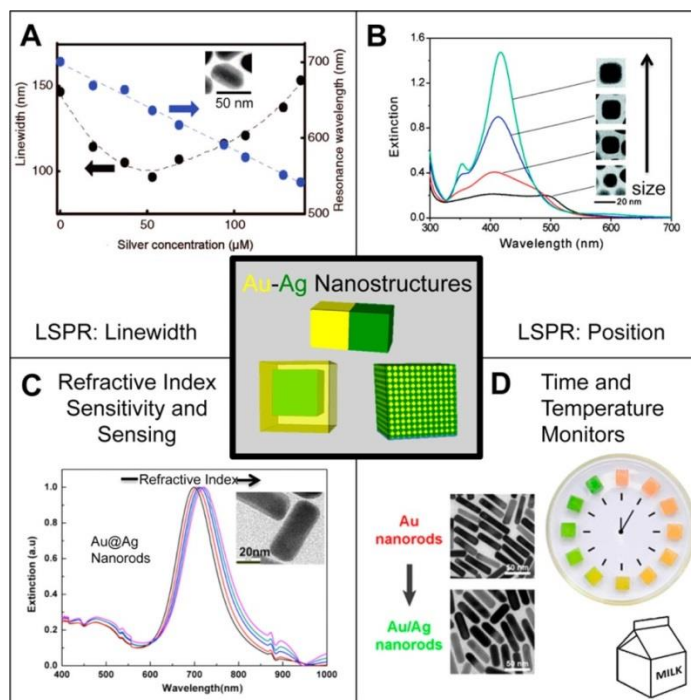


Figure 1.2. The center square represents the variety of Au–Ag nanomaterials that can be prepared by seeded methods and includes conformal core@shell nanocrystals, structures with regionally localized compositions, or alloyed shells. (A) Resonance wavelength (blue dots) and linewidth (black dots) with respect to the concentration of Ag present during the synthesis of Au@Ag nanorods. Reprinted from ref 52. (B) Extinction spectrum of Au@Ag nanocubes with increasing Ag shell thickness. Reprinted from ref 53. (C) Extinction spectra of Au@Ag nanorods in solvents with different RI. Reprinted from ref 55. (D) A schematic representing the color change during the time-temperature dependent synthesis of Au@Ag nanorods. As time increases, the thickness of the Ag shell increases. This modification results in a color change from red to green, which indicates the perishable good has expired. Reprinted from ref 61. Figure compiled in ref 27.

As these optical features often improve the properties of Au-only nanocrystals, Au@Ag nanorods and nanocubes are being considered for use as sensors based on RI sensitivity as their figure of merit (FOM) will be improved in ensemble measurements (FOM = RI sensitivity/fwhm, where fwhm is the full width at half-maximum of the resonance, see Mayer et al. for full discussion of calculations).^{31, 55} For example, the RI sensitivities of Au@Ag nanobars were compared to those of Au nanorod seeds as a function of Ag shell thickness by Fu et al. (**Figure 1.2C**).^{55, 56} They found that both the sensitivity and FOM increased with increasing Ag shell thickness (up to ~5 nm) despite the blue-shifted LSPR position of the Au@Ag nanorod samples relative to the Au nanorod seeds. Beyond a shell thickness of 5 nm, the sensitivity and FOM were found to decrease, and this observation was attributed to nonconformal Ag deposition onto the seeds and changes in the nanostructure shape. The RI sensitivity of Au@Ag nanobars was similarly compared to that of Au nanorods.⁵⁶ Although the surface terminations differ between these one-dimensional structures, larger RI sensitivities and greater FOMs were measured for the Au@Ag nanobars. Recently, Lu et al. demonstrated plasmon-induced circular dichroism resonance from Au@Ag nanocubes.⁵⁷ These structures provided between 85- and 103-fold enhancements per molecule when DNA was functionalized on their surfaces, and they represent plasmonic reporters of molecular chirality. Also, Au@Ag nanostructures are being used as SERS substrates for the high-throughput detection of proteins and nucleic acids as well as water contaminants such as mercuric ions.⁵⁸⁻⁶⁰ As an interesting variation on optical applications of Au@Ag nanostructures, Zhang et al. found that the rate of Ag deposition onto Au nanorods can be synchronized with the growth of *E. coli* to provide a chronochromic platform to track

food spoilage.⁶¹ Shown in **Figure 1.2D** is a schematic to illustrate this process. Initially, the Au nanorods appear red, but with time, Ag shells were deposited onto the Au nanorod “seeds.” The deposition of Ag shells resulted in a noticeable color change to green. These results highlight the opportunities enabled through the design of bimetallic nanostructures with core@shell architectures.

Finally, Au–Ag nanostructures with spatially segregated metal domains and alloyed compositions have been prepared via seeded methods. For example, Ag–Au–Ag segmented nanorods with a pentagonal cross section were prepared by depositing Ag onto decahedral Au seeds.⁶² Similarly, Ag can grow perpendicularly to the basal plane of circular Au nanoplates to form elongated Au@Ag polyhedral wherein the Au nanoplates are localized in the interior of the structure.⁶³ Localized overgrowth is typically achieved through manipulation of reaction kinetics, as recently demonstrated by Yang et al. in their study of Ag/Au nanorods from decahedral Au seeds. They found that slow growth yielded asymmetric Ag–Au–Ag nanorods, whereas fast growth allowed for uniform Ag coverage on both sides of the Au seed.⁶⁴ In most of these examples of bimetallic nanostructures with spatially segregated metal domains, the optical properties have not been extensively studied. However, one potential benefit of these heterostructures is that the Ag regions should provide higher SERS efficiencies than Au structures alone, and these domains can be partially etched via galvanic replacement to achieve nanostructures with hollow features.^{64, 65} Galvanic replacement with nanocrystals templates is inherently a seeded method, with the seed oxidized as the metal precursor is reduced by the seed. The most common examples involve shape-controlled Ag nanocrystals as seeds to form alloyed Au–Ag nanocage structures, where the light absorption and scattering properties

can be tuned by the extent of exchange.^{38, 66} These structures have garnered significant interest for biomedical applications on account of their optical properties.⁶⁷ We also note that galvanic replacement can be suppressed to achieve Ag@Au nanostructures, as demonstrated with Ag nanoplates as seeds.⁶⁸

These examples of Au–Ag bimetallic nanostructures provide general guidelines on how composition and structure can be integrated into one platform to achieve desirable light scattering and absorption properties. Although most research on colloidal plasmonics has been biased toward Au- and Ag-based platforms, current research is looking beyond these two metals. New nanostructures are being synthesized from metals that typically do not support LSPRs in the visible region in addition to those that do to provide additional function. Pd and Pt, for example, are catalysts for a range of reactions.^{32, 69, 70} Incorporating either of these metals into Au or Ag nanocrystals could provide nanoarchitectures with both optical and catalytic capabilities. In practice, numerous bimetallic compositions can be considered to provide multifunctional colloidal platforms with tunable plasmonic properties, although Au–Pd nanostructures have been some of the most actively investigated over the past 5 years.⁷¹ This emphasis can be accounted for by the ability to deposit Pd onto a variety of size-, shape-, and architecturally controlled Au nanostructures available for seed-mediated syntheses.

With the seed-mediated method, conformal deposition of Pd onto Au seeds has been found to form Au@Pd nanoparticles in a variety of shapes, including those terminating in low-index facets such as cubes and octahedra as well as those with high-index facets such as tetrahedra and concave cubes.⁷²⁻⁸¹ The core@shell architecture is particularly useful for catalysis because a smaller quantity of the more expensive Pd is

required per particle compared to the Pd-only analogues. However, Au@Pd nanoparticles without much anisotropy are not explored for their optical properties due to their blue-shifted LSPRs and damped signals.⁸² To capitalize on the optical properties of nanoscale Au in Au–Pd platforms, anisotropic Au nanostructures should be used as seeds for Pd deposition, considering that such structures provide intense LSPRs in the visible and near infrared regions of electromagnetic spectrum. Toward this end, a range of Au@Pd shapes have all been achieved by seed-mediated methods. Examples include nano-bars, nanorods, and trisoctahedra.^{79, 83, 84}

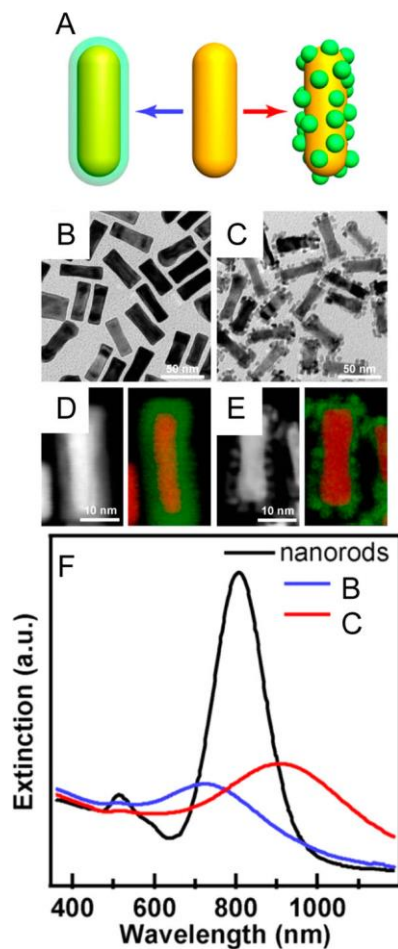


Figure 1.3. (A) Schematic of nanorods: Au@Pd, Au, and Au with Pd islands. (B) TEM image of Au@Pd nanorods and (C) Au nanorods with Pd islands. (D,E) STEM (left) and elemental mapping by EDX (right) of (D) Au@Pd nanorods and (E) Au nanorods with Pd islands, where Au is red and Pd is green. (F) Extinction spectra of Au nanorods, Au@Pd nanorods (the blue line corresponds to the sample in C). Reprinted from ref 86.

Similar to their Au@Ag analogues, Au@Pd nanorods and nanobars have LSPRs that depend on the thickness of the Pd shell. A blue shift of the LSPR is observed as the shell thickness increases, just as in the Au@Ag examples.⁸⁴ It is also noted that the LSPR absorption maximum dampens as the Pd shell thickness increases on account of the decreased surface electron density of Pd relative to Au.⁸⁵ Moreover, Crut et al.

investigated the acoustic vibrations of Au@Pd nanorods and Au nanorods via ultrafast pump-probe spectroscopy.⁸³ They found that the periods of their oscillations decreased for the extensional mode and increased for the breathing mode with increasing thickness of the Pd shell. These findings may provide design strategies toward ultrasensitive mechanical nanosensors and highlight the utility of this technique to understand the spatial distribution of dilute metals in bimetallic nanostructures. Understanding how the spatial distribution of metals influences the fundamental properties of bimetallic colloids is critical, considering advances in synthesis that now enable the selective localization of metal on specific features of seeds. For example, Chen et al. synthesized Au nanorods decorated with Pd islands and compared their optical properties to Au-only and Au@Pd nanorods with conformal Pd deposition (**Figure 1.3**).⁸⁶ Interestingly, the Au nanorods with Pd islands displayed a red-shifted LSPR relative to the Au nanorod seeds (**Figure 1.3F**). This observation contrasts with the blue-shifted LSPR from samples in which Pd is conformal with respect to the Au nanorod seeds. The red shift was attributed to the discontinuous Pd behaving like a dielectric shell. Further analysis found that the plasmon wavelength depended on the Pd volume fraction in the shell, with the LSPR transitioning from a red shift to a blue shift relative to the Au-only nanorods at ~70% Pd composition. This plasmonic percolation behavior was ascribed to the transition from positive to negative for the real part of the dielectric function for the shell. These results were corroborated with finite difference time domain (FDTD) simulations.⁸⁶

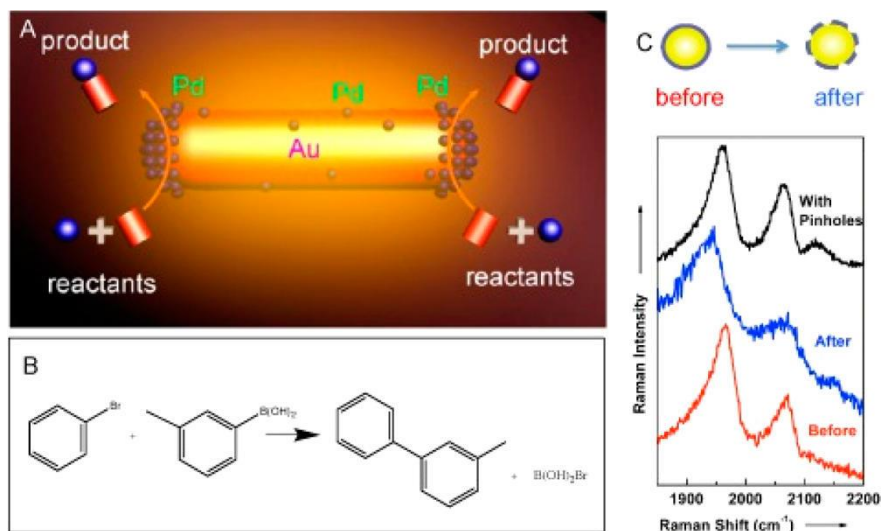


Figure 1.4. The plasmonic and catalytic capabilities of Au/Pd nanoparticles. (A) Schematic of Au nanorods with Pd islands as plasmon-based Suzuki cross-coupling catalysts. (B) Example of the Suzuki cross-coupling reaction between bromobenzene and *m*-tolylboronic acid, which is achieved with the nanostructure in (A). Reprinted from ref 87. (C) Surface-enhanced Raman spectra of adsorbed CO on Au@Pd nanoparticles before use as Suzuki-Miyaura cross-coupling catalysts, after catalysis, and on Au@Pd nanoparticles with pinholes exposing the Au core. Characteristic bands of CO on Pd are at 1960 and 2017 cm⁻¹ (before reaction, red). A third band appears at 2100 cm⁻¹ after the catalysis reaction (blue) due to exposed Au. The origin of this band is confirmed with Au@Pd nanoparticles exposed Au. Reprinted from ref 89.

With the optical properties of Au–Pd nanostructures being elucidated, new opportunities are opening up by coupling the chemistry of Pd with the optical properties of nanoscale Au. As shown in Figure 1.4, one area where the multifunctionality of bimetallic Au–Pd nanostructures is being utilized is catalysis. For example, Wang et al. used Au nanorods with Pd localized at the tips for catalysis for Suzuki cross-coupling

reactions (**Figure 1.4A**).⁸⁷ When illuminated with an 809 nm laser (1.68 W) at room temperature, a yield of nearly 99% was obtained for the reaction between bromobenzene and *m*-tolylboronic acid within 1 h (**Figure 1.4B**). In contrast, no product was obtained without illumination, and only an 18% yield was obtained from illumination of a mixture of discrete Au and Pd nanoparticles. The acceleration enabled by the Pd-tipped Au nanorods was attributed to both plasmonic photocatalysis and photothermal conversion. Similarly, Au@Pd nanowheels were found to be efficient photocatalysts for the oxidation of benzyl alcohol to benzaldehyde and the Suzuki coupling of iodobenzene with phenylboronic acid.⁸⁸ In related work, Fang et al. examined the mechanism of Suzuki—Miyaura cross-coupling reactions through the use of Au nanoparticles coated with thin Pd shells.⁸⁹ To evaluate whether or not Pd was leaching from the nanoparticle surface, they relied on the well-characterized SERS band of CO adsorbed on Pd and Au surfaces (**Figure 1.3C**). Prior to use of the Au@Pd nanoparticles, only bands consistent with CO bound to Pd were observed; however, a third band consistent with CO bound to Au appeared after the use of the particles. When coupled to electrochemical and ICP-MS analysis, it was determined that the observed activity arises primarily from Pd atoms or clusters leached from the surface. Considering this example and prior work by Wong and Halas, it should also be possible to identify and monitor reaction intermediates under operating conditions via plasmon-enhanced surface spectroscopies with appropriately designed bimetallic nanostructures.⁹⁰ Overall, Au@Pd nanostructures are part of a new class of bimetallic colloids that go beyond standard catalysis to provide multifunctional platforms for light harvesting and spectroscopic monitoring of catalytic processes through their modifiable plasmonic features.

1.5 Thesis Overview: Au/Pd Nanostructures as a Model System for Examining Seed-Mediated Co-reduction

As the previous examples illustrate, the seed-mediated method is typically used to deposit one metal on top of seeds. Conformal core@shell structures are prevalent in the literature and showcase the versatility of this technique. However, there is still work that can be done to better attenuate the surface composition of bimetallic nanostructures. For example, if a core@shell nanoparticle had an alloyed shell, a range of surface compositions—and thus surface chemistries—may be accessible. The work in this thesis looks to expand the field of synthetically feasible bimetallic nanostructures toward greater functionality by developing synthetic approaches to achieve a wider range of morphologies and compositions. Specifically, the central thrust of this thesis is the development of a synthetic approach termed “seed-mediated co-reduction” wherein two dissolved metal precursors are reduced simultaneously to deposit metal onto pre-formed metal seeds. The central hypothesis is that the interplay between two metal species during co-reduction would allow for core@alloy shell compositions. The test system was Au and Pd due to their small lattice mismatch ($\sim 4.6\%$), availability of precursors with similar reduction potentials and reduction kinetics, favorable miscibility of Au and Pd, and literature precedent for Au@Pd nanocrystals.⁹¹ In brief, the goal of core@alloy Au@Au/Pd shape-controlled nanocrystals was achieved. Unexpectedly, altering the pH of the growth solution during the co-reduction step facilitated the formation of concave nanocrystals. In particular, eight-branched nanostructures, termed “octopods” with O_h symmetry formed.

The work of this thesis involves the synthesis, characterization, and assembly of Au/Pd nanostructures using the seed-mediated co-reduction method. Chapter 2 addresses the initial hypothesis that shape-controlled core@alloy shell nanocrystals can be achieved by seed-mediated co-reduction and provides a comprehensive examination of the role various synthetic parameters contribute to structurally defined Au-Pd nanocrystals in general. Chapter 3 investigates the role of seed shape in determining the symmetry of branched nanostructures formed via seed-mediated co-reduction. Chapter 4 examines how the size and composition of Au/Pd octopods contribute to their tunable optical features. Chapter 5 describes an approach to enhance the monodispersity of stellated samples prepared via seed-mediated co-reduction to achieve large area assemblies. Finally, Chapter 6 gives a brief outlook into future directions of bimetallic nanostructures for plasmonic applications.

1.6 References

1. Xia, Y.; Xiong, Y.; Lim, B.; Skrabalak, S. E., Shape-Controlled Synthesis of Metal Nanocrystals: Simple Chemistry Meets Complex Physics? *Angew. Chem. Int. Ed.* **2009**, *48*, 60-103.
2. Li, C., A targeted approach to cancer imaging and therapy. *Nat. Mater.* **2014**, *13*, 110-115.
3. Ojea-Jiménez, I.; López, X.; Arbiol, J.; Puntès, V., Citrate-Coated Gold Nanoparticles As Smart Scavengers for Mercury(II) Removal from Polluted Waters. *ACS Nano* **2012**, *6*, 2253-2260.

4. Jain, P. K.; Huang, X.; El-Sayed, I. H.; El-Sayed, M. A., Noble Metals on the Nanoscale: Optical and Photothermal Properties and Some Applications in Imaging, Sensing, Biology, and Medicine. *Acc. Chem. Res.* **2008**, *41*, 1578-1586.
5. Linic, S.; Christopher, P.; Xin, H.; Marimuthu, A., Catalytic and Photocatalytic Transformations on Metal Nanoparticles with Targeted Geometric and Plasmonic Properties. *Acc. Chem. Res.* **2013**, *46*, 1890-1899.
6. Motl, N. E.; Smith, A. F.; DeSantis, C. J.; Skrabalak, S. E., Engineering plasmonic metal colloids through composition and structural design. *Chem. Soc. Rev.* **2014**, *43*, 3823-3834.
7. Lohse, S. E.; Murphy, C. J., The Quest for Shape Control: A History of Gold Nanorod Synthesis. *Chem. Mater.* **2013**, *25*, 1250-1261.
8. Alvarez-Puebla, R.; Liz-Marzán, L. M.; García de Abajo, F. J., Light Concentration at the Nanometer Scale. *J. Phys. Chem. Lett.* **2010**, *1*, 2428-2434.
9. Xu, H.; Bjerneld, E. J.; Kall, M.; Borjesson, L., Spectroscopy of single hemoglobin molecules by surface enhanced Raman scattering. *Phys. Rev. Lett.* **1999**, *83*, 4357-4360.
10. Khatua, S.; Chang, W.-S.; Swanglap, P.; Olson, J.; Link, S., Active Modulation of Nanorod Plasmons. *Nano Lett.* **2011**, *11*, 3797-3802.
11. Tian, N.; Zhou, Z.-Y.; Sun, S.-G.; Ding, Y.; Wang, Z. L., Synthesis of Tetrahedral Platinum Nanocrystals with High-Index Facets and High Electro-Oxidation Activity. *Science* **2007**, *316*, 732-735.
12. Kim, D. Y.; Im, S. H.; Park, O. O., Synthesis of Tetrahedral Gold Nanocrystals with High-Index Facets. *Cryst. Growth Des.* **2010**, *10*, 3321-3323.

13. Kim, D.; Lee, Y. W.; Lee, S. B.; Han, S. W., Convex Polyhedral Au@Pd Core–Shell Nanocrystals with High-Index Facets. *Angew. Chem. Int. Ed.* **2012**, *51*, 159-163.
14. Niu, W.; Zheng, S.; Wang, D.; Liu, X.; Li, H.; Han, S.; Chen, J.; Tang, Z.; Xu, G., Selective Synthesis of Single-Crystalline Rhombic Dodecahedral, Octahedral, and Cubic Gold Nanocrystals. *J. Am. Chem. Soc.* **2008**, *131*, 697-703.
15. Zhang, H.; Jin, M.; Xiong, Y.; Lim, B.; Xia, Y., Shape-Controlled Synthesis of Pd Nanocrystals and Their Catalytic Applications. *Acc. Chem. Res.* **2013**, *46*, 1783-1794.
16. Zhang, H.; Jin, M.; Xia, Y., Noble-Metal Nanocrystals with Concave Surfaces: Synthesis and Applications. *Angew. Chem. Int. Ed.* **2012**, *51*, 7656-7673.
17. Yuk, J. M.; Park, J.; Ercius, P.; Kim, K.; Hellebusch, D. J.; Crommie, M. F.; Lee, J. Y.; Zettl, A.; Alivisatos, A. P., High-Resolution EM of Colloidal Nanocrystal Growth Using Graphene Liquid Cells. *Science* **2012**, *336*, 61-64.
18. Rocha, T. C. R.; Zanchet, D., Structural Defects and Their Role in the Growth of Ag Triangular Nanoplates. *J. Phys. Chem. C* **2007**, *111*, 6989-6993.
19. Skrabalak, S. E.; Xia, Y., Pushing Nanocrystal Synthesis toward Nanomanufacturing. *ACS Nano* **2009**, *3*, 10-15.
20. Wiley, B. J.; Chen, Y.; McLellan, J. M.; Xiong, Y.; Li, Z.-Y.; Ginger, D.; Xia, Y., Synthesis and Optical Properties of Silver Nanobars and Nanorice. *Nano Lett.* **2007**, *7*, 1032-1036.
21. Lin, H.-x.; Lei, Z.-c.; Jiang, Z.-y.; Hou, C.-p.; Liu, D.-y.; Xu, M.-m.; Tian, Z.-q.; Xie, Z.-x., Supersaturation-Dependent Surface Structure Evolution: From Ionic, Molecular to Metallic Micro/Nanocrystals. *J. Am. Chem. Soc.* **2013**, *135*, 9311-9314.

22. Xia, X.; Zeng, J.; Zhang, Q.; Moran, C. H.; Xia, Y., Recent Developments in Shape-Controlled Synthesis of Silver Nanocrystals. *J. Phys. Chem. C* **2012**, *116*, 21647-21656.
23. Briggs, B. D.; Knecht, M. R., Nanotechnology Meets Biology: Peptide-based Methods for the Fabrication of Functional Materials. *J. Phys. Chem. Lett.* **2012**, *3*, 405-418.
24. Langille, M. R.; Personick, M. L.; Zhang, J.; Mirkin, C. A., Defining Rules for the Shape Evolution of Gold Nanoparticles. *J. Am. Chem. Soc.* **2012**, *134*, 14542-14554.
25. Personick, M. L.; Mirkin, C. A., Making Sense of the Mayhem behind Shape Control in the Synthesis of Gold Nanoparticles. *J. Am. Chem. Soc.* **2013**, *135*, 18238-18247.
26. Xiong, Y.; McLellan, J. M.; Chen, J.; Yin, Y.; Li, Z.-Y.; Xia, Y., Kinetically Controlled Synthesis of Triangular and Hexagonal Nanoplates of Palladium and Their SPR/SERS Properties. *J. Am. Chem. Soc.* **2005**, *127*, 17118-17127.
27. DeSantis, C. J.; Weiner, R. G.; Radmilovic, A.; Bower, M. M.; Skrabalak, S. E., Seeding Bimetallic Nanostructures as a New Class of Plasmonic Colloids. *J. Phys. Chem. Lett.* **2013**, *4*, 3072-3082.
28. Rycenga, M.; Cobley, C. M.; Zeng, J.; Li, W.; Moran, C. H.; Zhang, Q.; Qin, D.; Xia, Y., Controlling the Synthesis and Assembly of Silver Nanostructures for Plasmonic Applications. *Chem. Rev.* **2011**, *111*, 3669-3712.
29. Grzelczak, M.; Liz-Marzán, L. M., Colloidal Nanoplasmonics: From Building Blocks to Sensing Devices. *Langmuir* **2013**, *29*, 4652-4663.

30. Henry, A.-I.; Bingham, J. M.; Ringe, E.; Marks, L. D.; Schatz, G. C.; Van Duyne, R. P., Correlated Structure and Optical Property Studies of Plasmonic Nanoparticles. *J. Phys. Chem. C* **2011**, *115*, 9291-9305.
31. Mayer, K. M.; Hafner, J. H., Localized Surface Plasmon Resonance Sensors. *Chem. Rev.* **2011**, *111*, 3828-3857.
32. Pérez-Lorenzo, M., Palladium Nanoparticles as Efficient Catalysts for Suzuki Cross-Coupling Reactions. *J. Phys. Chem. Lett.* **2011**, *3*, 167-174.
33. Dreaden, E. C.; Alkilany, A. M.; Huang, X.; Murphy, C. J.; El-Sayed, M. A., The golden age: gold nanoparticles for biomedicine. *Chem. Soc. Rev.* **2012**, *41*, 2740-2779.
34. Mubeen, S.; Lee, J.; Singh, N.; Kraemer, S.; Stucky, G. D.; Moskovits, M., An autonomous photosynthetic device in which all charge carriers derive from surface plasmons. *Nat. Nanotechnol.* **2013**, *8*, 247-251.
35. Odom, T. W.; Nehl, C. L., How Gold Nanoparticles Have Stayed in the Light: The 3M's Principle. *ACS Nano* **2008**, *2*, 612-616.
36. Chen, H.; Shao, L.; Li, Q.; Wang, J., Gold nanorods and their plasmonic properties. *Chem. Soc. Rev.* **2013**, *42*, 2679-2724.
37. Mieszawska, A. J.; Mulder, W. J. M.; Fayad, Z. A.; Cormode, D. P., Multifunctional Gold Nanoparticles for Diagnosis and Therapy of Disease. *Molecular Pharmaceutics* **2013**, *10*, 831-847.
38. Skrabalak, S. E.; Chen, J.; Sun, Y.; Lu, X.; Au, L.; Cobley, C. M.; Xia, Y., Gold Nanocages: Synthesis, Properties, and Applications. *Acc. Chem. Res.* **2008**, *41*, 1587-1595.

39. Cortie, M. B.; McDonagh, A. M., Synthesis and Optical Properties of Hybrid and Alloy Plasmonic Nanoparticles. *Chem. Rev.* **2011**, *111*, 3713-3735.
40. Lu, X.; Rycenga, M.; Skrabalak, S. E.; Wiley, B.; Xia, Y., Chemical Synthesis of Novel Plasmonic Nanoparticles. *Annu. Rev. Phys. Chem.* **2009**, *60*, 167-192.
41. Motl, N. E.; Ewusi-Annan, E.; Sines, I. T.; Jensen, L.; Schaak, R. E., Au–Cu Alloy Nanoparticles with Tunable Compositions and Plasmonic Properties: Experimental Determination of Composition and Correlation with Theory. *J. Phys. Chem. C* **2010**, *114*, 19263-19269.
42. Moskovits, M.; Srnova-Sloufova, I.; Vlckova, B., Bimetallic Ag–Au nanoparticles: Extracting meaningful optical constants from the surface-plasmon extinction spectrum. *J. Chem. Phys.* **2002**, *116*, 10435-10446.
43. Habas, S. E.; Lee, H.; Radmilovic, V.; Somorjai, G. A.; Yang, P., Shaping binary metal nanocrystals through epitaxial seeded growth. *Nat. Mater.* **2007**, *6*, 692-697.
44. Fan, F.-R.; Liu, D.-Y.; Wu, Y.-F.; Duan, S.; Xie, Z.-X.; Jiang, Z.-Y.; Tian, Z.-Q., Epitaxial Growth of Heterogeneous Metal Nanocrystals: From Gold Nano-octahedra to Palladium and Silver Nanocubes. *J. Am. Chem. Soc.* **2008**, *130*, 6949-6951.
45. Liu; Guyot-Sionnest, P., Synthesis and Optical Characterization of Au/Ag Core/Shell Nanorods. *J. Phys. Chem. B* **2004**, *108*, 5882-5888.
46. Huang, C.-C.; Yang, Z.; Chang, H.-T., Synthesis of Dumbbell-Shaped Au–Ag Core–Shell Nanorods by Seed-Mediated Growth under Alkaline Conditions. *Langmuir* **2004**, *20*, 6089-6092.

47. Song, J. H.; Kim, F.; Kim, D.; Yang, P., Crystal Overgrowth on Gold Nanorods: Tuning the Shape, Facet, Aspect Ratio, and Composition of the Nanorods. *Chem. Eur. Jour.* **2005**, *11*, 910-916.
48. Xiang, Y.; Wu, X.; Liu, D.; Li, Z.; Chu, W.; Feng, L.; Zhang, K.; Zhou, W.; Xie, S., Gold Nanorod-Seeded Growth of Silver Nanostructures: From Homogeneous Coating to Anisotropic Coating. *Langmuir* **2008**, *24*, 3465-3470.
49. Zhu, J., Surface Plasmon Resonance from Bimetallic Interface in Au-Ag Core-Shell Structure Nanowires. *Nanoscale Res. Lett.* **2009**, *4*, 977-981.
50. Lombardi, J. R.; Birke, R. L., A Unified View of Surface-Enhanced Raman Scattering. *Acc. Chem. Res.* **2009**, *42*, 734-742.
51. Yu, K.; You, G.; Polavarapu, L.; Xu, Q.-H., Bimetallic Au/Ag Core-Shell Nanorods Studied by Ultrafast Transient Absorption Spectroscopy under Selective Excitation. *J. Phys. Chem. C* **2011**, *115*, 14000-14005.
52. Becker, J.; Zins, I.; Jakab, A.; Khalavka, Y.; Schubert, O.; Sönnichsen, C., Plasmonic Focusing Reduces Ensemble Linewidth of Silver-Coated Gold Nanorods. *Nano Lett.* **2008**, *8*, 1719-1723.
53. Ma, Y.; Li, W.; Cho, E. C.; Li, Z.; Yu, T.; Zeng, J.; Xie, Z.; Xia, Y., Au@Ag Core-Shell Nanocubes with Finely Tuned and Well-Controlled Sizes, Shell Thicknesses, and Optical Properties. *ACS Nano* **2010**, *4*, 6725-6734.
54. Park, G.; Seo, D.; Jung, J.; Ryu, S.; Song, H., Shape Evolution and Gram-Scale Synthesis of Gold@Silver Core-Shell Nanopolyhedrons. *J. Phys. Chem. C* **2011**, *115*, 9417-9423.

55. Fu, Q.; Zhang, D. G.; Yi, M. F.; Wang, X. X.; Chen, Y. K.; Wang, P.; Ming, H., Effect of shell thickness on a Au–Ag core–shell nanorods-based plasmonic nano-sensor. *J. Optics* **2012**, *14*, 085001.
56. Lee, Y. H.; Chen, H.; Xu, Q.-H.; Wang, J., Refractive Index Sensitivities of Noble Metal Nanocrystals: The Effects of Multipolar Plasmon Resonances and the Metal Type. *J. Phys. Chem. C* **2011**, *115*, 7997-8004.
57. Lu, F.; Tian, Y.; Liu, M.; Su, D.; Zhang, H.; Govorov, A. O.; Gang, O., Discrete Nanocubes as Plasmonic Reporters of Molecular Chirality. *Nano Lett.* **2013**, *13*, 3145-3151.
58. Wu, L.; Wang, Z.; Zong, S.; Huang, Z.; Zhang, P.; Cui, Y., A SERS-based immunoassay with highly increased sensitivity using gold/silver core-shell nanorods. *Biosens. Bioelectron.* **2012**, *38*, 94-99.
59. Wang, Z.; Zong, S.; Li, W.; Wang, C.; Xu, S.; Chen, H.; Cui, Y., SERS-Fluorescence Joint Spectral Encoding Using Organic–Metal–QD Hybrid Nanoparticles with a Huge Encoding Capacity for High-Throughput Biodetection: Putting Theory into Practice. *J. Am. Chem. Soc.* **2012**, *134*, 2993-3000.
60. Chen, S.; Liu, D.; Wang, Z.; Sun, X.; Cui, D.; Chen, X., Picomolar detection of mercuric ions by means of gold-silver core-shell nanorods. *Nanoscale* **2013**, *5*, 6731-6735.
61. Zhang, C.; Yin, A.-X.; Jiang, R.; Rong, J.; Dong, L.; Zhao, T.; Sun, L.-D.; Wang, J.; Chen, X.; Yan, C.-H., Time–Temperature Indicator for Perishable Products Based on Kinetically Programmable Ag Overgrowth on Au Nanorods. *ACS Nano* **2013**, *7*, 4561-4568.

62. Seo, D.; Yoo, C. I.; Jung, J.; Song, H., Ag–Au–Ag Heterometallic Nanorods Formed through Directed Anisotropic Growth. *J. Am. Chem. Soc.* **2008**, *130*, 2940-2941.
63. Hong, S.; Choi, Y.; Park, S., Shape Control of Ag Shell Growth on Au Nanodisks. *Chem. Mater.* **2011**, *23*, 5375-5378.
64. Yang, Y.; Wang, W.; Li, X.; Chen, W.; Fan, N.; Zou, C.; Chen, X.; Xu, X.; Zhang, L.; Huang, S., Controlled Growth of Ag/Au Bimetallic Nanorods through Kinetics Control. *Chem. Mater.* **2012**, *25*, 34-41.
65. González, E.; Arbiol, J.; Puntes, V. F., Carving at the Nanoscale: Sequential Galvanic Exchange and Kirkendall Growth at Room Temperature. *Science* **2011**, *334*, 1377-1380.
66. Chen, J.; McLellan, J. M.; Siekkinen, A.; Xiong, Y.; Li, Z.-Y.; Xia, Y., Facile Synthesis of Gold–Silver Nanocages with Controllable Pores on the Surface. *J. Am. Chem. Soc.* **2006**, *128*, 14776-14777.
67. Xia, Y.; Li, W.; Cobley, C. M.; Chen, J.; Xia, X.; Zhang, Q.; Yang, M.; Cho, E. C.; Brown, P. K., Gold Nanocages: From Synthesis to Theranostic Applications. *Acc. Chem. Res.* **2011**, *44*, 914-924.
68. Gao, C.; Lu, Z.; Liu, Y.; Zhang, Q.; Chi, M.; Cheng, Q.; Yin, Y., Highly Stable Silver Nanoplates for Surface Plasmon Resonance Biosensing. *Angew. Chem. Int. Ed.* **2012**, *51*, 5629-5633.
69. Chen, A.; Holt-Hindle, P., Platinum-Based Nanostructured Materials: Synthesis, Properties, and Applications. *Chem. Rev.* **2010**, *110*, 3767-3804.
70. Li, Y.; Somorjai, G. A., Nanoscale Advances in Catalysis and Energy Applications. *Nano Lett.* **2010**, *10*, 2289-2295.

71. Gu, J.; Zhang, Y.-W.; Tao, F., Shape control of bimetallic nanocatalysts through well-designed colloidal chemistry approaches. *Chem. Soc. Rev.* **2012**, *41*, 8050-8065.
72. Wang, F.; Li, C.; Sun, L.-D.; Wu, H.; Ming, T.; Wang, J.; Yu, J. C.; Yan, C.-H., Heteroepitaxial Growth of High-Index-Faceted Palladium Nanoshells and Their Catalytic Performance. *J. Am. Chem. Soc.* **2010**, *133*, 1106-1111.
73. Lu, C.-L.; Prasad, K. S.; Wu, H.-L.; Ho, J.-a. A.; Huang, M. H., Au Nanocube-Directed Fabrication of Au–Pd Core–Shell Nanocrystals with Tetrahedral, Concave Octahedral, and Octahedral Structures and Their Electrocatalytic Activity. *J. Am. Chem. Soc.* **2010**, *132*, 14546-14553.
74. Yang, C.-W.; Chanda, K.; Lin, P.-H.; Wang, Y.-N.; Liao, C.-W.; Huang, M. H., Fabrication of Au–Pd Core–Shell Heterostructures with Systematic Shape Evolution Using Octahedral Nanocrystal Cores and Their Catalytic Activity. *J. Am. Chem. Soc.* **2011**, *133*, 19993-20000.
75. Yu, Y.; Zhang, Q.; Liu, B.; Lee, J. Y., Synthesis of Nanocrystals with Variable High-Index Pd Facets through the Controlled Heteroepitaxial Growth of Trisoctahedral Au Templates. *J. Am. Chem. Soc.* **2010**, *132*, 18258-18265.
76. Wang, F.; Sun, L.-D.; Feng, W.; Chen, H.; Yeung, M. H.; Wang, J.; Yan, C.-H., Heteroepitaxial Growth of Core–Shell and Core–Multishell Nanocrystals Composed of Palladium and Gold. *Small* **2010**, *6*, 2566-2575.
77. Kim, D. Y.; Choi, K. W.; Zhong, X.-L.; Li, Z.-Y.; Im, S. H.; Park, O. O., Au@Pd core-shell nanocubes with finely-controlled sizes. *CrystEngComm* **2013**, *15*, 3385-3391.

78. Gong, J.; Zhou, F.; Li, Z.; Tang, Z., Controlled synthesis of non-epitaxially grown Pd@Ag core-shell nanocrystals of interesting optical performance. *Chem. Commun.* **2013**, *49*, 4379-4381.
79. Annan, W.; Qing, P.; Li, Y., Rod-Shaped Au–Pd Core–Shell Nanostructures. *Chem. Mater.* **2011**, *23*, 3217-3222.
80. Zhu, C.; Zeng, J.; Tao, J.; Johnson, M. C.; Schmidt-Krey, I.; Blubaugh, L.; Zhu, Y.; Gu, Z.; Xia, Y., Kinetically Controlled Overgrowth of Ag or Au on Pd Nanocrystal Seeds: From Hybrid Dimers to Nonconcentric and Concentric Bimetallic Nanocrystals. *J. Am. Chem. Soc.* **2012**, *134*, 15822-15831.
81. Xiang, Y.; Wu, X.; Liu, D.; Jiang, X.; Chu, W.; Li, Z.; Ma, Y.; Zhou, W.; Xie, S., Formation of Rectangularly Shaped Pd/Au Bimetallic Nanorods: Evidence for Competing Growth of the Pd Shell between the {110} and {100} Side Facets of Au Nanorods. *Nano Lett.* **2006**, *6*, 2290-2294.
82. Lu, L.; Wang, H.; Xi, S.; Zhang, H., Improved size control of large palladium nanoparticles by a seeding growth method. *J. Mater. Chem* **2002**, *12*, 156-158.
83. Cardinal, M. F.; Mongin, D.; Crut, A.; Maioli, P.; Rodríguez-González, B.; Pérez-Juste, J.; Liz-Marzán, L. M.; Del Fatti, N.; Vallée, F., Acoustic Vibrations in Bimetallic Au@Pd Core–Shell Nanorods. *J. Phys. Chem. Lett.* **2012**, *3*, 613-619.
84. Zhang, K.; Xiang, Y.; Wu, X.; Feng, L.; He, W.; Liu, J.; Zhou, W.; Xie, S., Enhanced Optical Responses of Au@Pd Core/Shell Nanobars. *Langmuir* **2008**, *25*, 1162-1168.

85. Hu, J.-W.; Li, J.-F.; Ren, B.; Wu, D.-Y.; Sun, S.-G.; Tian, Z.-Q., Palladium-Coated Gold Nanoparticles with a Controlled Shell Thickness Used as Surface-Enhanced Raman Scattering Substrate. *J. Phys. Chem. C* **2006**, *111*, 1105-1112.
86. Chen, H.; Wang, F.; Li, K.; Woo, K. C.; Wang, J.; Li, Q.; Sun, L.-D.; Zhang, X.; Lin, H.-Q.; Yan, C.-H., Plasmonic Percolation: Plasmon-Manifested Dielectric-to-Metal Transition. *ACS Nano* **2012**, *6*, 7162-7171.
87. Wang, F.; Li, C.; Chen, H.; Jiang, R.; Sun, L.-D.; Li, Q.; Wang, J.; Yu, J. C.; Yan, C.-H., Plasmonic Harvesting of Light Energy for Suzuki Coupling Reactions. *J. Am. Chem. Soc.* **2013**, *135*, 5588-5601.
88. Huang, X.; Li, Y.; Chen, Y.; Zhou, H.; Duan, X.; Huang, Y., Plasmonic and Catalytic AuPd Nanowheels for the Efficient Conversion of Light into Chemical Energy. *Angew. Chem. Int. Ed.* **2013**, *52*, 6063-6067.
89. Fang, P.-P.; Jutand, A.; Tian, Z.-Q.; Amatore, C., Au-Pd Core-Shell Nanoparticles Catalyze Suzuki-Miyaura Reactions in Water through Pd Leaching. *Angew. Chem. Int. Ed.* **2011**, *50*, 12184-12188.
90. Heck, K. N.; Janesko, B. G.; Scuseria, G. E.; Halas, N. J.; Wong, M. S., Observing Metal-Catalyzed Chemical Reactions in Situ Using Surface-Enhanced Raman Spectroscopy on Pd-Au Nanoshells. *J. Am. Chem. Soc.* **2008**, *130*, 16592-16600.
91. Ding, Y.; Fan, F.; Tian, Z.; Wang, Z. L., Atomic Structure of Au-Pd Bimetallic Alloyed Nanoparticles. *J. Am. Chem. Soc.* **2010**, *132*, 12480-12486.

Chapter 2: The Shape-controlled Synthesis of Au/Pd Nanocrystals using Seed-Mediated Co-reduction

2.1 Introduction¹

The construction of bimetallic nanostructures with defined composition, shape, and architecture is important to many applications.²⁻⁴ For example, shape-controlled alloyed nanoparticles and binary metal nanodendrites can be more effective catalysts than their monometallic counterparts for electrooxidation processes.⁵⁻⁹ Their enhanced performances are often attributed to the unique structure of the expressed surfaces and synergistic effects between the two metals that comprise the nanocrystals. Also, the optical properties of metal nanocrystals can be manipulated through the introduction of a second metal.¹⁰⁻¹² For example, core@shell and segmented bimetallic nanorods display surface plasmon resonances (SPRs) that are dependent on both their aspect ratios and composition.¹³⁻¹⁵ Despite these examples, achieving the necessary synthetic control to access new bimetallic nanostructures with defined features is not always straightforward given the different properties of each metal and their precursors used in a nanocrystal synthesis. For example, metal precursors may be reduced at different rates during co-reduction and limit the nucleation of defined mono- or bimetallic seeds.^{16, 17} Also, structure-directing agents can interact preferentially with different metal surfaces.¹⁸ Seed-mediated synthetic methods have the capacity to address some of the challenges associated with bimetallic nanocrystal synthesis, as primary nucleation is already accounted for by the seed.¹⁹⁻²² As we report here, seed-mediated co-reduction of two metal precursors represents a potentially general route to architecturally controlled bimetallic nanocrystals, including octopodal and concave core@shell nanocrystals as well as new shape-controlled alloy and hopper-like nanostructures.

When seeds are incorporated into a nanomaterial synthesis, the barrier to deposition is typically lower than the nucleation of a new phase (i.e., heterogeneous vs. homogeneous nucleation). This condition separates nanocrystal nucleation from growth, as the seeds represent preferential sites for the growth of the greater nanostructure. As a result, seed-mediated synthetic methods have the potential to yield nanocrystals with high degrees of precision and structural/compositional complexity.¹⁹⁻²³ For example, this method has been used to synthesize a variety of shape-controlled and core@shell metal nanocrystals as monodisperse samples (e.g., Au nanorods and those with high index facets expressed such as {730}-terminated Au@Pd tetrahedra and {221}-terminated Au@Pd trisoctahedra).²⁴⁻²⁷ Typically only one metal precursor is reduced in the presence of the metal seeds. In this thesis, it is demonstrated that coupling the co-reduction of two metal precursors with the seed-mediated method manipulates the kinetics of seeded growth and in turn the morphology of Au–Pd nanocrystals. In particular, architecturally distinct Au–Pd octopods (i.e., nanocrystals with eight branches) and concave core@shell Au@Pd nanocrystals were achieved. This chapter is segmented into two pieces: (i) the initial synthesis of Au–Pd octopods and concave nanocrystals and their related optical and catalytic properties (Section 2.2) and (ii) an in-depth analysis of the role of synthetic parameters during the co-reduction step in controlling the architecture of the nanostructure (Sections 2.3-2.5).

2.2 Synthesis of Au/Pd Octopods and Concave Nanocrystals²⁸

Advances in the synthesis of single metal nanostructures now allow for the precise assembly of atoms into particles of defined size and shape.^{29, 30} This ability provides a myriad of structures and enables control over their properties for optical,

catalytic, and biomedical applications.³¹⁻³⁹ However, it is often difficult to achieve bimetallic heterostructures with defined features because of different metal-to-capping agent interactions and rates of precursor reduction, galvanic replacement, and the thermodynamic miscibility of the two metal phases.¹⁶ In this section, we report the synthesis and characterization of multifunctional Au/Pd octopods and concave core@shell Au@Pd nanocrystals, achieved by coupling for the first time a seed-mediated synthetic method with co-reduction. Significantly, the integration of these two methods provides a means of manipulating the kinetics of seeded growth to control the morphology of the final nanocrystals in favor of two distinct kinetic products.

Octopodal and concave nanocrystals of even one metal are rare, with reports typically emphasizing the conditions which favor the formation of one of these structures in comparison to those which yield thermodynamically favored polyhedral nanocrystals.^{24, 40-48} Yet, on account of their high surface energies, both octopods and concave nanocrystals should be considered kinetic products.^{49, 50} Generally speaking, kinetic products are thought to form when reaction conditions favor high growth rates, wherein the rate of atomic addition to a surface exceeds that of adatom surface diffusion. As a result, adatoms are prohibited from migrating on the surface to adopt their lowest energy configurations and in turn the polyhedral structures favored by thermodynamics.^{3, 50} As found in this chapter, binary octopods and concave nanostructures can be independently accessed under similar reaction conditions simply by controlling the kinetics of seeded growth.

Seed-mediated synthetic methods separate particle nucleation from growth by providing preformed crystals as building blocks to construct the greater structure upon.³

Pioneered with the synthesis of Au nanorods,^{51, 52} such syntheses have recently enabled heteroepitaxial deposition on the nanoscale, with a variety of shape-controlled core@shell structures reported.^{19, 21, 25, 53-55} Related to this section, Huang and co-workers recently reported the Au nanocube-directed synthesis of Au@Pd nanocrystals with tetrahedral and concave octahedral Pd shells while Lee and co-workers achieved heteroepitaxial deposition of Pd atop trisoctahedral Au nanocrystals.^{24, 25} In both of these examples, a Pd precursor was reduced in the presence of Au seeds, with the final structures achieved being primarily attributed to the Au–Pd epitaxial relationship and the structure-directing effects of capping agents or additives (i.e., a thermodynamic means of controlling crystal habit). As we have found, by coupling the co-reduction of Au and Pd precursors with a seed-mediated synthesis, the morphology of the final product can be controllably tuned to yield two distinct yet structurally related kinetic products.

To synthesize Au/Pd octopods and concave Au@Pd nanocrystals, Au seeds (diameter <10 nm) are prepared and serve as preferential platforms for the growth of larger Au nanocrystals, referred herein as Au cores. Additional Au precursor (HAuCl₄) and Pd precursor (H₂PdCl₄) are then simultaneously added to an aqueous solution containing the Au cores and cetyltrimethylammonium bromide (CTAB). Finally, L-ascorbic acid (L-aa) is added. See **Appendix A2.2** for details. This approach yields Au/Pd octopods and concave Au@Pd nanocrystals (**Figure 2.1**), with the specific structure formed being dependent on the Au:Pd precursor ratio.

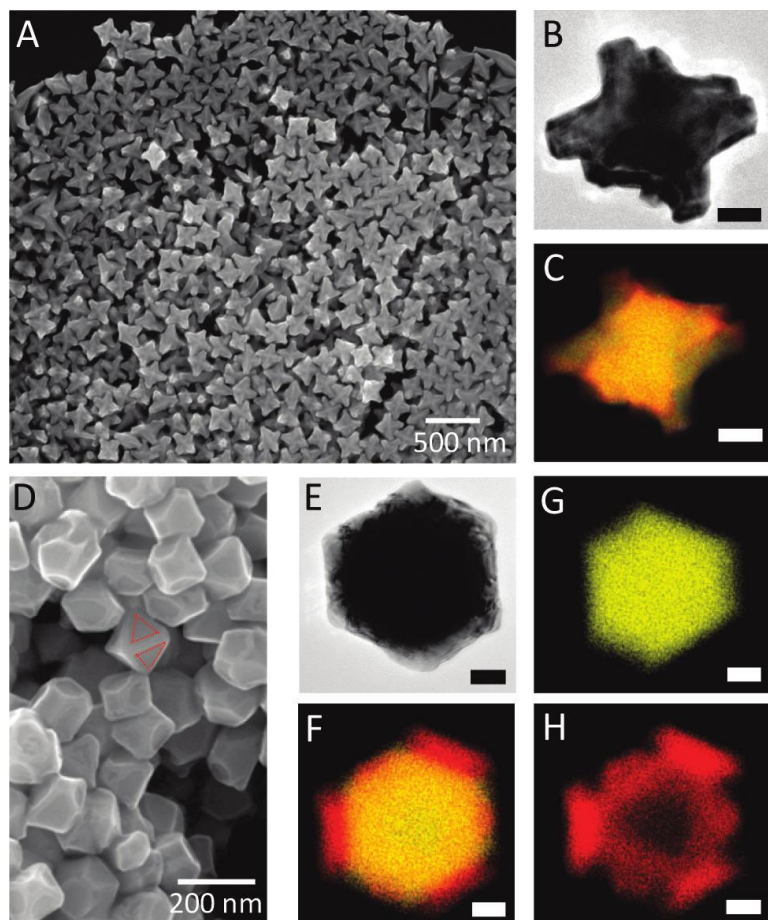


Figure 2.1. Au/Pd octopods characterized by (A) SEM, (B) TEM, and (C) STEM-EDX elemental mapping, where Au is yellow and Pd is red (in panels B and C, scale bars are 25 nm). Concave Au@Pd nanocrystals characterized by (D) SEM, (E) TEM, and (F–H) STEM-EDX elemental mapping. In panel D, two concave faces in an individual particle are outlined in red. In panel F, an overlay of the Au and Pd signals, presented separately in panels G and H, respectively (in panels E–H, scale bars are 25 nm).

Shown in **Figure 2.1A** is a scanning electron microscopy (SEM) image of Au/Pd octopods obtained from a 1-to-0.1 Au:Pd mole ratio of precursors. Many particles orient with four of their branches positioned toward the substrate, yet each one has eight branches extending 50 nm from its center. The branches are separated by 65°. The

electron diffraction (ED) pattern from an individual particle oriented with four branches toward the substrate can be indexed as being projected along a Au [100] zone axis (**Appendix B Supplementary Figure S2.1**). This structural analysis is consistent with growth along the 111 directions of a cuboctahedron consisting of six {100} facets and eight {111} facets.⁵⁰ Interestingly, the Au cores used to prepare the octopods already display some branching along the <111> directions before Au and Pd precursor addition, having formed from quasi-spherical seeds (**Figure S2.2**). However, it should be noted that other Au and Pd seed shapes can also yield octopods, as discussed in Chapter 3 and elsewhere.⁵⁶ Transmission electron microscopy (TEM, **Figure 2.1B**) reveals that the tips of each branch are flattened, corresponding with the expression of {111} facets. STEM-EDX mapping indicates that, while Pd is dispersed all over the surface of the octopod, it localizes at the tips of each branch (**Figure 2.1C**). Interestingly, the Au:Pd ratio in a synthesis dictates the extent to which the terminating {111} facets are expressed.

In **Figure 2.2A** are SEM images of particles prepared in the absence of Pd precursor and when the Au:Pd mole ratio is varied from 1-to-0.01 to 1-to-0.1, 1-to-0.2, 1-to-0.5, and 1-to-1 (left to right). The concentrations of Au precursor, CTAB, and L-aa were held constant. See **Figure S2.3** for SEM images highlighting sample homogeneity as well as TEM and STEM-EDX mapping of particles. When only Au precursor is reduced in the presence of Au cores, malformed Au cubes are produced. Yet, adding a small amount of Pd precursor (1-to-0.01) yields starlike particles (**Figure S2.3B-D**). Like the sample prepared with a 1-to-0.1 Au:Pd ratio, the particles have eight uniform branches. However, each branch is sharply terminated rather than flattened. Such sharp features should concentrate and amplify the local electric field associated with these

highly uniform nanostars, making them attractive platforms for surface-enhanced Raman scattering (SERS) applications and localized surface plasmon resonance (LSPR) sensing.⁵⁷⁻⁶⁰ With increasing Pd precursor, the tips become flattened and terminated with $\{111\}$ sheets perpendicular to the $\langle 111 \rangle$ growth directions of the branches. STEM-EDX mapping of the “sheeted-octopods” indicates that the $\{111\}$ sheets are enriched with Pd (e.g., **Figure S2.3E-J**).

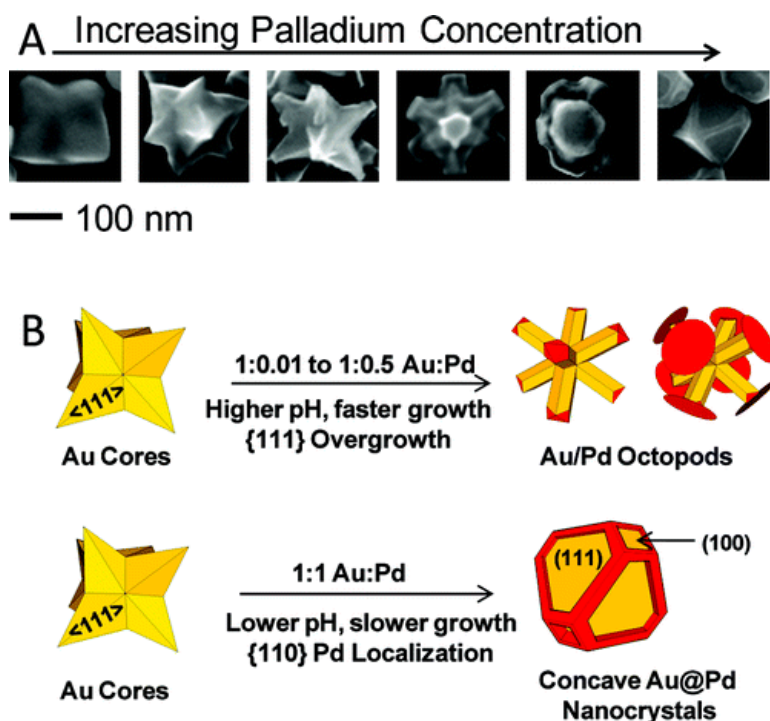


Figure 2.2. (A) SEM images showing the evolution in nanocrystal shape as a function of Au:Pd mole ratio in a synthesis. From left to right: 1-to-0, 1-to-0.01, to 1-to-0.1, 1-to-0.2, 1-to-0.5, and 1-to-1. (B) Schematic summarizing the structural characterization and synthetic parameters governing the formation of Au/Pd octopods (overgrowth along the $\langle 111 \rangle$ directions) and concave nanocrystals (localization along the $\{110\}$ edges) from branched Au cores. Yellow corresponds to Au-rich regions of the nanocrystals while red corresponds to Pd-rich regions.

Distinctly different structures, concave octahedra and cuboctahedra with depressions on the $\{111\}$ and $\{100\}$ faces, form at a 1:1 Au:Pd ratio (**Figure 2.1D,E**). As expected, analysis by ED gave rise to an assortment of patterns due to the random orientations of the octahedral particles on the supporting grid. However, the ED pattern from a concave cuboctahedral particle with a (100)-terminating facet perpendicular to the electron beam can be indexed as being projected along a $[100]$ zone axis, as expected (**Figure S2.1**). STEM-EDX analysis provides remarkable insight into the 3-D structure of these concave nanocrystals, which consists of a convex Au interior and a nonconformal Pd shell consistent with the depressions (**Figure 2.1F–H**). The observation of a convex Au interior indicates that that branched Au cores (**Figure S2.2D**) adopt a new structure during overgrowth, while Pd localizes along the $\{110\}$ edges of the Au core, extending out as partial $\{111\}$ or $\{100\}$ faces. These results contrast with octopodal formation wherein overgrowth occurs along the $\langle 111 \rangle$ directions. This analysis is summarized in **Figure 2.2B**.

Given the structural complexity and potential utility of these nanocrystals, understanding the parameters that govern their formation is desirable. With regards to branched nanocrystal formation, recent in situ synchrotron XRD studies by Tilley and co-workers found that Pt multipods form under conditions which favor high growth rates, whereas Xia and co-workers reported the synthesis of Rh octopods when Rh precursor is injected into reducing media at a fast rate.^{40, 49} These studies indicate that overgrowth is favored when metal addition is faster than adatom diffusion at a given surface (i.e., a kinetic growth regime; **Figure 2.2B**).^{49, 50} From the previously shown results it is reasonable to assume that Au/Pd octopod formation follows similar conditions; these

conditions will be clarified in Sections 2.3-2.5. Interestingly, a series of experiments found that the structure of the Au cores and the co-reduction method were essential to Au/Pd octopod formation. In a typical synthesis, Au cores are prepared by adding tiny Au seeds to a growth solution. Unlike previous seeded methods, our Au seeds are aged before use.^{51, 52} When the aging time exceeds 3 days, branched Au cores and subsequent Au/Pd octopods form (**Figures S2.2 and 2.1A-C**). When used immediately, the Au cores are octahedral, and the final nanocrystals adopt a convex core@shell structure (**Figures S2.2 and 2.3A-C**). Remarkably, the only noticeable difference between the fresh and aged seeds is their size (**Figure S2.2**), with the aged seeds being larger, forming presumably via Ostwald ripening. Through this process, the concentrations of the metal precursors are greater per seed as is the diffusion length for metal adatoms. These conditions favor Au overgrowth and the formation of suitable Au cores.^{49, 50} The role of seed shape and branched growth is discussed in greater detail in Chapter 3.

Yet, epitaxial overgrowth on the branched Au cores does not account for the formation of Au/Pd octopods. Recall that, in the absence of H_2PdCl_4 , malformed Au cubes form, not Au octopods (**Figure S2.3A**). This observation suggests that the Pd precursor or some component of it contributes to octopodal and concave nanocrystal formation. To test this hypothesis, the H_2PdCl_4 was replaced with Na_2PdCl_4 , NaCl, or HCl to hold the concentration of Pd(II), Cl^- , or pH constant with the conditions which yielded Au/Pd octopods. With Na_2PdCl_4 , Au/Pd octopods with sharper tips than those shown in **Figure 2.1** form (**Figure S2.4A**). With NaCl, malformed cubes form (**Figure S2.4B**), while HCl facilitates the formation of indented cubes, reminiscent of poorly developed octopods (**Figure S2.4C**). These experiments indicate that the Pd, either in its

precursor or reduced state, contributes to the formation of octopods. Although its exact role is unclear from these results alone, studies of the seeded synthesis of Au nanorods report an active role for Ag^+ added to most nanorod syntheses. In particular, Ag^+ is thought to stabilize higher energy $\{110\}$ facets and atomic steps through an underpotential deposition mechanism.⁶¹ In our system, it is noted that Pd localizes on high energy features (i.e., branch tips to form “sheeted-octopods” and $\{110\}$ edges to form concave nanocrystals), and a mechanism similar to what is observed in the Au nanorod system may account for the observed segregation of Au and Pd. Additional experiments aimed at clarifying the role of Pd are presented in Section 2.4.

These experiments also indicate that HCl can contribute to the shaping of these nanocrystals. As discussed in Section 2.1, nanocrystal overgrowth is favored at high growth rates. The dramatic change in nanocrystal morphology from octopodal to concave at a high concentration of Pd precursor (and thus high concentration of HCl and lower pH) suggest a change in growth rate. Interestingly, it is known that the reducing ability of L-aa is diminished and the oxidation/etching of Au by Au(III)–CTAB complexes is enhanced by lowering pH.⁶²⁻⁶⁴ Both changes would slow the growth rate, and when considering the co-reduction method employed here, both may contribute to the switch in kinetics. It is also worth noting that etching from Au(III)–CTAB complexes may account for the observed shape change of the Au cores used in these syntheses (**Figure S2.2D** compared to **Figure 2.1G**). Our observations are consistent with the recent study by Xia and co-workers where it was found that the morphology of Rh nanocrystals could be controlled by manipulating the growth kinetics.⁴⁹ In their system, the growth kinetics were tuned via the rate of precursor injection, whereas here, similar control is afforded in

a binary system by coupling co-reduction with a seed-mediated synthetic method. Interestingly, when H_2PdCl_4 is replaced with Na_2PdCl_4 to hold the concentration of Pd(II) constant with the conditions which yield concave nanocrystals, micrometer-sized flakes of metal form (in addition to a few octopodal structures, **Figure S2.4D**). This observation indicates that, in addition to seeded growth, nucleation of new structures is favored at high concentrations of Na_2PdCl_4 . Yet, by slowing the rate of precursor reduction through the use of H_2PdCl_4 , the driving force for new nanocrystal nucleation is diminished and seeded growth predominates with the formation of concave nanocrystals. This result further illustrates the important role of reduction rate in the shaping of nanocrystals prepared by seeded methods and that the kinetics of seeded growth can be manipulated via co-reduction. Significantly, neither seed age nor core structure (branched vs. convex) influenced concave nanocrystal formation. Shown in panels D-H of **Figure 2.3** is characterization of the nanocrystals prepared with fresh Au seeds and subsequent convex Au cores. The concave structure, while not as pronounced, is evident from the TEM image.

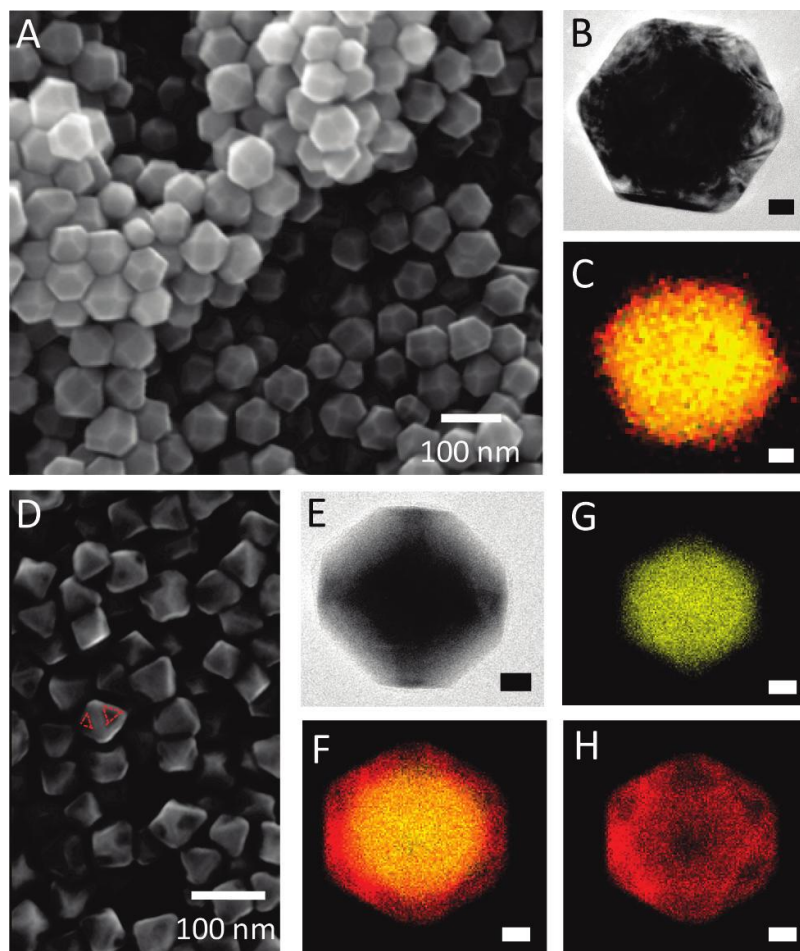


Figure 2.3. Convex Au@Pd nanocrystals characterized by (A) SEM, (B) TEM, and (C) STEM-EDX mapping, where Au is yellow and Pd is red (in panels B and C, scale bars are 25 nm). Concave Au@Pd nanocrystals characterized by (D) SEM, (E) TEM, and (F–H) STEM-EDX elemental mapping. In panel D, two concave faces in an individual particle are outlined in red. In panel F, an overlay of the Au and Pd signals, presented separately in panels G and H, respectively (in panels E–H, scale bars are 25 nm).

On account of their unique features, these nanocrystals may display favorable optical and catalytic properties. Shown in **Figure 2.4A** are the absorbance spectra for the nanocrystals highlighted in **Figure 2.2A**. The malformed Au cubes have their primary

absorbance centered at 740 nm. As Pd is added to the synthesis and the nanocrystals adopt an octopodal structure, a red shift is observed, with the furthest shift (absorbance centered at 1030 nm) being represented by the sample in Figure 2.1A. This shift is consistent with the larger size and greater charge polarization achievable with the octopods.⁶⁵ With the addition of more Pd, a blue shift and gradual broadening are observed. The concave Au@Pd nanocrystals have their most prominent absorbance below 400 nm. A similar blue shift was reported for Au@Pd nanorods, wherein the optical signature was also dampened with an increase in shell thickness.⁶⁶

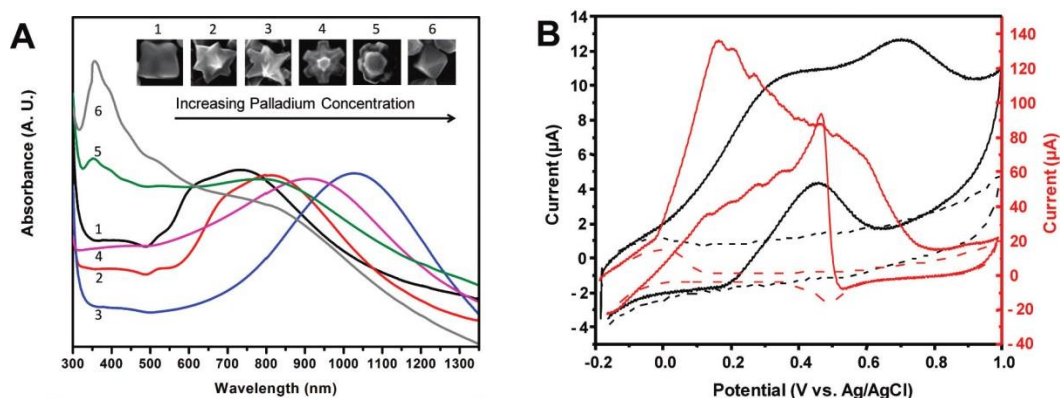


Figure 2.4. (A) Absorbance spectra for samples represented by Figure 2.2A, labeled 1–6 corresponding to left from right. (B) CVs obtained from Au/Pd octopods (black) and concave nanocrystals (red) in the absence (dashed) and presence of formic acid (solid).

Cyclic voltammetry (**Figure 2.4B**) was used to evaluate both the Au/Pd octopods (black curves) and concave nanocrystals (red curves) for their ability to promote the oxidation of formic acid in an aqueous 0.1 M H₂SO₄ medium. From control experiments carried out in the absence of formic acid (dashed black and red curves), it was established that oxidation of H₂, cathodically deposited into Pd at -0.2 V, gives rise to a small anodic current at ca. -0.01 V. In the same control experiments, it was confirmed that oxidation

of Pd begins at ca. +0.8 V. Concave Au/Pd nanocrystals, which are synthesized with 10 times more Pd than the octopods, display a well-defined cathodic peak at +0.5 V for the reduction of palladium oxide (dashed red curve). For either the Au/Pd octopods or concave nanocrystals, the oxidation of formic acid manifests itself by the large rise in anodic current that commences at -0.07 V. With the octopodal nanocrystals (solid black curve), the presence of formic acid gives rise to two anodic peaks at +0.36 and +0.70 V, along with a catalytic peak in the reverse (cathodic) scan at +0.45 V. On the other hand, in the presence of formic acid, using concave nanocrystals gives rise to one anodic peak at +0.16 V with a shoulder at +0.51 V and one catalytic peak in the reverse scan at +0.47 V (solid red curve). Previous studies of model Pd(100), Pd(110), and Pd(111) surfaces for the electrooxidation of formic acid revealed anodic peaks at potentials of +0.42, +0.22, and +0.07 V, respectively, with the appearance of a second oxidation peak at +0.50 V for the Pd(110) surface.^{19, 67} Thus, both the Au/Pd octopods and concave nanocrystals exhibit catalytic properties that resemble a mixture of Pd surfaces, consistent with their structures as discussed earlier. Comparison of the anodic peak potentials reveals that the concave nanocrystals exhibit more Pd(111) character than the octopods. Finally, it is possible to observe catalytic oxidation of formic acid for up to 10 repetitive potential scans with Au/Pd octopods and for up to 25 repetitive scans with concave nanocrystals; in each instance, however, the extent of catalytic oxidation of formic acid gradually diminishes.

Here, we have discovered that the kinetics of seeded growth can be manipulated through the incorporation of a co-reduction technique. This integration allows for the morphology of the final binary structure to be tuned between two distinct kinetic products—Au/Pd octopods and concave Au@Pd nanocrystals. These nanocrystals are

electrochemically active while also displaying optical signatures throughout the visible and near-IR region. As such, they may serve as multifunctional probes for a host of applications while the synthetic methodology may enable the preparation of other bimetallic nanocrystals as kinetic products with unique 3-D structures.^{68, 69}

2.3 Investigation of Synthetic Conditions that Control Architecture of Au/Pd Nanostructures Prepared by Seed-Mediated Co-Reduction¹

Since the initial demonstration discussed in Section 2.2, others have also reported new structures using seed-mediated co-reduction. For example, Han and co-workers synthesized convex Au–Pd hexahedral-like nanostructures by seed-mediated co-reduction.⁷⁰ Likewise, Xia and co-workers recently achieved Pd–Pt alloyed nanocages by coupling co-reduction and galvanic replacement during a seed-mediated synthesis.⁹ Collectively, these results highlight the promise of this technique toward achieving unique bimetallic architectures. However, a greater understanding of how this method can be used to control morphology and composition is required to apply it to other bimetallic systems.

In the initial demonstration of this technique a double seeded approach was employed. First, tiny Au seeds (<10 nm) were prepared. Then, Au precursor (HAuCl₄) was reduced to deposit metal on top of the seeds to make larger Au nanocrystals i.e. Au cores. Finally, additional Au precursor and Pd precursor (H₂PdCl₄) were added to the Au core solution and reduced with L-aa in the presence of CTAB. The Au:Pd precursor ratio determined the final nanocrystal morphology. A series of control experiments found that HCl released from the Pd precursor was integral to morphology control, with its

concentration altering the rates of (i) metal precursor reduction with L-aa and (ii) likely Au core etching via Au(III)-CTAB complexes. The interplay between these two mechanisms at different reaction conditions accounted for the array of nanostructures observed. Palladium itself (in either its precursor state or reduced form) also contributed to structure formation. Thus, understanding the role of each synthetic component and how to manipulate these parameters during synthesis will expand our ability to predictably achieve architecturally distinct bimetallic nanostructures via seed-mediated co-reduction.

In the following sections, a comprehensive set of experiments is described that provide critical insight into the kinetic control achieved by coupling co-reduction of two metal precursors with the seed-mediated synthetic approach. First, the independent roles of the Au:Pd precursor ratio and reaction pH on nanostructure formation are elucidated by systematically altering each parameter. This study revealed general principles for new nanocrystal design by achieving, for example, shape-controlled alloyed nanocrystals through manipulation of nanocrystal growth kinetics during seed-mediated co-reduction. Second, the role of CTAB as a capping agent is evaluated. Manipulation of particle shape through the use of various capping agents is typically considered a thermodynamic means of structure direction, as facet-selective adsorbate interactions can alter the relative energies of the expressed surfaces.²⁹ Our study found that Br⁻ either from CTAB or added extraneously plays a critical role during the overgrowth process but contributes to morphology development by temporally separating Au and Pd precursor reduction. In fact, manipulation of this parameter facilitated the growth of hopper-like nanocrystals with deep angular concavities on what would be the {100} facets of cuboctahedral

nanocrystals otherwise. These results provide a greater understanding of seed-mediated co-reduction and will facilitate the synthesis of new bimetallic nanocrystals with well-defined and controllable properties.

2.4 Synthetic Control of Au/Pd Nanostructures¹

The general protocol for coupling co-reduction with the seed-mediated synthetic technique is outlined in Section 2.3, and the details of this approach can be found in **Appendix A2.3**, **Table A2.1**, and **Scheme A2.1**. In the initial demonstration of this technique, the amount of Pd precursor was varied relative to Au precursor in the overgrowth solution at Au:Pd ratios of 1:X where X is 0.01, 0.1, 0.2, 0.5, 1.0, and 2.0. SEM images of the products obtained are shown in **Figure 2.5** as Column A. Branching and the formation of octopods are evident with the addition of even a small amount of Pd precursor (e.g., sample 1A). The tips of the octopods become flattened as the amount of Pd precursor increases relative to Au precursor (e.g., sample 3A vs. 5A), and eventually concave core@shell architectures are adopted at very high Pd precursor concentrations (**Figure S2.5**). Given that these structures do not form in the absence of the seed-mediated method or when the Au and Pd precursors are reduced independently (**Figure S2.6**), it is interesting to understand how the co-reduction process contributes to this morphology development and can be controlled.

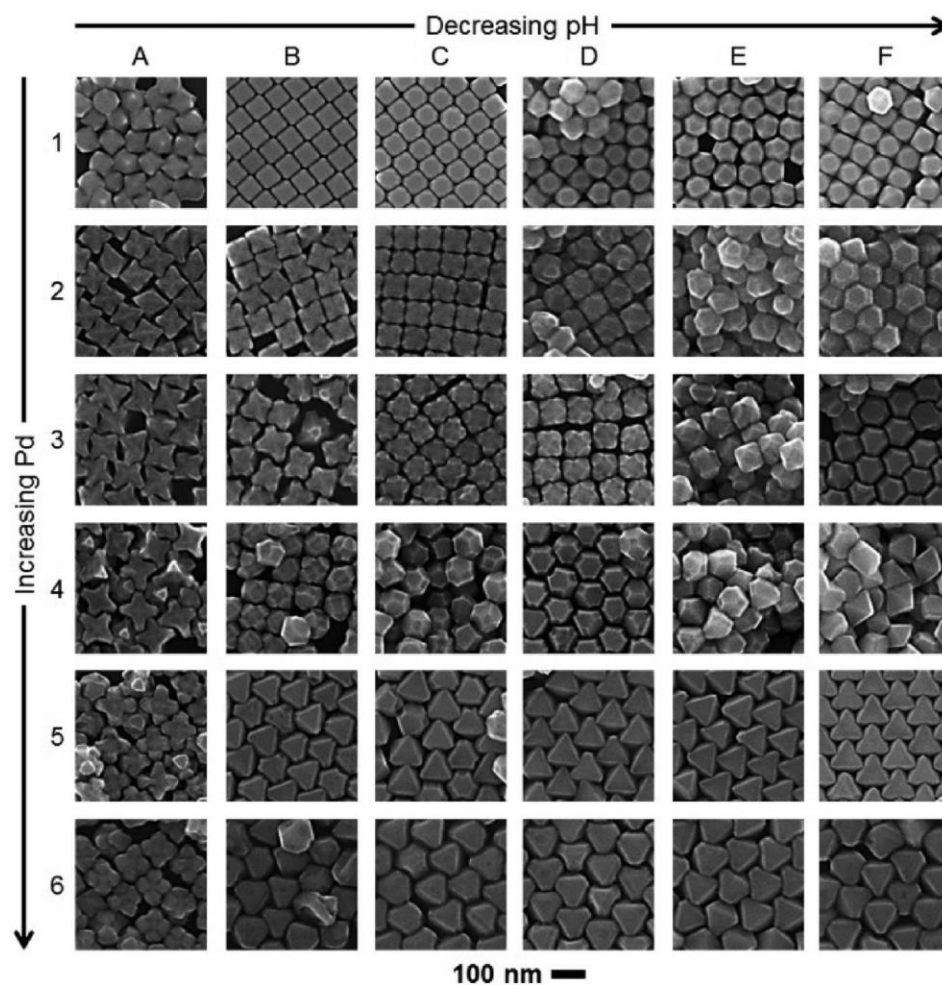


Figure 2.5. SEM images of Au–Pd nanocrystals synthesized by seed-mediated co-reduction. The synthetic results represented by Columns A–F involved 2 mL of aqueous HCl solution being added to the Au core solution prior to co-reduction at concentrations of 0.0, 12.5, 25.0, 37.5, 50.0, and 62.5 mM, respectively. The synthetic results represented by Rows 1–6 were obtained with Au:Pd precursor ratios of 1:X where X is 0.01, 0.1, 0.2, 0.5, 1.0, and 2.0 during co-reduction, respectively. See **Tables A2.1** and **S2.2** for a summary of synthetic conditions. Samples referred to by number-letter notation in the main text are based on this figure.

Our previous study discovered that the Pd precursor itself provides HCl to the reaction media as a function of concentration (i.e., H_2PdCl_4 is prepared in excess HCl from PdCl_2 , and it also complexes as $[\text{CTA}]_2\text{PdBr}_4$ and related species under conditions similar to our synthesis, as reported by Berhault and co-workers).^{28, 71} Replacing H_2PdCl_4 with Na_2PdCl_4 during seed-mediated co-reduction accelerated the rate of precursor reduction and provided the high driving force required for new nanocrystal nucleation, with large metal flakes observed at high Na_2PdCl_4 concentrations. It was concluded that HCl from the Pd precursor provided control over morphology by manipulating the kinetics of seeded growth. However, no additional studies were conducted to decouple the roles of reaction pH and Au:Pd precursor ratio in morphology development. Yet, experiments by Nishimura and co-workers have shown that the aspect ratio of Au nanorods can be controlled by the pH of the overgrowth solution, and similar observations have been made in other nanomaterial syntheses.⁷²⁻⁷⁴ Thus, it is imperative to study the effect of reaction pH on morphology independent of the Au:Pd precursor ratio. This goal is achieved here by systematically adding different concentrations of HCl to the overgrowth solution prior to the co-reduction process at fixed Au:Pd precursor ratios. These results are also presented in **Figure 2.5**. The concentration of HCl added to the overgrowth solution increases from left to right in a row (A–F corresponds to 2 mL of 0.0, 12.5, 25.0, 37.5, 50.0, and 62.5 mM HCl added, respectively; the total reaction volume is 30.6 mL; see **Table S2.2** for measurements of pH at different stages of synthesis), with each row corresponding to a different Au:Pd precursor ratio defined previously. Concave, cuboctahedral, and octahedral nanocrystals form in addition to the octopodal nanocrystals. These results contrast with those obtained when the Au and Pd

precursors are independently reduced in the presence of the Au cores and CTAB as a function of pH (**Figure S2.6**).

Examination of **Figure 2.5** in more detail reveals some interesting trends. Across a given row, nanocrystal size remains relatively constant, but branch lengths decrease and tips become flattened as HCl content increases (e.g., sample 4A vs. 4B). Eventually, the nanocrystals adopt cuboctahedral or octahedral shapes (e.g., sample 4F). However, many of the intermediate samples contain concavities or depressions along specific facets (e.g., sample 4D). This trend toward convex solids is unsurprising, as decreasing pH should slow the rate of metal precursor reduction and in turn nanocrystal growth. Slower growth allows nanocrystals to undergo relaxation processes and adopt thermodynamically favored morphologies rather than branched architectures.^{40, 75} Down a column, the overall size of the nanocrystals increases gradually with increasing metal content in the overgrowth solution. The tips of the branched nanocrystals also become flattened with increasing Pd precursor in the overgrowth solution, and cuboctahedral nanostructures with some concavities are observed (e.g., samples 2B, 3B, and 4B, respectively). At sufficiently high concentrations of Pd precursor, octahedra (sample 6B) form. Interestingly, the addition of HCl to a synthesis facilitates the formation of octahedra at lower concentrations of Pd (e.g., sample 4F vs. sample 6B). All samples are prepared in good yield (>90%), and this observation is attributed to the use of a seed-mediated method. In fact, the high monodispersity contributes to the uniform assembly of many samples, with the cubic particles often adopting cubic packing (e.g., sample 1B) and the cuboctahedral and octahedral particles often adopting hexagonally packed arrangements (e.g., samples 4D and 5D, respectively).

Many samples were characterized in more detail to better understand the structural changes observed as well as to correlate the results with changes in the Au–Pd distribution in the final nanostructures. Shown in **Figure S2.7** is a TEM image and the corresponding ED of an individual octopodal nanocrystal oriented with four branches toward the TEM grid and four branches away (sample 4A). The square symmetry of the ED pattern indicates that the eight branches of the octopod grow along the $\langle 111 \rangle$ directions from the interior of the nanostructure, and the flattened tips correspond with the expression of $\{111\}$ facets. Adding a sufficient amount of HCl to this overgrowth solution facilitated the formation of octahedral nanocrystals during co-reduction (sample 4F). ED of an individual particle is consistent with the octahedral shape (**Figure S2.7**). High magnification SEM images, structural models, TEM images, STEM images, and elemental mapping by STEM/EDX analysis of individual particles from Row 4 are shown in **Figure 2.6** from top to bottom. TEM and STEM-EDX elemental mapping provide remarkable insight into the changes in both morphology and composition that occur as a function of reaction pH. Palladium is dispersed all over the surface of the octopods and localizes along the tips of the branched nanostructures, with Au predominating in the interior of the particles (samples 4A and 4B; Pd-rich regions will appear lighter in TEM and STEM as $Z_{\text{Au}} > Z_{\text{Pd}}$). With decreasing pH, the SEM images reveal regions of negative curvature associated with the absence of $\{100\}$ facets of what would otherwise be cuboctahedral particles (samples 4C and 4D). Structural models based on these SEM observations are provided in Row 2. TEM and STEM-EDX mapping reveal again that the exteriors of the nanocrystals are Pd-rich. Interestingly, a core@shell Au@Pd particle structure is not obvious from microscopy analysis of the octahedral

nanostructures (sample 4F), although it was initially assumed given the use of Au cores during synthesis and the tendency of Au precursors to reduce and deposit before Pd precursors. To our surprise, powder X-ray diffraction (XRD) of sample 4F indicates that the octahedra are primarily a Au-rich Au–Pd alloy (**Figure S2.8**). Note that according to the Au–Pd phase diagram, Au and Pd are soluble over a wide range of compositions.⁷⁶ Presumably this alloy exists as a shell on top of Au-based cores. This result confirms the original hypothesis when undertaking seed-mediated co-reduction as a synthetic route to bimetallic nanocrystals—that the shape of a seed can be transferred to a bimetallic shell via co-deposition. Thus, controlling the kinetics of seed-mediated bimetallic deposition may represent a general route to shape-controlled alloy nanocrystals. As is evident from the STEM-EDX elemental mapping, the shape of the Au-rich interior of the Au–Pd nanocrystals changes as a function of HCl addition, as does the distribution of Pd in the final nanocrystals. The chemical origin of these changes will be discussed in more detail later, but it is noted that there is very little variation in the Au:Pd ratio in the final nanostructures as a function of reaction pH (**Table 2.1**).

Table 2.1. Ratio of Au:Pd (as X:1) in Various Nanocrystals As Obtained by EDX Analysis.

		Decreasing pH →				
Row 4	4A	4B	4C	4D	4E	4F
X	0.87	1.01	1.02	0.85	1.14	0.98
		Increasing Pd →				
Column A	1A	2A	3A	4A	5A	6A
X	19.7	3.55	1.73	0.87	0.4	0.28

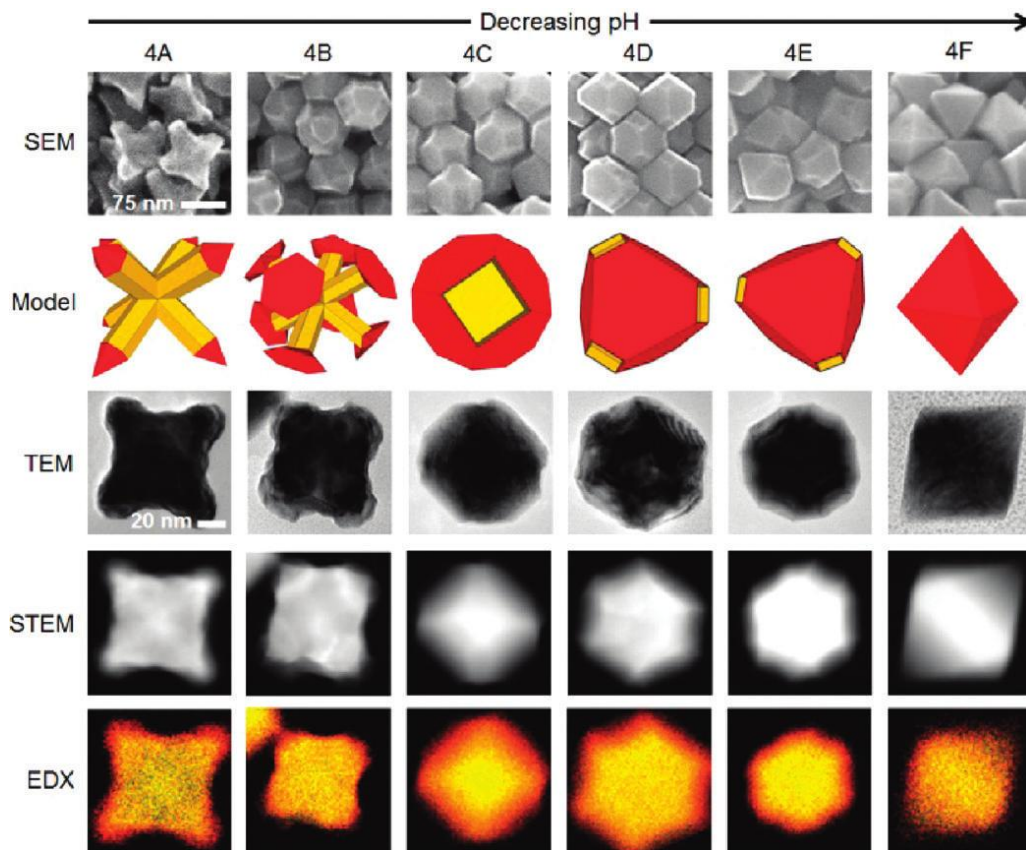


Figure 2.6. From top to bottom, Au–Pd nanocrystals (row 4, **Figure 2.5**) characterized by higher magnification SEM as well as 3-D models (yellow represents Au-rich and red represents Pd-rich regions), TEM, STEM, and STEM-EDX mapping (yellow indicates Au and red indicates Pd). Note: all SEM images are at the same magnification. Similarly, TEM, STEM, and STEM-EDX mapping are at the same magnification.

Similar characterization was conducted for nanocrystals formed as a function of Au:Pd precursor ratio with no HCl added to the overgrowth solution (Column A). It is noted that there is a slight decrease in reaction pH down Column A as the Pd precursor

itself provides HCl to the reaction media; however, the change from one panel to the next is small compared to Row 4 experiments, and similar structural changes are observed as a function of Au:Pd precursor ratio when the H_2PdCl_4 is replaced with Na_2PdCl_4 (see **Table A2.1** and **Figure S2.9**). Shown in **Figure 2.7** are TEM images and STEM-EDX elemental maps of individual particles from the samples in Column A. As the amount of Pd precursor increases in the synthesis, the tips of the branches become substantially flattened. The STEM-EDX elemental maps indicate that these flattened tips are enriched with Pd relative to the rest of the nanostructure. The elemental maps also indicate that the branched nature of the Au-rich interior is generally maintained as a function of Au:Pd precursor ratio, unlike with the addition of HCl to the overgrowth solution. ED of sample 6A again indicates that branches of the octopods grow along the 111 directions of the core (**Figure S2.7**). Powder XRD of sample 6A indicates a complex composition composed of Au, Pd, and a Au–Pd alloy from the shoulder reflections at 38.2 and 40.1 degrees 2θ , consistent with diffraction from the Au and Pd {111} planes, respectively, and the broad reflection in between (**Figure S2.8**). Interestingly, the reflection at 40.1 degrees 2θ for Pd is not evident in the powder XRD pattern of sample 4A (**Figure S2.8**). Sample 4A is prepared with slightly less Pd precursor than sample 6A, and the width of the sheets terminating the branches of these octopods is also less than observed with sample 6A. This comparative analysis suggests that the Pd region is localized at the tips of the “sheeted” octopods. The amount of Pd in the final nanocrystals increases with increasing Pd precursor in the overgrowth solution as expected (**Table 2.1**). Taken with the results obtained at fixed Au:Pd precursor but different HCl contents, these findings

illustrate that the Pd content and location can be predictably manipulated during seed-mediated co-reduction.

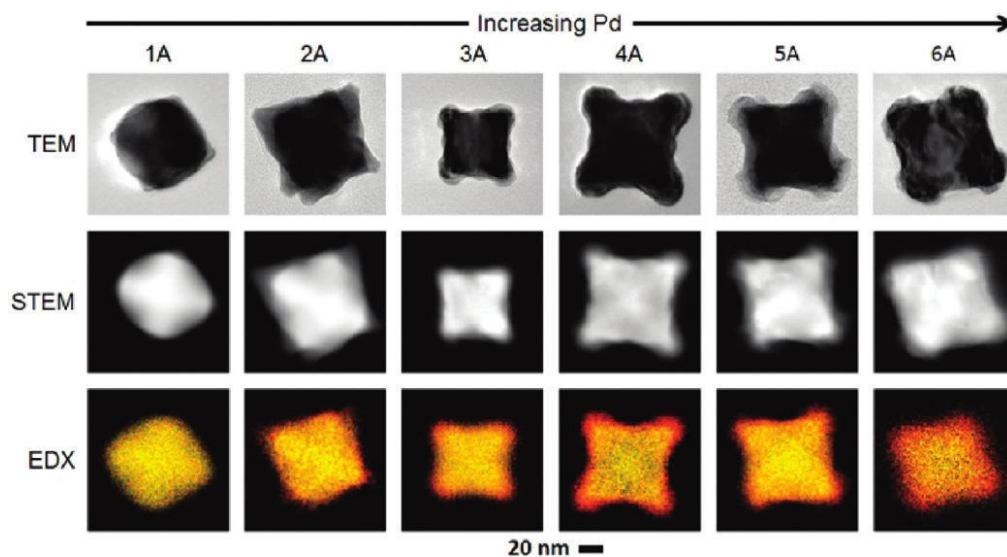


Figure 2.7. From top to bottom, Au–Pd nanocrystals (Column A, Figure 2.5) characterized by TEM, STEM, and STEM-EDX elemental mapping (yellow indicates Au and red indicates Pd).

Additional experiments are still required to fully decouple the roles of HCl content and Au:Pd precursor ratio in morphology control. Mainly, it is important to consider the structure of the Au cores in nanocrystal formation, as the facets expressed and their internal twins can contribute to morphology development in seed-mediated syntheses.^{29, 77} Shown in **Figure S2.10** is an SEM image of the Au cores used in this synthesis. They appear octahedral-like, with some particles showing rounded corners or minor protrusions. The use of single-crystalline octahedral-like cores is consistent with the final morphologies adopted by the Au–Pd nanocrystals. However, nanoparticles often restructure in solution in response to changes in their environment (*e.g.*, the addition of a

capping agent).^{34, 78} It is possible that the addition of HCl to the overgrowth solution contributed to a change in core structure and in turn final nanostructure morphology. However, SEM analysis of Au cores exposed to HCl prior to the co-reduction step did not reveal any substantial changes in structure (**Figure S2.10**). Thus, the changes in final nanostructure morphology as a function of HCl do not arise from changes in core shape prior to co-reduction. Yet STEM-EDX elemental mapping of Row 4 samples revealed Au-rich interiors of different shapes as a function of HCl content (**Figure 2.6**). At low HCl content (high pH), the Au-rich interiors are branched. Such structures are not favored by thermodynamics and typically form under conditions of fast growth, wherein metal deposition occurs at a faster rate than metal surface diffusion.⁷⁵ At higher HCl content (low pH), the Au-rich interiors are cuboctahedral or octahedral, which are thermodynamically more favored. These observations are consistent with the pH-dependent reducing capabilities of L-aa.⁷⁹ It is also noted that Au can be etched with Au(III)-CTAB complexes and that the rate of this oxidation is pH dependent, with points of high curvature being most susceptible to etching at low pH.⁶³ Finally, recent time studies using ICP-MS suggest that CTAB arrangement may be altered depending upon pH.⁸⁰ It is likely that all three factors account for the different shapes observed in the Au-rich interiors of the Au–Pd nanocrystals as a function of HCl content, particularly as the addition of NaCl to the overgrowth solution rather than HCl did not facilitate similar morphology changes. Shown in **Figure S2.11** are the results obtained when NaCl was added to the overgrowth solution rather than HCl, with all other synthetic conditions consistent with Row 2 samples. High-quality octopodal structures were obtained at all concentrations. Finally, as the Pd precursor (H_2PdCl_4) provides HCl to the reaction media

itself, it was replaced with Na_2PdCl_4 at the Au:Pd precursor ratio consistent with Row 5 and the pH of the reaction media adjusted through the addition of HCl prior to co-reduction. The results are shown in Figure S2.9 and are similar to those obtained with H_2PdCl_4 as a function of reaction pH (A–F correspond to 2 mL of 0.0, 12.5, 25.0, 37.5, 50.0, and 62.5 mM HCl added, respectively; the total reaction volume is 30.6 mL). Thus, the addition of HCl extraneously, not exclusively from the metal precursor, provides similar kinetic control of seed-mediated co-reduction. It is noted that adding a small amount of NaOH to the overgrowth solution also facilitated the formation of octopodal structures (**Figure S2.12**). This observation is consistent with branched nanostructures forming under fast growth conditions, as precursor reduction with L-aa is more facile at high pH.⁷⁹ Yet polydisperse quasi-spheres form at sufficiently high pH and may arise from uncontrolled precursor reduction and the decreased stability of the CTAB bilayers adsorbed to the surface of the growing nanocrystals (**Figure S2.12**).⁷⁹

The discussed experiments highlight the important role of growth rate in morphology development. Time studies provide similar insight. Shown in **Figure 2.8** are SEM images of the product obtained as a function of reaction time for samples 2F, 4A, and 4F. In the early stages of reaction all samples are ill-defined and reminiscent in form to the original Au cores. However, the morphologies of the nanostructures are similar to those shown in **Figure 2.5** within 45 min and indicate that our sampling technique does not appreciably alter the growth processes. Interestingly, sample 2F adopts a “sheeted” octopodal morphology, but it does not appear to proceed through an octopodal intermediate without sheets, as one might interpret from **Figure 2.5**. Similarly, sample 4F adopts an octahedral-like morphology without proceeding through a branched

morphology first. Yet octopodal structures form during the early stages of synthesis for sample 4A (15 min), which is prepared with less HCl in the overgrowth solution than sample 4F. This observation highlights the important role of reaction pH and fast growth in achieving branched nanocrystals. Otherwise, slow growth will predominate, as will convex structures. Significantly, these findings indicate that the different morphologies of the Au-rich phase formed initially during co-reduction direct the subsequent deposition of the Pd-rich phase.

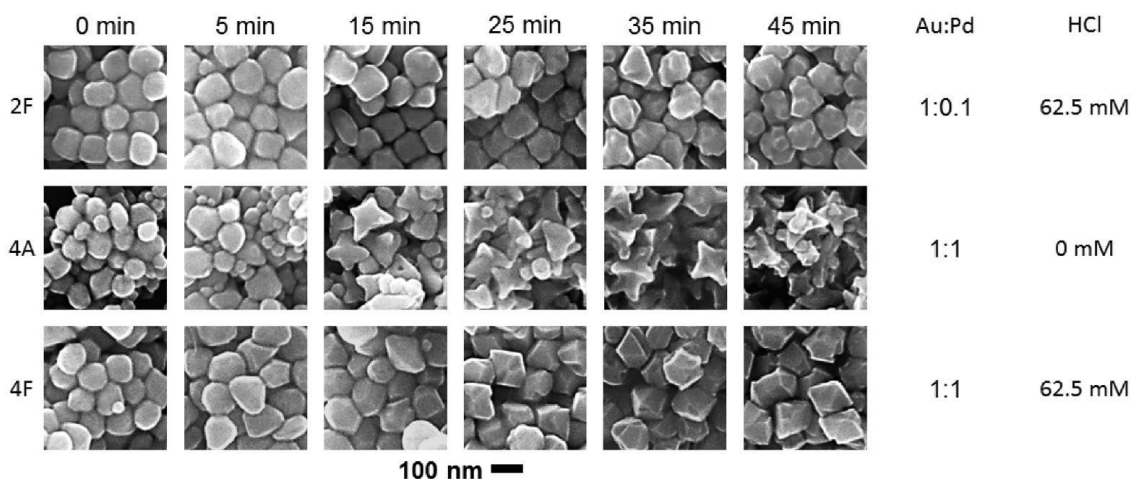


Figure 2.8. SEM images of the products obtained by analyzing aliquots at different times after the co-reduction step. From top to bottom: samples 2F, 4A, and 4F.

2.5 Evaluation of Capping Agents¹

In addition to the important role of precursor reduction rate on morphology development, structure direction can be achieved in a nanosynthesis through the use of capping agents (either intentionally added to the solution or present during a nanosynthesis from precursor selection).⁷⁸ In considering this seed-mediated co-reduction synthesis, the role of CTAB must be evaluated, as it is used as a stabilizing surfactant.

CTAB is also used in Au nanorod syntheses, where it forms a bilayer, and the bromide is thought to electrostatically stabilize {100} facets relative to {111} facets given the prevalence of cube and rod-like structures prepared in its presence.^{33, 81, 82} Thus, CTAB was replaced with cetyltrimethylammonium chloride (CTAC) to elucidate the role of Br⁻ during the synthesis of Au–Pd nanocrystals via seed-mediated co-reduction. Note that the CTAB was replaced with CTAC after Au core formation but prior to co-reduction to ensure that any observed changes in morphology are from the change in surfactant and not the shape of the Au core (see **Appendix A2.3.6**). CTAB and CTAC are both quaternary ammonium salts and differ only in their counteranion, Br⁻ vs. Cl⁻. Interestingly, Mirkin and co-workers recently found that replacing CTAB with CTAC facilitated the formation of concave Au nanocubes rather than tetrahexahedra when all other synthetic parameters were held constant.⁴⁶ The origin of this difference was not elucidated but indicates that subtle changes in a synthesis can facilitate unique outcomes. Shown in **Figure 2.9A,B** are comparative SEM images of the Au–Pd nanostructures formed at a 1:0.1 Au:Pd precursor ratio in the presence of equal concentrations of CTAC and CTAB, respectively. Octopods form in both cases. Yet the tips of the octopods prepared in the presence of CTAC are much sharper than those prepared with CTAB, which display flattened tips corresponding to Pd-rich {111} facets. Adding KBr to the CTAC system led to the expression of similarly flattened tips at low concentrations (CTAC:Br⁻ = 1:0.75; **Figure 2.9C**).

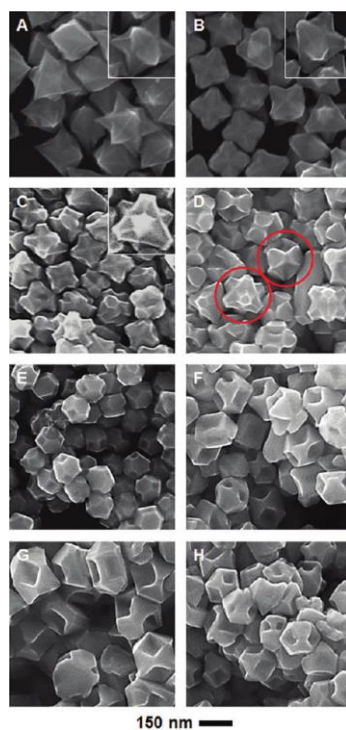


Figure 2.9. SEM images of Au–Pd nanocrystals formed via seed-mediated co-reduction at a Au:Pd precursor ratio of 1:0.1. (A) CTAC and (B) CTAB were used as stabilizing agents, respectively. The concentration of CTA^+ is the same (see **Appendix A2.3.6**). KBr solution was added to the CTAC-based synthesis prior to co-reduction at CTAC-to- Br^- ratios of 1:X where X is (C) 0.75, (D) 0.875, (E) 1.0, (F) 1.125, (G) 1.25, and (H) 1.375. A low concentration of HCl was added to the syntheses of samples (C)–(H), as it improved sample monodispersity (see **Appendix A2.3.5** and **Figure S2.11** for control experiment). Circled in (D) are two different particle architectures, where one particle has $\{111\}$ facets that have fused together to generate a hopper-like nanocrystal and the other does not.

It is curious that Pd-rich $\{111\}$ facets are widened with increasing Br^- content rather than $\{100\}$ facets expressed. We interpret this observation to mean that the

addition of Br^- to the synthesis has its greatest effect on Pd precursor reduction rather than habit modification via surface stabilization or the reduction properties of the Au precursor. It is known that Pd(II) can coordinate as $[\text{CTA}]_2\text{PdBr}_4$ and related species and that the reduction rate associated with $[\text{PdBr}_4]^{2-}$ is slow relative to $[\text{PdCl}_4]^{2-}$.⁷¹ This condition could provide greater temporal separation between the reduction of the Au and Pd precursors. The association of Pd(II) with Br^- in our system was verified via UV-visible spectroscopy (see **Figure S2.13**). On the basis of these findings, we believe that adding Br^- to the synthesis temporally separates reduction of the Au and Pd precursors and, in turn, their addition to the growing nanostructures. We note that the Au precursor may be similarly coordinated with Br^- , but the observation of Au-based branches suggests that the kinetics of its reduction are not as strongly influenced by this factor. Regardless, temporally separating the reduction of different precursors would lead to the spatial separation of Au-rich and Pd-rich regions in the final nanostructures at sufficiently high Br^- concentrations. Since Pd-exclusive surfaces would be thermodynamically favorable for Au/Pd nanocrystals, post-synthesis surface segregation is unlikely to occur.^{83, 84}

As the amount of Br^- in the syntheses increases further, the nanocrystals adopt octopodal structures with truncated tips that in some cases appear fused together (CTAC: Br^- = 1:0.875; **Figure 2.9D**). Remarkably, at even higher Br^- concentrations, the $\{111\}$ tips are so wide that nanocrystals form with deep angular concavities on what would be the $\{100\}$ facets of cuboctahedral nanocrystals otherwise (**Figure 2.9E–H**). Control experiments found that adding more Br^- to the traditional CTAB-based synthesis of octopods facilitated the formation of similar structures (**Figure S2.14A**), while adding

additional Cl^- to the bromide-free/CTAC synthesis gave sharply tipped octopods (**Figure S2.14B**). These concave crystals bear a resemblance to hopper crystals, which contain face-centered pits and whose name derives from the railway cars that carry grain.⁸⁵⁻⁸⁸ Such crystals form under kinetically controlled growth conditions wherein crystal edges grow faster than crystal faces. However, in our system no concavities are observed within the $\{111\}$ facets, as would be expected from such overgrowth of cuboctahedra, and suggests that a different growth mechanism is operating.⁸⁸ Interestingly, Mirkin and co-workers recently reported the Ag^+ -mediated synthesis of Au octahedra with deep angular concavities similar to those observed in our Au–Pd hopper-like nanocrystals.⁸⁹ They attributed the formation of their structures to slowed precursor reduction and kinetically controlled growth conditions that favor metal deposition on the highest energy features, as is observed here as well. Additional characterization is provided in **Figure 2.10**. A STEM image of an individual hopper-like particle reveals that the $\{111\}$ facets on opposite sides of the crystal are both truncated triangles but rotated 45° from one another. STEM-EDX elemental mapping indicates that Pd is dispersed all over the surface with the structure consisting of a Au-based cuboctahedral core.

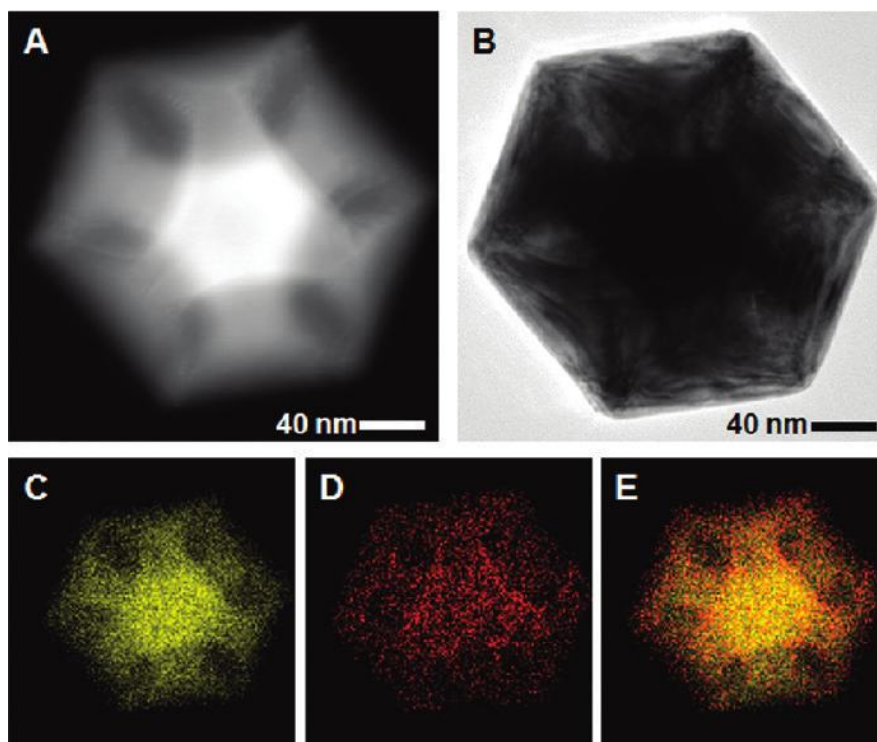


Figure 2.10. (A) STEM and (B) TEM images of a hopper-like nanocrystal as prepared in Figure 2.9G. The nanocrystal was also characterized using STEM-EDX elemental mapping: (C) Au only, (D) Pd only, and (E) an overlay of the Au and Pd signals.

From this detailed analysis, it is evident that morphology development during seed-mediated co-reduction is sensitive to factors that influence growth kinetics. A complicating factor of this analysis is that each metal precursor can respond differently to synthetic parameters that govern kinetics. In our Au–Pd system, reaction pH had its greatest effect in directing the growth of the Au-rich phase and thus its shape. This observation can be accounted for by the pH-dependent rates of (i) metal precursor reduction with L-aa and (ii) Au core etching via Au(III)-CTAB complexes. Interestingly, revisiting the results presented in **Figure S2.6** reveals a similar pH dependence for the seed-mediated growth of Au nanostructures. Gold cuboctahedra, Au nanocubes, and a

mixture of Au nanocubes and octahedra form with increasing HCl content in the overgrowth solution containing only Au precursor. In contrast, the reduction of only Pd precursor yields {111}-terminated Au@Pd octahedra with increasing HCl content in the overgrowth solution. The different behaviors observed in the Au and Pd systems manifest in the bimetallic system as well, with the Au-rich regions adopting an assortment of shapes dependent on pH and the Pd-rich regions expressing {111} facets. Thus, studying the trends observed in monometallic nanocrystal syntheses may facilitate the predictive synthesis of bimetallic nanostructures via seed-mediated co-reduction.

2.6 Optical Properties of Au—Pd Nanocrystals¹

On account of their unique structures, various samples were also characterized by UV–visible spectroscopy. Anisotropic nanocrystals composed of Au, including branched nanostars and 1-D nanorods, have attracted much attention on account of their tunable SPRs in the visible and near-IR region.^{59, 79, 90} This region is of technological relevance for biomedical applications and chemical sensing modalities via Raman spectroscopy.³² Much less is known about the optical properties of such structures when they incorporate a second metal, such as Pd. However, studies of Au@Pd nanobars show that layers of Pd blue shift and broaden the LSPR on account of the difference in dielectric constant between Au and Pd and increased damping from the Pd shell.⁶⁶ The normalized UV–visible spectra for the Au–Pd nanocrystals in Row 4 are shown in **Figure 2.11A**, with the primary area of interest enlarged in **Figure 2.11B**. The SPR for sample 4A is located at 700 nm. This SPR position in the near-IR is consistent with the branched nature of the Au–Pd nanocrystals.⁹⁰ Recall that adding HCl to the overgrowth solution yielded nanocrystals of similar size but with decreasing branch length and flattened tips. These

changes in morphology are correlated with a blue shift to 400 nm, followed by slight red shifts to 550 nm as the nanocrystals adopt an octahedral shape. These observations are consistent with studies of other branched structures wherein a decrease in branch length manifested initially as a blue shift.⁹⁰ The resonance associated with sample 4F is slightly to the blue compared to octahedral Au nanocrystals of similar size and is the result of Pd on the surface of the nanocrystal.⁶⁶

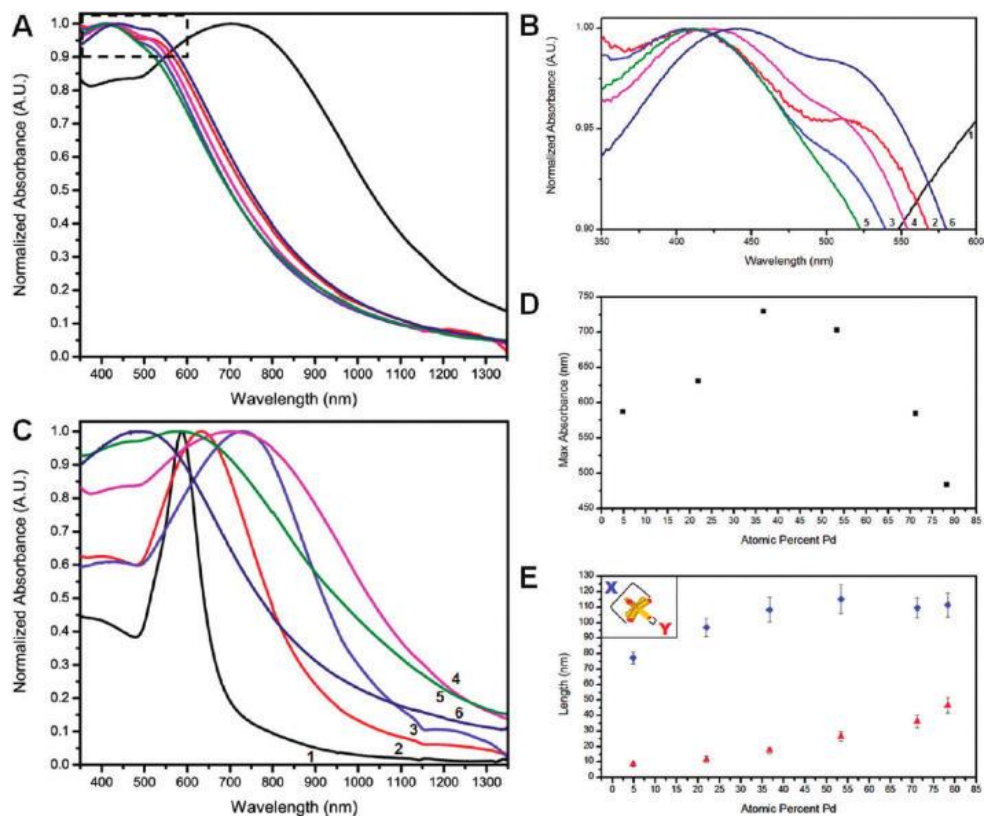


Figure 2.11. (A) Normalized absorbance spectra of Au–Pd nanocrystals (Row 4, **Figure 2.5**) and (B) inset of the spectra with labels 1–6 corresponding to samples 4A–4F, respectively. (C) Normalized absorbance spectra of Au–Pd nanocrystals (Column A, **Figure 2.5**) with labels 1–6 corresponding to samples 1A–6A, respectively. (D) Wavelength of maximum SPR absorbance and (E) corresponding dimensions of the nanocrystals (Column A, **Figure 2.5**) plotted as a function of atomic percent Pd in the synthesis.

The UV–visible spectra are presented in **Figure 2.11C** for the Au–Pd octopods with different Pd loadings at their tips (Column A). A sharp SPR is observed at 600 nm for sample 1A. There is a gradual red shift with increasing Pd precursor in the overgrowth solution (samples 2A through 4A) followed by a blue shift to 500 nm with

sample 6A. Given the structural similarities between all of the samples, the position of the SPR was analyzed as a function of both branch length and tip width for the Au–Pd octopods (**Figure 2.7D** and **E**). This analysis found that the red shift arises primarily with an elongation in branch length denoted as “X” in **Figure 2.11E**, which increases consistently for samples 1A–4A (**Figure 2.7E**). On the other hand, the blue shift correlates with an increase in tip width denoted as “Y” in **Figure 2.11E**, which increases most for samples 4A–6A (**Figure 2.11E**). The optical properties of the Au–Pd octopods will be analyzed in a more systematic manner in Chapter 4. Elucidating the synthetic parameters that govern structure formation allows for the optical properties of these Au–Pd nanocrystals to be facilely and predictably manipulated via seed-mediated co-reduction.

2.7 Conclusions

The synthesis of bimetallic nanostructures with defined features is often daunting with traditional co-reduction methods on account of the different properties of each metal precursor. Yet as demonstrated here, coupling co-reduction with a seed-mediated synthesis represents a versatile route to architecturally controlled bimetallic nanostructures with Au–Pd octopods, concave nanostructures including new hopper-like nanocrystals with deep angular concavities, and shape-controlled alloy nanocrystals achieved. Our systematic study of the reaction conditions attributes the formation of these distinct nanostructures to the careful manipulation of growth kinetics, with observations in the bimetallic system being similar to those in the monometallic analogues. As such, seed-mediated co-reduction represents a potentially powerful means of achieving bimetallic nanostructures with well-defined and controllable features. Also, these results

provide insight into how self-seeding co-reduction techniques could be exploited to achieve one-step approaches toward architecturally controlled bimetallic nanostructures.⁹¹⁻⁹³

2.8 References

1. DeSantis, C. J.; Sue, A. C.; Bower, M. M.; Skrabalak, S. E., Seed-Mediated Co-reduction: A Versatile Route to Architecturally Controlled Bimetallic Nanostructures. *ACS Nano* **2012**, *6*, 2617-2628.
2. Wang, D.; Li, Y., Bimetallic Nanocrystals: Liquid-Phase Synthesis and Catalytic Applications. *Adv. Mater.* **2011**, *23*, 1044-1060.
3. Skrabalak, S. E.; Xia, Y., Pushing Nanocrystal Synthesis toward Nanomanufacturing. *ACS Nano* **2009**, *3*, 10-15.
4. González, E.; Arbiol, J.; Puntès, V. F., Carving at the Nanoscale: Sequential Galvanic Exchange and Kirkendall Growth at Room Temperature. *Science* **2011**, *334*, 1377-1380.
5. Hong, J. W.; Kim, D.; Lee, Y. W.; Kim, M.; Kang, S. W.; Han, S. W., Atomic-Distribution-Dependent Electrocatalytic Activity of Au–Pd Bimetallic Nanocrystals. *Angew. Chem. Int. Ed.* **2011**, *50*, 8876-8880.
6. Wang, L.; Nemoto, Y.; Yamauchi, Y., Direct Synthesis of Spatially-Controlled Pt-on-Pd Bimetallic Nanodendrites with Superior Electrocatalytic Activity. *J. Am. Chem. Soc.* **2011**, *133*, 9674-9677.
7. Ataee-Esfahani, H.; Wang, L.; Nemoto, Y.; Yamauchi, Y., Synthesis of Bimetallic Au@Pt Nanoparticles with Au Core and Nanostructured Pt Shell toward Highly Active Electrocatalysts. *Chem. Mater.* **2010**, *22*, 6310-6318.

8. Allgeyer, E. S.; Pongan, A.; Browne, M.; Mason, M. D., Optical Signal Comparison of Single Fluorescent Molecules and Raman Active Gold Nanostars. *Nano Lett.* **2009**, *9*, 3816-3819.
9. Zhang, H.; Jin, M.; Liu, H.; Wang, J.; Kim, M. J.; Yang, D.; Xie, Z.; Liu, J.; Xia, Y., Facile Synthesis of Pd–Pt Alloy Nanocages and Their Enhanced Performance for Preferential Oxidation of CO in Excess Hydrogen. *ACS Nano* **2011**, *5*, 8212-8222.
10. Cortie, M. B.; McDonagh, A. M., Synthesis and Optical Properties of Hybrid and Alloy Plasmonic Nanoparticles. *Chem. Rev.* **2011**, *111*, 3713-3735.
11. Major, K.; De, C.; Obare, S., Recent Advances in the Synthesis of Plasmonic Bimetallic Nanoparticles. *Plasmonics* **2009**, *4*, 61-78.
12. Xia, Y.; Li, W.; Cobley, C. M.; Chen, J.; Xia, X.; Zhang, Q.; Yang, M.; Cho, E. C.; Brown, P. K., Gold Nanocages: From Synthesis to Theranostic Applications. *Acc. Chem. Res.* **2011**, *44*, 914-924.
13. Liu; Guyot-Sionnest, P., Synthesis and Optical Characterization of Au/Ag Core/Shell Nanorods. *J. Phys. Chem. B* **2004**, *108*, 5882-5888.
14. Becker, J.; Zins, I.; Jakab, A.; Khalavka, Y.; Schubert, O.; Sönnichsen, C., Plasmonic Focusing Reduces Ensemble Linewidth of Silver-Coated Gold Nanorods. *Nano Lett.* **2008**, *8*, 1719-1723.
15. Seo, D.; Yoo, C. I.; Jung, J.; Song, H., Ag–Au–Ag Heterometallic Nanorods Formed through Directed Anisotropic Growth. *J. Am. Chem. Soc.* **2008**, *130*, 2940-2941.
16. Zhou, S.; Jackson, G. S.; Eichhorn, B., AuPt Alloy Nanoparticles for CO-Tolerant Hydrogen Activation: Architectural Effects in Au-Pt Bimetallic Nanocatalysts. *Adv. Funct. Mater.* **2007**, *17*, 3099-3104.

17. Ortiz, N.; Skrabalak, S. E., Controlling the Growth Kinetics of Nanocrystals via Galvanic Replacement: Synthesis of Au Tetrapods and Star-Shaped Decahedra. *Cryst. Growth Des.* **2011**, *11*, 3545-3550.
18. Niu, W.; Zhang, L.; Xu, G., Shape-Controlled Synthesis of Single-Crystalline Palladium Nanocrystals. *ACS Nano* **2010**, *4*, 1987-1996.
19. Habas, S. E.; Lee, H.; Radmilovic, V.; Somorjai, G. A.; Yang, P., Shaping binary metal nanocrystals through epitaxial seeded growth. *Nat. Mater.* **2007**, *6*, 692-697.
20. Carbone, L.; Kudera, S.; Carlino, E.; Parak, W. J.; Giannini, C.; Cingolani, R.; Manna, L., Multiple Wurtzite Twinning in CdTe Nanocrystals Induced by Methylphosphonic Acid. *J. Am. Chem. Soc.* **2005**, *128*, 748-755.
21. Fan, F.-R.; Liu, D.-Y.; Wu, Y.-F.; Duan, S.; Xie, Z.-X.; Jiang, Z.-Y.; Tian, Z.-Q., Epitaxial Growth of Heterogeneous Metal Nanocrystals: From Gold Nano-octahedra to Palladium and Silver Nanocubes. *J. Am. Chem. Soc.* **2008**, *130*, 6949-6951.
22. Banin, U., Nanocrystals: Tiny seeds make a big difference. *Nat. Mater.* **2007**, *6*, 625-626.
23. Sau, T. K.; Murphy, C. J., Room Temperature, High-Yield Synthesis of Multiple Shapes of Gold Nanoparticles in Aqueous Solution. *J. Am. Chem. Soc.* **2004**, *126*, 8648-8649.
24. Lu, C.-L.; Prasad, K. S.; Wu, H.-L.; Ho, J.-a. A.; Huang, M. H., Au Nanocube-Directed Fabrication of Au-Pd Core-Shell Nanocrystals with Tetrahedral, Concave Octahedral, and Octahedral Structures and Their Electrocatalytic Activity. *J. Am. Chem. Soc.* **2010**, *132*, 14546-14553.

25. Yu, Y.; Zhang, Q.; Liu, B.; Lee, J. Y., Synthesis of Nanocrystals with Variable High-Index Pd Facets through the Controlled Heteroepitaxial Growth of Trisoctahedral Au Templates. *J. Am. Chem. Soc.* **2010**, *132*, 18258-18265.
26. Yang, C.-W.; Chanda, K.; Lin, P.-H.; Wang, Y.-N.; Liao, C.-W.; Huang, M. H., Fabrication of Au–Pd Core–Shell Heterostructures with Systematic Shape Evolution Using Octahedral Nanocrystal Cores and Their Catalytic Activity. *J. Am. Chem. Soc.* **2011**, *133*, 19993-20000.
27. Wang, F.; Li, C.; Sun, L.-D.; Wu, H.; Ming, T.; Wang, J.; Yu, J. C.; Yan, C.-H., Heteroepitaxial Growth of High-Index-Faceted Palladium Nanoshells and Their Catalytic Performance. *J. Am. Chem. Soc.* **2010**, *133*, 1106-1111.
28. DeSantis, C. J.; Peverly, A. A.; Peters, D. G.; Skrabalak, S. E., Octopods versus Concave Nanocrystals: Control of Morphology by Manipulating the Kinetics of Seeded Growth via Co-Reduction. *Nano Lett.* **2011**, *11*, 2164-2168.
29. Xia, Y.; Xiong, Y.; Lim, B.; Skrabalak, S. E., Shape-Controlled Synthesis of Metal Nanocrystals: Simple Chemistry Meets Complex Physics? *Angew. Chem. Int. Ed.* **2009**, *48*, 60-103.
30. Tao, A. R.; Habas, S.; Yang, P., Shape control of colloidal metal nanocrystals. *Small* **2008**, *4*, 310-325.
31. Kamat, P. V., Photophysical, Photochemical and Photocatalytic Aspects of Metal Nanoparticles. *J. Phys. Chem. B* **2002**, *106*, 7729-7744.
32. Willets, K. A.; Van Duyne, R. P., Localized surface plasmon resonance spectroscopy and sensing. *Annu. Rev. Phys. Chem.* **2007**, *58*, 267-297.

33. Murphy, C. J.; Sau, T. K.; Gole, A. M.; Orendorff, C. J.; Gao, J.; Gou, L.; Hunyadi, S. E.; Li, T., Anisotropic Metal Nanoparticles: Synthesis, Assembly, and Optical Applications. *J. Phys. Chem. B* **2005**, *109*, 13857-13870.
34. Narayanan, R.; El-Sayed, M. A., Catalysis with Transition Metal Nanoparticles in Colloidal Solution: Nanoparticle Shape Dependence and Stability. *J. Phys. Chem.* **2005**, *109*, 12663-12676.
35. Somorjai, G. A.; Park, J. Y., Colloid Science of Metal Nanoparticle Catalysts in 2D and 3D Structures. Challenges of Nucleation, Growth, Composition, Particle Shape, Size Control and Their Influence on Activity and Selectivity. *Top. Catal.* **2008**, *49*, 126-135.
36. Rosi, N. L.; Mirkin, C. A., Nanostructures in Biodiagnostics. *Chem. Rev.* **2005**, *105*, 1547-1562.
37. Lal, S.; Clare, S. E.; Halas, N. J., Nanoshell-Enabled Photothermal Cancer Therapy: Impending Clinical Impact. *Acc. Chem. Res.* **2008**, *41*, 1842-1851.
38. Skrabalak, S. E.; Chen, J.; Sun, Y.; Lu, X.; Au, L.; Cobley, C. M.; Xia, Y., Gold Nanocages: Synthesis, Properties, and Applications. *Acc. Chem. Res.* **2008**, *41*, 1587-1595.
39. Murphy, C. J.; Gole, A. M.; Stone, J. W.; Sisco, P. N.; Alkilany, A. M.; Goldsmith, E. C.; Baxter, S. C., Gold Nanoparticles in Biology: Beyond Toxicity to Cellular Imaging. *Acc. Chem. Res.* **2008**, *41*, 1721-1730.
40. Cheong, S.; Watt, J.; Ingham, B.; Toney, M. F.; Tilley, R. D., In Situ and Ex Situ Studies of Platinum Nanocrystals: Growth and Evolution in Solution. *J. Am. Chem. Soc.* **2009**, *131*, 14590-14595.

41. Mulvihill, M. J.; Ling, X. Y.; Henzie, J.; Yang, P., Anisotropic Etching of Silver Nanoparticles for Plasmonic Structures Capable of Single-Particle SERS. *J. Am. Chem. Soc.* **2009**, *132*, 268-274.
42. Hong, J. W.; Lee, Y. W.; Kim, M.; Kang, S. W.; Han, S. W., One-pot synthesis and electrocatalytic activity of octapodal Au-Pd nanoparticles. *Chem. Commun.* **2011**, *47*, 2553-2555.
43. Watt, J.; Young, N.; Haigh, S.; Kirkland, A.; Tilley, R. D., Synthesis and Structural Characterization of Branched Palladium Nanostructures. *Adv. Mater.* **2009**, *21*, 2288-2293.
44. Chou, S.-W.; Zhu, C.-L.; Neeleshwar, S.; Chen, C.-L.; Chen, Y.-Y.; Chen, C.-C., Controlled Growth and Magnetic Property of FePt Nanostructure: Cuboctahedron, Octapod, Truncated Cube, and Cube. *Chem. Mater.* **2009**, *21*, 4955-4961.
45. Huang, X.; Tang, S.; Zhang, H.; Zhou, Z.; Zheng, N., Controlled Formation of Concave Tetrahedral/Trigonal Bipyramidal Palladium Nanocrystals. *J. Am. Chem. Soc.* **2009**, *131*, 13916-13917.
46. Zhang, J.; Langille, M. R.; Personick, M. L.; Zhang, K.; Li, S.; Mirkin, C. A., Concave Cubic Gold Nanocrystals with High-Index Facets. *J. Am. Chem. Soc.* **2010**, *132*, 14012-14014.
47. Wang, L.; Wu, X.; Li, X.; Wang, L.; Pei, M.; Tao, X., Facile synthesis of concave gold nanoplates in hexagonal liquid crystal made of SDS/water system. *Chem. Commun.* **2010**, *46*, 8422-8423.

48. Yu, Y.; Zhang, Q.; Lu, X.; Lee, J. Y., Seed-Mediated Synthesis of Monodisperse Concave Trisoctahedral Gold Nanocrystals with Controllable Sizes. *J. Phys. Chem. C* **2010**, *114*, 11119-11126.
49. Zhang, H.; Li, W.; Jin, M.; Zeng, J.; Yu, T.; Yang, D.; Xia, Y., Controlling the Morphology of Rhodium Nanocrystals by Manipulating the Growth Kinetics with a Syringe Pump. *Nano Lett.* **2010**, *11*, 898-903.
50. Lim, B.; Xia, Y., Metal Nanocrystals with Highly Branched Morphologies. *Angew. Chem. Int. Ed.* **2011**, *50*, 76-85.
51. Jana, N. R.; Gearheart, L.; Murphy, C. J., Wet Chemical Synthesis of High Aspect Ratio Cylindrical Gold Nanorods. *J. Phys. Chem. B* **2001**, *105*, 4065-4067.
52. Nikoobakht, B.; El-Sayed, M. A., Preparation and Growth Mechanism of Gold Nanorods (NRs) Using Seed-Mediated Growth Method. *Chem. Mater.* **2003**, *15*, 1957-1962.
53. Carbone, L.; Cozzoli, P. D., Colloidal heterostructured nanocrystals: Synthesis and growth mechanisms. *Nano Today* **2010**, *5*, 449-493.
54. Zorić, I.; Zäch, M.; Kasemo, B.; Langhammer, C., Gold, Platinum, and Aluminum Nanodisk Plasmons: Material Independence, Subradiance, and Damping Mechanisms. *ACS Nano* **2011**, *5*, 2535-2546.
55. Lee, Y. W.; Kim, M.; Kim, Z. H.; Han, S. W., One-Step Synthesis of Au@Pd Core-Shell Nanooctahedron. *J. Am. Chem. Soc.* **2009**, *131*, 17036-17037.
56. Weiner, R. G. D., Christopher J.; Cardoso, Mariana B.T.; Skrabalak, Sara E., Diffusion and Seed Shape: Intertwined Parameters in the Synthesis of Branched Metal Nanostructures. *ACS Nano* **2014**, *Submitted*.

57. Hao, F.; Nehl, C. L.; Hafner, J. H.; Nordlander, P., Plasmon Resonances of a Gold Nanostar. *Nano Lett.* **2007**, *7*, 729-732.
58. Nehl, C. L.; Liao, H.; Hafner, J. H., Optical Properties of Star-Shaped Gold Nanoparticles. *Nano Lett.* **2006**, *6*, 683-688.
59. Kumar, P. S.; Pastoriza-Santos, I.; Rodríguez-González, B.; Abajo, F. J. G. d.; Liz-Marzán, L. M., High-yield synthesis and optical response of gold nanostars. *Nanotechnology* **2008**, *19*, 015606.
60. Barbosa, S.; Agrawal, A.; Rodríguez-Lorenzo, L.; Pastoriza-Santos, I.; Alvarez-Puebla, R. n. A.; Kornowski, A.; Weller, H.; Liz-Marzán, L. M., Tuning Size and Sensing Properties in Colloidal Gold Nanostars. *Langmuir* **2010**, *26*, 14943-14950.
61. Liu; Guyot-Sionnest, P., Mechanism of Silver(I)-Assisted Growth of Gold Nanorods and Bipyramids. *J. Phys. Chem. B* **2005**, *109*, 22192-22200.
62. Khan, M. M. T.; Martell, A. E., The kinetics of the reaction of iron(III) chelates of aminopolycarboxylic acids with ascorbic acid. *J. Am. Chem. Soc.* **1968**, *90*, 3386-3389.
63. Rodríguez-Fernández, J.; Pérez-Juste, J.; Mulvaney, P.; Liz-Marzán, L. M., Spatially-Directed Oxidation of Gold Nanoparticles by Au(III)-CTAB Complexes. *J. Phys. Chem. B* **2005**, *109*, 14257-14261.
64. Tsuji, M.; Miyamae, N.; Hashimoto, M.; Nishio, M.; Hikino, S.; Ishigami, N.; Tanaka, I., Shape and size controlled synthesis of gold nanocrystals using oxidative etching by AuCl₄⁻ and Cl⁻ anions in microwave-polyol process. *Colloids Surf., A* **2007**, *302*, 587-598.
65. Naumov, I. I.; Li, Z.; Bratkovsky, A. M., Plasmonic resonances and hot spots in Ag octopods. *Appl. Phys. Lett.* **2010**, *96*, 033105/1-033105/3.

66. Zhang, K.; Xiang, Y.; Wu, X.; Feng, L.; He, W.; Liu, J.; Zhou, W.; Xie, S., Enhanced Optical Responses of Au@Pd Core/Shell Nanobars. *Langmuir* **2008**, *25*, 1162-1168.
67. Baldauf, M.; Kolb, D. M., Formic Acid Oxidation on Ultrathin Pd Films on Au(hkl) and Pt(hkl) Electrodes. *J. Phys. Chem.* **1996**, *100*, 11375-11381.
68. Hu, J.-W.; Li, J.-F.; Ren, B.; Wu, D.-Y.; Sun, S.-G.; Tian, Z.-Q., Palladium-Coated Gold Nanoparticles with a Controlled Shell Thickness Used as Surface-Enhanced Raman Scattering Substrate. *J. Phys. Chem. C* **2006**, *111*, 1105-1112.
69. Heck, K. N.; Janesko, B. G.; Scuseria, G. E.; Halas, N. J.; Wong, M. S., Observing Metal-Catalyzed Chemical Reactions in Situ Using Surface-Enhanced Raman Spectroscopy on Pd–Au Nanoshells. *J. Am. Chem. Soc.* **2008**, *130*, 16592-16600.
70. Kim, D.; Lee, Y. W.; Lee, S. B.; Han, S. W., Convex Polyhedral Au@Pd Core–Shell Nanocrystals with High-Index Facets. *Angew. Chem. Int. Ed.* **2012**, *51*, 159-163.
71. Berhault, G.; Bausach, M.; Bisson, L.; Becerra, L.; Thomazeau, C.; Uzio, D., Seed-Mediated Synthesis of Pd Nanocrystals: Factors Influencing a Kinetic- or Thermodynamic-Controlled Growth Regime. *J. Phys. Chem. C* **2007**, *111*, 5915-5925.
72. Okitsu, K.; Sharyo, K.; Nishimura, R., One-Pot Synthesis of Gold Nanorods by Ultrasonic Irradiation: The Effect of pH on the Shape of the Gold Nanorods and Nanoparticles. *Langmuir* **2009**, *25*, 7786-7790.
73. Goia, D. V.; Matijevic, E., Tailoring the particle size of monodispersed colloidal gold. *Colloids Surf., A* **1999**, *146*, 139-152.

74. Trigari, S.; Rindi, A.; Margheri, G.; Sottini, S.; Dellepiane, G.; Giorgetti, E., Synthesis and modelling of gold nanostars with tunable morphology and extinction spectrum. *J. Mater. Chem* **2011**, *21*, 6531-6540.
75. Watt, J.; Cheong, S.; Toney, M. F.; Ingham, B.; Cookson, J.; Bishop, P. T.; Tilley, R. D., Ultrafast Growth of Highly Branched Palladium Nanostructures for Catalysis. *ACS Nano* **2009**, *4*, 396-402.
76. Massalski, T. B., *Binary Alloy Phase Diagrams*. 2nd ed.; ASM Int.: Materials Park, OH, 1990.
77. Tsuji, M.; Miyamae, N.; Lim, S.; Kimura, K.; Zhang, X.; Hikino, S.; Nishio, M., Crystal Structures and Growth Mechanisms of Au@Ag Core–Shell Nanoparticles Prepared by the Microwave–Polyol Method. *Cryst. Growth Des.* **2006**, *6*, 1801-1807.
78. Zeng, J.; Zheng, Y.; Rycenga, M.; Tao, J.; Li, Z.-Y.; Zhang, Q.; Zhu, Y.; Xia, Y., Controlling the Shapes of Silver Nanocrystals with Different Capping Agents. *J. Am. Chem. Soc.* **2010**, *132*, 8552-8553.
79. Bullen, C.; Zijlstra, P.; Bakker, E.; Gu, M.; Raston, C., Chemical Kinetics of Gold Nanorod Growth in Aqueous CTAB Solutions. *Cryst. Growth Des.* **2011**, *11*, 3375-3380.
80. Bower, M. M.; DeSantis, C. J.; Skrabalak, S. E., A Quantitative Analysis of Anions and pH on the Growth of Bimetallic Nanostructures. *J. Phys. Chem. C* **2014**, Accepted.
81. Murphy, C. J.; Thompson, L. B.; Alkilany, A. M.; Sisco, P. N.; Boulos, S. P.; Sivapalan, S. T.; Yang, J. A.; Chernak, D. J.; Huang, J., The Many Faces of Gold Nanorods. *J. Phys. Chem. Lett.* **2010**, *1*, 2867-2875.

82. Xiong, Y.; Cai, H.; Wiley, B. J.; Wang, J.; Kim, M. J.; Xia, Y., Synthesis and Mechanistic Study of Palladium Nanobars and Nanorods. *J. Am. Chem. Soc.* **2007**, *129*, 3665-3675.
83. Vitos, L.; Ruban, A. V.; Skriver, H. L.; Kollár, J., The surface energy of metals. *Surf. Sci.* **1998**, *411*, 186-202.
84. Ringe, E.; DeSantis, C. J.; Collins, S. M.; Skrabalak, S. E.; Midgley, P. A., Composition, Crystallography, and Plasmonic Response of Single Au/Pd Octopods. **2014**, Submitted.
85. Inoue, S.; Driess, M., Isolable Metallo-Germylene and Metallo-Stannylene σ -Complexes with Iron. *Organometallics* **2009**, *28*, 5032-5035.
86. Xie, S.; Lu, N.; Xie, Z.; Wang, J.; Kim, M. J.; Xia, Y., Synthesis of Pd-Rh Core-Frame Concave Nanocubes and Their Conversion to Rh Cubic Nanoframes by Selective Etching of the Pd Cores. *Angew. Chem. Int. Ed.* **2012**, *51*, 10266-10270.
87. Dickinson, S. R.; McGrath, K. M., Switching between kinetic and thermodynamic control: calcium carbonate growth in the presence of a simple alcohol. *J. Mater. Chem.* **2003**, *13*, 928-933.
88. Murray, B. J.; Li, Q.; Newberg, J. T.; Menke, E. J.; Hemminger, J. C.; Penner, R. M., Shape- and Size-Selective Electrochemical Synthesis of Dispersed Silver(I) Oxide Colloids. *Nano Lett.* **2005**, *5*, 2319-2324.
89. Langille, M. R.; Personick, M. L.; Zhang, J.; Mirkin, C. A., Bottom-Up Synthesis of Gold Octahedra with Tailorable Hollow Features. *J. Am. Chem. Soc.* **2011**, *133*, 10414-10417.

90. Kim, D. Y.; Yu, T.; Cho, E. C.; Ma, Y.; Park, O. O.; Xia, Y., Synthesis of Gold Nano-hexapods with Controllable Arm Lengths and Their Tunable Optical Properties. *Angew. Chem. Int. Ed.* **2011**, *50*, 6328-6331.
91. Wang, L.; Yamauchi, Y., Autoprogrammed Synthesis of Triple-Layered Au@Pd@Pt Core-Shell Nanoparticles Consisting of a Au@Pd Bimetallic Core and Nanoporous Pt Shell. *J. Am. Chem. Soc.* **2010**, *132*, 13636-13638.
92. Jiang, X.; Zeng, Q.; Yu, A., A self-seeding coreduction method for shape control of silver nanoplates. *Nanotechnology* **2006**, *17*, 4929-4935.
93. Sun, Y.; Xia, Y., Large-scale synthesis of uniform silver nanowires through a soft, self-seeding, polyol process. *Adv. Mater.* **2002**, *14*, 833-837.

**Chapter 3: Elucidating the Role of Seed Structure in the Synthesis of Symmetrically
Branched Nanocrystals**

3.1 Introduction¹

Branched metal nanoparticles such as nanostars and nanodendrites are exciting plasmonic and catalytic platforms on account of their often large surface areas, multiple high-angle edges, and sharp tips.² The small radius of curvature of sharp tips can concentrate electromagnetic fields at these features of Au and Ag nanostructures to achieve high sensitivity in plasmon-enhanced surface spectroscopies.³⁻⁵ Also, through size-controlled syntheses of branched metal nanoparticles, the extinction features of their localized surface plasmon resonance (LSPR) can be tuned.^{6, 7} However, most branched metal nanoparticles are asymmetric. As a result, their properties are not as well-defined or precisely and reproducibly manipulated compared to nanostructures with defined symmetries.⁸⁻¹³ Chapter 2 discussed the synthesis of stellated nanostructures through seed-mediated co-reduction. In this chapter, the role of seed structure in branched nanocrystal synthesis is elucidated by growing compositionally different branches from shape-controlled seeds. Elemental mapping of the resultant bimetallic structures allows the number and symmetry of the branches to be directly associated with the structural features of the seeds.^{14, 15} Whereas a paradigm toward convex nanocrystal synthesis has emerged with seeds of a particular structure leading to a limited number of shape-controlled nanocrystals, the analogous model for concave and branched nanocrystals is incomplete.¹⁶⁻¹⁸ Significantly, this seed-directed approach begins to fill in the gaps by enabling the synthesis of new symmetrically branched nanocrystals and providing a foundation for the rational design of concave nanostructures in general.

The uncertain relationship between seed structure and branched nanocrystal symmetry arises from difficulty in imaging the tiny seeds present during a synthesis and

their subsequent ability to restructure during overgrowth. For example, CdTe tetrapods can be rationalized to form from either sphalerite octahedra or wurtzite pyramids based on crystal symmetry arguments, but the small sizes of the nanocrystal cores can preclude a definitive assignment.¹⁹ Likewise, Pd/Pt nanodendrites have been synthesized from cuboctahedral Pd seeds, but the hyper-branched nature of the dendrites makes correlating their three-dimensional (3-D) structures to the shape of the seeds difficult.²⁰ Finally, as reported in Chapter 2, the synthesis of eight-branched Au/Pd octopods with O_h symmetry by seed-mediated co-reduction, wherein Au and Pd precursors were co-reduced to deposit metal onto $\{111\}$ -terminated octahedral Au seeds.²¹ Both Au and Pd precursors are necessary as the co-reduction technique itself manipulates the kinetics of seeded growth in favor of branched nanocrystal formation rather than platonic core@shell nanocrystals.²¹ However, the role of the seeds in directing overgrowth remains unclear.²² Mainly, the branches of the Au/Pd octopods extend along the $\langle 111 \rangle$ directions from the cores of the nanostructures and suggest that growth occurs preferentially from the eight $\{111\}$ facets of the octahedral seeds. Yet, crystal growth theory argues that growth rates should be greatest at the highest energy features of seeds; i.e., the six vertices of each octahedron. Thus, it was postulated in Section 2.2 that the Au seeds restructure during growth to cubic-like structures. Unfortunately, verifying this hypothesis is difficult in this system as Au deposits before Pd and provides no differentiation between the Au seeds and overgrowth metal.²³ Lack of elemental distinction is common in nanocrystal syntheses and is overcome here by replacing the Au seeds with shape-controlled Pd nanostructures. This change provides compositional boundaries between the seed and overgrowth metals as Au deposits first onto the now Pd seeds and enables visualization of

the relationship between seed structure and the symmetry of branched nanocrystals by electron microscopy (EM). In effect, the shape-controlled Pd nanocrystals serve as TEM labels, just as single-crystalline Au seeds were used to follow the growth of twinned Ag icosahedral shells.²⁴

3.2 Results and Discussion

In this section, HAuCl_4 and H_2PdCl_4 were co-reduced with l-ascorbic acid (L-aa) in the presence of shape-controlled Pd seeds with either CTAB or CTAC/ Br^- as a stabilizing agent. The Pd seeds included $\{100\}$ -faceted nanocubes, nanobars, and right bipyramids as well as $\{111\}$ -faceted octahedra and tetrahedra and $\{110\}$ -faceted rhombic dodecahedra. All seeds were prepared by standard methods.^{9, 25, 26} The concentrations of L-aa and CTA^+ were held constant for each synthesis, but the concentrations of HAuCl_4 , H_2PdCl_4 , and Br^- were optimized for each seed shape on account of their different surface areas and number of vertices per seed, which yields different numbers of branches per vertex depending on the shape. See details in **Appendix A3.2**. The co-reduction of Au and Pd precursors with Pd nanocubes as seeds (**Figure 3.1A**) gives nanocrystals with eight branches and O_h symmetry (**Figure 3.1B**). Electron diffraction (ED) from two particles with different orientations confirms that the branches grow along the $\langle 111 \rangle$ directions (**Appendix B Figure S3.1A–D**). Elemental mapping by STEM/EDX analysis (**Figure 3.1C–F**) shows that the nanocrystal cores consist of the Pd nanocubes, with no evidence of seed restructuring. Both elemental mapping and a TEM tilt study (**Figure S3.2** and **Video 3.1**) show that the Au-based branches emerge from each of the eight vertices of each nanocube. Pd decorates the surfaces of the octopods as its deposition, which is required for branch formation, is temporally separated from that

of Au.²² A structural model is provided as an inset to **Figure 3.1B**. Likewise, Pd nanobars (**Figure 3.1G**) also yield eight-branched nanocrystals (**Figure 3.1H**), only now with bowtie-like particle architectures and D_{4h} symmetry that is consistent with the long axis of the nanobar seeds. Elemental mapping by STEM/EDX analysis shows that branching occurs again from the vertices of intact Pd seeds (**Figure 3.1I–L**), and ED indicates that the branches proceed along the $\langle 111 \rangle$ directions (**Figure S3.1E,F**). A structural model is in the inset to **Figure 3.1H**.

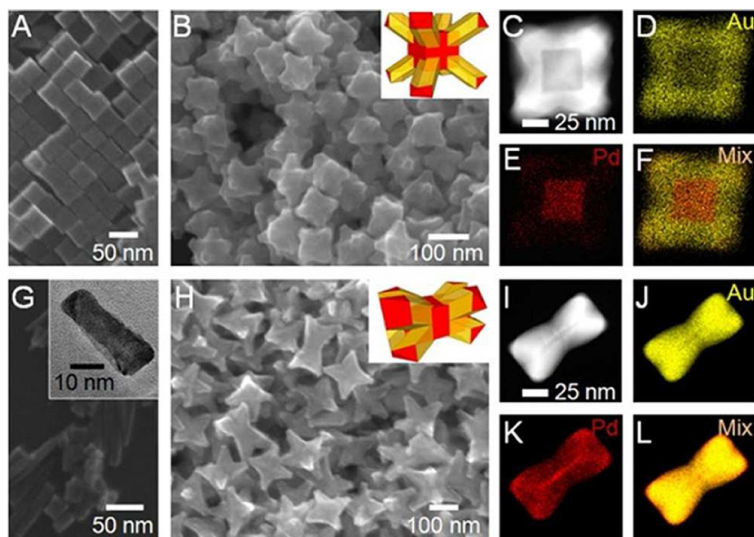


Figure 3.1. SEM images of (A) Pd nanocubes and (B) Au/Pd octopods (inset: a structural model). (C) A STEM image of a Au/Pd octopod and (D–F) elemental map by STEM-EDX analysis. Yellow, Au; red, Pd. SEM images of (G) Pd nanobars (inset: TEM image) and (H) Au/Pd bowties (inset: a structural model). (I) A STEM image of a Au/Pd bowtie and (J–L) elemental map by STEM-EDX analysis. Yellow, Au; red, Pd

Right bipyramids are an impurity in some Pd nanocube syntheses and result from a $\{111\}$ twin plane being introduced.^{27, 28} They express six $\{100\}$ -facets and five vertices (**Figure 3.2A**). Interestingly, five-branched pentapods with trigonal bipyramidal D_{3h}

symmetry are produced from co-reducing Au and Pd precursors in the presence of these seeds (**Figure 3.2B**). A TEM tilt study of a particle reveals the three in-plane and two axial branches of a pentapod (**Figure 3.2C,D**). Structural models are included. Elemental mapping by STEM/EDX analysis indicates that overgrowth occurs again from the vertices of the Pd seeds (Figure 3.2E,F). The ED pattern obtained from a pentapod positioned with axial branches parallel with the electron beam is close to the [111] zone axis and consistent with the axial branches extending along $\langle 111 \rangle$ directions perpendicular to the (111) twin plane of the Pd seed (**Figure S3.3**). Considering the in-plane branches, they are each 90° from the axial branches and at 120° from one another. Thus, the in-plane branches proceed along $\langle 112 \rangle$ directions (**Figure S3.3**). Tilting an in-plane branch of a pentapod toward the [110] zone axis reveals that the twin plane that bisects the Pd right bipyramidal seeds extends the lengths of the branches (**Figures 3.3 and S3.4** for a second example). FFTs of the regions on each side of the twin are nearly mirror images (**Figure 3.3D–F**), and lattice spacings of 0.22 nm are measured at the same angle on each side of the twin (**Figure S3.5**).²⁹ Overall, a trend is evident from the results obtained with the use of {100}-terminated Pd seeds: one branch emerges from each seed vertex. Fundamentally, nucleation and growth is preferential at the highest energy features of the seeds.

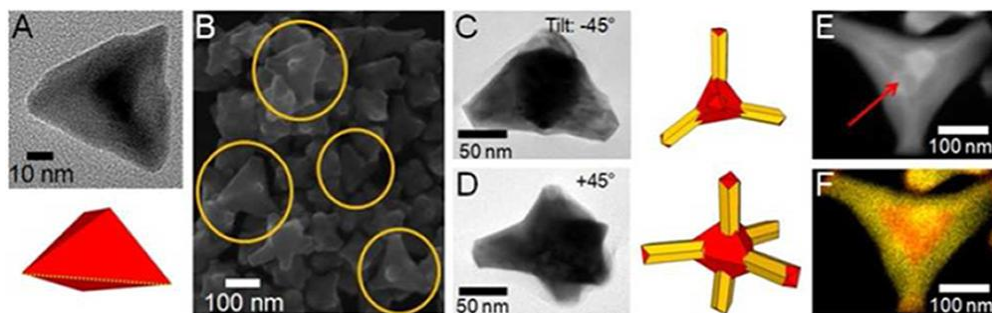


Figure 3.2. (A) A TEM image of a Pd right bipyramid and structural model below. (B) A SEM image of Au/Pd pentapods. (C, D) TEM images of a pentapod at two perspectives to reveal the in-plane (top) and axial (bottom) branches; structural models included. (E) A STEM image of a pentapod with the fifth branch projected toward the TEM grid and (F) elemental mapping by STEM/EDX analysis. Yellow, Au; red, Pd.

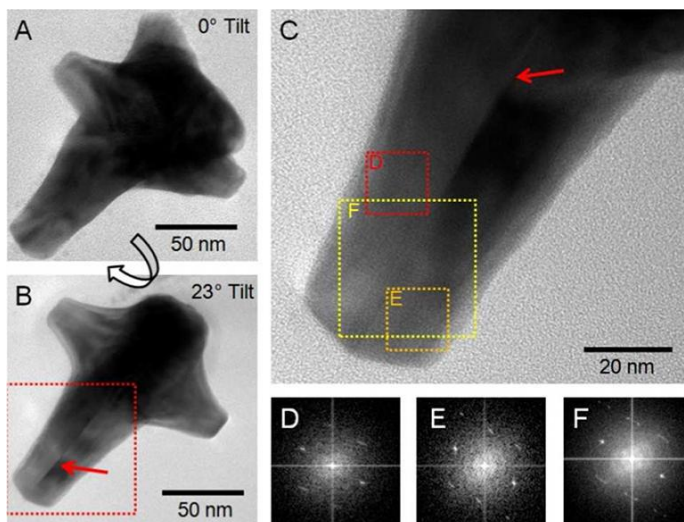


Figure 3.3. TEM images of a pentapod at (A) 0° and (B) 23° tilt (arrow denotes location of twin plane). (C) Higher magnification TEM image of region from (B). (D–F) FFTs of regions in (C).

To test if this trend is general to branched metal nanocrystal formation, {111}-terminated Pd nanocrystals were also used as seeds. From octahedra (Figure 3.4A),

particles with complex and asymmetric branching were obtained from preliminary experiments (**Figure S3.6**). SEM of the structures revealed poorly developed branches which we ascribed to insufficient space for their growth. Thus, the Br^- concentration in the synthesis was optimized by replacing CTAB with CTAC and adding back Br^- in lower amounts as this procedure was shown in Section 2.5 to produce metal nanocrystals with thinner branches and sharper tips.²² 24-branched nanocrystals with O_h symmetry were achieved (**Figure 3.4B**). A particle oriented on the imaging substrate for structural analysis is circled and reveals four branches positioned away from the substrate much like with the octopods and bowties. Four regions of additional overgrowth are evident from the sides of the particle. Tilting a similar particle in 15° increments during SEM revealed that the side overgrowths also consist of four branches (**Figure 3.4C–E**). STEM imaging, elemental mapping, and ED indicate that the branches grow along $\langle 111 \rangle$ directions, with four branches beginning from each vertex of an octahedron for a total of 24 branches (**Figures S3.7, S3.8**).³⁰ Models are included in **Figures 3.4** and **S3.8**.

Quenching this growth process as a function of reaction time then analyzing the samples by EM further confirms preferential nucleation at the seed vertices (**Figure S3.9**). After 1 min, metal collects at some of the vertices of the octahedra but branching is not observed (**Figure S3.9A,B**). Lattice registration and an epitaxial relationship between the seed and overgrowth metals are evident as is also the case when the metal precursor concentrations are decreased relative to that of the seeds (**Figure S3.10**). By 3 min, anisotropic growth from the initial site of metal deposition is evident (**Figure S3.9C,D**). The 24-branched nanocrystals form within 10 min (**Figure S3.9G**). Just as with the $\{100\}$ -terminated Pd seeds, overgrowth occurs preferentially where surface energy is

highest, i.e., the vertices. The emergence of four branches from each vertex rather than one also signifies that branched growth is not merely dependent upon the number of vertices and will enable new branched crystals to be envisioned.

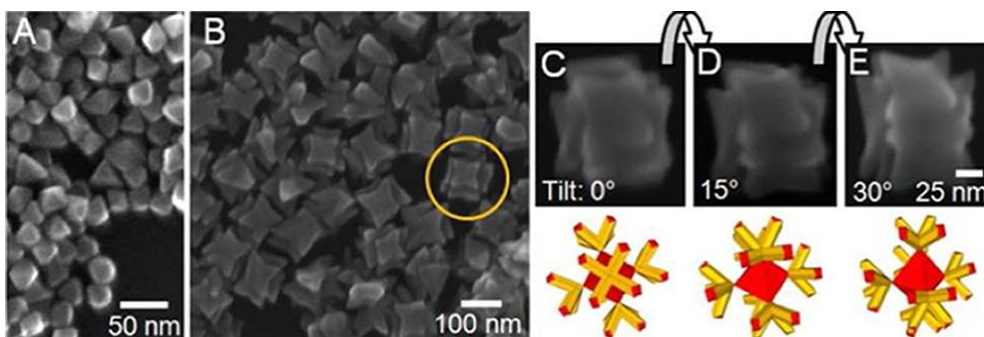


Figure 3.4. SEM images of (A) Pd octahedra and (B–E) 24-branched Au/Pd nanocrystals. In (B), a particle oriented with four branches away from the substrate is circled. (C–E) SEM images of a particle that is tilted by 15° then 30° to reveal another set of four branches (models below).

To evaluate the possibility of other branching patterns, Pd tetrahedra were also used as seeds (**Figure 3.5A**). Again, structures with more branches than seed vertices form (**Figure 3.5B**). Elemental mapping by STEM-EDX analysis confirms the presence of Pd cores and the emergence of multiple branches per vertex (**Figure 3.5C–F**). A TEM tilt study of an individual particle in 15° increments reveals that three branches emerge per vertex although only three of the overgrowth regions can be fully imaged due to the fourth being positioned on the imaging substrate (**Figure S3.11**). From the crystallographic orientation of a tetrahedral nanocrystal, we propose that the branches proceed again along $\langle 111 \rangle$ directions for a total of 12 branches per particle and T_d

symmetry (see **Scheme S3.1** and models in **Figures 3.5, S3.11**). The T_d symmetry of the branched structure is conserved from seed to overgrowth.

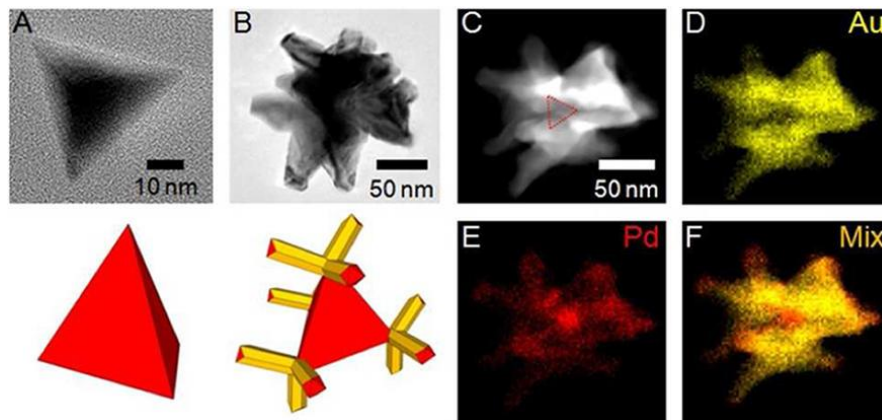


Figure 3.5. (A) A TEM image of a Pd tetrahedron and corresponding model below. (B) A TEM image of a multibranched Au/Pd nanocrystal and proposed model below. (C) A STEM image of a multibranched Au/Pd nanocrystal and (D–F) corresponding STEM/EDX elemental mapping. Yellow, Au; red, Pd.

Seed-mediated co-reduction was also performed with Pd rhombic dodecahedra as seeds.³¹ **Figure 3.6A** shows a TEM image of a typical Pd rhombic dodecahedron prepared by literature protocol.³² The corresponding electron diffraction pattern (top right inset of **Figure 3.6A**) indicates that the particle is oriented in the [110] direction from the electron beam as shown in the model in the bottom right of **Figure 3.6A**. After seed-mediated co-reduction, SEM images (**Figure 3.6B**) of the resultant branched structures reveal that, while the branching symmetry is the same as the Au-seed analogue, the branches are much wider at the base than such octopodal samples (e.g., **Figure 3.1B**).

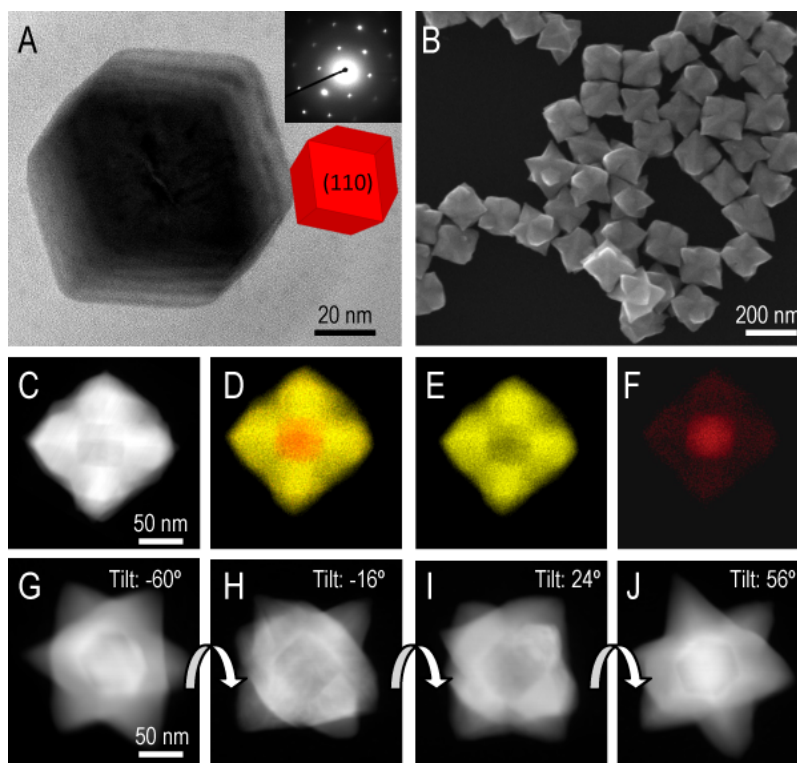


Figure 3.6. (A) TEM image of Pd rhombic dodecahedron (top inset: electron diffraction of the same particle). (B) SEM image of Au/Pd octopods from Pd rhombic dodecahedra. (C) STEM on an individual octopod built from a rhombic dodecahedral seed. (D-F) STEM-EDX elemental mapping of the octopod where Au is represented by yellow and Pd is red; (D) is an overlay of Au and Pd signals, shown separately in (E) and (F). (G-J) STEM tilt series of a Au/Pd octopod built from a Pd rhombic dodecahedron to reveal the structural relationship between the seed vertices and nanocrystal branches.

Characterization by STEM (Figure 3.6C) indicates that the rhombic dodecahedral Pd seeds remain intact after seed-mediated co-reduction. The two-dimensional (2-D) projection of this particle oriented along the [100] zone axis, confirmed by electron diffraction, is shown in **Figure S3.12A,B**. This particle was also characterized by STEM-EDX elemental mapping (shown in **Figure 3.6D-F**). On first examination, the shape of

the Pd seed may appear cubic from the STEM image (**Figure 3.6C**); however, it is simply the rhombic dodecahedron lying on the substrate so that a vertex is oriented in the [100] zone axis. An illustration of this orientation is shown in **Figures S3.12C-F**. This assignment is supported by the Pd map (**Figure 3.6F**) which reveals that the exterior of this seed is less enhanced with Pd compared to the interior. Additional STEM imaging provides corroborating evidence of a rhombic dodecahedral Pd interior with the hexagonal interior of an octopod oriented with two branches pointed away from the substrate, roughly the [110] orientation (**Figure S3.12**). The shape of the 2-D projection of the Pd seed in the STEM image is indicative of a rhombic dodecahedral interior and is not observed with octopods built from Pd nanocubes (**Figure 3.1B**).

One may expect more than eight branches from a rhombic dodecahedral Pd seed due to its 14 vertices. However, further investigations indicate that the branched overgrowth on Pd rhombic dodecahedra seeds is similar to what has been observed with other single-crystalline seeds. Rhombic dodecahedra have six vertices along $\langle 100 \rangle$ directions and eight vertices along $\langle 111 \rangle$ directions. These different vertices are denoted herein as V_{100} and V_{111} , respectively. To understand the overgrowth at the vertices, TEM and STEM images were acquired as a particle was tilted 30 degrees. This tilt series has been reconstructed into a short movie, which is included as **Video 3.2**. **Figure 3.6G-J** show four stills from the STEM tilt series which indicate that eight branches grow, one from each of the eight V_{111} along $\langle 111 \rangle$ directions of the rhombic dodecahedra. These results parallel those from Pd nanocubic seeds which yielded octopods, with one branch emerging from each V_{111} of a cube (**Figure 3.1B**). However, Pd rhombic dodecahedra also have six V_{100} which are maintained during seed-mediated co-reduction. Growth in

the $\langle 111 \rangle$ directions (along the edges of rhombic dodecahedral seeds) from one V_{100} would result in four branches, similar to growth of branches from the V_{100} of Pd octahedra (**Figure 3.4B**). Thus, additional growth from the V_{100} accounts for the enhanced branch thickness at the bases of these structures compared to octopods built from nanocubes. A summary scheme is provided as **Scheme S3.2**.

From the data presented, two parameters are identified as significant to branched metal nanocrystal growth: (1) the number of seed vertices and (2) the growth directions of the branches. The former reflects the preference for nucleation and growth to originate from the vertices of the nanocrystals and can be rationalized in terms of surface energy; i.e., the growth rate will be greatest at the highest energy features under kinetically controlled growth conditions.³³ This idea is represented in **Scheme S3.3** as Stage 1.

The latter reflects the preference for 1-D growth to proceed along $\langle 111 \rangle$ directions of single-crystalline seeds (i.e., those without twins or other defects) regardless of shape and is shown in **Scheme S3.3** as Stage 2. The origin of this trend is less obvious and may be attributed to several factors. For example, the 1-D growth of Au nanorods is rationalized both in terms of surface stabilization and minimization of strain, and these factors may be relevant to the synthesis of symmetrically branched nanocrystals. Specifically, CTAB is thought to minimize the surface energy of the $\{100\}/\{110\}$ side facets of Au nanorods and facilitate their expression relative to the poorly stabilized $\{111\}$ ends, and the branches of the nanocrystals reported here have similarities to Au nanorods.³⁴ However, it should be noted that octopods can still be prepared when CTAB is replaced by CTAC, as shown in Section 2.5. Also, the decahedral seeds from which some Au nanorods originate can be thought of as five tetrahedral single-crystals joined

with {111} twin planes. An atom deficient gap is accommodated by bond elongation, and lateral growth rather than axial would increase internal lattice strain.¹⁶ With the exception of the right bipyramids, the seeds used in these syntheses do not have such structural defects, but there is a 4.7 % lattice mismatch between Pd and Au and this difference may facilitate anisotropic growth as a means of minimizing strain when Au deposits on the Pd cores. Such nonconformal growth was observed in Yang and coworkers' study of heteroepitaxial deposition in 3-D and could account for the differences we observed with the use of Au and Pd octahedra.³⁵

Although these factors may account for branch formation generally, they do not account fully for our observations. For example, the vertices of both the cubic and tetrahedral seeds can accommodate more branches along $\langle 111 \rangle$ directions (e.g., in addition to the three branches that proceed normal to the side facets of a tetrahedron, a fourth branch could proceed in the [111] direction normal to the base facet). Our preliminary analysis suggests that the acuteness of the vertices coupled with the crystallographic orientation of the vertices relative to available growth directions accounts for the different number of branches emerging per vertex depending on seed shape. We also note that the number and acuteness of the vertices per seed may limit the number of branches that can form due to overcrowding. This idea is reflected in our preliminary study of octahedral seeds (**Figure S3.6**) and in our results obtained with cuboctahedral Pd seeds (**Figure S3.13A**) which gave nanocrystals with intricate branching patterns (**Figure S3.13B**). There is good uniformity in structure but the individual branch lengths and widths vary. Elemental mapping confirms the presence of the Pd core although its orientation relative to the branching pattern could not be verified

(**Figure S3.13C–H**). EM tilt studies of individual particles highlight the difficulty in assigning symmetry due to multiple branches emerging from the many vertices of each seed (**Figure S3.14**).

On account of their composition, symmetry, and sharp tips, these nanocrystals are intriguing platforms for the study of Pd-adsorbate interactions by plasmon-enhanced surface spectroscopies.³⁶ Toward that aim, we previously demonstrated that Au/Pd octopods built from Au seeds are suitable catalysts for the electrooxidation of formic acid and have useful optical properties such as size-dependent LSPRs and high refractive index sensitivities.^{6, 21} We anticipate that the branched Au/Pd nanocrystals built from Pd seeds have similar properties and as expected have LSPRs positioned in the visible and near-IR. Compared in **Figure S3.15** are the LSPRs of Au/Pd octopods built from Pd nanocubes (**Figure 3.1B**), 24-branched nanocrystals with O_h symmetry built from Pd octahedra (**Figure 3.4B**), and Au/Pd octopods built from Au seeds (**Figure S3.16**). All have similar branch widths (~20 nm) and lengths (~115 nm) but differ in either their symmetry or internal composition. As a result, the position of the LSPR maximum for Au/Pd octopods from Au seeds is red-shifted by 100 nm compared to Au/Pd octopods built from Pd nanocubes; the 24-branched nanostructures exhibit a maximum LSPR positioned slightly further in the red than both samples of octopods. These results indicate that both the internal composition and symmetry of branched nanocrystals contribute to their optical properties and provide synthetic levers that can be manipulated to achieve tailored colloidal plasmonic platforms.

3.3 Conclusions

Seed structure is known to play a critical role in the synthesis of convex shape-controlled nanocrystals and core@shell nanocrystals, and understanding its role in concave and branched nanocrystal synthesis will enable new nanocrystals with well-defined structures and properties to be achieved.^{16, 37, 38} Here, a general route to symmetrically branched metal nanocrystals is outlined, wherein the shape of the initial seeds determines the overgrowth process by providing referential sites for branched growth. This research focused on a model Au/Pd system to provide direct visualization of the seed-symmetry relationships but the principles outlined should hold for other systems as well.

3.4 References

1. DeSantis, C. J.; Skrabalak, S. E., Core Values: Elucidating the Role of Seed Structure in the Synthesis of Symmetrically Branched Nanocrystals. *J. Am. Chem. Soc.* **2012**, *135*, 10-13.
2. Lim, B.; Xia, Y., Metal Nanocrystals with Highly Branched Morphologies. *Angew. Chem. Int. Ed.* **2011**, *50*, 76-85.
3. Hao, F.; Nehl, C. L.; Hafner, J. H.; Nordlander, P., Plasmon Resonances of a Gold Nanostar. *Nano Lett.* **2007**, *7*, 729-732.
4. Khoury, C. G.; Vo-Dinh, T., Gold Nanostars For Surface-Enhanced Raman Scattering: Synthesis, Characterization and Optimization. *J. Phys. Chem. C* **2008**, *112*, 18849-18859.

5. Kumar, P. S.; Pastoriza-Santos, I.; Rodríguez-González, B.; Abajo, F. J. G. d.; Liz-Marzán, L. M., High-yield synthesis and optical response of gold nanostars. *Nanotechnology* **2008**, *19*, 015606.
6. DeSantis, C. J.; Skrabalak, S. E., Size-Controlled Synthesis of Au/Pd Octopods with High Refractive Index Sensitivity. *Langmuir* **2012**, *28*, 9055-9062.
7. Barbosa, S.; Agrawal, A.; Rodríguez-Lorenzo, L.; Pastoriza-Santos, I.; Alvarez-Puebla, R. n. A.; Kornowski, A.; Weller, H.; Liz-Marzán, L. M., Tuning Size and Sensing Properties in Colloidal Gold Nanostars. *Langmuir* **2010**, *26*, 14943-14950.
8. Kim, D. Y.; Yu, T.; Cho, E. C.; Ma, Y.; Park, O. O.; Xia, Y., Synthesis of Gold Nano-hexapods with Controllable Arm Lengths and Their Tunable Optical Properties. *Angew. Chem. Int. Ed.* **2011**, *50*, 6328-6331.
9. Huang, X.; Tang, S.; Zhang, H.; Zhou, Z.; Zheng, N., Controlled Formation of Concave Tetrahedral/Trigonal Bipyramidal Palladium Nanocrystals. *J. Am. Chem. Soc.* **2009**, *131*, 13916-13917.
10. Mulvihill, M. J.; Ling, X. Y.; Henzie, J.; Yang, P., Anisotropic Etching of Silver Nanoparticles for Plasmonic Structures Capable of Single-Particle SERS. *J. Am. Chem. Soc.* **2009**, *132*, 268-274.
11. Dai, Y.; Mu, X.; Tan, Y.; Lin, K.; Yang, Z.; Zheng, N.; Fu, G., Carbon Monoxide-Assisted Synthesis of Single-Crystalline Pd Tetrapod Nanocrystals through Hydride Formation. *J. Am. Chem. Soc.* **2012**, *134*, 7073-7080.
12. Hong, J. W.; Lee, Y. W.; Kim, M.; Kang, S. W.; Han, S. W., One-pot synthesis and electrocatalytic activity of octapodal Au-Pd nanoparticles. *Chem. Commun.* **2011**, *47*, 2553-2555.

13. Xia, X.; Zeng, J.; McDearmon, B.; Zheng, Y.; Li, Q.; Xia, Y., Silver Nanocrystals with Concave Surfaces and Their Optical and Surface-Enhanced Raman Scattering Properties. *Angew. Chem. Int. Ed.* **2011**, *50*, 12542-12546.
14. Wang, F.; Li, C.; Sun, L.-D.; Wu, H.; Ming, T.; Wang, J.; Yu, J. C.; Yan, C.-H., Heteroepitaxial Growth of High-Index-Faceted Palladium Nanoshells and Their Catalytic Performance. *J. Am. Chem. Soc.* **2010**, *133*, 1106-1111.
15. Lu, C.-L.; Prasad, K. S.; Wu, H.-L.; Ho, J.-a. A.; Huang, M. H., Au Nanocube-Directed Fabrication of Au–Pd Core–Shell Nanocrystals with Tetrahedral, Concave Octahedral, and Octahedral Structures and Their Electrocatalytic Activity. *J. Am. Chem. Soc.* **2010**, *132*, 14546-14553.
16. Xia, Y.; Xiong, Y.; Lim, B.; Skrabalak, S. E., Shape-Controlled Synthesis of Metal Nanocrystals: Simple Chemistry Meets Complex Physics? *Angew. Chem. Int. Ed.* **2009**, *48*, 60-103.
17. Zhang, H.; Jin, M.; Xia, Y., Noble-Metal Nanocrystals with Concave Surfaces: Synthesis and Applications. *Angew. Chem. Int. Ed.* **2012**, *51*, 7656-7673.
18. Maksimuk, S.; Teng, X.; Yang, H., Roles of Twin Defects in the Formation of Platinum Multipod Nanocrystals. *J. Phys. Chem. C* **2007**, *111*, 14312-14319.
19. Carbone, L.; Kudera, S.; Carlino, E.; Parak, W. J.; Giannini, C.; Cingolani, R.; Manna, L., Multiple Wurtzite Twinning in CdTe Nanocrystals Induced by Methylphosphonic Acid. *J. Am. Chem. Soc.* **2005**, *128*, 748-755.
20. Lim, B.; Jiang, M.; Camargo, P. H. C.; Cho, E. C.; Tao, J.; Lu, X.; Zhu, Y.; Xia, Y., Pd-Pt Bimetallic Nanodendrites with High Activity for Oxygen Reduction. *Science* **2009**, *324*, 1302-1305.

21. DeSantis, C. J.; Peverly, A. A.; Peters, D. G.; Skrabalak, S. E., Octopods versus Concave Nanocrystals: Control of Morphology by Manipulating the Kinetics of Seeded Growth via Co-Reduction. *Nano Lett.* **2011**, *11*, 2164-2168.
22. DeSantis, C. J.; Sue, A. C.; Bower, M. M.; Skrabalak, S. E., Seed-Mediated Co-reduction: A Versatile Route to Architecturally Controlled Bimetallic Nanostructures. *ACS Nano* **2012**, *6*, 2617-2628.
23. Bower, M. M.; DeSantis, C. J.; Skrabalak, S. E., A Quantitative Analysis of Anions and pH on the Growth of Bimetallic Nanostructures. *Journal of Physical Chemistry C* **2014**, Accepted.
24. Langille, M. R.; Zhang, J.; Personick, M. L.; Li, S.; Mirkin, C. A., Stepwise Evolution of Spherical Seeds into 20-Fold Twinned Icosahedra. *Science* **2012**, *337*, 954-957.
25. Zhang, J.; Zhang, L.; Xie, S.; Kuang, Q.; Han, X.; Xie, Z.; Zheng, L., Synthesis of Concave Palladium Nanocubes with High-Index Surfaces and High Electrocatalytic Activities. *Chem. Eur. Jour.* **2011**, *17*, 9915-9919.
26. Hong, J. W.; Kim, D.; Lee, Y. W.; Kim, M.; Kang, S. W.; Han, S. W., Atomic-Distribution-Dependent Electrocatalytic Activity of Au-Pd Bimetallic Nanocrystals. *Angew. Chem. Int. Ed.* **2011**, *50*, 8876-8880.
27. Wiley, B. J.; Xiong, Y.; Li, Z.-Y.; Yin, Y.; Xia, Y., Right Bipyramids of Silver: A New Shape Derived from Single Twinned Seeds. *Nano Lett.* **2006**, *6*, 765-768.
28. Zhang, J.; Li, S.; Wu, J.; Schatz, G. C.; Mirkin, C. A., Plasmon-Mediated Synthesis of Silver Triangular Bipyramids. *Angew. Chem., Int. Ed.* **2009**, *48*, 7787-7791, S7787/1-S7787/4.

29. Lim, B.; Jiang, M.; Tao, J.; Camargo, P. H. C.; Zhu, Y.; Xia, Y., Shape-Controlled Synthesis of Pd Nanocrystals in Aqueous Solutions. *Adv. Funct. Mater.* **2009**, *19*, 189-200.
30. Kim, M.-J.; Cho, Y.-S.; Park, S.-H.; Huh, Y.-D., Facile Synthesis and Fine Morphological Tuning of Ag₂O. *Cryst. Growth Des.* **2012**, *12*, 4180-4185.
31. Weiner, R. G.; DeSantis, C. J.; Cardoso, M. B. T.; Skrabalak, S. E., Diffusion and Seed Shape: Intertwined Parameters in the Synthesis of Branched Metal Nanostructures. **2014**, Submitted.
32. Niu, W.; Zhang, L.; Xu, G., Shape-Controlled Synthesis of Single-Crystalline Palladium Nanocrystals. *ACS Nano* **2010**, *4*, 1987-1996.
33. Langille, M. R.; Personick, M. L.; Zhang, J.; Mirkin, C. A., Bottom-Up Synthesis of Gold Octahedra with Tailorable Hollow Features. *J. Am. Chem. Soc.* **2011**, *133*, 10414-10417.
34. Gao, J.; Bender, C. M.; Murphy, C. J., Dependence of the Gold Nanorod Aspect Ratio on the Nature of the Directing Surfactant in Aqueous Solution. *Langmuir* **2003**, *19*, 9065-9070.
35. Habas, S. E.; Lee, H.; Radmilovic, V.; Somorjai, G. A.; Yang, P., Shaping binary metal nanocrystals through epitaxial seeded growth. *Nat. Mater.* **2007**, *6*, 692-697.
36. Fang, P.-P.; Jutand, A.; Tian, Z.-Q.; Amatore, C., Au-Pd Core-Shell Nanoparticles Catalyze Suzuki-Miyaura Reactions in Water through Pd Leaching. *Angew. Chem. Int. Ed.* **2011**, *50*, 12184-12188.
37. Jin, M.; Zhang, H.; Wang, J.; Zhong, X.; Lu, N.; Li, Z.; Xie, Z.; Kim, M. J.; Xia, Y., Copper Can Still Be Epitaxially Deposited on Palladium Nanocrystals To Generate

Core–Shell Nanocubes Despite Their Large Lattice Mismatch. *ACS Nano* **2012**, *6*, 2566-2573.

38. Yang, C.-W.; Chanda, K.; Lin, P.-H.; Wang, Y.-N.; Liao, C.-W.; Huang, M. H., Fabrication of Au–Pd Core–Shell Heterostructures with Systematic Shape Evolution Using Octahedral Nanocrystal Cores and Their Catalytic Activity. *J. Am. Chem. Soc.* **2011**, *133*, 19993-20000.

Chapter 4: Optical Properties of Au/Pd Nanoparticles with Defined Architectures

4.1 Introduction¹

As explained in Chapter 1, noble metal nanostructures are of continued interest on account of their fascinating optical properties that are not observed in the bulk. The ability to control the size, shape, and composition of metal nanostructures provides facile manipulation of their corresponding localized surface plasmon resonance (LSPR).²⁻⁴ In turn, this tunable optical feature is being exploited for the development of nanomedicine, theranostics, and colorimetric sensors as well as in surface enhanced Raman spectroscopy (SERS) applications for the detection of low concentration analytes and reaction intermediates.⁵⁻¹⁰ Advances in synthesis are providing nanostructures with new architectures and compositions, and thus functionality.^{3, 11-13} Consequently, there is a need to understand how these parameters affect the optical properties of such nanostructures.¹⁴ Chapter 2 described a synthetic route to monodisperse Au/Pd octopods, nanostructures with eight branches and a primarily Au interior, while Chapter 3 depicted a method to achieve Au/Pd octopods with a Pd cube core. This chapter explores the optical properties of Au/Pd octopods with compositionally controlled interiors. Sections 4.2-4.6 investigate the contributions of branch length and tip width to the LSPR position and refractive index (RI) sensitivity. Interestingly, the LSPR maximum wavelength shifts into the red as these two structural features increase in dimension, and high RI sensitivity (>500 nm/RIU) was achieved in ensemble measurements. The Au/Pd octopods also were found to be suitable substrates for SERS. On account of their unique composition, these findings represent a significant advance forward in the development of multifunctional nanostructures. Sections 4.7-4.10 explore the relationship between architecture and LSPR maxima as the Pd cores in Au/Pd octopods are removed. To do so, Au/Pd octopods with

hollow, cubic interiors were synthesized by etching core@shell Pd@Au/Pd octopods to selectively remove their Pd interiors. The integration of hollow and branched architectures into one structure results in plasmonic bimetallic colloids with far red-shifted LSPRs. Collectively, the results in Chapter 4 show the versatility of seed-mediated co-reduction to provide branched nanostructures with tunable plasmonic properties.

4.2 Size-Dependent Optical Properties of Au/Pd Octopods¹

In order for metal nanostructures to be useful as LSPR sensors of chemical or biological events (e.g., detection of volatile organic compounds or antibody–antigen binding events), a large change in LSPR position must be observed in response to small changes in the local RI.^{8, 9, 15, 16} For example, Rubinstein and co-workers developed a gas sensor wherein Au island films were coated with polymers which swell or shrink when exposed to different gases.¹⁷ These changes in polymer configuration induce changes in the local RI and in turn the position of the LSPR. A number of promising LSPR sensing modalities have been developed based on RI sensitivity, and a survey of the current literature finds that Au and Ag nanostructure platforms predominate.^{7-9, 15, 16, 18-20} The introduction of other metals into LSPR sensing platforms could provide unique functionality (e.g., Pd and Pt are both widely used catalysts); however, there is a limited number of studies which focus on the optical properties of nanostructures composed of such metals.²¹⁻²⁵ Shown here high RI sensitivities (>500 nm/RIU) are achieved in a bimetallic system through the synthesis and use of size-controlled Au/Pd octopods.

Particle shape and architecture are important factors contributing to the RI sensitivity of Au-based nanostructures.²⁶ For example, Wang and co-workers measured the RI sensitivities of many Au nanostructures, including nanobranched, nanobipyrimids, nanocubes, and nanorods.²⁷ They found that the nanobranched provided higher RI sensitivities than other similarly sized Au nanoparticles, and this property was attributed to the sharpness of their tips. In addition, calculations of the near-field properties of a Au nanostar by the finite-difference time-domain method as well as experimental evidence provided by photoemission electron spectroscopy revealed that the sharp tips of the nanostar branches can concentrate the associated electric field and provide enhancements of molecular Raman signals.²⁸⁻³⁰ Central to this demonstration is the ability to tune the LSPR position for overlap with the Raman excitation wavelength. On account of these distinct optical properties, Au nanostars are finding use in photothermal therapy and sensing platforms.³¹⁻³⁴ However, the branching patterns of Au nanostars are typically asymmetric and nonuniform from particle to particle. Thus, studying how the specific attributes of nanostars contribute to their optical characteristics and ensuring reproducibility from one experiment to the next can be difficult.

The optical properties of a nanocrystal can be altered through compositional changes in ways that size and shape changes cannot accomplish alone. Seed-mediated synthetic strategies are being used to achieve binary metal nanostructures.³⁵⁻³⁸ These nanostructures often adopt core@shell particle architectures, wherein the shell thickness is controlled by the concentration of precursor reduced and then deposited on the core during the overgrowth process.³⁹ Such bimetallic nanostructures display optical properties unique from their monometallic counterparts.^{40, 41} For example, Xie and co-

workers observed a blue shift in the LSPR of Au@Pd nanobars with increasing thickness of the Pd shell and their measured RI sensitivities were greater than that of Au nanobars.⁴² In addition, Au@Pd nanobars with Pd shells less than 1.1 nm in thickness were suitable substrates for SERS applications. Combining Au and Pd together into one nanostructure has the capacity to provide functionality and chemical insight that cannot be achieved by either metal alone. For example, Atamore and co-workers used the Pd of Au@Pd nanoparticles as a catalyst for Suzuki-Miyaura cross-coupling and the SERS enhancement provided by the binary structure to demonstrate the role of Pd leaching in the catalytic cycle.⁴³ As this example illustrates, combining the catalytic and optical properties of the two metals into one nanostructure provides a multifunctional platform with the ability to give insight into a catalytic process not otherwise achievable.

Chapter 2 reported the synthesis of Au/Pd octopods from seed-mediated co-reduction.^{44, 45} These nanostructures contain eight symmetrical branches growing along the <111> directions of a cuboctahedral Au core. The Pd localizes along the tips of the branches and is dispersed on the exterior of the particle. In Sections 4.3 to 4.6 the size-dependent optical properties of Au/Pd octopods are investigated. Our seed-mediated synthetic strategy provides a facile means of size control and in turn the LSPR maximum wavelength. Significantly, the larger Au/Pd octopods provide RI sensitivities > 500 nm/RIU while the smaller Au/Pd octopods enhance molecular Raman signatures when functionalized with model compounds. Overall, this study provides a greater understanding of the optical properties of bimetallic and symmetrically branched nanostructures with potential applications in sensing.

4.3 Synthesis of Au/Pd Octopods and the Influence of Particle Size on LSPR Position¹

Au/Pd octopods were prepared as they were in Chapter 2.^{44, 45} First, tiny Au seeds (<10 nm) are synthesized by reducing HAuCl₄ with the strong reducing agent, NaBH₄. These seeds are then built upon by reducing additional HAuCl₄ with L-aa to form larger octahedral-like Au particles (<50 nm) herein termed “cores”. Finally, HAuCl₄ and H₂PdCl₄ were simultaneously co-reduced with L-aa in the presence of CTAB, which serves as a stabilizing agent, to form uniformly branched eight-armed nanostructures. As noted in Chapter 2, the co-reduction technique is required for branched nanostructure formation. It was also found that increasing the concentration of the Pd precursor relative to the Au precursor during the co-reduction step led to a thickening of the tips of the eight branches, eventually forming “sheeted” octopods with the expression of {111} facets. These tips or “sheets” were enriched with Pd relative to the rest of the structure. As we report here, the size of these Au/Pd octopods can be tuned over a wide range (60–150 nm) without appreciably altering their shape. This control is afforded by changing the total concentration of precursors in the overgrowth solution relative to the Au core concentration while maintaining the Au:Pd precursor ratio at 10:1. Shown in **Figure 4.1A–G** are SEM images of seven samples of Au/Pd octopods with different average sizes. These samples are referred hereafter as samples A–G (see Table S1). As expected, the size of the Au/Pd octopods increases with increasing precursor concentration in the overgrowth solution. All samples are produced in excellent yield, and their size and structural homogeneity often lead to the ordered packing of the particles during preparation of the samples for SEM analysis. A model of the octopodal structure is

shown in **Figure 4.1H**. TEM and STEM-EDX elemental mapping images corroborate well with characterization in Chapter 2 and the Au seed-mediated method, with Au located primarily in the interior of the particle and Pd decorating the surface and localizing at the tips of the particle branches (**Figure 4.2**).

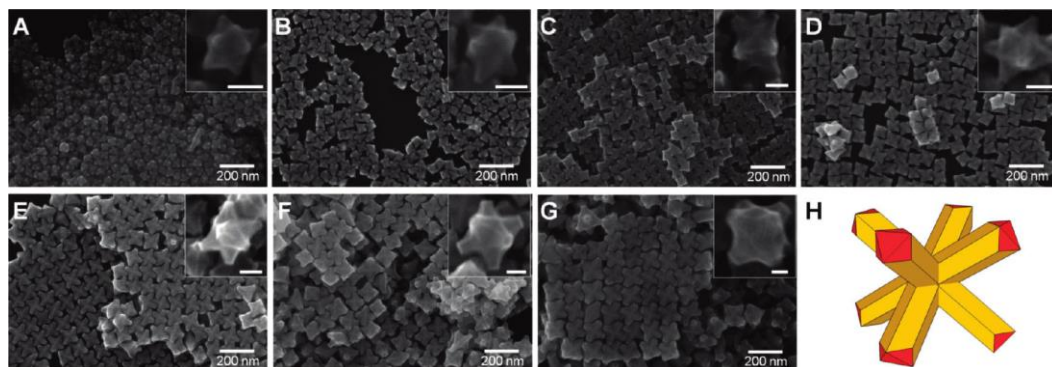


Figure 4.1. (A–G) SEM images of Au/Pd octopods synthesized at seven different sizes (inset scale bars: 50 nm). (H) Structural model of an octopod.

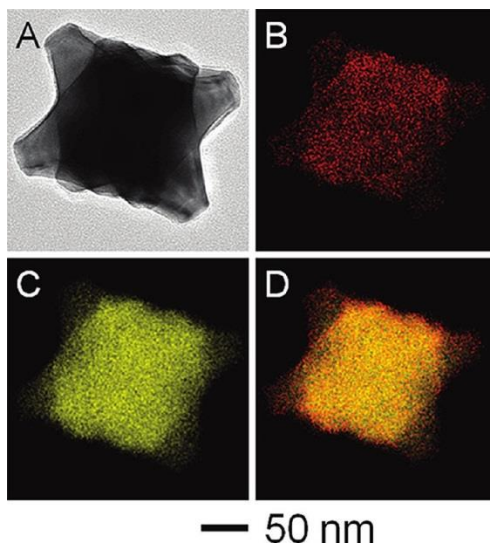


Figure 4.2. (A) TEM image of an individual octopod (sample G) and (B–D) corresponding elemental map obtained by STEM-EDX analysis. (B) Pd only (red). (C) Au only (yellow). (D) Overlay of Au and Pd signals.

Size measurements were made from 500 particles in each sample (A–G) by analysis of SEM images. These measurements were made along two parameters: the tip-to-tip distance between opposite branches (denoted as “X” in **Figure 4.3A** inset) and the tip width of the branch terminus (denoted as “Y” in **Figure 4.3A** inset). These measurements are summarized in **Figure 4.3A** and quantify the increase in size evident in Figure 4.1. In general, the Au/Pd octopods increase in both the X and Y dimensions as additional metal precursor is added to the overgrowth solution, although the change in X is slightly greater than that observed in Y. The octopods develop longer branches and flatter tips as more metal precursor is added to the overgrowth solution, with the largest size demonstrated being 145 nm along X. Low standard deviations in the X and Y measurements highlight the monodisperse nature of the nanocrystals. We attribute the ability to synthesize Au/Pd nanocrystals with such high uniformity to the seed-mediated method, which allows for systematic overgrowth of metal as well as the separation of primary nucleation and growth steps.³⁵ The co-reduction method also aides in achieving these branched nanocrystals, as both metal precursors must be present in the overgrowth solution to achieve octopods. The role of the co-reduction technique in morphology development is discussed in detail in Chapter 2.

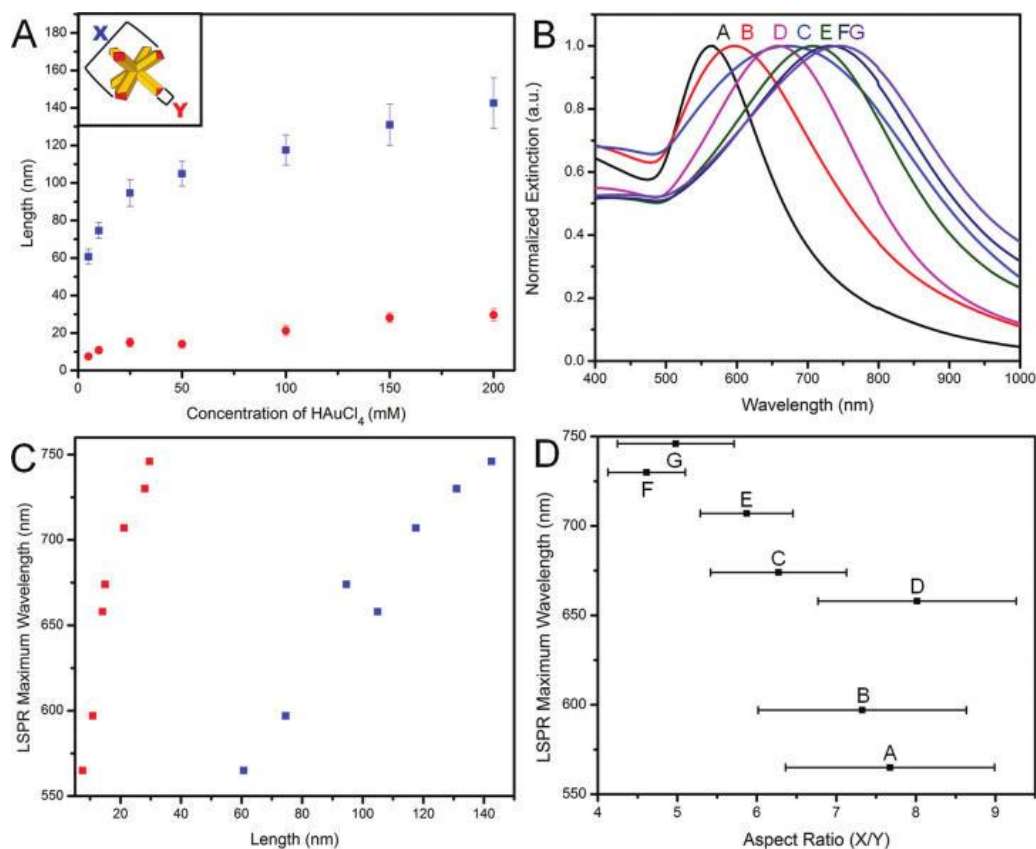


Figure 4.3. (A) Plot of octopodal dimensions (X = branch length in blue; Y = branch width in red) vs. concentration of HAuCl₄ in the overgrowth solution, where the Au/Pd precursor ratio is kept at 10:1. Error bars denote one standard deviation. (B) UV-visible spectra of Au/Pd octopods, samples A–G. (C) Plot of LSPR maximum wavelength vs. branch length (blue) and width (red). (D) Plot of LSPR maximum wavelength vs. aspect ratio (defined as X/Y). Error bars denote one standard deviation.

The UV-visible spectra for samples A–G are in **Figure 4.3B**. One feature dominates for all samples, which shifts into the red and broadens as the octopods increase in size. Extinction spectra of Ag octopods with different branch lengths were simulated by Bratkovsky and co-workers with the discrete dipole approximation (DDA) method.⁴⁶ Their spectra consisted of three resonances, which were assigned as two quadrupolar

resonances and a dipolar resonance at longer wavelengths. The blue-most quadrupolar resonance was relatively unaffected by changes in octopodal size and positioned below 400 nm. However, both the dipolar and red-most quadrupolar resonances shifted to longer wavelengths as the branch lengths of the octopods increased, with substantial overlap of these two features at larger sizes. These results suggest that the dominant feature in our spectra consists of two unresolved resonances, although differences in composition and size are unaccounted in this comparison. Work is underway to deconvolute the two resonances through single particle spectroscopy techniques.⁴⁷

Figure 4.3C quantifies the relationship between octopodal size and the LSPR maximum wavelength, with branch length (X) in blue and tip width (Y) in red. In general, a red shift was observed as the size of the octopods increased. This trend is consistent with the greater charge separation that can be achieved, which reduces the restoring force for electron oscillation and in turn shifts the resonance to lower energy.⁴⁸ The LSPR associated with the Au/Pd octopods also broadens somewhat with increasing size and can be accounted for by the slightly greater variation in particle size observed with the largest samples and/or increased radiative damping or contributions from higher order modes.⁴⁹ These results are consistent with other branched nanostructures such as Au nanostars and symmetrically branched Au hexapods.^{50, 51}

Finally, the aspect ratios of the individual octopods (defined as X/Y) generally decreased as they became larger. This trend was accompanied with a red shift in the LSPR maximum wavelength (**Figure 4.3D**). This relationship is the inverse to that observed in Au nanobar, nanorod, and branched nanostructure systems, where an increase in aspect ratio leads to a red shift in the LSPR.^{42, 50, 52} While the origin of this observation

is unclear at this time, Kim and co-workers found that the SPR of Ag nanorods blue-shifted with an increase in aspect ratio if the width of the nanorods decreased faster than the length of the nanorods.⁵³ Such a situation may account for our observation, but a full analysis is difficult given the tapered nature of the branches and the variations between individual particles in the ensembles. Alternatively, the distribution of Pd in the nanostructures may vary with size. Recall that the deposition of Pd shells on Au nanobars results in a blue shift, which increases in magnitude with shell thickness.⁴²

4.4 Refractive Index Sensitivities of Au/Pd Octopods¹

In addition to correlating the LSPR position to the structural features of the Au/Pd octopods, their sensitivities to changes in RI were measured to evaluate their potential utility in LSPR sensor platforms. In particular, the Au/Pd octopods were stabilized with Na-PSS to ensure colloidal stability in both water and DMSO/water solutions (see **Figure S4.1** for DLS data). RI sensitivities of samples A–G were then measured by dispersing the Na-PSS-modified Au/Pd octopods in DMSO/water solutions and measuring the LSPR of a given sample by UV–visible spectroscopy. As an example, the LSPR spectra obtained with sample F in media with different RIs are shown in **Figure 4.4A**. A red shift is evident with an increase in RI while the fwhm and general shape associated with the LSPR were unchanged. Similar shifts into the red were observed with the other samples (**Figure S4.2**). **Figure 4.4B** indicates a linear relationship between the RI and SPR shift for samples A–G. The observed linearity is predicted from the Drude model over small ranges of RI and indicates that changes in LSPR maximum wavelength arise from the change in local RI and not other phenomena.¹⁵ The RI sensitivities and FOMs for samples A–G are summarized in **Table 4.1** and compared to their LSPR maximum

wavelength and structural features. Significantly, the larger Au/Pd octopods achieve high RI sensitivities (>500 nm/RIU) and moderate FOMs (>1.5). As FOM is determined by dividing the RI sensitivity by the fwhm of the resonance, nanostructures which provide narrower LSPR line widths would improve the FOMs. However, larger particles tend to have broadened resonances from radiative damping and multipolar excitations.¹⁵ Still, the performance of the large Au/Pd octopods may be enhanced slightly by improving sample homogeneity, although we are unaware of any Pd-containing colloidal system with better properties currently. For comparison, the reported RI sensitivities of Au nanostar ensembles vary between 200 and 350 nm/RIU depending on their size and specific structure.⁵⁰

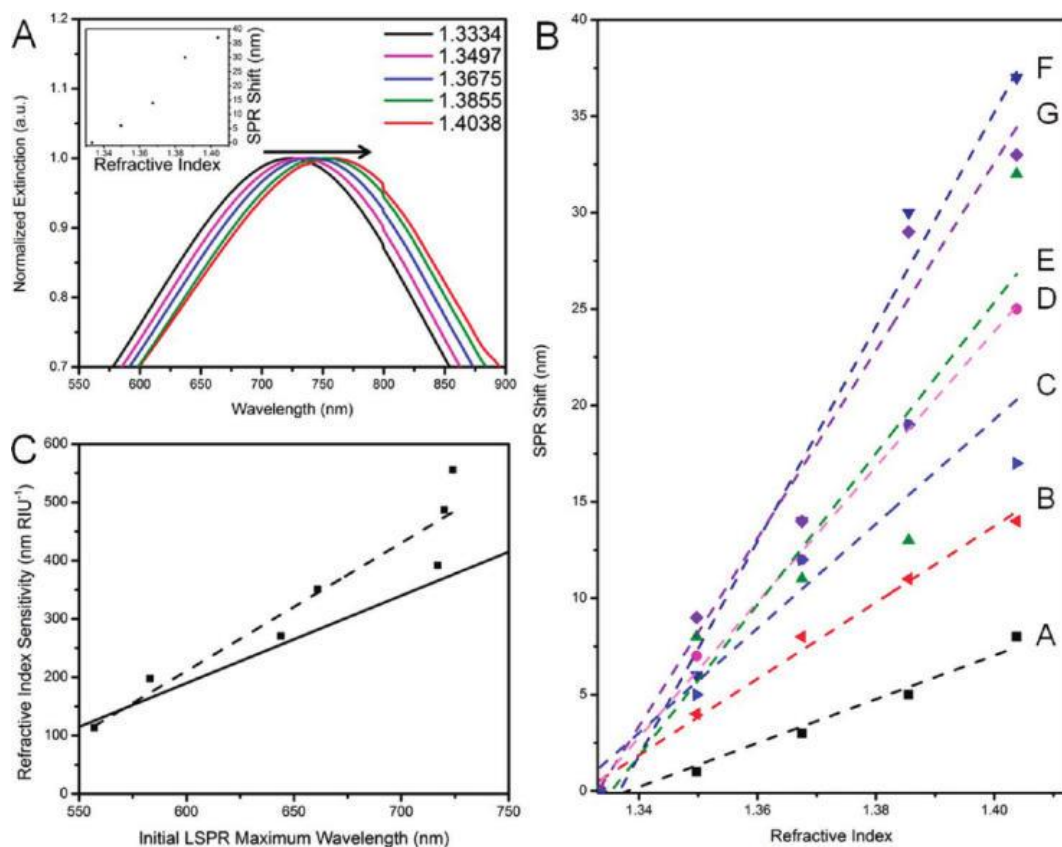


Figure 4.4. (A) Extinction spectra of sample F in solvents with different RI (denoted in figure). Inset: a plot of SPR shift vs. RI. (B) Plots of SPR shift vs. RI for samples A–G. (C) Plot of RI sensitivity vs. initial LSPR position for Samples A–G. The dashed line corresponds to the linear trend line obtained from the experimental data and the solid line corresponds to the analytical approximation provided by Miller and Lazarides for Au nanoparticles in water.⁵⁴

Table 4.1. Size and Optical Characteristics of Seven Au/Pd Octopod Samples^a

Sample	Length X (nm)	Width Y (nm)	Aspect ratio (X/Y)	LSPR (nm)	fwhm (nm)	RI sensitivity (nm/RIU)	FOM
A	61 (4)	8 (1)	7.7 (1.3)	565	172	114	0.66
B	75 (4)	11 (2)	7.3 (1.3)	597	224	198	0.88
C	95 (7)	15 (2)	6.3 (0.9)	674	391	271	0.69
D	105 (7)	14 (2)	8.0 (1.2)	658	292	351	1.20
E	118 (8)	21 (3)	5.9 (0.6)	707	263	392	1.49
F	131 (11)	28 (3)	4.6 (0.5)	730	280	556	1.98
G	143 (14)	30 (3)	5.0 (0.7)	746	309	487	1.58

a Numbers in parenthesis denote one standard deviation.

Interestingly, electrodynamic simulations by Miller and Lazarides found that the RI sensitivity of Au nanoparticles varies linearly with initial LSPR position.^{15, 54} Thus, it is important to decouple whether the RI sensitivities associated with samples A–G arise primarily from their initial LSPR position or intrinsic structural features. A plot of RI sensitivity vs. initial LSPR position is provided in **Figure 4.4C** and compared to the analytical approximation provided by Miller and Lazarides for Au nanoparticles in water. As expected, the RI sensitivities associated with samples A–G increase as the initial LSPR position increases. However, the slope of the experimental trend line is slightly greater than that predicted and suggests that either intrinsic shape effects or composition contribute to the RI sensitivity in addition to the initial LSPR position effect.¹⁵ Such deviations have been reported for structures such as nanostars.¹⁵ We note that achieving larger Au/Pd octopods with further red-shifted LSPRs should be possible by either increasing the size of the Au cores used in the synthesis or increasing the metal precursor concentrations relative to core concentration. Also, modifying the synthesis to maintain

the sharpest tips possible should yield Au/Pd octopods with further red-shifted LSPRs, as demonstrated in Section 2.6.⁴⁵ Significantly, the incorporation of Pd to the nanostructure does not limit the RI sensitivity achieved despite its different dielectric function.¹⁵ This finding is consistent with studies of patterned metal gratings comprised of nanopyramids which were evaluated as LSPR sensors for protein–protein binding events. In particular, the Pd grating provided a plasmon resonance shift similar to a Au grating upon the binding of avidin to biotin.²⁴

4.5 SERS Activities of Au/Pd Octopods¹

Au and Ag surfaces and nanocrystals are the most widely employed substrates for SERS applications.⁵⁵ Yet the Au/Pd octopods with their tunable LSPR, which overlaps well with typical SERS excitation wavelengths, could provide insight into Pd-based surface chemistry via SERS. As an initial study of their SERS activity, Raman spectra for 4-mercaptopyridine (4-MPy) derivatized on the surfaces of samples A–G were obtained by standard methods described in **Appendix A4.2.7**. All experiments were run in triplicate, with similar results obtained. Shown in **Figure 4.5A** are the SERS spectra obtained from derivatized samples A, C, and E. The spectrum obtained from sample A prior to derivitization is shown in **Figure S4.3**, with no molecular signatures evident. The spectrum obtained from a large crystal of 4-MPy is included in **Figure 4.5A** for reference. These comparisons illustrate that well-resolved SERS spectra are obtained through the use of Au/Pd octopods as the substrate. In particular, the pronounced relative intensity at 1100 cm⁻¹ associated with the trigonal ring-breathing mode of the C=S bond signifies surface enhancement of adsorbed molecules.^{56, 57} In comparing these three

samples, it is also evident that the intensities of signals achieved with sample A are much greater than those from samples C and E.

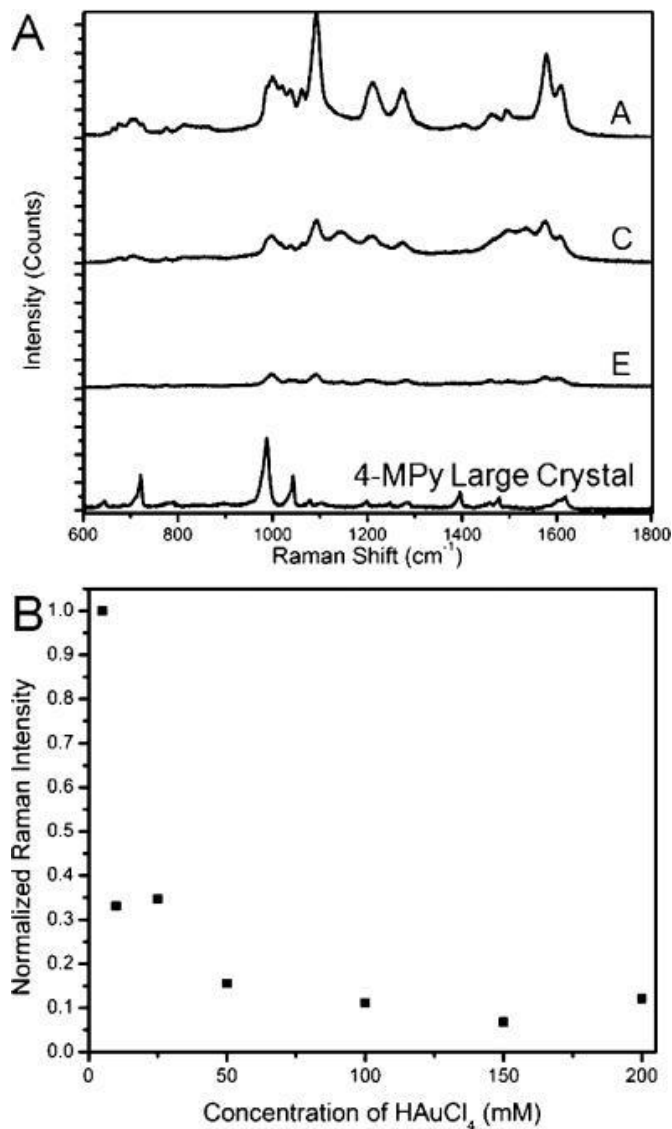


Figure 4.5. (A) Raman spectra obtained from drop-casted samples A, C, and E derivatized with 4-MPy. The spectrum obtained from a large crystal of 4-MPy is included for reference. (B) Normalized Raman intensities at 1100 cm⁻¹ for samples A–G compared to the most enhanced signal (obtained with sample A)

This difference in intensity is quantified in **Figure 4.5B** by normalizing the signal intensity at 1100 cm^{-1} for samples A–G to the most enhanced signal (obtained with sample A). This analysis found that sample A provided the greatest enhancement while samples B and C provided less, but still significant, enhancement. Less signal enhancement was obtained from samples D–G. Interestingly, the samples providing the greatest enhancements also have the least LSPR overlap with the excitation laser wavelength (785 nm). Thus, the greater signal enhancement provided by sample A cannot be attributed to its LSPR position alone. Many factors likely contribute to this enhancement. For example, the smaller octopods have a higher surface area which can provide greater 4-MPy coverage. The smaller octopods also have sharper tips which can concentrate the electric field for maximum enhancement of molecular Raman signals. A study discussed in Section 2.5 of Au/Pd octopod formation by seed-mediated co-reduction found that the presence of bromide during the synthesis contributed to the widening of the tip widths and that the sharpest tips could be achieved by replacing the stabilizing CTAB with the chloride analogue, CTAC.⁴⁵ Thus, it should be possible to decouple branch length from tip width synthetically to achieve Au/Pd octopods with both the sharpest tips and maximum LSPR overlap with the laser excitation wavelength. Significantly, these results illustrate that the Au/Pd octopods $< 100\text{ nm}$ in size are especially active substrates for the detection of molecular species via SERS, and greater enhancements may be possible with further synthetic advances.

4.6 Summary of Findings from the LSPR Properties of Size-Controlled Au/Pd Octopods¹

As outlined in Section 1.3, until recently, studies of plasmonic nanocrystals

focused on the properties of Au and Ag nanostructures. The introduction of other metals such as Pd into plasmonic structures can impart unique functionality; however, a greater understanding of how structure and composition compound to influence the optical properties of bimetallic nanostructures is needed. Here, the optical properties of size-controlled Au/Pd octopods were studied in detail. It was found that manipulation of seed-mediated co-reduction facilitated the predictable synthesis of monodisperse Au/Pd octopods over the size range of 60–150 nm. Controlling the size of the Au/Pd octopods, in turn, allowed for their corresponding LSPR to be tuned from 550 to 750 nm. Their RI sensitivities and activity for SERS were evaluated for the first time, with size dependences being correlated to performance in both cases. In particular, the largest Au/Pd octopods provided high RI sensitivity (>500 nm/RIU), while the smallest Au/Pd octopods provided substantial enhancement of molecular Raman signatures. On account of their unique particle architecture and composition, Au/Pd octopods are a promising multifunctional platform for applications in optics and sensing.

4.7 Manipulating the Optical Properties of Symmetrically Branched Au/Pd Nanocrystals through Interior Design⁵⁸

As shown in Sections 4.2-4.6, the optical properties of branched nanostructures are dependent upon their size. Composition also plays an important role in determining the applications of a nanomaterial, with bimetallic nanostructures often providing multifunctional platforms and new properties. For example, Au@Pd nanospheres were designed as multifunctional tools that could serve both as catalysts and a platform for surface-enhanced Raman spectroscopy, enabling the active species in Suzuki cross-coupling reactions to be identified.⁴³ Moreover, the optical properties of Au@Pd

nanoparticles are a function of the dielectrics for both metals, displaying tunable LSPRs that depend on the distribution of the two metals within the structures.⁴² Here, Au/Pd octopods with hollow, cubic interiors are achieved where the integration of hollow and branched architectures into one structure results in plasmonic bimetallic colloids with far red-shifted LSPRs.

One could argue that the introduction of hollow domains within a nanostructure is analogous to a change in composition as they too are a contrasting medium. As a LSPR can exist at any interface where the real components of the dielectrics for the two materials have opposite signs, hollow features can impart strong influence over the optical properties of plasmonic colloids.⁵⁹ Au nanoshells and nanocages are two popular examples that showcase how exploiting both the exteriors and the interiors of nanostructures can provide nanoscale platforms in which optical properties can be facilely manipulated.^{6, 59} For Au nanoshells, altering the size of the interior oxide colloid can change the hybridization of the inner and outer sphere plasmons and in turn the LSPR peak intensity and position.⁵⁹ Likewise, the hollow interiors of Au nanocages result in far red-shifted LSPRs compared to similar nanostructures with solid interiors, with the hollow interior also providing new function as containers for the delivery of molecular cargo.⁶⁰ Here, we integrate the hollow interior of a cage structure with the stellated exterior of a branched structure to achieve plasmonic colloids with an LSPR positioned past 900 nm. This architectural control is demonstrated in a Au/Pd platform, where the far red-shifted LSPR is remarkable given the poor plasmonic properties of Pd. Extending the LSPR of bimetallic nanostructures into the near IR can enable plasmon-enhanced surface spectroscopies with longer wavelength excitations and provide greater sensitivity

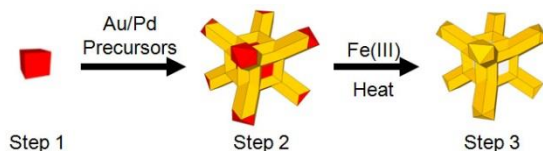
to changes in refractive index.⁶¹ This far red-shifted LSPR is attributed to both the hollow interior and stellated exterior, where the electric field can concentrate at features with a small radius of curvature (e.g., branch tips). Taken together, compositional and architectural control of nanostructures is leading to plasmonic colloids with enhanced and multifunctional properties.⁶¹

Central to achieving these new nanostructures is the use of a seed-mediated synthetic method to prepare precursor nanostructures composed of removable seeds. Seed-mediated methods are a premier route to high quality nanostructures with defined compositions and architectures. When synthesizing bimetallic nanostructures via seed-mediated methods, often core@shell architectures are accessed as one metal precursor is reduced to deposit metal onto the seeds in a conformal manner.^{36, 37} However, as shown in Chapter 2, reducing Au and Pd precursors simultaneously to deposit both metals onto shape-controlled seeds yields symmetrically branched nanostructures.⁴⁴ Sections 4.8 to 4.10 employ this synthetic method to build octopods atop removable nanocubic Pd seeds; these structures serve as precursors to branched Au/Pd nanocrystals with hollow, cubic interiors.

4.8 Interior Design of Au/Pd Octopods through Selective Etching⁵⁸

Scheme 4.1 highlights the three-step synthesis to Au/Pd octopods with hollow, cubic interiors and O_h symmetry. First, Pd nanocubes are prepared for use as seeds. These seeds then direct the overgrowth of Au and Pd when deposited via seed-mediated co-reduction, where one branch emerges per vertex of the cubic seed and proceeds along a $\langle 111 \rangle$ direction.⁶² This process produces core@shell Pd@Au/Pd octopods with O_h symmetry. Finally, the Pd nanocubes at the interiors of the nanostructures are selectively

removed via chemical etching with Fe(III). Central to achieving Au/Pd octopods with hollow interiors is the selection of sufficiently large Pd nanocubes relative to the amount of metal being deposited. This selection inhibits complete coverage of the Pd seeds during overgrowth, allowing the etchant to have access to the interiors of the nanostructures.



Scheme 4.1. The three-step synthesis of hollow Au/Pd octopods.

Pd nanocubes (edge length ~ 40 nm) were synthesized by a modified protocol and were characterized by SEM (**Figure 4.6A**).⁶³ Next, core@shell Pd@Au/Pd octopods were prepared by seed-mediated co-reduction, wherein Au and Pd precursors at a 4:1 ratio were reduced with L-aa to deposit metal onto the Pd nanocubes in the presence of CTAB. Experimental details can be found in **Appendix A4.7**. The structures were characterized by SEM, TEM and STEM/EDX for elemental mapping (**Figure 4.6B-D**). SEM imaging shows a good yield of core@shell Pd@Au/Pd octopods (**Figure 4.6B**). These stellated structures have O_h symmetry and the branches proceed along $\langle 111 \rangle$ directions. Some structures with non-uniform branching are also observed as an impurity, which we attribute to overgrowth from Pd nanocubes with rounded corners or possibly Pd cuboctahedra (**Figure 4.6B**).[†] STEM/EDX elemental mapping of the core@shell Pd@Au/Pd octopods clearly shows the Pd nanocubes in the interiors of the nanocrystals, with branches emerging from the vertices (**Figure 4.6 C-D**). Pd is also distributed along the surfaces of the structures.

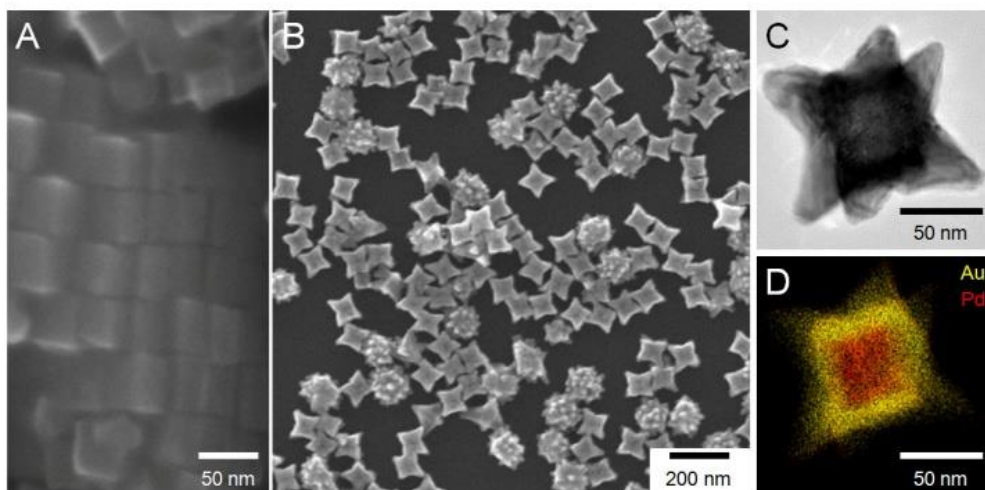


Figure 4.6. SEM images of (A) Pd nanocubes and (B) Pd@Au/Pd octopods. (C) A TEM image of a Pd@Au/Pd octopod and (D) elemental map by STEM/EDX analysis. Yellow, Au; red, Pd.

In the final step, the Pd nanocubes in the core@shell Pd@Au/Pd octopods are removed by etching. This process was achieved by adding FeCl₃, HCl, NaBr, and CTAB to a concentrated aqueous solution of core@shell Pd@Au/Pd octopods which was left stirring vigorously at 90 °C for 24 hours. These new nanostructures were characterized by SEM (**Figure 4.7A**), TEM (**Figure 4.7B,C**), and STEM/EDX elemental mapping (**Figure 4.7D,E**). The nanocrystals still have eight branches that proceed along $\langle 111 \rangle$ directions and O_h symmetry, but holes are observed between the branches (**Figure 4.7A**). The higher magnification inset of Figure 2A shows an individual particle where the hollow interior of the particle is clearly exposed. This hollow feature is also apparent in the TEM images (**Figure 4.7B,C**). STEM/EDX elemental mapping of individual particles shows the absence of both Au and Pd in the interior of the branched nanostructures, confirming that Pd etching has taken place to remove the cubic Pd seeds (**Figure 4.7D,E**). No Fe is present by EDX (**Figure S4.4**) or XPS analysis (**Figure S4.5**).

Interestingly, the structures with random branching patterns also experience etching during this process to remove their Pd interiors (**Figure S4.6**).

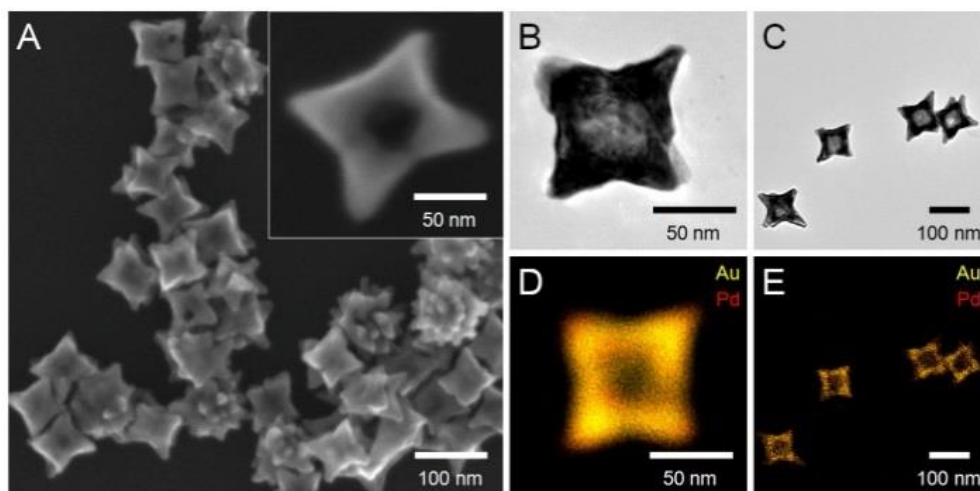
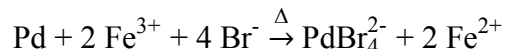


Figure 4.7. (A) SEM images of hollow Au/Pd octopods. (B-C) TEM images of hollow Au/Pd octopods and (D-E) their corresponding STEM/EDX mapping. Yellow, Au; red, Pd.

These changes in composition were quantified by SEM/EDX, where the concentration of Pd relative to Au dropped from roughly 36 atomic % before etching to 23 atomic % after. STEM/EDX elemental mapping indicates that the residual Pd is distributed along the exterior surfaces of the nanostructures. XPS analysis comparing the area under the curve for Au 4f_{7/2} and Pd 3d_{5/2} reveals that the surface decreases from 56.7 ± 6.0 atomic % Pd before etching to 24.1 ± 0.8 atomic % after etching (**Figure S4.7** and **S4.8**). Collectively, these results give important insight into the underlying mechanism of the etching process and how this strategy may be applied to achieve other bimetallic nanostructures with hollow features. The etching process can be described by the following reaction, where Fe^{III} is the oxidant and Br⁻ and heat have been added to drive the etching process (the standard oxidation potential of the Pd/PdBr₄²⁻ pair is -0.49 V vs.

SHE and -0.59 V vs. SHE for the Pd/PdCl₄²⁻ pair):⁶⁴



The more facile removal of Pd relative to Au from the nanostructures is consistent with the standard electrical potentials for the possible redox processes, where the standard reduction potential for Fe^{III}/Fe^{II} is 0.77 V vs. SHE. Interestingly, when the Pd interior is not exposed at the surface to the etchant, removal of the Pd core cannot be achieved (**Figure S4.9**). Incomplete removal of Pd from the surface of the Au/Pd octopods is consistent with an alloyed Au-Pd exterior, in which the electrochemical driving force for etching would be diminished relative to pure Pd.

We note that this etching process would need to be optimized when applied to new nanostructures. For example, here the pH of the etching solution was lowered by adding HCl to prevent formation of insoluble Fe(OH)₂.⁶⁴ Also, additional CTAB was added to the solution to counteract the decreasing colloidal stability of the octopods at low pH. Otherwise, inhomogeneous etching was observed. Finally, a very small amount of FeCl₃ relative to Au/Pd nanocrystals must be used as excessive Fe^{III} will oxidize the Au in the structures to AuBr₃, resulting in the dissolution of the nanostructures completely. Finally, applying heat to the octopods for excessive time (<48 h at 90 °C) can result in structural deformations toward more thermodynamically favored shapes (**Figure S4.10**).

4.9 LSPR Properties of Au/Pd Octopods with Compositionally Controlled Interiors⁵⁸

As discussed in Section 4.3, branched Au/Pd octopods have tunable LSPRs dependent upon structural parameters such as branch length and tip thickness.¹ **Figure**

4.8 shows the LSPRs of Au/Pd octopods with similar branch lengths (~118 nm) and tip thicknesses (~12 nm) but varying external and/or internal composition. When core@shell Pd@Au/Pd octopods are etched only on their exteriors, a broadening is observed and the extinction maxima shifts very little compared to the unetched core@shell Pd@Au/Pd octopods (700 nm vs. 765 nm, respectively). Interestingly, when the interiors and the exteriors of the core@shell Pd@Au/Pd octopods are etched to completely remove the interior Pd nanocubes, the LSPR shifts from 765 nm to 903 nm. The resonance also broadens. This large shift is attributed to the large change in the internal dielectric constant that occurs when the Pd core is removed. The broadening of the LSPRs observed in both etched samples may be due to lack of uniformity in the etching process. As shown in **Figure 4.7A**, holes open during the etching of the core@shell Pd@Au/Pd octopods and are not positioned symmetrically on the particles. Moreover, variations in pitting are observed when comparing particles. These small structural variations can give rise to large differences in the LSPRs of individual nanoparticles and manifests as a broadening in ensemble measurements.⁶⁵

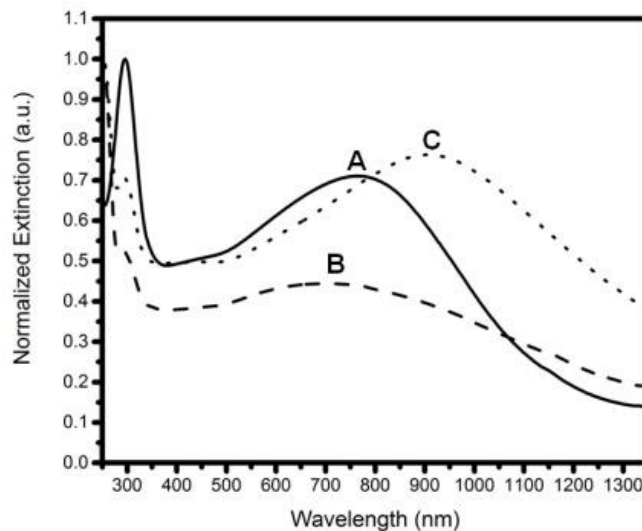


Figure 4.8. UV/Visible spectra of octopods under the following conditions: A) Pd@Au/Pd octopods before etching (see **Fig. 4.6B**), B) Pd@Au/Pd octopods where the exterior is etched (see **Fig. S4.9**), C) Au/Pd octopods where the interior and exterior are etched (see **Fig. 4.7A**).

4.10 Summary of the Findings from the Synthesis and Optical Properties of Au/Pd Octopods with Compositionally Controlled Interiors⁵⁸

We have demonstrated a means to integrate multiple architectural features into individual nanostructures that include a bimetallic composition, hollow interior, and symmetrically stellated exterior. This control provided a route to eight branched Au/Pd nanocrystals with hollow, cubic interiors and O_h symmetry. This route involves the seed-mediated co-reduction of Au and Pd precursors onto Pd nanocubes to achieve core@shell Pd@Au/Pd octopods, where the cubic shape of the seeds directs the overgrowth process. On account of their composition, these nanocubic Pd seeds can then be etched selectively with Fe(III) to achieve hollow interiors. The Pd core must be exposed to the surface prior to the etching process. Successful execution of this etching process provides Au/Pd

nanostructures with an LSPR positioned beyond 900 nm. Control of both the interior seed size and shape as well as branch lengths provides a route to stellated Au/Pd nanostructures with hollow interiors and tunable LSPRs.¹ This work provides a model for the design of new nanostructures, where combining bimetallic compositions with multiple architectural features into one structure can provide multifunctional plasmonic platforms.

4.11 Overall Conclusions

This chapter investigated the optical properties of Au/Pd octopods. Both size and composition play a role in the location of the LSPR peak maxima. In addition, size-adjusted Au/Pd octopods can have high refractive index sensitivities (>500 RIU). These nanostructures could therefore be useful as sensing platforms. Chapter 5 further explores branched Au/Pd nanostructures as substrates through assembly. Overall, seed-mediated co-reduction allows for a range of structural features that can be manipulated, including branch length, tip thickness, interior composition, and branch symmetry. In turn, new plasmonic properties are potentially accessible.

4.12 Notes and References

† As noted in ref. 62, multiple branches can originate from a single vertex of {111}-terminated structures. Higher-branched particles may also be due to rounding of the cubes, which would have more vertices.

1. DeSantis, C. J.; Skrabalak, S. E., Size-Controlled Synthesis of Au/Pd Octopods with High Refractive Index Sensitivity. *Langmuir* **2012**, *28*, 9055-9062.
2. Cortie, M. B.; McDonagh, A. M., Synthesis and Optical Properties of Hybrid and Alloy Plasmonic Nanoparticles. *Chem. Rev.* **2011**, *111*, 3713-3735.

3. Xia, Y.; Xiong, Y.; Lim, B.; Skrabalak, S. E., Shape-Controlled Synthesis of Metal Nanocrystals: Simple Chemistry Meets Complex Physics? *Angew. Chem. Int. Ed.* **2009**, *48*, 60-103.
4. Zhang, J.; Noguez, C., Plasmonic Optical Properties and Applications of Metal Nanostructures. *Plasmonics* **2008**, *3*, 127-150.
5. Mirkin, C. A. N., A. N.; Thaxton, S., Applications: Nanobiosystems, Medicine, and Health. In *Nanotechnology Research Directions for Societal Needs in 2020*, Roco, M. C., Mirkin, Chad A., Hersam, Mark C., Ed. Springer: Dordrecht, 2011; pp 305-374.
6. Xia, Y.; Li, W.; Cobley, C. M.; Chen, J.; Xia, X.; Zhang, Q.; Yang, M.; Cho, E. C.; Brown, P. K., Gold Nanocages: From Synthesis to Theranostic Applications. *Acc. Chem. Res.* **2011**, *44*, 914-924.
7. Peng, B.; Li, G.; Li, D.; Dodson, S.; Zhang, Q.; Zhang, J.; Lee, Y. H.; Demir, H. V.; Yi Ling, X.; Xiong, Q., Vertically Aligned Gold Nanorod Monolayer on Arbitrary Substrates: Self-Assembly and Femtomolar Detection of Food Contaminants. *ACS Nano* **2013**, *7*, 5993-6000.
8. Stewart, M. E.; Anderton, C. R.; Thompson, L. B.; Maria, J.; Gray, S. K.; Rogers, J. A.; Nuzzo, R. G., Nanostructured Plasmonic Sensors. *Chem. Rev.* **2008**, *108*, 494-521.
9. Anker, J. N.; Hall, W. P.; Lyandres, O.; Shah, N. C.; Zhao, J.; Van Duyne, R. P., Biosensing with plasmonic nanosensors. *Nat. Mater.* **2008**, *7*, 442-453.
10. Willets, K. A.; Van Duyne, R. P., Localized surface plasmon resonance spectroscopy and sensing. *Annu. Rev. Phys. Chem.* **2007**, *58*, 267-297.
11. Major, K.; De, C.; Obare, S., Recent Advances in the Synthesis of Plasmonic Bimetallic Nanoparticles. *Plasmonics* **2009**, *4*, 61-78.

12. Chen, H. M.; Liu, R.-S., Architecture of Metallic Nanostructures: Synthesis Strategy and Specific Applications. *J. Phys. Chem. C* **2011**, *115*, 3513-3527.
13. Tao, A. R.; Habas, S.; Yang, P., Shape control of colloidal metal nanocrystals. *Small* **2008**, *4*, 310-325.
14. Jain, P. K.; Huang, X.; El-Sayed, I. H.; El-Sayed, M. A., Noble Metals on the Nanoscale: Optical and Photothermal Properties and Some Applications in Imaging, Sensing, Biology, and Medicine. *Acc. Chem. Res.* **2008**, *41*, 1578-1586.
15. Mayer, K. M.; Hafner, J. H., Localized Surface Plasmon Resonance Sensors. *Chem. Rev.* **2011**, *111*, 3828-3857.
16. Homola, J.; Yee, S. S.; Gauglitz, G., Surface plasmon resonance sensors: review. *Sens. Actuators, B* **1999**, *54*, 3-15.
17. Karakouz, T.; Vaskevich, A.; Rubinstein, I., Polymer-Coated Gold Island Films as Localized Plasmon Transducers for Gas Sensing. *J. Phys. Chem. B* **2008**, *112*, 14530-14538.
18. Charles, D. E.; Aherne, D.; Gara, M.; Ledwith, D. M.; Gun'ko, Y. K.; Kelly, J. M.; Blau, W. J.; Brennan-Fournet, M. E., Versatile Solution Phase Triangular Silver Nanoplates for Highly Sensitive Plasmon Resonance Sensing. *ACS Nano* **2009**, *4*, 55-64.
19. Jakab, A.; Rosman, C.; Khalavka, Y.; Becker, J.; Trügler, A.; Hohenester, U.; Sönnichsen, C., Highly Sensitive Plasmonic Silver Nanorods. *ACS Nano* **2011**, *5*, 6880-6885.
20. Lee, Y. H.; Chen, H.; Xu, Q.-H.; Wang, J., Refractive Index Sensitivities of Noble Metal Nanocrystals: The Effects of Multipolar Plasmon Resonances and the Metal Type. *J. Phys. Chem. C* **2011**, *115*, 7997-8004.

21. Niu, Z.; Zhen, Y.-R.; Gong, M.; Peng, Q.; Nordlander, P.; Li, Y., Pd nanocrystals with single-, double-, and triple-cavities: facile synthesis and tunable plasmonic properties. *Chemical Science* **2011**, *2*, 2392-2395.
22. Xiong, Y.; Chen, J.; Wiley, B.; Xia, Y.; Yin, Y.; Li, Z.-Y., Size-Dependence of Surface Plasmon Resonance and Oxidation for Pd Nanocubes Synthesized via a Seed Etching Process. *Nano Lett.* **2005**, *5*, 1237-1242.
23. Xiong, Y.; McLellan, J. M.; Chen, J.; Yin, Y.; Li, Z.-Y.; Xia, Y., Kinetically Controlled Synthesis of Triangular and Hexagonal Nanoplates of Palladium and Their SPR/SERS Properties. *J. Am. Chem. Soc.* **2005**, *127*, 17118-17127.
24. Gao, H.; Henzie, J.; Lee, M. H.; Odom, T. W., Screening plasmonic materials using pyramidal gratings. *Proc. Natl. Acad. Sci. U. S. A.* **2008**, *105*, 20146-20151.
25. Heck, K. N.; Janesko, B. G.; Scuseria, G. E.; Halas, N. J.; Wong, M. S., Observing Metal-Catalyzed Chemical Reactions in Situ Using Surface-Enhanced Raman Spectroscopy on Pd–Au Nanoshells. *J. Am. Chem. Soc.* **2008**, *130*, 16592-16600.
26. Chen, H.; Shao, L.; Woo, K. C.; Ming, T.; Lin, H.-Q.; Wang, J., Shape-Dependent Refractive Index Sensitivities of Gold Nanocrystals with the Same Plasmon Resonance Wavelength. *J. Phys. Chem. C* **2009**, *113*, 17691-17697.
27. Chen, H.; Kou, X.; Yang, Z.; Ni, W.; Wang, J., Shape- and Size-Dependent Refractive Index Sensitivity of Gold Nanoparticles. *Langmuir* **2008**, *24*, 5233-5237.
28. Nehl, C. L.; Liao, H.; Hafner, J. H., Optical Properties of Star-Shaped Gold Nanoparticles. *Nano Lett.* **2006**, *6*, 683-688.
29. Hao, F.; Nehl, C. L.; Hafner, J. H.; Nordlander, P., Plasmon Resonances of a Gold Nanostar. *Nano Lett.* **2007**, *7*, 729-732.

30. Hrelescu, C.; Sau, T. K.; Rogach, A. L.; Jäckel, F.; Laurent, G.; Douillard, L.; Charra, F., Selective Excitation of Individual Plasmonic Hotspots at the Tips of Single Gold Nanostars. *Nano Lett.* **2011**, *11*, 402-407.
31. Wei, Q.; Song, H.-M.; Leonov, A. P.; Hale, J. A.; Oh, D.; Ong, Q. K.; Ritchie, K.; Wei, A., Gyromagnetic Imaging: Dynamic Optical Contrast Using Gold Nanostars with Magnetic Cores. *J. Am. Chem. Soc.* **2009**, *131*, 9728-9734.
32. Dondapati, S. K.; Sau, T. K.; Hrelescu, C.; Klar, T. A.; Stefani, F. D.; Feldmann, J., Label-free Biosensing Based on Single Gold Nanostars as Plasmonic Transducers. *ACS Nano* **2010**, *4*, 6318-6322.
33. Su, Q.; Ma, X.; Dong, J.; Jiang, C.; Qian, W., A Reproducible SERS Substrate Based on Electrostatically Assisted APTES-Functionalized Surface-Assembly of Gold Nanostars. *ACS Appl. Mater. Interfaces* **2011**, *3*, 1873-1879.
34. Xie, J.; Zhang, Q.; Lee, J. Y.; Wang, D. I. C., The Synthesis of SERS-Active Gold Nanoflower Tags for In Vivo Applications. *ACS Nano* **2008**, *2*, 2473-2480.
35. Skrabalak, S. E.; Xia, Y., Pushing Nanocrystal Synthesis toward Nanomanufacturing. *ACS Nano* **2009**, *3*, 10-15.
36. Habas, S. E.; Lee, H.; Radmilovic, V.; Somorjai, G. A.; Yang, P., Shaping binary metal nanocrystals through epitaxial seeded growth. *Nat. Mater.* **2007**, *6*, 692-697.
37. Yu, Y.; Zhang, Q.; Liu, B.; Lee, J. Y., Synthesis of Nanocrystals with Variable High-Index Pd Facets through the Controlled Heteroepitaxial Growth of Trisoctahedral Au Templates. *J. Am. Chem. Soc.* **2010**, *132*, 18258-18265.

38. Park, G.; Seo, D.; Jung, J.; Ryu, S.; Song, H., Shape Evolution and Gram-Scale Synthesis of Gold@Silver Core–Shell Nanopolyhedrons. *J. Phys. Chem. C* **2011**, *115*, 9417-9423.
39. Cui, L.; Wang, A.; Wu, D.-Y.; Ren, B.; Tian, Z.-Q., Shaping and Shelling Pt and Pd Nanoparticles for Ultraviolet Laser Excited Surface-Enhanced Raman Scattering. *J. Phys. Chem. C* **2008**, *112*, 17618-17624.
40. Ma, Y.; Li, W.; Cho, E. C.; Li, Z.; Yu, T.; Zeng, J.; Xie, Z.; Xia, Y., Au@Ag Core–Shell Nanocubes with Finely Tuned and Well-Controlled Sizes, Shell Thicknesses, and Optical Properties. *ACS Nano* **2010**, *4*, 6725-6734.
41. Xiang, Y.; Wu, X.; Liu, D.; Li, Z.; Chu, W.; Feng, L.; Zhang, K.; Zhou, W.; Xie, S., Gold Nanorod-Seeded Growth of Silver Nanostructures: From Homogeneous Coating to Anisotropic Coating. *Langmuir* **2008**, *24*, 3465-3470.
42. Zhang, K.; Xiang, Y.; Wu, X.; Feng, L.; He, W.; Liu, J.; Zhou, W.; Xie, S., Enhanced Optical Responses of Au@Pd Core/Shell Nanobars. *Langmuir* **2008**, *25*, 1162-1168.
43. Fang, P.-P.; Jutand, A.; Tian, Z.-Q.; Amatore, C., Au–Pd Core–Shell Nanoparticles Catalyze Suzuki–Miyaura Reactions in Water through Pd Leaching. *Angew. Chem. Int. Ed.* **2011**, *50*, 12184-12188.
44. DeSantis, C. J.; Peverly, A. A.; Peters, D. G.; Skrabalak, S. E., Octopods versus Concave Nanocrystals: Control of Morphology by Manipulating the Kinetics of Seeded Growth via Co-Reduction. *Nano Lett.* **2011**, *11*, 2164-2168.

45. DeSantis, C. J.; Sue, A. C.; Bower, M. M.; Skrabalak, S. E., Seed-Mediated Co-reduction: A Versatile Route to Architecturally Controlled Bimetallic Nanostructures. *ACS Nano* **2012**, *6*, 2617-2628.
46. Naumov, I. I.; Li, Z.; Bratkovsky, A. M., Plasmonic resonances and hot spots in Ag octopods. *Appl. Phys. Lett.* **2010**, *96*, 033105/1-033105/3.
47. Ringe, E.; DeSantis, C. J.; Collins, S. M.; Skrabalak, S. E.; Midgley, P. A., Composition, Crystallography, and Plasmonic Response of Single Au/Pd Octopods. **2014**, Submitted.
48. Lu, X.; Rycenga, M.; Skrabalak, S. E.; Wiley, B.; Xia, Y., Chemical Synthesis of Novel Plasmonic Nanoparticles. *Annu. Rev. Phys. Chem.* **2009**, *60*, 167-192.
49. Zorić, I.; Zäch, M.; Kasemo, B.; Langhammer, C., Gold, Platinum, and Aluminum Nanodisk Plasmons: Material Independence, Subradiance, and Damping Mechanisms. *ACS Nano* **2011**, *5*, 2535-2546.
50. Barbosa, S.; Agrawal, A.; Rodríguez-Lorenzo, L.; Pastoriza-Santos, I.; Alvarez-Puebla, R. n. A.; Kornowski, A.; Weller, H.; Liz-Marzán, L. M., Tuning Size and Sensing Properties in Colloidal Gold Nanostars. *Langmuir* **2010**, *26*, 14943-14950.
51. Kim, D. Y.; Yu, T.; Cho, E. C.; Ma, Y.; Park, O. O.; Xia, Y., Synthesis of Gold Nano-hexapods with Controllable Arm Lengths and Their Tunable Optical Properties. *Angew. Chem. Int. Ed.* **2011**, *50*, 6328-6331.
52. Huang, X.; El-Sayed, I. H.; Qian, W.; El-Sayed, M. A., Cancer Cell Imaging and Photothermal Therapy in the Near-Infrared Region by Using Gold Nanorods. *J. Am. Chem. Soc.* **2006**, *128*, 2115-2120.

53. Lim, J. K.; Imura, K.; Nagahara, T.; Kim, S. K.; Okamoto, H., Imaging and dispersion relations of surface plasmon modes in silver nanorods by near-field spectroscopy. *Chem. Phys. Lett.* **2005**, *412*, 41-45.
54. Miller, M. M.; Lazarides, A. A., Sensitivity of Metal Nanoparticle Surface Plasmon Resonance to the Dielectric Environment. *J. Phys. Chem. B* **2005**, *109*, 21556-21565.
55. Tian, Z.-Q.; Ren, B.; Wu, D.-Y., Surface-Enhanced Raman Scattering: From Noble to Transition Metals and from Rough Surfaces to Ordered Nanostructures. *J. Phys. Chem. B* **2002**, *106*, 9463-9483.
56. Zhang, L.; Bai, Y.; Shang, Z.; Zhang, Y.; Mo, Y., Experimental and theoretical studies of Raman spectroscopy on 4-mercaptopyridine aqueous solution and 4-mercaptopyridine/Ag complex system. *Journal of Raman Spectroscopy* **2007**, *38*, 1106-1111.
57. Yu, H.-Z.; Xia, N.; Liu, Z.-F., SERS Titration of 4-Mercaptopyridine Self-Assembled Monolayers at Aqueous Buffer/Gold Interfaces. *Anal. Chem.* **1999**, *71*, 1354-1358.
58. DeSantis, C. J.; Skrabalak, S. E., Manipulating the optical properties of symmetrically branched Au/Pd nanocrystals through interior design. *Chem. Commun.* **2014**, DOI: 10.1039/C3CC48441F.
59. Bardhan, R.; Lal, S.; Joshi, A.; Halas, N. J., Theranostic Nanoshells: From Probe Design to Imaging and Treatment of Cancer. *Acc. Chem. Res.* **2011**, *44*, 936-946.
60. Moon, G. D.; Choi, S.-W.; Cai, X.; Li, W.; Cho, E. C.; Jeong, U.; Wang, L. V.; Xia, Y., A New Theranostic System Based on Gold Nanocages and Phase-Change

Materials with Unique Features for Photoacoustic Imaging and Controlled Release. *J. Am. Chem. Soc.* **2011**, *133*, 4762-4765.

61. DeSantis, C. J.; Weiner, R. G.; Radmilovic, A.; Bower, M. M.; Skrabalak, S. E., Seeding Bimetallic Nanostructures as a New Class of Plasmonic Colloids. *J. Phys. Chem. Lett.* **2013**, *4*, 3072-3082.

62. DeSantis, C. J.; Skrabalak, S. E., Core Values: Elucidating the Role of Seed Structure in the Synthesis of Symmetrically Branched Nanocrystals. *J. Am. Chem. Soc.* **2012**, *135*, 10-13.

63. Niu, W.; Li, Z.-Y.; Shi, L.; Liu, X.; Li, H.; Han, S.; Chen, J.; Xu, G., Seed-Mediated Growth of Nearly Monodisperse Palladium Nanocubes with Controllable Sizes. *Cryst. Growth Des.* **2008**, *8*, 4440-4444.

64. Xie, S.; Lu, N.; Xie, Z.; Wang, J.; Kim, M. J.; Xia, Y., Synthesis of Pd-Rh Core-Frame Concave Nanocubes and Their Conversion to Rh Cubic Nanoframes by Selective Etching of the Pd Cores. *Angew. Chem. Int. Ed.* **2012**, *51*, 10266-10270.

65. Ringe, E.; Sharma, B.; Henry, A.-I.; Marks, L. D.; Van Duyne, R. P., Single nanoparticle plasmonics. *Phys. Chem. Chem. Phys.* **2013**, *15*, 4110-4129.

**Chapter 5: Shaping the Synthesis and Assembly of Symmetrically Stellated Au/Pd
Nanocrystals with Aromatic Additives**

5.1 Introduction¹

There is increasing interest in the study of metal nanomaterials and their interaction with light.² The use of plasmonic nanoscale materials in chemical sensing, nanomedicine, and catalysis continues to rise.^{3, 4} Both the structural properties (i.e., crystallite size, shape, and architecture) of individual metal nanoparticles as well as their spatial arrangement relative to one another dictate the properties of plasmonic ensembles. For example, branched metal nanostructures can concentrate light at tips with a small radius of curvature to facilitate plasmon-enhanced surface spectroscopies.⁵ Platforms composed of assembled plasmonic nanostructures can also provide enhancement through the creation of “hot spots” and have optical properties (i.e., photonic and plasmonic band gaps) that depend on the superstructure generated. For example, Yang and co-workers were able to assemble large arrays of Ag nanocubes, cuboctahedra, and octahedra through sedimentation.^{6, 7} In addition, they were able to tune the volume fraction of the supercrystal, which corresponded with a change in the photonic passbands measured by specular reflectance spectroscopy.⁶ These results were attributed to the intense near-field plasmonic coupling that can occur in close-packed arrays and were corroborated by finite-difference time-domain (FDTD) simulations. In general, assembly of nanostructures into superstructures with collective properties represents an appealing alternative to lithographic “top down” approaches to such materials.

Such superstructures have not been realized from stellated plasmonic building blocks, although recent work with octopodal metal chalcogenide nanostructures indicates that structures with such symmetry can be used as building blocks.⁸ The lack of self-assembled superstructures from stellated metal nanocrystals likely arises from the

challenges associated with achieving monodisperse samples, where nanocrystals with inhomogeneous branching or sizes can serve as point defects in larger structures.⁹ Thus, both the symmetry and size of branched nanostructures need to be precisely controlled.⁸ Although most examples of branched nanostructures are asymmetric, as we reported in Chapter 2, controlled overgrowth can yield symmetrically branched metal nanostructures where the initial structure of seeds directs the branching pattern.¹⁰⁻¹² However, even with this structural control, most colloidal syntheses to nanostructures yield samples with some structural impurities. For example, the typical seed-mediated route to Au nanorods yields > 10% structural impurities such as spherical particles that hamper the ability of the nanorods to self-assemble into larger structures.^{13, 14} Recently, the Murray group found that the homogeneity of Au nanorod samples could be improved with the use of aromatic additives such as 5-bromosalicylic acid or sodium salicylate in the typical synthesis.¹⁴ Through extensive characterization they found that these molecules intercalate into the bilayer of the surfactant cetyltrimethylammonium bromide (CTAB), with their polar functional groups oriented toward the head group of CTAB and away from its hydrophobic chains. This configuration can increase the micellar packing parameter and promote the transition from spherical to rod-like micelles, the latter of which has been cited to promote nanorod formation.¹⁵ With improved structural uniformity, self-assembly of Au nanorods was achievable with typical domain sizes of $\sim 10 \mu\text{m}^2$.^{14, 16}

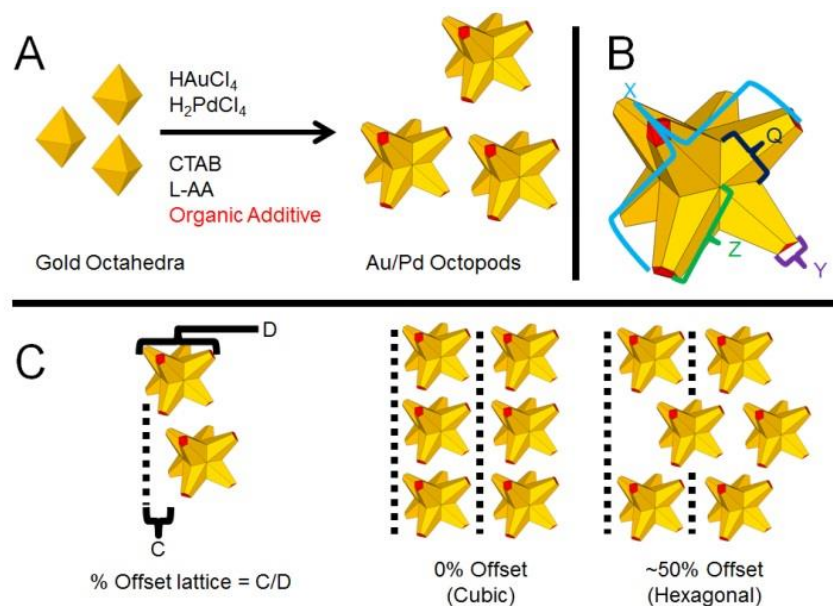
As reported in this chapter, these aromatic additives are used in conjunction with the seed-mediated co-reduction method described in Chapter 2 to achieve symmetrically branched octopodal Au/Pd nanocrystals as samples with unprecedented structural

uniformity.¹⁰ The enhanced homogeneity of these samples facilitates larger-scale assembly of these stellated nanocrystals, where strong electromagnetic coupling may be realized between particles on account of their sharp tips. Importantly, we also report that these aromatic additives provide subtle shape modifications to features such as branch thickness and tip thickness. In turn, these changes affect the packing lattice observed from the self-assembly of the octopods into supercrystals. Our work provides a basis for achieving assemblies of stellated nanostructures and a broader framework for the use of aromatic additives in nanostructure synthesis to achieve homogeneous samples.

5.2 Results and Discussion

The Au/Pd octopods were prepared by seed-mediated co-reduction, with the procedure detailed in **Appendix A5** and depicted in **Scheme 5.1A**. Synthetic details are also provided in Chapter 2. In brief, metal precursors HAuCl_4 and H_2PdCl_4 were reduced simultaneously with L-ascorbic acid in aqueous media to deposit metal onto pre-synthesized Au octahedra which serve as seeds. CTAB was used as a stabilizing agent. The aromatic additives were incorporated to the metal precursor growth solution during the co-reduction step and those studied include: 3-methylsalicylic acid, sodium salicylate, 2, 6-dihydroxybenzoic acid, 5-bromosalicylic acid, or 5-aminosalicylic acid. For each aromatic additive studied, a range of concentrations were surveyed to find if structural features of the octopods were altered and if sample homogeneity improved. Scanning electron microscopy (SEM) images of the products obtained from these optimization experiments are shown in **Appendix B Figures S5.1-S5.5**. In general, excessive concentrations of any additive led to polydisperse malformed particles, though for each additive there was a narrow concentration range where sample homogeneity was

enhanced relative to the control samples made without aromatic additives. This dependence on concentration will be discussed in more depth later.



Scheme 1. (A) Schematic depicting the components involved in the typical synthesis of Au/Pd octopods *via* seed-mediated co-reduction, (B) the definition of the three measured parameters X, Y, and Q as well as the calculated parameter Z reported in **Table 5.2** (for more information, see **Appendix C**), and (C) the definition of the offset value measured in Au/Pd octopod superlattices reported in **Table 5.1** (refer to **Figure S5.12** for more details).

Figure 5.1 shows SEM and transmission electron microscopy (TEM) images as well as elemental mapping by scanning transmission electron microscopy coupled with energy-dispersive X-ray spectroscopy (STEM/EDX) of Au/Pd octopods prepared without aromatic additives (**Figure 5.1A**) and with an aromatic additive at a concentration optimized for the least proportion of particles with structural defects (**Figure 5.1B-F**). When imaged by SEM, most octopods orient with only four branches in view; however,

TEM confirms that eight branches form in each particle, arranged in O_h symmetry. Elemental mapping by STEM/EDX shows that there is a similar distribution of Pd along the surfaces of particles in each of the samples. Importantly, through the addition of aromatic additives sample homogeneity improved. By counting ($n > 300$ per sample) the proportion of symmetrically branched octopods relative to asymmetric octopods and other shape impurities such as rods, every sample synthesized with an aromatic additive under optimized conditions had a greater percentage of symmetrically branched structures compared to control samples. The results are summarized in **Table 5.1**. Samples prepared with 5-bromosalicylic acid or sodium salicylate gained more than ten percent sample homogeneity compared to the control. In addition to the improved sample homogeneity, subtle differences in structural features can be observed between samples prepared with different additives. For example, samples prepared with 3-methylsalicylic acid (**Figure 5.1B**) and sodium salicylate (**Figure 5.1C**) have branches that appear thinner both at the tips and at the base compared to the control samples. In contrast, samples prepared with 2, 6-dihydroxybenzoic acid (**Figure 5.1D**) have structures with branches that are shorter and wider than the other samples.

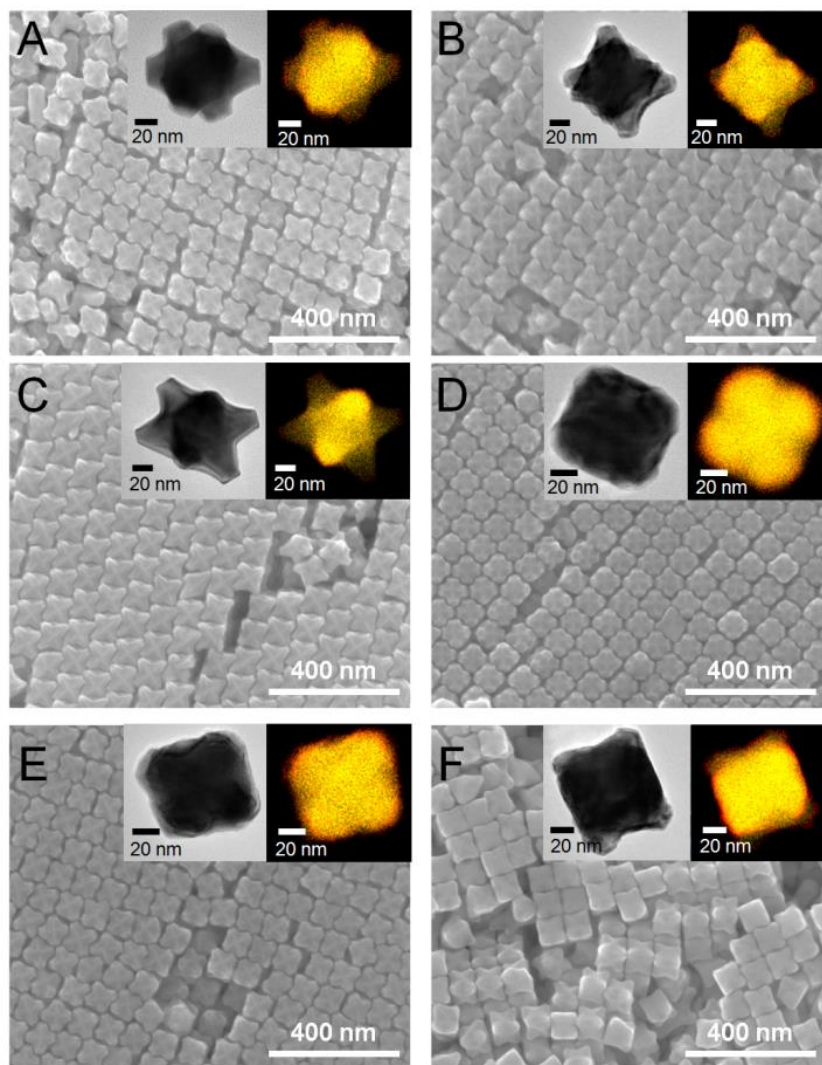


Figure 5.1. SEM, TEM (inset, left), and elemental maps by STEM/EDX analysis (inset, right) of Au/Pd octopods prepared (A) without additives and with 2 mL of (B) 20 mM 3-methylsalicylic acid, (C) 40 mM sodium salicylate, (D) 16 mM 2, 6-dihydroxybenzoic acid, (E) 8 mM 5-bromosalicylic acid, and (F) 6 mM 5-aminosalicylic acid added to otherwise identical synthetic conditions. For the STEM/EDX maps, yellow is Au and red is Pd.

Table 5.1. Calculations of percent homogeneity and percent lattice offset for nanocrystals prepared with different aromatic additives.^a

Additive	% Sample Homogeneity	% Lattice Offset
NONE	84	26 (7)
3-Methylsalicylic acid	92	33 (11)
Sodium salicylate	96	33 (10)
2, 6-Dihydroxybenzoic acid	84	25 (7)
5-Bromosalicylic acid	97	23 (5)
5-Aminosalicylic acid	92	10 (4)

^a*The values in parenthesis indicate standard deviation.*

Previously, the reaction pH was found to have a dramatic impact on the morphology of Au/Pd nanocrystals prepared by seed-mediated co-reduction, with octopods prepared at lower pH conditions adopting “sheets” at the tips (see Chapter 2, **Figure 2.6**).¹⁰ Thus, we initially speculated that the changes in morphology observed with different aromatic additives may arise from changes in reaction pH. For example, the addition of 2, 6-dihydroxybenzoic acid at the optimized conditions lowers the pH of the growth solution from 2.43 to 2.27 (**Table S5.1**). However, the growth solution used to prepare octopods with 5-bromosalicylic acid has a similar pH (2.34) yet the octopods appear to be similar structurally with those prepared under the control conditions. The most dramatic difference in nanocrystal shape compared to the control occurs when 5-aminosalicylic acid is added to the seed-mediated co-reduction synthesis. Instead of nanocrystals with well-defined stellations, these nanocrystals adopt a nearly cube-like appearance. The growth solution used to prepare octopods with 5-aminosalicylic acid is at roughly the same pH (2.56) as it is without the use of the aromatic additive (2.55), which indicates that pH is not always a primary factor in the change in structure when aromatic additives are added to the growth solution.

To make quantitative comparisons of shape changes between samples, three measurements were made from SEM images ($n = 50$ for each sample). These measurements are defined in **Scheme 5.1B** as the following parameters: X , which is the length of one branch tip to its opposing branch tip; Y , which is branch tip thickness; and Q , which is the thickness of the branch at the base of the structure. These parameters along with the calculated branch length, Z (see **Scheme 5.1B**) and octopod volume and surface area are presented in **Table 5.2**. Derivations for parameter Z , surface area, and volume are presented in **Appendix C**. These quantitative measurements corroborate the qualitative observations from **Figure 5.1** previously detailed. Octopods prepared with 3-methylsalicylic acid (**Figure 5.1B**) and sodium salicylate (**Figure 5.1C**) had branch lengths of 67 ± 2 nm and 65 ± 1 nm, respectively, which were larger than the control of 62 ± 3 nm. The tip thicknesses for the octopods prepared with 3-methylsalicylic acid (**Figure 5.1B**) and sodium salicylate (**Figure 5.1C**) were 18 ± 2 nm and 17 ± 1 nm, which were shorter than the control, with a tip thickness of 20 ± 2 nm. The octopods prepared with 2, 6-dihydroxybenzoic acid had the shortest branch length (Z) and largest branch tip at 57 ± 1 nm and 12 ± 1 nm, respectively. All of the samples, including the control, had similar volumes of $\sim 4.7 \times 10^5$ nm³ except for those prepared with 5-bromosalicylic acid or 5-aminosalicylic acid, which had volumes of $4.1 \times 10^5 \pm 3.9 \times 10^4$ nm³ and $5.6 \times 10^5 \pm 1.1 \times 10^5$ nm³. For the samples prepared with 5-bromosalicylic acid, the relatively lower volume measurement suggests that less precursor is reduced when using 5-bromosalicylic acid as an additive than the others and thus may explain why no structural changes are observed in this system despite a pH that is lower than the control. It has been hypothesized that the addition of 5-bromosalicylic acid can hamper

autocatalytic reduction of Au^I to Au⁰ when using ascorbic acid as a reducing agent.¹⁷ The cube-like octopods that were prepared with 5-aminosalicylic acid (**Figure 5.1D**) had the shortest tip thicknesses at 12 ± 6 nm and the largest base thicknesses at 50 ± 7 nm. For this sample, the standard deviation for each branch thickness measurement was larger than the other samples because of the inherent difficulty of ascertaining where the branches extrude from the center of the particle. Even so, the observed shape difference was measurable as this sample had a small surface area relative to the other samples yet also had the largest volume. Overall, these quantitative measurements show that subtle shape changes do occur when preparing Au/Pd nanocrystals with aromatic additives, with the specific structural features depending on the aromatic additive used.

Table 2. Size, surface area, and volume measurements of Au/Pd octopods prepared with various aromatic additives.^a

Additive	X (nm)	Y (nm)	Q (nm)	Z (nm)	Area (nm²)	Volume (nm³)
NONE	102 (2)	20 (1)	47 (1)	62 (3)	578000 (36000)	471000 (31000)
3-Methyl salicylic acid	109 (3)	18 (2)	47 (2)	67 (2)	545000 (55000)	485000 (32000)
Sodium salicylate	106 (2)	17 (1)	47 (1)	65 (1)	509000 (38000)	471000 (29000)
2, 6-Dihydroxybenzoic acid	92.6 (1)	26 (1)	47 (1)	57 (1)	696000 (43000)	454000 (24000)
5-Bromosalicylic acid	97.0 (2)	17 (1)	45 (2)	59 (1)	446000 (34000)	409000 (39000)
5-Aminosalicylic acid	106 (3)	12 (6)	51 (7)	65 (2)	393000 (93000)	564000 (112000)

^aThe values in parenthesis indicate standard deviation.

As outlined by Ye et al., the addition of these aromatic additives to the traditional Au nanorod synthesis is thought to stabilize the spherical to rod-like micellar transition for CTAB, with the additives residing within the bilayer near the Au surface.¹⁴ This mediated binding of CTAB to certain facets allows for uniform addition of metal at the exposed facets and provides an explanation for the enhanced sample homogeneity. However, this model does not adequately explain the shape modifications that occur when different aromatic additives are used during the synthesis of Au/Pd structures via seed-mediated co-reduction and which are absent during the synthesis of Au nanorods on account of their 1-D shape. Contrastingly, Chiu et al. were able to selectively control faceting of Pt nanoparticles through aromatic additives that adsorbed preferentially onto surfaces, as characterized by Raman spectroscopy.¹⁸ They found that organic additives that have electrostatic potentials that best match with a (111) surface could be used as capping agents for the synthesis of {111}-terminated Pt nanoparticles such as tetrahedra and octahedra. Conversely, organic additives with electrostatic potentials that best match with a (100) surface could be used as capping agents for the synthesis of {100}-terminated Pt cubes. Although CTAB was not used as a stabilizing agent in this system, this study gives precedence for aromatic additives behaving as capping agents with preference for specific facets.

A number of experiments were conducted to better understand the role of aromatic additives in our system. Ye et al. relied heavily on NMR analysis of the Au nanorods prepared in the presence of aromatic additives, observing increased shielding in the region of the aliphatic protons of the CTAB headgroup to Au nanorod/CTAB samples after the addition of an aromatic additive. From this characterization, they rationalized

that the aromatic additives intercalated into the CTAB bilayer. We attempted similar experiments with our symmetrically branched Au/Pd nanocrystals but were unable to detect the additives *via* NMR. Thus, FT-IR (**Figure S5.6**) and X-ray photoelectron spectroscopy (XPS) (**Figure S5.7-5.9**) were used to confirm the presence of the aromatic additives. The –COOH broad stretch ca. 3300 cm⁻¹ is present in the FT-IR spectra of all samples with aromatic additives and absent in samples without aromatic additives (**Figure S6**), which indicates that the aromatic additives are present after washing and collection of the product, likely within the CTAB bilayer. Furthermore, XPS analysis of the Au 4f_{5/2}, Au 4f_{7/2}, and Pd 3p_{1/2} regions indicate significant shifts to lower binding energies for samples prepared with aromatic additives compared to those prepared without aromatic additives (**Figure S5.8A,B**) and were reproducible and beyond the error of measurement (**Figure S5.9**). Such shifts may arise from the aromatic additives modifying the distribution of Au and Pd at the surfaces of the nanocrystals; however, XPS analysis indicates that the ratio of Au:Pd on the surface of the nanocrystals is consistent in all samples. Such shifts may also arise from the aromatic additives adsorbing onto the Au-Pd surfaces. These different surface adsorbate interactions may account for the measurable differences in octopodal shape when samples are prepared with an aromatic additive compared to samples prepared without an aromatic additive. Interestingly, Zeta potential measurements of samples (**Figure S5.10**) prepared at optimized conditions yielded no significant difference in the local electrostatic potential between any of the additives used or to the control. A change in zeta potential measurements only occurs when an excessive concentration of aromatic additives is added, often tenfold the concentration typically used to achieve homogeneous samples

(**Figure S5.11**). We therefore conclude that the aromatic additives likely preferentially adsorb onto the surfaces of the nanostructures during growth but do not contribute to a change in the total surface charge of the colloids.

Through the use of aromatic additives, the structural homogeneity of samples increased in all cases and in four cases above 90%. This measure of monodispersity is on par with what is required to achieve superlattices from nanoscale building blocks, including the recent demonstration of assembly from CdS octopods.¹⁹ Thus, simple gravitational sedimentation experiments were undertaken to evaluate the feasibility for assembly. Shown in **Figure 5.2** are typical low-magnification SEM images of octopods prepared by dropcasting and drying a concentrated solution of octopods as a colloidal solution on a silicon wafer followed by a wash with methanol. Consistent with our percent yield calculations, samples prepared without aromatic additives (**Figure 5.2A,B**) only partially self-assembled and had small grain sizes. Assembled samples that were prepared with aromatic additives (**Figure 5.2C-L**) had grain sizes that can exceed $3 \mu\text{m}^2$. Although these assembled grain sizes are smaller than the $10 \mu\text{m}^2$ grains of assembled Au nanorods, large grain sizes for octopodal nanocrystals assemblies has not yet been claimed.^{8, 14} For example, shown in **Figure 5.2C** is an SEM image of octopods prepared with 3-methylsalicylic acid after they have assembled into a $\sim 2 \mu\text{m}^2$ supercrystal that contains only a few void and substitutional defects.

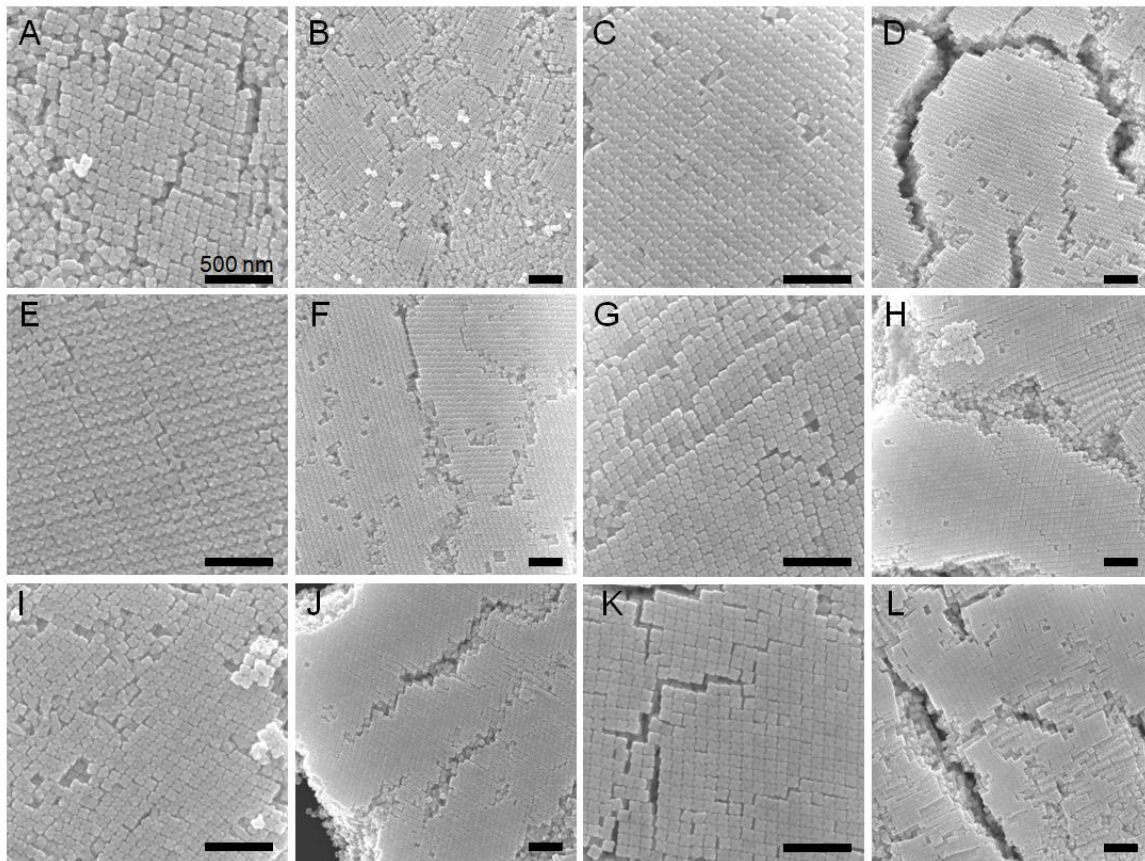


Figure 5.2. SEM images at two magnifications of assemblies of Au/Pd octopods prepared (A,B) without additives and with (C,D) 3-methylsalicylic acid, (E,F) sodium salicylate, (G,H) 2, 6-dihydroxybenzoic acid, (I,J) 5-bromosalicylic acid, and (K,L) 5-aminosalicylic acid at optimized conditions. All scale bars are 500 nm.

As observed in **Figure 5.2**, the organization of octopods into superlattice assemblies depends upon the shape characteristics of the sample, from the assembly of octopods with branches interlocked shown in **Figure 5.2C** to the almost simple cubic crystal structure of the assembly shown in **Figure 5.2I**. Dijkstra and coworkers have computed the assembly of octopods with cylinder-like branches using a Floppy Box Monte Carlo algorithm.^{8, 20-22} From these models and experimental results of CdSe@CdS

octopods, they were able to generate a phase diagram depicting the relationship between the ratio of octopod length to diameter and its packing volume fraction.⁸ Particles with wide, short branches packed in a rhombic crystal but particles with long, thin branches could pack in a simple cubic, or if the branches are sufficiently long and thin, a body-centered cubic crystal. Here, octopods with short, wide arms also similarly pack in a rhombic crystal (**Figure 5.2E**). However, our measured X/Y of octopods that pack in a rhombic crystal (3.5) is below the X/Y maxima for CdSe octopods packing in a similar structure (4.8) and could be accounted for by subtle structural differences. In addition, we found that all of the Au/Pd octopods assemble into superstructures with rhombic symmetry regardless of the structural features of the building blocks. We attribute some of these differences to the structure of the octopods themselves, as the Au/Pd octopods taper to the tip and therefore may not be universally consistent with a system that is modeled with cylindrical branches.

Table 5.1 shows the calculated lattice offset from a (100) cubic face to a rhombic face, as defined in **Scheme 5.1C**. An example measurement used to calculate lattice offset is shown in **Figure S5.12**. Octopods prepared with 3-methylsalicylic acid (**Figure 5.2C,D**) and sodium salicylate (**Figure 5.2K,L**) – those with the relatively long, thin branches – had the largest lattice offset at ~33%. Contrastingly, octopods prepared with 5-aminosalicylic acid (**Figure 5.2I,J**) – octopods that appear more “cube-like” as they have relatively short branches, wide interior branch lengths, and thin tips – have only a 9% offset and are therefore closer to a basic cubic crystal structure. We therefore conclude that the interior branch width and tip width are important factors for determining whether branch arms can interlock and thus provide greater lattice offset.

Upon first examination of the supercrystals, one may interpret that different packing arrangements of the building blocks are achieved as the surface terminations of the different domains often appear different. For example, dropcasted arrays of Au/Pd octopods prepared with 5-aminosalicylic acid, which packs closely to cubic crystal symmetry, have multiple surface-terminated arrangements. Three domains are circled in an SEM image after such assembly (**Figure 5.3A**). The branches are positioned with four facing toward and four away from the substrate (**Figure 5.3B**), two facing toward, four parallel, and two away from the substrate (**Figure 5.3G**), or one facing toward, six parallel, and one away from the substrate (**Figure 5.3L**). However, these different surface expressions arise from the same packing arrangement of octopods; the superstructures are just positioned differently on the underlying Si substrate. For example, if each building block octopod were represented by a sphere and the crystal structure of the blocks were assumed to be cubic, the surface arrangements in **Figures 5.3B, G, and L** would correspond to the low-index facets (100), (110), and (111), respectively. Corresponding models show the arrangement of octopods in (100) (**Figure 5.3C-F**), (110) (**Figure 5.3H-K**), and (111) (**Figure 5.3M-P**) surfaces, assuming cubic symmetry. As shown in the SEM image of a (100) face of assembled octopods in **Figure 5.3B** and the models in **Figure 5.3C-F**, four branches point toward the substrate while four point away from the substrate. The (100) face is the most commonly observed facet, which we believe is because this orientation provides the greatest structural stability as four branches per particle rest on the substrate underlying for the first crystal layer. Significantly, these images show for the first time that stellated noble metal structures can assemble with their sharp tips pointing towards one another, which should facilitate strong plasmonic

coupling between two or more adjacent nanoparticles.²³ This feature may provide ensembles of branched nanostructures with “hot spots” of similar size and intensity. The optical properties of plasmonic nanocrystal ensembles, including electromagnetic “hot spots” and bulk electromagnetic resonances, are dependent upon both the spacing and packing arrangement of the superstructure as well as the structural features of the individual components.⁶ Chapter 4 demonstrated that octopods have size-dependent localized surface plasmon resonances (LSPRs).²⁴ Now, efforts are underway to achieve octopodal assemblies on the order of 6-10 μm^2 from in order to systematically investigate how building block structure, assembly, and composition couple to their dark field scattering.

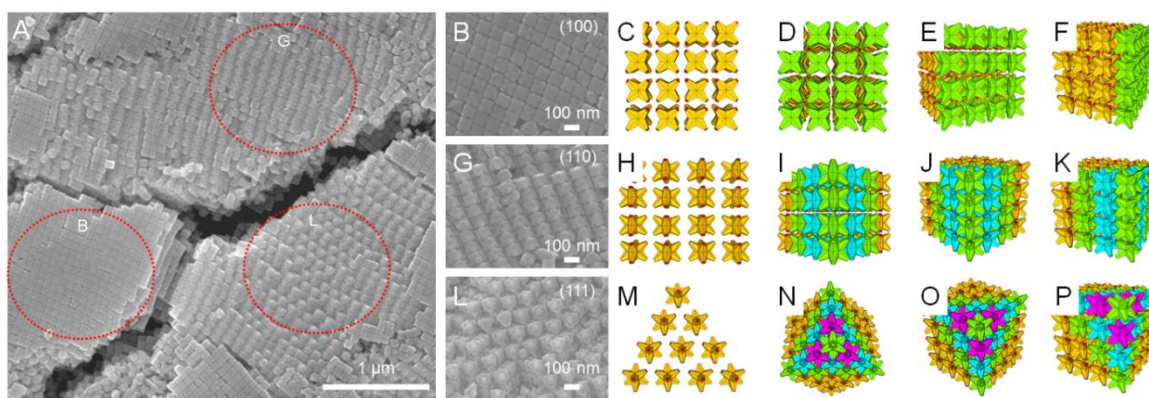


Figure 5.3. (A) SEM image of an assembly of Au/Pd octopods prepared with 5-aminosalicylic acid where red circles highlight different orientations of the supercrystal assembly, (B, G, and L) SEM images of Au/Pd octopods with the (100), (110), and (111) faces, respectively, expressed (assuming cubic crystal symmetry), (C, H, and M) models of the (100), (110), and (111) surfaces, respectively, of an assembly of Au/Pd octopods, (D-F,I-K, and N-P) models that show how the (100), (110), and (111) surfaces are arranged in relation to the larger supercrystal structure.

5.3 Conclusions

Samples of Au/Pd octopods with high homogeneity and tailorable structural features were synthesized through the addition of aromatic additives to seed-mediated co-reduction. Sample homogeneity improved upon the addition of aromatic additives. These structural changes and improvements to homogeneity can be attributed to the interaction of the aromatic additives to the Au and Pd surfaces during nanoparticle growth. Higher sample homogeneity allowed for larger regions of uniform self-assembly. Although the rhombic crystal structure was preserved for all samples, octopods with thinner, longer branches had a greater degree of interlocked branches while the more “cube-like” octopods with short branches that are thin at the tip and wide near the center had very little interlocking and thus packed in an almost cubic supercrystal structure. Supercrystals of octopods were found to express a range of facets – including (100), (110), and (111) – with each surface having a different arrangement of branches extruding from the surface. This work provides an important step in achieving tailored assembly of branched structures onto substrates, with the potential to impact the construction of nano-devices for chemical sensing and detection.

5.4 References

1. DeSantis, C. J.; Sue, A. C.; Radmilovic, A.; Liu, H.; Losovyj, Y. B.; Skrabalak, S. E., Shaping the Synthesis and Assembly of Symmetrically Stellated Au/Pd Nanocrystals with Aromatic Additives. *Nano Lett.* **2014**, *14*, 4145-4150.
2. Motl, N. E.; Smith, A. F.; DeSantis, C. J.; Skrabalak, S. E., Engineering plasmonic metal colloids through composition and structural design. *Chem. Soc. Rev.* **2014**, *43*, 3823-3834.

3. DeSantis, C. J.; Weiner, R. G.; Radmilovic, A.; Bower, M. M.; Skrabalak, S. E., Seeding Bimetallic Nanostructures as a New Class of Plasmonic Colloids. *J. Phys. Chem. Lett.* **2013**, *4*, 3072-3082.
4. Peng, B.; Li, G.; Li, D.; Dodson, S.; Zhang, Q.; Zhang, J.; Lee, Y. H.; Demir, H. V.; Yi Ling, X.; Xiong, Q., Vertically Aligned Gold Nanorod Monolayer on Arbitrary Substrates: Self-Assembly and Femtomolar Detection of Food Contaminants. *ACS Nano* **2013**, *7*, 5993-6000.
5. Hao, F.; Nehl, C. L.; Hafner, J. H.; Nordlander, P., Plasmon Resonances of a Gold Nanostar. *Nano Lett.* **2007**, *7*, 729-732.
6. Tao, A. R.; Ceperley, D. P.; Sinsermsuksakul, P.; Neureuther, A. R.; Yang, P., Self-Organized Silver Nanoparticles for Three-Dimensional Plasmonic Crystals. *Nano Lett.* **2008**, *8*, 4033-4038.
7. Henzie, J.; Gruenwald, M.; Widmer-Cooper, A.; Geissler, P. L.; Yang, P., Self-assembly of uniform polyhedral silver nanocrystals into densest packings and exotic superlattices. *Nat. Mater.* **2012**, *11*, 131-137.
8. Qi, W.; Graaf, J. d.; Qiao, F.; Marras, S.; Manna, L.; Dijkstra, M., Ordered Two-Dimensional Superstructures of Colloidal Octapod-Shaped Nanocrystals on Flat Substrates. *Nano Lett.* **2012**, *12*, 5299-5303.
9. Miszta, K.; de Graaf, J.; Bertoni, G.; Dorfs, D.; Brescia, R.; Marras, S.; Ceseracciu, L.; Cingolani, R.; van Roij, R.; Dijkstra, M.; Manna, L., Hierarchical self-assembly of suspended branched colloidal nanocrystals into superlattice structures. *Nat Mater* **2011**, *10*, 872-876.

10. DeSantis, C. J.; Sue, A. C.; Bower, M. M.; Skrabalak, S. E., Seed-Mediated Co-reduction: A Versatile Route to Architecturally Controlled Bimetallic Nanostructures. *ACS Nano* **2012**, *6*, 2617-2628.
11. DeSantis, C. J.; Skrabalak, S. E., Core Values: Elucidating the Role of Seed Structure in the Synthesis of Symmetrically Branched Nanocrystals. *J. Am. Chem. Soc.* **2012**, *135*, 10-13.
12. Teng, X.; Yang, H., Synthesis of Platinum Multipods: An Induced Anisotropic Growth. *Nano Lett.* **2005**, *5*, 885-891.
13. Nikoobakht, B.; El-Sayed, M. A., Preparation and Growth Mechanism of Gold Nanorods (NRs) Using Seed-Mediated Growth Method. *Chem. Mater.* **2003**, *15*, 1957-1962.
14. Ye, X.; Jin, L.; Caglayan, H.; Chen, J.; Xing, G.; Zheng, C.; Doan-Nguyen, V.; Kang, Y.; Engheta, N.; Kagan, C. R.; Murray, C. B., Improved Size-Tunable Synthesis of Monodisperse Gold Nanorods through the Use of Aromatic Additives. *ACS Nano* **2012**, *6*, 2804-2817.
15. Murphy, C. J.; Thompson, L. B.; Alkilany, A. M.; Sisco, P. N.; Boulos, S. P.; Sivapalan, S. T.; Yang, J. A.; Chernak, D. J.; Huang, J., The Many Faces of Gold Nanorods. *J. Phys. Chem. Lett.* **2010**, *1*, 2867-2875.
16. Ye, X.; Gao, Y.; Chen, J.; Reifsnnyder, D. C.; Zheng, C.; Murray, C. B., Seeded Growth of Monodisperse Gold Nanorods Using Bromide-Free Surfactant Mixtures. *Nano Lett.* **2013**.
17. Scarabelli, L.; Grzelczak, M.; Liz-Marzán, L. M., Tuning Gold Nanorod Synthesis through Prereduction with Salicylic Acid. *Chem. Mater.* **2013**, *25*, 4232-4238.

18. Chiu, C.-Y.; Wu, H.; Yao, Z.; Zhou, F.; Zhang, H.; Ozolins, V.; Huang, Y., Facet-Selective Adsorption on Noble Metal Crystals Guided by Electrostatic Potential Surfaces of Aromatic Molecules. *J. Am. Chem. Soc.* **2013**, *135*, 15489-15500.
19. Miszta, K.; de Graaf, J.; Bertoni, G.; Dorfs, D.; Brescia, R.; Marras, S.; Ceseracciu, L.; Cingolani, R.; van Roij, R.; Dijkstra, M.; Manna, L., Hierarchical self-assembly of suspended branched colloidal nanocrystals into superlattice structures. *Nat. Mater.* **2011**, *10*, 872-876.
20. de Graaf, J.; van Roij, R.; Dijkstra, M., Dense Regular Packings of Irregular Nonconvex Particles. *Phys. Rev. Lett.* **2011**, *107*, 155501.
21. Qi, W.; de Graaf, J.; Qiao, F.; Marras, S.; Manna, L.; Dijkstra, M., Phase diagram of octapod-shaped nanocrystals in a quasi-two-dimensional planar geometry. *J. Chem. Phys.* **2013**, *138*, 15404.
22. de Graaf, J.; Filion, L.; Marechal, M.; van Roij, R.; Dijkstra, M., Crystal-structure prediction via the Floppy-Box Monte Carlo algorithm: Method and application to hard (non)convex particles. *J. Chem. Phys.* **2012**, *137*, 214101.
23. Shao, L.; Woo, K. C.; Chen, H.; Jin, Z.; Wang, J.; Lin, H.-Q., Angle- and Energy-Resolved Plasmon Coupling in Gold Nanorod Dimers. *ACS Nano* **2010**, *4*, 3053-3062.
24. DeSantis, C. J.; Skrabalak, S. E., Size-Controlled Synthesis of Au/Pd Octopods with High Refractive Index Sensitivity. *Langmuir* **2012**, *28*, 9055-9062.

Chapter 6: Summary and Outlook

6.1 Summary of Chapters 2-5

The seed-mediated method is typically used to deposit one metal on top of seeds. Chapter 2 demonstrated the possibility of seed-mediated co-reduction wherein two metal precursors are simultaneously reduced to deposit two metals onto seeds.¹ This new synthetic strategy enabled the deposition of bimetallic alloyed shells, with the shape of the seeds being transferred to that of the shells.² The kinetics of seeded growth can also be manipulated by the co-reduction technique itself, and they provide a means of morphological control. Of particular interest was the synthesis of symmetrically branched Au/Pd nanostructures such as octopods, which have eight branches that proceed along $\langle 111 \rangle$ directions and O_h symmetry. Structural parameters such as branch length and tip thickness can be easily controlled via the synthetic conditions.² For example, as shown in Section 2.4, the use of low concentrations of Pd precursor relative to Au precursor during the co-reduction step results in octopods with very sharp tips; increasing the amount of Pd precursor relative to Au precursor results in a broadening of the tips and the expression of $\{111\}$ facets.

Chapter 3 demonstrated that seed structure itself can dictate the branching symmetry.³ This correlation between seed shape and branching symmetry was verified by establishing a TEM-label approach analogous to the use of fluorophores with confocal microscopy, where the Au-Pd nanostructure was built from shape-controlled Pd seeds that provide a compositional boundary between the seeds and overgrowth metals. This boundary can be roughly imaged by STEM-EDX mapping. Through the study of differently shaped nanocrystals, the relationships between seed and concave nanocrystal

symmetry are being established to provide design criteria for new mono- and bimetallic plasmonic colloids, including those with more robust optical properties.

Chapter 4 demonstrated the ability to control the size of the octopods by varying the amount of metal to be deposited relative to the number of seeds.⁴ Larger octopods are achieved when more metal is available to be deposited per seed. In addition, Chapter 4 investigated the optical properties of Au/Pd octopodal ensembles with seven different average sizes.⁵ A positive linear correlation between branch length and the LSPR maximum wavelength was found. When defining the aspect ratio of an octopod as its branch length divided by the tip thickness, a red shift in the LSPR maximum wavelength was observed with decreasing aspect ratio. This trend is the inverse to what is observed with Au nanorods. The origin of this observation is currently unclear but may arise on account of the tapered nature of the octopodal branches or variations in the Pd distribution as a function of particle size. The sensitivity of the Au/Pd octopods to changes in RI was also examined and found to be very large. For example, a sensitivity of 550 nm/RI unit was measured for octopods with a starting LSPR in water of 730 nm. A modest FOM (2) for ensemble measurements was obtained. These results indicate that Au–Pd nanostructures excel over their monometallic analogues in terms of their response to changes in RI, which, in turn, should enable the design of more sensitive RI probes. Chapter 4 also discussed the design of nanostructures with multiple architectural features—branches and hollow interiors—through a selective etching process.⁴ Collectively, the results shown in Chapter 4 demonstrate that the size, shape, and composition of branched Au/Pd nanostructures can be manipulated and, in turn, so can their optical properties.

Finally, Chapter 5 highlights the improvement of sample homogeneity through the use of aromatic additives with seed-mediate co-reduction.⁶ Improved sample homogeneity allowed for large-scale self-assembly, which in turn could provide for uniform platforms for nanosensing.

6.2 Outlook⁷

New applications for plasmonic colloids that capitalize on the bimetallic composition can now be envisioned. For example, Tang et al. demonstrated hydrogen storage and sensing from Au@Pd nanocrystals. In this system, a change in the optical properties of the nanocrystals was correlated with a change in the RI of the Pd shell upon hydride formation.⁸ It should be noted that many of these Au–Pd nanostructures were also evaluated as platforms for SERS with model adsorbates. Enhancements were typically observed compared to analysis of the molecules in the absence of any nanostructures, although the signal intensity was less than that in the presence of Au-only structures. For example, Zhang et al. found that 63 nm Au nanobars with an aspect ratio of 4 provided a SERS enhancement factor of 1.5×10^3 , whereas 66 nm Au@Pd nanobars with a 1.1 nm Pd shell provided a SERS enhancement factor of 2.3×10^2 for rhodamine 6G with an incident laser wavelength of 785 nm.⁹ These results further indicate that Au–Pd nanostructures may be useful platforms for studying Pd-specific surface chemistry via plasmon-enhanced surface spectroscopies. This consideration is made feasible given the advances noted in this thesis with seed-mediated co-reduction to enable the synthesis of symmetrically branched Au/Pd nanocrystals with sharp tips.

Opportunities are emerging from the study of bimetallic nanostructures and their optical properties. Central to these advances in colloidal plasmonics is the demonstration of new synthetic strategies toward architecturally controlled bimetallic nanostructures. Through the use of seed-mediated synthetic methods, it is now possible to control the spatial distribution of metals in bimetallic nanostructures to achieve heterostructures, core@shell nanocrystals, and shape-controlled alloyed particles. These innovations in synthesis are enabled by manipulation of the kinetic and thermodynamic parameters that govern nanostructure formation and, in particular, the selection of reagents such as capping agents and metal precursors. Such advances are highlighted in recent reviews by Niu et al. and Zhang et al. and are now being applied to new compositions.^{10, 11} Interest in multifunctional nanostructures composed of Ag–Pd, Ag–Pt, and Au–Pt is increasing, and the optical properties of such structures are anticipated to be similar to the Au–Pd examples discussed here. Research in colloidal plasmonics is even moving beyond bimetallic compositions, with seed-mediated methods being used to generate structurally defined trimetallic nanostructures. For example, Yu et al. controlled the localization and direction of both Ag and Pd overgrown on {111} and/or {100} terminated Au nanoparticles by manipulating the order and rate at which Ag and Pd deposited onto the seed crystals.¹¹ Many branched and concave structures were achieved, opening the door for optical studies of trimetallic nanostructures.

Finally, it may be worthwhile to move beyond noble metal systems and take advantage of more cost-effective and abundant materials. Copper is of particular interest for non-noble metal plasmonics because it has a λ_{max} between Au and Ag and a narrower fwhm, as revealed by the study of similarly sized triangular particles prepared by

nanosphere lithography.¹² As Cu readily oxidizes, incorporating a second metal is often necessary in order to take advantage of the plasmonic properties of Cu, and the seeded method is providing improved shape control of nanostructures containing Cu. For example, Jin et al. achieved epitaxial growth of Cu onto Pd nanocubes and octahedra despite their large lattice mismatch through the use of hexadecylamine as a stabilizing agent.¹³ Chen et al. also recently demonstrated the synthesis of Cu-containing bimetallic nanostructures with tunable optical properties via seed-mediated co-reduction.¹⁴ In this system, co-reduction provides heterogeneous nucleation and growth of both metal components to form Cu₃Au, CuAu, Cu₃Pt, or Cu₃Pd nanorods with tunable aspect ratios. In turn, these structures have LSPRs that can be tuned from 300 to 800 nm by the modification of composition and aspect ratio. On the horizon, softer and more electronegative metals such as Al, Ga, In, Sn, Tl, Pb, and Bi (termed “poor metals”) are being explored as alternatives to Au and Ag.¹⁵ These poor metals, as 20–200 nm nanoparticles, were found through calculations based on Mie theory to have LSPRs in the ultraviolet and visible regions, where they could be used as SERS biochemical sensors. For example, the LSPRs of triangular Al nanoparticles fabricated by nanosphere lithography can be tuned from 390 to 810 nm by increasing their in-plane size.¹⁶ This size control was achieved by increasing the size of the colloids used to create the nanosphere mask. Ga nanoparticles have also been shown to provide SERS enhancement factors as high as 10⁷ for crystal violet as a model adsorbate when excited at 325 nm.¹⁷ The main challenge to utilizing these metals is the lack of synthetic strategies that provide structural control on par with that of the colloids based on noble metals. Seeded methods may

facilitate the incorporation of one of these poor metals while increasing functionality and maintaining low cost for colloidal plasmonic platforms.

Analytical techniques in development are providing greater insight into the optical properties of bimetallic nanostructures as well. Atomic-resolution STEM resolves interfacial boundaries between two compositions, providing precise knowledge of each metal component within a nanoparticle.¹⁸⁻²⁰ Nanoelectron diffraction can determine faceting of nanostructures and can be useful for developing complete descriptions of nanostructures with complex geometries.²¹ With insight into the finer details of composition and structure for bimetallic nanoparticles, accurate modeling could be undertaken to predict how the interactions between each metal component contribute to the overall LSPRs. Thus far, accurately modeling bimetallic systems is difficult when the two metals mix because a simple linear combination of the two dielectric constants based on nanostructure composition has proven insufficient.²²

Moreover, single-particle spectroscopic techniques are rapidly developing to provide useful insight into the optical characteristics of nanostructures.²³ Typically, the light scattering or absorption properties of an individual nanoparticle are obtained. These properties are then correlated with its structure, which is obtained by high-resolution electron microscopy through the use of registered substrates.²⁴ This technique represents a premier means of studying the size and shape dependence of the LSPR for metal nanostructures. Also, the near-field properties of metal nanostructures can be examined with high spatial (1 nm) and energy resolution (0.1–0.3 eV) using electron energy loss spectroscopy (EELS) in conjunction with STEM.²⁵ This technique is helping to elucidate the location and nature of the plasmonic “hot spots” that are implicated in single-

molecule level detection via plasmon-enhanced spectroscopies. Furthermore, STEM/EELS can provide information about the composition of bimetallic nanostructures and should facilitate a greater understanding of how composition contributes to the plasmonic properties of emerging nanostructures. We note, however, that this technique is inappropriate for noble metals. Overall, analytical techniques are advancing in parallel to the progress of nanoparticle synthesis. There is still a need for better application of these techniques to new nanostructures. Due to their inherent added complexity, bimetallic systems can pose a greater challenge in characterization, and new techniques may need to be developed to provide the depth necessary to understand the structure and properties of bimetallic nanoparticles in sufficient detail.

Together, these advances in synthesis and nanomaterial characterization are giving better insight into the relationship between metal species in bimetallic nanoparticle systems and their optical properties. Improved theoretical models as well as systematic experimental studies should provide the needed details to establish structure–property relationships, which will in turn guide plasmonic-based synthesis and applications. Although much of the current work is still focused on establishing these relationships, in the future, designing nanostructures with desired plasmonic features and functionality from basic principles should be possible.²⁶ This transition from “explore” to “design” will allow for wider implementation of colloidal plasmonic platforms in industrial or medical settings. Overall, a bright future exists for bimetallic nanostructures in colloidal plasmonics, considering the diversity of compositions available and recent advances in synthesis, theory, and nanomaterials characterization.

6.3 References

1. DeSantis, C. J.; Peverly, A. A.; Peters, D. G.; Skrabalak, S. E., Octopods versus Concave Nanocrystals: Control of Morphology by Manipulating the Kinetics of Seeded Growth via Co-Reduction. *Nano Lett.* **2011**, *11*, 2164-2168.
2. DeSantis, C. J.; Sue, A. C.; Bower, M. M.; Skrabalak, S. E., Seed-Mediated Co-reduction: A Versatile Route to Architecturally Controlled Bimetallic Nanostructures. *ACS Nano* **2012**, *6*, 2617-2628.
3. DeSantis, C. J.; Skrabalak, S. E., Core Values: Elucidating the Role of Seed Structure in the Synthesis of Symmetrically Branched Nanocrystals. *J. Am. Chem. Soc.* **2012**, *135*, 10-13.
4. DeSantis, C. J.; Skrabalak, S. E., Manipulating the optical properties of symmetrically branched Au/Pd nanocrystals through interior design. *Chem. Commun.* **2014**, DOI: 10.1039/C3CC48441F.
5. DeSantis, C. J.; Skrabalak, S. E., Size-Controlled Synthesis of Au/Pd Octopods with High Refractive Index Sensitivity. *Langmuir* **2012**, *28*, 9055-9062.
6. DeSantis, C. J.; Sue, A. C.; Radmilovic, A.; Liu, H.; Losovyj, Y. B.; Skrabalak, S. E., Shaping the Synthesis and Assembly of Symmetrically Stellated Au/Pd Nanocrystals with Aromatic Additives. *Nano Lett.* **2014**, *14*, 4145-4150.
7. DeSantis, C. J.; Weiner, R. G.; Radmilovic, A.; Bower, M. M.; Skrabalak, S. E., Seeding Bimetallic Nanostructures as a New Class of Plasmonic Colloids. *J. Phys. Chem. Lett.* **2013**, *4*, 3072-3082.

8. Tang, M. L.; Liu, N.; Dionne, J. A.; Alivisatos, A. P., Observations of Shape-Dependent Hydrogen Uptake Trajectories from Single Nanocrystals. *J. Am. Chem. Soc.* **2011**, *133*, 13220-13223.
9. Zhang, K.; Xiang, Y.; Wu, X.; Feng, L.; He, W.; Liu, J.; Zhou, W.; Xie, S., Enhanced Optical Responses of Au@Pd Core/Shell Nanobars. *Langmuir* **2008**, *25*, 1162-1168.
10. Niu, W.; Zhang, L.; Xu, G., Seed-mediated growth of noble metal nanocrystals: crystal growth and shape control. *Nanoscale* **2013**, *5*, 3172-3181.
11. Zhang, H.; Jin, M.; Xiong, Y.; Lim, B.; Xia, Y., Shape-Controlled Synthesis of Pd Nanocrystals and Their Catalytic Applications. *Acc. Chem. Res.* **2013**, *46*, 1783-1794.
12. Chan, G. H.; Zhao, J.; Hicks, E. M.; Schatz, G. C.; Van Duyne, R. P., Plasmonic Properties of Copper Nanoparticles Fabricated by Nanosphere Lithography. *Nano Lett.* **2007**, *7*, 1947-1952.
13. Jin, M.; Zhang, H.; Wang, J.; Zhong, X.; Lu, N.; Li, Z.; Xie, Z.; Kim, M. J.; Xia, Y., Copper Can Still Be Epitaxially Deposited on Palladium Nanocrystals To Generate Core-Shell Nanocubes Despite Their Large Lattice Mismatch. *ACS Nano* **2012**, *6*, 2566-2573.
14. Chen, S.; Jenkins, S. V.; Tao, J.; Zhu, Y.; Chen, J., Anisotropic Seeded Growth of Cu-M (M = Au, Pt, or Pd) Bimetallic Nanorods with Tunable Optical and Catalytic Properties. *J. Phys. Chem. C* **2013**, *117*, 8924-8932.
15. McMahon, J. M.; Schatz, G. C.; Gray, S. K., Plasmonics in the ultraviolet with the poor metals Al, Ga, In, Sn, Tl, Pb, and Bi. *Phys. Chem. Chem. Phys.* **2013**, *15*, 5415-5423.

16. Chan, G. H.; Zhao, J.; Schatz, G. C.; Van Duyne, R. P., Localized Surface Plasmon Resonance Spectroscopy of Triangular Aluminum Nanoparticles. *J. Phys. Chem. C* **2008**, *112*, 13958-13963.
17. Yang, Y.; Callahan, J. M.; Kim, T.-H.; Brown, A. S.; Everitt, H. O., Ultraviolet Nanoplasmonics: A Demonstration of Surface-Enhanced Raman Spectroscopy, Fluorescence, and Photodegradation Using Gallium Nanoparticles. *Nano Lett.* **2013**, *13*, 2837-2841.
18. Khanal, S.; Casillas, G.; Velazquez-Salazar, J. J.; Ponce, A.; Jose-Yacaman, M., Atomic Resolution Imaging of Polyhedral PtPd Core–Shell Nanoparticles by Cs-Corrected STEM. *J. Phys. Chem. C* **2012**, *116*, 23596-23602.
19. Nguyen, V. L.; Ohtaki, M.; Matsubara, T.; Cao, M. T.; Nogami, M., New Experimental Evidences of Pt–Pd Bimetallic Nanoparticles with Core–Shell Configuration and Highly Fine-Ordered Nanostructures by High-Resolution Electron Transmission Microscopy. *J. Phys. Chem. C* **2012**, *116*, 12265-12274.
20. Sanchez, S. I.; Small, M. W.; Zuo, J.-m.; Nuzzo, R. G., Structural Characterization of Pt–Pd and Pd–Pt Core–Shell Nanoclusters at Atomic Resolution. *J. Am. Chem. Soc.* **2009**, *131*, 8683-8689.
21. Shah, A. B.; Sivapalan, S. T.; DeVetter, B. M.; Yang, T. K.; Wen, J.; Bhargava, R.; Murphy, C. J.; Zuo, J.-M., High-Index Facets in Gold Nanocrystals Elucidated by Coherent Electron Diffraction. *Nano Lett.* **2013**, *13*, 1840-1846.
22. Lu, X.; Rycenga, M.; Skrabalak, S. E.; Wiley, B.; Xia, Y., Chemical Synthesis of Novel Plasmonic Nanoparticles. *Annu. Rev. Phys. Chem.* **2009**, *60*, 167-192.

23. Ringe, E.; Sharma, B.; Henry, A.-I.; Marks, L. D.; Van Duyne, R. P., Single nanoparticle plasmonics. *Phys. Chem. Chem. Phys.* **2013**, *15*, 4110-4129.
24. Slaughter, L.; Chang, W.-S.; Link, S., Characterizing Plasmons in Nanoparticles and Their Assemblies with Single Particle Spectroscopy. *J. Phys. Chem. Lett.* **2011**, *2*, 2015-2023.
25. Iberi, V.; Mirsaleh-Kohan, N.; Camden, J. P., Understanding Plasmonic Properties in Metallic Nanostructures by Correlating Photonic and Electronic Excitations. *J. Phys. Chem. Lett.* **2013**, *4*, 1070-1078.
26. Odom, T. W.; Nehl, C. L., How Gold Nanoparticles Have Stayed in the Light: The 3M's Principle. *ACS Nano* **2008**, *2*, 612-616.

Appendix A: Experimental

A1.1 Note Regarding Experimental in Noble Metal Nanoparticle Synthesis

In some procedures (such as A2.2) seed solutions were not collected by centrifugation prior to use. For those cases, the solution was used as a growth medium during seed-mediated co-reduction. For other procedures (such as A3.2) the seeds were collected by centrifugation, concentrated, and added to another growth solution for seed-mediated co-reduction. As the growth solution for Au@Au/Pd octopods is similar in both cases, the direct-deposition approach is often used for its ease. The two-pot synthetic protocol is most often used when the growth solution for the seeds is modified.

Chapter 2

A2.2 Synthesis of Octopods and Concave Nanocrystals

A2.2.1 Chemicals

Ascorbic acid (L-aa, C₆H₈O₆, 99%), palladium(II) chloride (PdCl₂, 99.98%), chloroauric acid (HAuCl₄·3H₂O, 99.9%), cetyltrimethylammonium bromide (CTAB, 98%), sodium tetrachloropalladate (Na₂PdCl₄, 98%), and sodium borohydride (NaBH₄) were used as purchased from Sigma Aldrich. Formic acid (90% in water) was purchased from J. T. Baker. Nanopure water was used in all experiments. A 10 mM H₂PdCl₄ solution was prepared by heating at ~40 °C and stirring dissolved PdCl₂ (44.5 mg) in 25 mL of HCl (0.1 M) for one hour.

A2.2.2 Gold Nanoparticle Seeds

To make the initial Au seeds, 4 mL of H₂O and then 1 mL of HAuCl₄ (2.5 mM) solution were added to 5 mL of CTAB (150 mM) solution in a 30 mL reaction vial. 0.6 mL of ice-cold NaBH₄ (10 mM) solution was added immediately with stirring, forming a clear brown solution. This solution was capped and allowed to stir at room temperature for 3 hours. A 0.3 mL aliquot was then diluted with 29.7 mL of H₂O.

This seed solution can then be used for the synthesis of Au cores. The seeds may be used immediately to prepare Au cores for Au@Pd nanocrystal formation (either convex or concave). Alternatively, the seeds may be aged at room temperature and used after 3 days to prepare Au cores for Au/Pd octopod or concave nanocrystal formation.

A2.2.3 Gold Nanoparticle Cores

To synthesize the Au cores, 0.1 mL of H₂AuCl₄ (10 mM) solution was added to 2 mL of CTAB (0.2 M) solution followed immediately by 1.5 mL of L-aa (0.1 M) solution. This solution was immediately diluted to 25 mL with H₂O followed promptly by adding 0.3 mL of the seed solution. This reaction vial was capped and allowed to sit undisturbed in a 25 °C oil bath for 8 hours.

A2.2.4 Gold/Palladium Nanocrystal Formation For the formation of nanostars (**Figure S2.4B**), octopods (**Figure 2.1A**), and concave nanocrystals (**Figure 2.1D**), the 10 mM H₂PdCl₄ solution was diluted to 0.05 mM, 0.5 mM, and 5.0 mM, respectively, with water. To the entire Au core solution (prepared from aged seeds), 2 mL of the diluted H₂PdCl₄ solution and 0.1 mL of the H₂AuCl₄ (100 mM) solution are simultaneously added via separate pipettes, followed promptly by the addition of 0.5 mL of L-aa (0.1 M) solution. The reaction vial was capped and allowed to sit undisturbed in a 25 °C oil bath for 30 minutes. For the formation of convex Au@Pd nanocrystals (**Figure 2.3A**), 2 mL of the 0.5 mM H₂PdCl₄ solution and 0.1 mL of the H₂AuCl₄ (100 mM) solution were simultaneously added via separate pipettes to the freshly prepared Au core solution, followed by the addition of 0.5 mL of L-aa (0.1 M) solution.

A2.2.5 Characterization

Images of the nanoparticles were taken via a JEOL JEM 1010 Transmission Electron Microscope (TEM) with a ROM CCD camera and on a FEI Quanta 600F Environmental Scanning Electron Microscope (SEM) operated at 30 kV and a spot size of 3. Composition of nanoparticles was determined with an Oxford INCA Energy Dispersive

X-Ray operated at 30 kV. High-resolution images were taken on a JEOL JEM 3200FS Transmission Electron Microscope at 300 kV and a spot size of 1 with a Gatan 4k x 4k Ultrascan 4000. Energy dispersive X-ray spectra were obtained with an Oxford INCA Dispersive X-ray system interfaced to the JEM 3200FS TEM, operating at 300 kV. Samples for TEM analysis were prepared by drop-casting a dispersed particle solution onto a carbon-coated copper grid and then washing the grid twice with H₂O. Samples for SEM and EDX analysis were prepared by drop-casting a dispersed particle solution onto a silicon wafer and then washing the wafer twice with methanol after initial solvent evaporation. The optical properties of various samples were measured with a Varian CARY 5000 Bio UV-Visible Spectrophotometer, using a quartz cuvette and a background scan of water.

A2.2.6 Electrochemical Catalysis

Electrochemical measurements were performed on an Obbligato & Objectives, Inc. Faraday MP system scanning from -0.2 to 1.0 to -0.2 V at a rate of 50 mV s⁻¹. A three-electrode cell was used with Ag/AgCl as the reference electrode and a platinum wire as the counter electrode. Samples of the Au/Pd octopods or concave nanocrystals were shaken until evenly dispersed in water and then 10.0 μL of this mixture was added dropwise to a glassy carbon electrode (area = 0.077 cm²) and allowed to dry under ambient conditions. For all experiments, the electrolyte solution, 0.1 M H₂SO₄ in nanopure water was sparged with argon for 10 min before an experiment

A2.3 The Role of Synthetic Parameters in the Seed-Mediated Co-Reduction of Shape-Controlled Au/Pd Nanostructures

A2.3.1 Chemicals

L-aa ($C_6H_8O_6$, 99%), palladium(II) chloride ($PdCl_2$, 99.98%), chloroauric acid ($HAuCl_4 \cdot 3H_2O$, 99.9%), CTAB (98%, lot #'s: 050M01711 V and 120M01411 V), cetyltrimethylammonium chloride (CTAC, 0.78M, lot #'s: MKBB4924 and STBC2574), sodium chloride ($NaCl$, 99%), potassium bromide (KBr , 99%), and sodium borohydride ($NaBH_4$, 98.5%) were used as purchased from Sigma Aldrich. Sodium hydroxide ($NaOH$, 97%) was used as purchased from EMD. Aqueous, concentrated hydrochloric acid (12.1M) was purchased from Mallinckrodt. Nanopure water ($18.2 M\Omega \cdot cm$) was used in all experiments. An aqueous 10 mM H_2PdCl_4 solution was prepared by heating at 70 °C and stirring dissolved $PdCl_2$ (44.6 mg) in 25 mL of HCl (pH 1.69) for 1 h.

A2.3.2 Gold Nanoparticle Seeds

See A2.2.2 for the synthesis of Au seeds.

A2.3.3 Gold Nanoparticle Cores

To synthesize the Au cores, 0.1 mL of $HAuCl_4$ (9 mM) solution was added to 2 mL of CTAB (0.2 M) solution followed immediately by 1.5 mL of L-aa (0.1 M) solution. This solution was immediately diluted to 25 mL with H_2O followed promptly by adding 1.0 mL of the seed solution. This reaction vial was capped and allowed to sit undisturbed in a 25 °C oil bath for 24 h.

A2.3.4 Gold–Palladium Nanocrystal Formation

To prepare the various Au–Pd nanocrystals, 2 mL of either water or HCl acid solution (concentration denoted in the text and **Table A2.1**) was added to the entire Au core solution. This procedure was followed by the simultaneous addition via separate pipettes of 2 mL of H_2PdCl_4 and 0.1 mL of HAuCl_4 solution (concentrations denoted in the text and **Table A2.1**). The vials were gently mixed by inversion followed promptly by the addition of 0.5 mL of L-aa (0.1 M) solution. The reaction vial was capped and allowed to sit undisturbed in a 25 °C oil bath for 24 h. It is noted that HCl solutions were prepared by diluting concentrated HCl (12.1 M) to the desired concentration and checking the solution pH (included in **Table S2.2**). The H_2PdCl_4 solution was similarly prepared by dilution of the 10 mM H_2PdCl_4 solution described under A2.3.1.

A2.3.5 Control Experiments with Sodium Chloride or Sodium Hydroxide

NaCl or NaOH was substituted for HCl at the acid addition step using identical concentrations (as denoted in **Table A2.1**). Otherwise, the experimental procedure was identical to that used for Au–Pd nanocrystal formation.

A2.3.6 Hopper-Like Nanocrystal Formation

The Au core solution, as prepared earlier, was spun down by centrifugation, and the supernatant—containing the dissolved CTAB used in preparation—was removed by decantation. The Au cores were then resuspended in water to 1 mL for later use. One

milliliter of a KBr solution (varying concentrations: 0.30, 0.35, 0.40, 0.45, 0.50, and 0.55 M as denoted in the text) was added to a 1 mL solution of 0.4 M CTAC. To this solution were added sequentially 0.1 mL of a 200 mM H₂AuCl₄ solution and 0.2 mL of a 10 mM H₂PdCl₄ solution (Au:Pd = 1:0.1), followed by 1.5 mL of a 0.2 M L-aa solution. Depending on the synthesis, 2 mL of water or 25 mM HCl solution was then added, as denoted in the text. The HCl improved sample homogeneity. Finally, this solution was diluted to 25 mL using Nanopure water, then 1 mL of the core solution was added.

A2.3.7 Characterization

See section 2.2.5.

The optical properties of various samples were measured with a Varian CARY 5000 Bio UV–visible spectrophotometer, using a quartz cuvette and a background scan of water. Samples for powder XRD were deposited on amorphous glass slides and analyzed with Siemens/Bruker D-5000 using Cu K α radiation ($\lambda = 0.15418$ nm).

Table A2.1. The concentration of the reagents added during the overgrowth step.

Au:Pd	reagent concentration (mM)					
1:0.01	Au ^a -50.0	Au-50.0	Au-50.0	Au-50.0	Au-50.0	Au-50.0
	Pd ^b -0.025	Pd-0.025	Pd-0.025	Pd- 0.025	Pd- 0.025	Pd-0.025
	HCl ^c -0.0	HCl-12.5	HCl-25.0	HCl-37.5	HCl-50.0	HCl-62.5
1:0.1	Au-50.0	Au-50.0	Au-50.0	Au-50.0	Au-50.0	Au-50.0
	Pd-0.25	Pd-0.25	Pd-0.25	Pd-0.25	Pd-0.25	Pd-0.25
	HCl-0.0	HCl-12.5	HCl-25.0	HCl-37.5	HCl-50.0	HCl-62.5
1:0.2	Au-50.0	Au-50.0	Au-50.0	Au-50.0	Au-50.0	Au-50.0
	Pd-0.50	Pd-0.50	Pd-0.50	Pd-0.50	Pd-0.50	Pd-0.50
	HCl-0.0	HCl-12.5	HCl-25.0	HCl-37.5	HCl-50.0	HCl-62.5
1:0.5	Au-50.0	Au-50.0	Au-50.0	Au-50.0	Au-50.0	Au-50.0
	Pd-1.25	Pd-1.25	Pd-1.25	Pd-1.25	Pd-1.25	Pd-1.25
	HCl-0.0	HCl-12.5	HCl-25.0	HCl-37.5	HCl-50.0	HCl-62.5
1:1	Au-50.0	Au-50.0	Au-50.0	Au-50.0	Au-50.0	Au-50.0
	Pd-2.50	Pd-2.50	Pd-2.50	Pd-2.50	Pd-2.50	Pd-2.50
	HCl-0.0	HCl-12.5	HCl-25.0	HCl-37.5	HCl-50.0	HCl-62.5
1:2	Au-50.0	Au-50.0	Au-50.0	Au-50.0	Au-50.0	Au-50.0
	Pd-5.0	Pd- 5.0	Pd- 5.0	Pd-5.0	Pd-5.0	Pd-5.0
	HCl-0.0	HCl-12.5	HCl-25.0	HCl-37.5	HCl-50.0	HCl-62.5

a. Au denotes HAuCl₄ (volume added: 0.1 mL)

b. Pd denotes H₂PdCl₄ (volume added: 2.0 mL)

c. Volume added: 2.0 mL

Chapter 3

A3.1 Chemicals

L-aa ($C_6H_8O_6$, 99%), palladium(II) chloride ($PdCl_2$, 99.98%), sodium tetrachloropalladate (Na_2PdCl_4 , 98%), chloroauric acid ($HAuCl_4 \cdot 3H_2O$, 99.9%), CTAB (98%, lot # 120M01411 V), CTAC (0.78 M, lot #'s: MKBB4924 and STBC2574), potassium bromide (KBr, 99%), potassium iodide (KI, 99%), sodium borohydride ($NaBH_4$, 98.5%), and bis(p-sulfonatophenyl) phenylphosphine dihydrate dipotassium salt (BSPP, 97%) were used as purchased from Sigma Aldrich. Citric acid ($C_6H_8O_7$, 99.5%) was used as purchased from VWR BDH. Sodium hydroxide (NaOH, 97%) was used as purchased from EMD. Concentrated hydrochloric acid (HCl, 12.1M) was purchased from Mallinckrodt. Nanopure water ($18.2 M\Omega \cdot cm$) was used in all experiments. An aqueous 10 mM H_2PdCl_4 solution was prepared by stirring dissolved $PdCl_2$ (44.6 mg) in 25 mL of HCl (pH 1.69) for 1 h while heating at $\sim 70^\circ C$.

A3.2 Shape-Controlled Pd Seed Preparation.

Pd seeds were prepared either by a seed-mediated method starting with Au nanoparticles (nanobars, right bipyramids, and cuboctahedra) or through literature protocols (nanocubes, octahedra, and rhombic dodecahedra). Tetrahedral Pd seeds were used as received from Dr. Nanfeng Zheng's research group in Xiamen University (China).

Au Seed Solution: The syntheses of Pd nanobars, right bipyramids, and cuboctahedra require Au seeds (about 20 nm in diameter) described in A2.2.2. The seeds were aged at room temperature and used after 3 days to prepare Pd nanobars, right bipyramids, and cuboctahedra, as described below.

Pd Nanobars: 1.0 mL NaBr (50 mM) solution, 0.1 mL H₂PdCl₄ (10 mM) solution, and 1.5 mL L-aa (0.1 M) solution were added to 1.0 mL CTAC (0.2 M) solution. Then, 21.4 mL water was added followed by 0.1 mL KI (1 mM) solution and 0.3 mL of the Au seed solution. The reaction vial was shaken lightly and left at 25 °C for 24 hours followed by collection of the nanobars via centrifugation for 30 minutes at 3000 RPM. The final volume after redispersing the particles with water was 3 mL.

Pd Right Bipyramids: Pd right bipyramids are an impurity in Pd nanocube syntheses. Samples with larger proportions of Pd right bipyramids were prepared by modifying a Au-nanoparticle mediated synthesis to Pd nanocubes. Specifically, 0.1 mL H₂PdCl₄ (10 mM) solution and 1.5 mL L-aa (0.1 M) solution were added to 2.0 mL CTAB (0.2 M) solution. Then, 21.4 mL water was added followed by 0.3 mL of the Au seed solution. The reaction vial was shaken lightly and left at 25 °C for 24 hours followed by collection of the right bipyramids via centrifugation for 30 minutes at 3000 RPM. The final volume after redispersing the particles with water was 3 mL.

Pd Cuboctahedra: 1.0 mL NaBr (1 M) solution, 0.1 mL H₂PdCl₄ (10 mM) solution, and 1.5 mL L-aa (0.1 M) solution were added to 1.0 mL CTAC (0.2 M) solution. Then, 21.4 mL water was added followed by 1 mL KI (1 mM) solution and 0.3 mL of the Au seed solution. This solution was left at 25 °C for 24 hours and followed by collection of the cuboctahedra by centrifugation for 30 minutes at 3000 RPM. The final volume after redispersing the particles with water was 3 mL.

Pd Nanocubes: Pd nanocubes were prepared by literature protocol.¹ Briefly, 5 mL of H₂PdCl₄ (0.6 mM) solution was added to 5 mL CTAB (10 mM) solution followed by 0.1

mL L-aa (0.1 M) solution. This solution was left at 30 °C for 7 hours followed by collection of the nanocubes via centrifugation for 30 minutes at 3000 RPM. The final volume after redispersing the particles with water was 3 mL.

Pd Octahedra: Pd octahedra were prepared by literature protocol.² Briefly, citric acid (60 mg) and L-aa (60 mg) were added to 8 mL CTAC (100 mM) solution, which was heated to 100 °C. Once at 100 °C, 3 mL of Na₂PdCl₄ (0.20 mM) solution was added. This solution was stirred at 100 °C for 3 hours followed by collection of the octahedra via centrifugation for 30 minutes at 3000 RPM. The particles were redispersed with water and the procedure repeated three more times. The final volume after redispersing the particles with water was 3 mL.

Pd Tetrahedra: Pd tetrahedra were provided by Dr. Nanfeng Zheng's research group at Xiamen University, China.³ In preparation for Au/Pd precursor co-reduction, the tetrahedral nanoparticles were diluted twice. First, 0.01 mL of concentrated Pd tetrahedra was added to 2 mL of water. 1 mL of this solution was then diluted with 4 mL water.

Pd Rhombic Dodecahedra: Pd rhombic dodecahedra seeds were prepared following literature protocol. Briefly, 1.00 mL of H₂PdCl₄ (10.0 mM) was added to 20.0 mL CTAB (12.5 mM) and heated to 95 °C under 800 RPM stirring for 5 min. Next, 160 µL L-aa (100 mM) was rapidly injected into the solution via pipette, and the solution was kept stirring at 95 °C for 20 min. This seed solution was left stirring at 30 °C for 2.5 hours. To prepare the rhombic dodecahedra cores, 2.50 mL CTAC (200 mM), 2.50 NaBr (100 mM), 15 µL KI (1 mM), 0.125 mL H₂PdCl₄ (10 mM), 0.050 mL L-aa (100 mM), and 0.040 mL of the Pd seed solution were combined. This solution was allowed to heat,

unstirred, at 60 °C for 2 hours. The brown-black solution was centrifuged at 3000 RPM for 30 min, the supernatant was removed, and the particles were redispersed in water. The final volume for the redispersed rhombic dodecahedral core solution was 3 mL.

A3.3 Symmetrically Branched Nanocrystal Growth

For branched nanocrystal growth from **all Pd shapes except octahedral seeds**, 2 mL CTAB (0.2 M) solution was added to a reaction vial. Next, 0.1 mL H₂PdCl₄ (5 mM for Pd tetrahedral seeds; 10 mM for all other shaped seeds) solution and 0.1 mL of HAuCl₄ (100 mM for Pd nanocubes and right bipyramids; 10 mM for nanobars and cubooctahedra; 5 mM for tetrahedra) solution were added followed by 1.5 mL L-aa (0.1 M) solution. Then 21.4 mL of water was added, followed by shape-controlled Pd seed solution (1.0 mL of the nanocube or right bipyramid seed solutions; 0.30 mL of the nanobar or cubooctahedra seed solutions; 0.10 mL of the tetrahedral seed solution). These reaction vials were gently shaken then capped and allowed to sit undisturbed in a 25 °C oil bath for 24 hours.

For branched nanocrystal **growth from Pd octahedra**, 2 mL CTAC (0.2 M) solution and 2 mL NaBr (50 mM) solution were added to a reaction vial. Next, 0.1 mL H₂PdCl₄ (10 mM) solution and 0.1 mL HAuCl₄ (100 mM) solution were added followed by 1.5 mL L-aa (0.1 M) solution. Then 19.4 mL of water was added, followed by 0.15 mL octahedral seed solution. This reaction vial was gently shaken then capped and allowed to sit undisturbed in a 25 °C oil bath for 24 hours. The results in Figure S3.5 were obtained by decreasing the HAuCl₄ solution concentration to 10 mM and the H₂PdCl₄ solution to 0.1 mM while increasing the volume of octahedral Pd seed solution to 1 mL.

These conditions are summarized in **Table A3.1**.

Table A3.1: Volumes and concentrations of precursors used during the overgrowth step to prepare symmetrically-branched Au/Pd nanocrystals.

Shape- Controlled Pd Seed	CTAB (2 mL)	CTAC (2 mL)	NaBr (2 mL)	HAuCl₄ (0.1 mL)	H₂PdCl₄ (0.1 mL)	L-aa (1.5 mL)	Seed Volume
Nanocube	0.2 M	0	0	100 mM	10 mM	0.1 M	1.0 mL
Nanobar	0.2 M	0	0	10 mM	10 mM	0.1 M	0.30 mL
Right Bipyramid	0.2 M	0	0	100 mM	10 mM	0.1 M	1.0 mL
Octahedra	0	0.2 M	50 mM	100 mM	10 mM	0.1 M	0.15 mL
Tetrahedra	0.2 M	0	0	5 mM	5 mM	0.1 M	0.10 mL
Cuboctahedra	0.2 M	0	0	10 mM	10 mM	0.1 M	0.30 mL
Rhombic Dodecahedra	0.2 M	0	0	100 mM	10 mM	0.1 M	3.0 mL

A3.4 Time Study

Syntheses of 24-branched Au/Pd nanostructures were quenched by adding 0.1 mL of 100 mM of BSPP at different times. The quenched samples were then immediately collected by centrifugation and the samples decanted.

A3.5 Characterization

See Section A2.2.5.

Chapter 4

A4.2 Size-dependent Optical Properties of Au/Pd Octopods

A4.2.1 Chemicals

L-aa ($C_6H_8O_6$, 99%), palladium(II) chloride ($PdCl_2$, 99.98%), chloroauric acid ($HAuCl_4 \cdot 3H_2O$, 99.9%), CTAB (98%), 4-mercaptopyridine (4-MPy, 95%), and sodium borohydride ($NaBH_4$, 98.5%) were used as purchased from Sigma Aldrich. Dimethyl sulfoxide (DMSO, ACS grade) was purchased from Fluka. Poly(styrene sulfonic acid) sodium salt (Na-PSS, MW 700 000) was used as purchased from Alfa Aesar. Nanopure water ($18.2 \text{ M}\Omega \cdot \text{cm}$) was used in all experiments. An aqueous 10 mM H_2PdCl_4 solution was prepared by heating at $70 \text{ }^\circ\text{C}$ and stirring dissolved $PdCl_2$ (44.6 mg) in 25 mL of HCl (pH 1.69) for 1 h.

A4.2.2 Synthesis of Au Nanoparticle Seeds

See Section A2.2.2.

A4.2.3 Synthesis of Au Nanoparticle Cores

See Section A2.3.3.

A4.2.4 Synthesis of Au/Pd Octopods

Au/Pd octopods of various sizes were prepared by the simultaneous addition via separate pipettes of 2 mL H_2PdCl_4 and 0.1 mL of $HAuCl_4$ to the Au core solution. The size of the Au/Pd octopods was controlled by varying the concentrations of the Pd and Au precursors while maintaining the same 10:1 Au/Pd mole ratio of the precursor (see **Table**

A4.1). The vials were gently mixed by inversion followed promptly by the addition of 0.5 mL of 1-aa (0.1 M) solution. The reaction vial was capped and allowed to sit undisturbed in a 25 °C oil bath for 24 h.

Table A4.1 Concentrations of Precursors Added during the Co-reduction Step for Samples A-G

Sample	Concentration of 1mL H₂AuCl₄ added	Concentration of 2 mL H₂PdCl₄ added
A	5	0.025
B	10	0.05
C	25	0.125
D	50	0.25
E	100	0.5
F	150	0.75
G	200	1

A4.2.5 Instrumentation

See A2.2.5 for most details.

Dynamic light scattering (DLS) of prepared solutions was performed on a Malvern Zetasizer Nano Zs instrument at 25 °C with a 633 nm laser.

A4.2.6 Refractive Index Sensitivity Measurements

Water/DMSO solutions with a percentage of DMSO ranging from 0 to 50% at 12.5% intervals were used to change the RI experienced by the Au/Pd octopods. The Lorentz—Lorenz equation was used to calculate the RI of the various water-DMSO solutions:⁴

$$\frac{n_{12}^2 - 1}{n_{12}^2 + 2} = \varphi_1 \frac{n_1^2 - 1}{n_1^2 + 2} + \varphi_2 \frac{n_2^2 - 1}{n_2^2 + 2}$$

where n_{12} is the RI of the mixture, n_1 (1.33) and n_2 (1.48) are the RIs of water and DMSO, respectively, and φ_1 and φ_2 are their volume fractions. For RI sensitivity measurements, nanoparticle samples were collected via centrifugation, decanted to 3 mL, and then dispersed with 12 mL of a 2 mg/mL Na-PSS aqueous solution. Finally, the samples were concentrated via centrifugation and fractioned into five samples, each being dispersed to 3 mL in the desired DMSO/water solution for analysis. The figure of merit (FOM) is calculated by dividing the sensitivity by the full width at half maximum (fwhm) of the LSPR.

A4.2.7 SERS Measurements with Au/Pd Octopods

Thin films of Au/Pd octopods were prepared by drop casting 4 μ L of a triply washed sample (redispersed in water to a volume of 5 mL) onto a Si wafer. The surfaces of the Au/Pd octopods were derivatized with 4-MPy by submerging the wafer into a 4 mM solution of 4-MPy for 30 min. The wafer was removed from the incubation solution, rinsed, and dried in air. SERS spectra were collected with a Renishaw InVia microscope with 10 s acquisitions, with 10 scans at a laser power of 3 mW. A laser excitation wavelength of 785 nm was used. Acquisitions were obtained through a 1 μ m pinhole, with sample completely covering that entire area. For each sample, experiments were run at least in triplicate and found to provide similar spectral profiles and intensities.

A4.7 Manipulating the Optical Properties of Symmetrically Branched Au/Pd Nanocrystals through Interior Design

A4.7.1 Chemicals:

L-aa ($C_6H_8O_6$, 99%), palladium(II) chloride ($PdCl_2$, 99.98%), chloroauric acid ($HAuCl_4 \cdot 3H_2O$, 99.9%), iron III chloride ($FeCl_3 \cdot 6H_2O$, 98%), CTAB (98%, lot # SLBD0174 V), CTAC (0.78 M, lot # STBC 7888 V), and potassium bromide (KBr, 99%) were used as purchased from Sigma Aldrich. Concentrated hydrochloric acid (HCl, 12.1 M) was purchased from Mallinckrodt. Nanopure water ($18.2 M\Omega \cdot cm$) was used in all experiments. An aqueous 10 mM H_2PdCl_4 solution was prepared by stirring dissolved $PdCl_2$ (44.6 mg) in 25 mL of HCl (pH 1.69) for 1 h while heating at $\sim 70^\circ C$.

A4.7.2 Synthesis of Pd Nanocube Seeds

The Pd nanocubes for use with seed-mediated co-reduction are prepared by a seeded method as well, and the procedure for Pd nanocubes was adapted from prior protocol.⁵ In a 25 mL vial, 10.0 mL CTAB (12.5 mM) and 0.500 mL H_2PdCl_4 (10.0 mM) were heated at $95^\circ C$ for 5 minutes under moderate stirring. Next, 0.080 L-aa (100 mM) was rapidly added and the reaction was allowed to stir at $95^\circ C$ for 30 minutes. The orange-brown clear solution was transferred to a $30^\circ C$ oil bath to be used as seeds for the synthesis of Pd nanocubes. In two separate 20 mL vials, 2.50 mL CTAC (200 mM), 2.5 mL NaBr (100 mM), and 0.125 mL H_2PdCl_4 (10.0 mM) were combined, followed by 0.040 mL of the Pd seeds and 0.050 mL L-aa. This solution was allowed to sit, without stirring, at $40^\circ C$ for 13 hours 30 minutes. Once the two reactions were complete these two solutions were combined and the solution was washed and redispersed in 3 mL water.

A4.7.3 Synthesis of core@shell Pd@Au/Pd Octopods

The procedure for Pd@Au/Pd octopods was adapted from prior protocol A2.2.⁶ First, 2.00 mL CTAB (0.200 M) solution was added to a reaction vial. Next, 0.100 mL H₂PdCl₄ (10.0 mM) solution and 0.040 mL of HAuCl₄ (100 mM) solution were added followed by 1.50 mL L-aa (0.10 M) solution. Then 21.4 mL of water was added, followed by 3 mL of the Pd nanocube seed solution. These reaction vials were gently shaken then capped and allowed to sit undisturbed in a 25 °C oil bath for 24 hours. Afterward the dark blue colloidal solution was washed and redispersed in 3 mL water.

A4.7.4 Synthesis of Au/Pd Octopods with Hollow Interiors

In a 25 mL vial, 10 mg NaBr, 60 mg CTAB, 0.25 mg FeCl₃·6H₂O, and 5.5 mL H₂O were added. Next, the Pd@Au/Pd octopods were added, followed by 0.10 mL concentrated HCl (12.1 M). This solution was heated at 90 °C for 24 hours under vigorous stirring. Afterward the gray-blue colloidal solution was washed and redispersed in 3 mL water.

A4.7.5 Characterization

See Sections 2.2.5 and 2.3.7. XPS was performed with a PHI VersaProbe II Scanning X-ray Microprobe system.

Chapter 5

A5.1 Chemicals. L-aa ($C_6H_8O_6$, 99%), palladium(II) chloride ($PdCl_2$, 99.98%), chloroauric acid ($HAuCl_4 \cdot 3H_2O$, 99.9%), sodium borohydride ($NaBH_4$, 98.5%), CTAB (98%, lot # SLBD0174 V), and sodium salicylate ($NaC_6H_5O_3$, 99.5 %) were used as purchased from Sigma Aldrich. 3-Methyl salicylic acid ($C_8H_8O_3$, 98%), 2, 6-dihydroxybenzoic acid ($C_7H_6O_4$, 98%), 5-bromosalicylic acid ($C_7H_5BrO_3$, 99%), and 5-aminosalicylic acid ($C_7H_7NO_3$ 98%). Concentrated hydrochloric acid (HCl, 12.1 M) was purchased from Mallinckrodt. Nanopure water ($18.2 \text{ M}\Omega \cdot \text{cm}$) was used in all experiments. An aqueous 10 mM H_2PdCl_4 solution was prepared by stirring dissolved $PdCl_2$ (44.6 mg) in 25 mL of HCl (pH 1.69) for 1 h while heating and stirring at 70 °C.

A5.2 Synthesis Details. Au-Pd octopods are prepared by a double seeded method in which gold nanoparticle seeds are prepared first. These seeds are then used to make gold nanoparticle cores, which are then used to synthesize Au-Pd octopods via seed-mediated co-reduction. Each step is described below.

A5.2.1 Gold Nanoparticle Seeds.

See Section A2.2.2.

A5.2.2 Gold Nanoparticle Cores.

See Section A2.2.3.

A5.2.3 Gold-Palladium Octopods. To prepare Au/Pd octopods, 2 mL of water or a solution containing an aromatic additive (3-methylsalicylic acid (20 mM), sodium salicylate (40 mM), 2, 6-dihydroxybenzoic acid (16 mM), 5-bromosalicylic acid (8 mM),

or 5-aminosalicylic acid (6 mM)) was added to the entire Au core solution. This procedure was followed by the simultaneous addition via separate pipettes of 2 mL H_2PdCl_4 (1 mM) and HAuCl_4 (200 mM). The vial was gently mixed by inversion followed promptly by the addition of 0.5 mL of L-aa (0.1 M) solution. This vial was then capped and allowed to sit, without stirring, in a 25 °C oil bath for 24 h.

5.3 Characterization.

See Section 2.2.5.

Zeta potentials of prepared solutions were performed on a Malvern Zetasizer Nano Zs instrument at 25 °C with a 633 nm laser. To prepare the zeta potential measurements, concentrated samples were diluted 20:1 in water resulting in an attenuator of 9 and a UV/vis peak absorbance of 0.222. FT-IR was performed on a Vertex 70v. For FT-IR experiments, 0.1 mL of each unwashed sample was individually dropcasted onto a clean silicon wafer and vacuum dried for at least 3 hours.

XPS experiments were performed using PHI *VersaProbe* II instrument equipped with monochromatic Al $K\alpha$ source. Instrument base pressure was ca. 4.8×10^{-10} torr. An X-ray power of 25 W at 15 kV was used for all experiments with a 100 μm beam size. The instrument work function was calibrated to give a binding energy (BE) of 84.0 eV for Au 4f_{7/2} line for metallic gold and the spectrometer dispersion was adjusted to give a BEs of 932.7 eV and 368.3 eV for Cu 2p_{3/2} and Ag 3d_{5/2} photoemission lines, respectively. The ultimate *VersaProbe* II instrumental resolution was determined to be 0.12 eV using the Fermi edge of the valence band for metallic silver for UPS (HeII line). Dual charge compensation was used on all samples. High-resolution Au 4f, Pd 3p and C 1s spectra

were taken with a minimum of 10 - 60s scans using a 0.1 eV step and pass energies 23.5 eV, 93.9 eV, and 11.75 eV, respectively, using PHI software *SmartSoft –XPS* v2.0 and processed using PHI *MultiPack* v9.0 and CasaXPS v.2.3.14. The carbon 1s peak was fitted using a combination of Gaussians and Lorentzians with 30-50% of Lorentzian contents. Shirley background was used for curve-fitting.

For XPS experiments, the samples were drop casted onto native surface of silicon wafer (see Figure S5.9E), dried, and then washed at least three times with methanol until no excess surfactant was observable. With the 1.3 x 1.3 mm² field of view in secondary electron x-ray imaging (SXI) mode the samples were examined in order to select the region with the best uniformity and was representative of the sample (see Figure S5.9B-D). To confirm reproducibility of XPS measurements, spectra was collected from three spots per sample labelled B-1, B-2, B-3; C-1, C-2, C-3 and D-1, D-2, D-3 (Figure S5.9 A-D) for samples prepared with 2 mL of 0.04 M sodium salicylate, 2 mL 0.006 M 5-aminosalicylic acid, and without additives, respectively. The resulting spectra showed a good consistency even for the spots separated as far as ~1000 μm as seen from the Figure S5.9A for Pd 3p_{1/2} transition, the weakest feature among selected regions of study.

The Au 4f and Pd 3p levels binding energies reported here were measured in relation to adventitious (aliphatic) carbon (deconvoluted C 1s component of at 284.8 eV, see Fig. S5.8C). The convoluted carbon 1s suggests the presence of sp² (at the same as adventitious component binding energy of 284.8 eV) and sp³ (~286 eV) C species and consistent with the literature reports.⁷

References

1. Zhang, J.; Zhang, L.; Xie, S.; Kuang, Q.; Han, X.; Xie, Z.; Zheng, L., Synthesis of Concave Palladium Nanocubes with High-Index Surfaces and High Electrocatalytic Activities. *Chem. Eur. Jour.* **2011**, *17*, 9915-9919.
2. Hong, J. W.; Kim, D.; Lee, Y. W.; Kim, M.; Kang, S. W.; Han, S. W., Atomic-Distribution-Dependent Electrocatalytic Activity of Au–Pd Bimetallic Nanocrystals. *Angew. Chem. Int. Ed.* **2011**, *50*, 8876-8880.
3. Huang, X.; Tang, S.; Zhang, H.; Zhou, Z.; Zheng, N., Controlled Formation of Concave Tetrahedral/Trigonal Bipyramidal Palladium Nanocrystals. *J. Am. Chem. Soc.* **2009**, *131*, 13916-13917.
4. Barbosa, S.; Agrawal, A.; Rodríguez-Lorenzo, L.; Pastoriza-Santos, I.; Alvarez-Puebla, R. n. A.; Kornowski, A.; Weller, H.; Liz-Marzán, L. M., Tuning Size and Sensing Properties in Colloidal Gold Nanostars. *Langmuir* **2010**, *26*, 14943-14950.
5. Yu, Y.; Zhang, Q.; Lu, X.; Lee, J. Y., Seed-Mediated Synthesis of Monodisperse Concave Trisoctahedral Gold Nanocrystals with Controllable Sizes. *J. Phys. Chem. C* **2010**, *114*, 11119-11126.
6. DeSantis, C. J.; Skrabalak, S. E., Core Values: Elucidating the Role of Seed Structure in the Synthesis of Symmetrically Branched Nanocrystals. *J. Am. Chem. Soc.* **2012**, *135*, 10-13.
7. Osswald, S.; Yushin, G.; Mochalin, V.; Kucheyev, S. O.; Gogotsi, Y., Control of sp²/sp³ Carbon Ratio and Surface Chemistry of Nanodiamond Powders by Selective Oxidation in Air. *J. Am. Chem. Soc.* **2006**, *128*, 11635-11642.

Appendix B: Supplemental Figures

Chapter 2

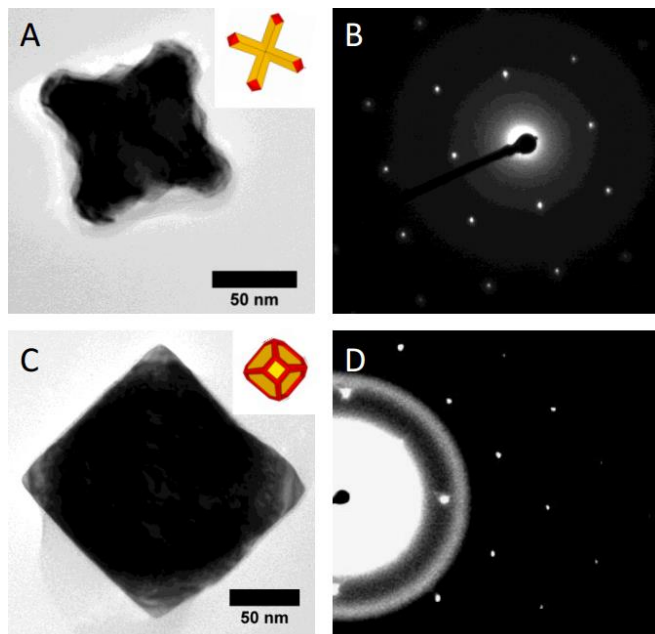


Figure S2.1. (A) TEM and (B) electron diffraction from an individual Au/Pd octopod oriented with four branches toward the substrate. (C) TEM and (D) electron diffraction from a concave Au@Pd cuboctahedron oriented with a (100)-terminating facet perpendicular to the electron beam.

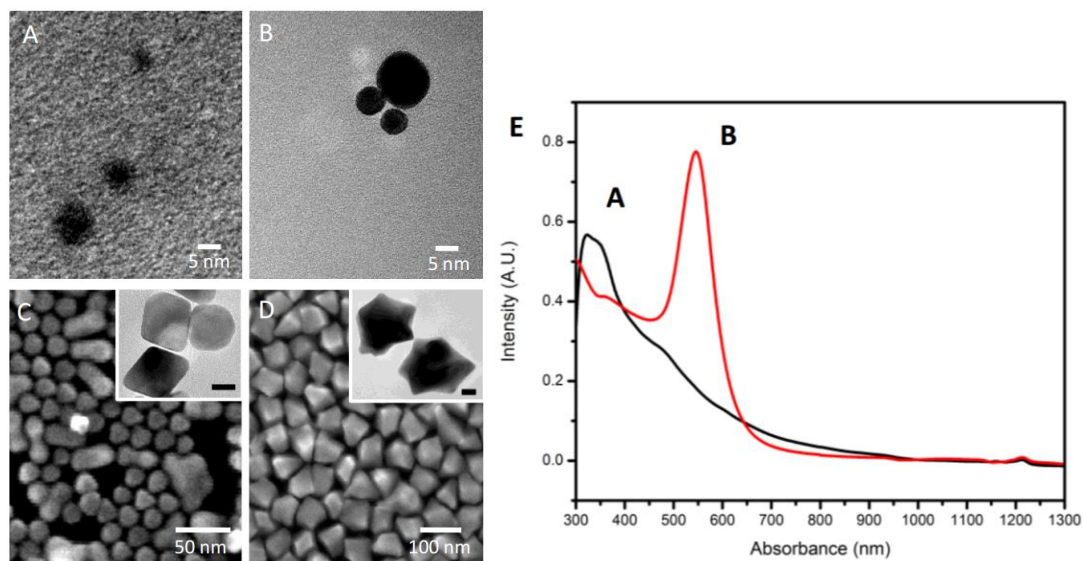


Figure S2.2. TEM images of Au seeds (A) freshly prepared and (B) after they are aged. SEM images, insets TEM images (scale bars 10 nm), of (C) Au cores prepared from freshly prepared Au seeds and (D) after the seeds were aged. In (E), the absorbance spectra for the freshly prepared and aged seeds, denoted A and B. The red-shift associated with the aged seeds is consistent with their larger size.

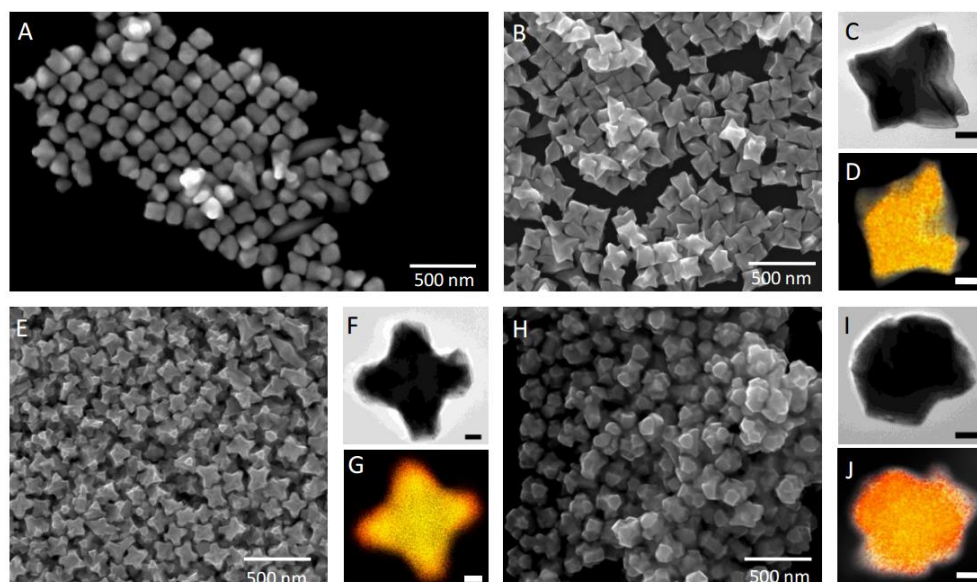


Figure S2.3. SEM (A, B, E, and H), TEM (C, F, and I) and STEM-EDX elemental mapping (D, G, and J) of Au/Pd nanoparticles, where yellow corresponds to Au and red corresponds to Pd. The Au:Pd mole ratio of precursors were: (A) 1-to-0, (B-D) 1-to-0.01, (E-G) 1-to-0.2, and (H-J) 1-to-0.5. Scale bars 25 nm (C, D, F, G, I, and J).

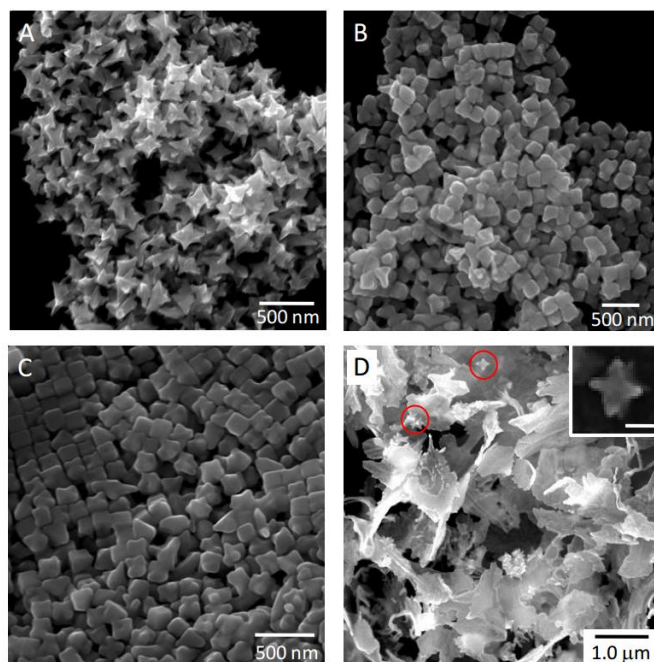


Figure S2.4. SEM images of the product obtained in control experiments, wherein H_2PdCl_4 was replaced with (A) Na_2PdCl_4 (1.0-to-0.1 Au:Pd ratio), (B) NaCl , (C) HCl , and (D) Na_2PdCl_4 (1.0-to-1.0 Au:Pd ratio). In (A) 2 mL of a 0.5 mM Na_2PdCl_4 solution was added to the synthesis to match the Pd(II) concentration used in the Au/Pd octopod synthesis. In (B) 2 mL of a 2.0 mM NaCl solution was added to match the Cl- concentration used in the Au/Pd octopod synthesis. In (C) 2 mL of a 5.0 mM HCl solution was added to match that from the H_2PdCl_4 precursor added to the Au/Pd octopod synthesis. In (D) 2 mL of a 5 mM Na_2PdCl_4 solution was added to match the Pd(II) concentration used in the concave Au@Pd nanocrystal synthesis. Branched particles were observed occasionally, with several examples circled. The inset provides a high magnification image of one of these branched nanocrystals (inset scale bar = 100 nm).

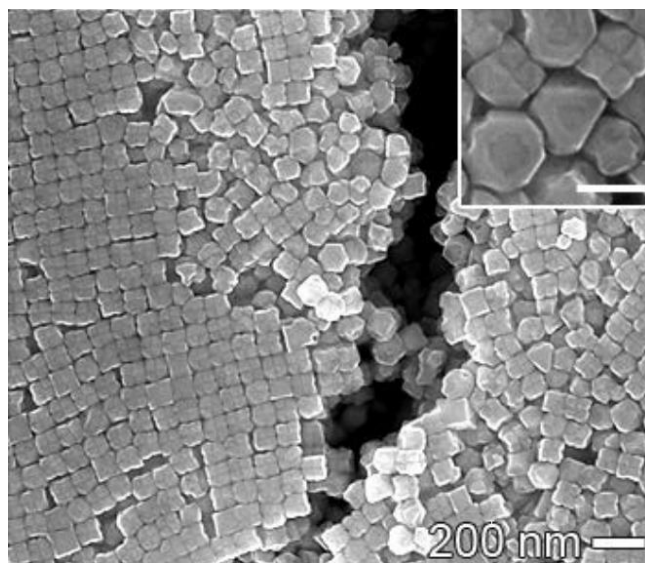


Figure S2.5. SEM image of concave Au@Pd nanocrystals prepared at a Au:Pd precursor ratio of 1:3.6 (inset scale bar = 100 nm).

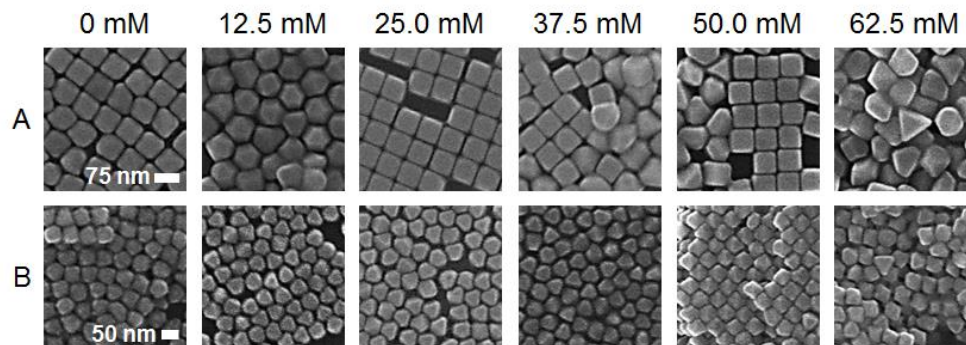


Figure S2.6. SEM images of nanocrystals prepared when only one of the metal precursors is reduced in the presence of the Au cores. Row A corresponds to the addition of 0.1 mL 50 mM HAuCl₄ and 2 mL of nanopure water (in place of the Pd precursor). Row B corresponds to the addition of 2 mL 0.25 mM H₂PdCl₄ and 0.1 mL of nanopure water (in place of the Au precursor). The pH of the overgrowth solution was varied across a row with the addition of HCl solution. From left to right: 2 mL of aqueous HCl solution added to the Au core solution prior to co-reduction at concentrations of 0.0, 12.5, 25.0, 37.5, 50.0, and 62.5 mM, respectively.

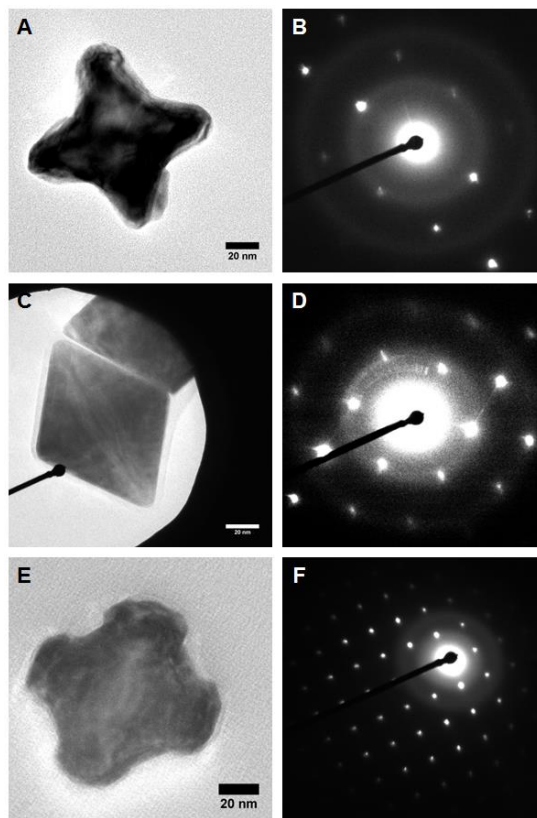


Figure S2.7. (A) TEM and (B) electron diffraction from an individual Au-Pd octopod (sample 4A) oriented with four branches toward the substrate. (C) TEM and (D) electron diffraction from an octahedron (sample 4F). (E) TEM and (F) electron diffraction from an individual Au-Pd sheeted octopod (sample 6A) oriented with four branches toward the substrate.

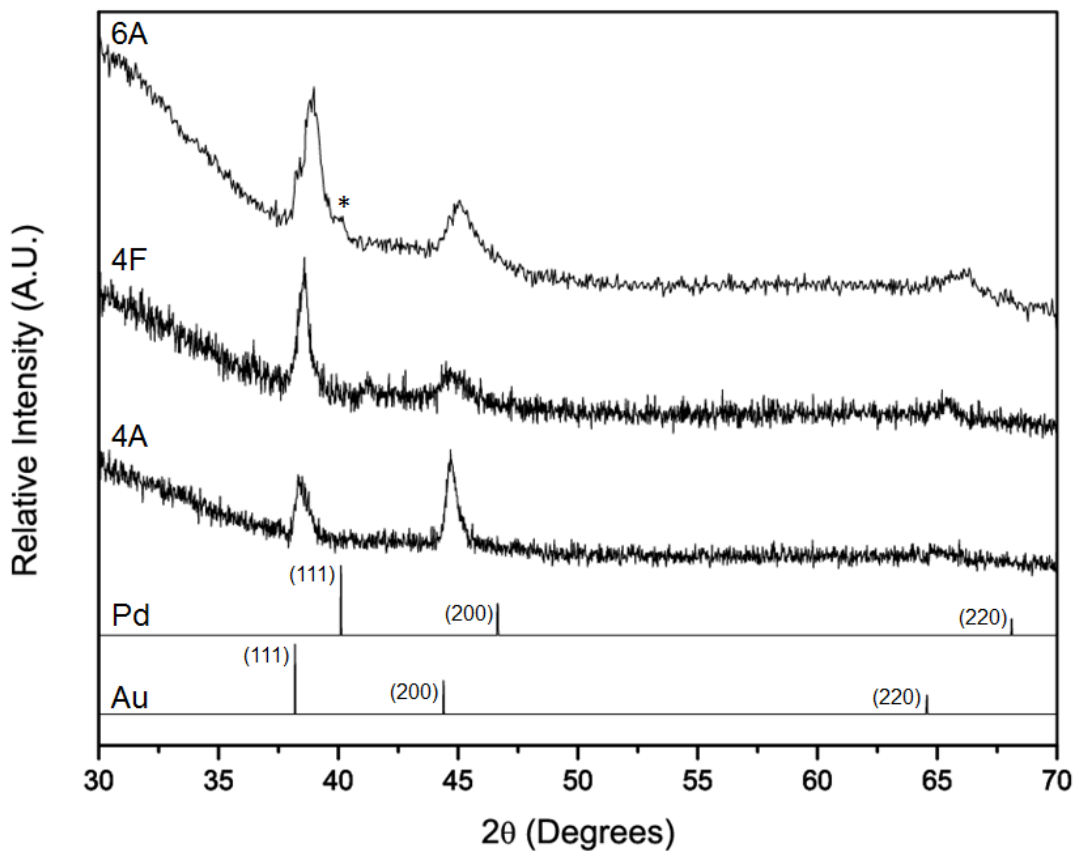


Figure S2.8. Powder XRD patterns of samples 4A, 4F, and 6A of **Figure 2.5**. The asterisk (*) denotes a shoulder corresponding to Pd. Reference Pd (PDF: 5-681) and Au (PDF: 4-784) are included as well. Note: while the relative intensities of the {111} and {200} reflections are different between samples, no preferential orientation effects were confirmed.

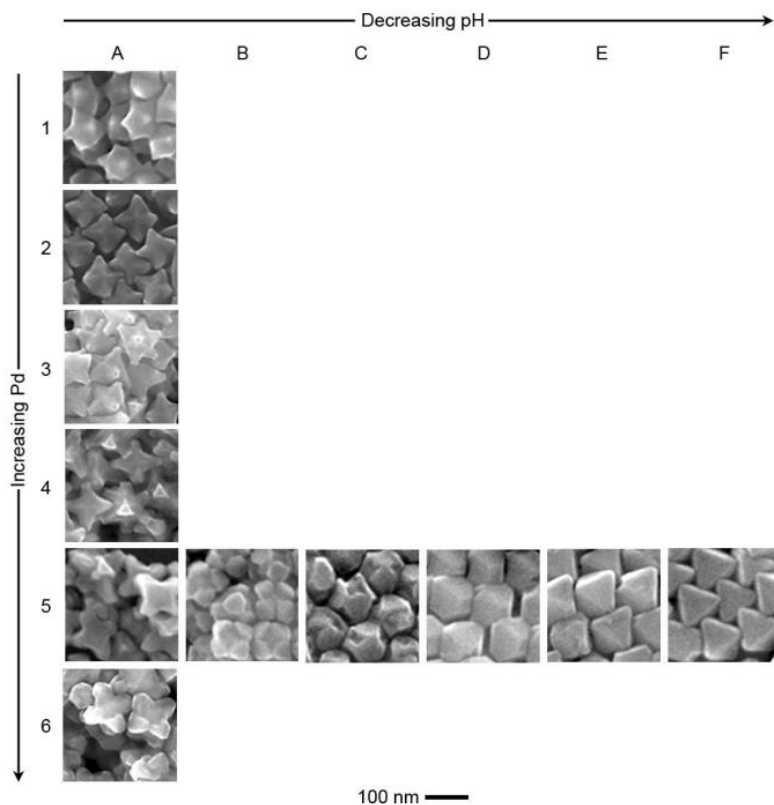


Figure S2.9. SEM images of Au-Pd nanostructures prepared with Na_2PdCl_4 as the Pd precursor. The synthetic results represented by 1-6 were obtained with Au:Pd precursor ratios of 1:X where X is 0.01, 0.1, 0.2, 0.5, 1.0, and 2.0 during co-reduction, respectively. Samples A-F corresponds to when 2 mL of aqueous HCl solution were added to the Au core solution prior to co-reduction at concentrations of 0.0, 12.5, 25.0, 37.5, 50.0, and 62.5 mM, respectively. Note: the morphology development observed in Row 5 is shifted slightly from that observed in Figure 2.5, Row 5. We attribute this observation to slight differences in Pd concentration between H_2PdCl_4 and Na_2PdCl_4 , although the difference was not verified by ICP-MS.

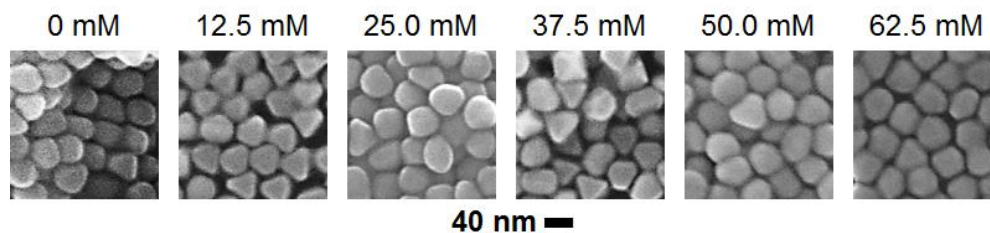


Figure S2.10. SEM images of Au cores with varying concentrations of 2 mL aliquots of HCl (concentrations denoted) added to their solution 24 hours after preparation.

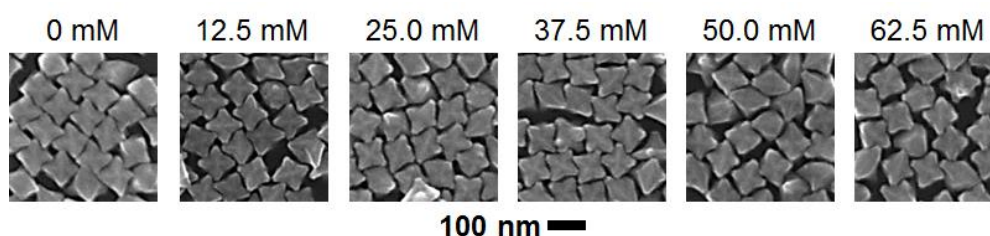


Figure S2.11. SEM images of Au-Pd nanocrystals (Au:Pd ratio of 1:0.1) prepared by substituting HCl with 2 mL NaCl solution (concentrations denoted) prior to the deposition step.

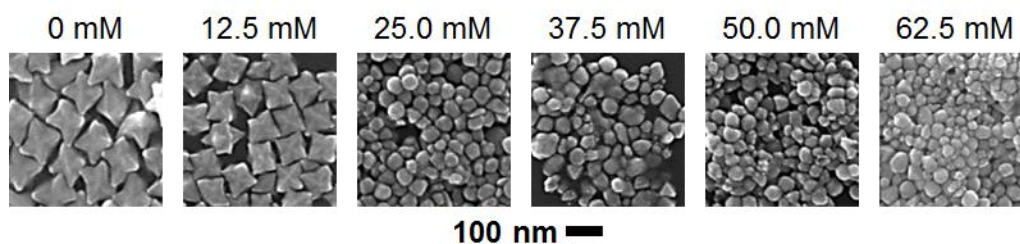


Figure S2.12. SEM images of Au-Pd nanocrystals (Au:Pd ratio of 1:0.1) prepared by substituting HCl with 2 mL NaOH solution (concentrations denoted) prior to the deposition step.

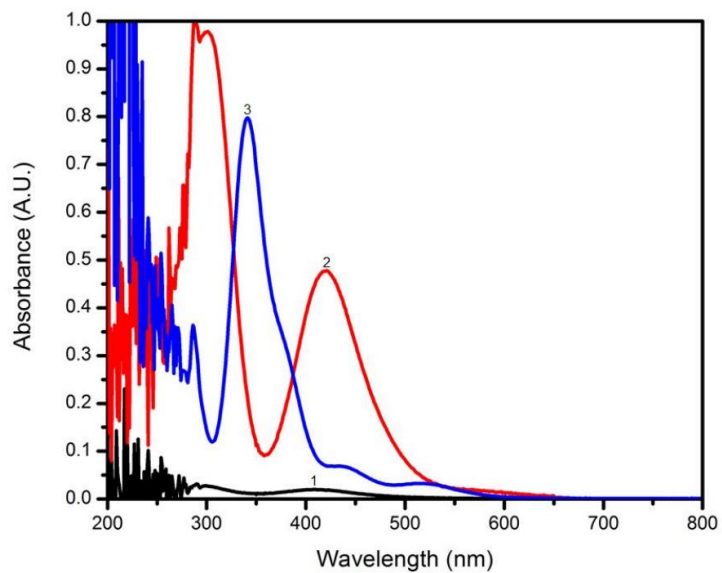


Figure S2.13. UV-visible spectra of H₂PdCl₄ at (1) experimental Row 4 concentration in water only and at (2) a much higher concentration. (3) The UV-visible spectrum of an aqueous solution of H₂PdCl₄ and CTAB at Row 4 concentrations. The position of the absorbance is consistent with Pd(II)-CTAB complexes.

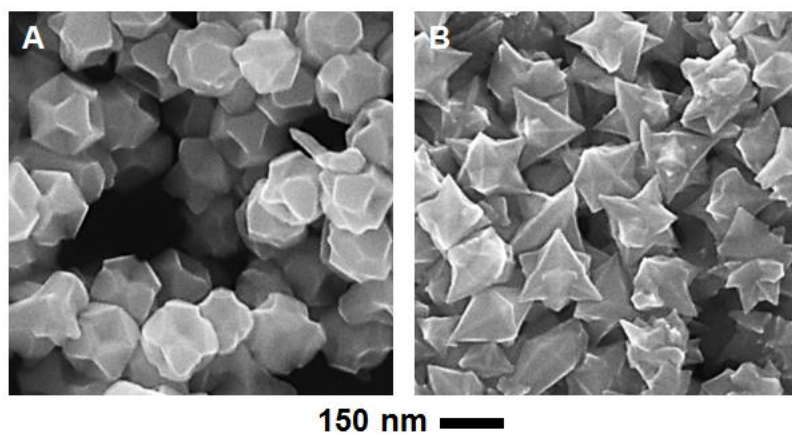
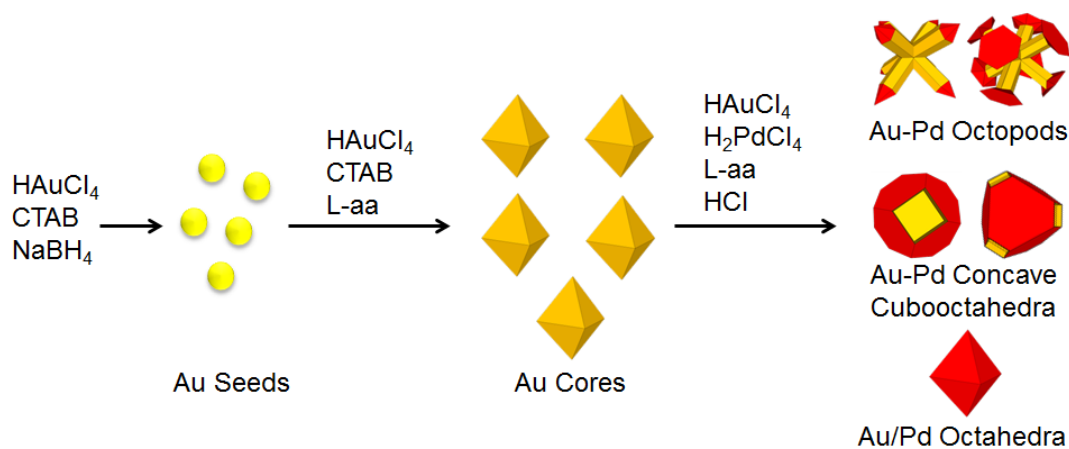


Figure S2.14. Au-Pd nanocrystals prepared when (A) additional Br^- is added to the traditional CTAB-based synthesis of octopods (Au:Pd = 1:01; CTAB-to-KBr = 1:0.5) prior to co-reduction and (B) HCl solution (2 mL of 25 mM HCl) is added to traditional CTAC-based synthesis (**Figure 2.9**) rather than water.



Scheme S2.1. An illustration of the steps involved in Au-Pd nanocrystal synthesis.

Table S2.1 Summary of the structures achieved under different experimental parameters.

Seed Age^a	Au Core Structure	Au:Pd Ratio	pH/Growth Rate	Synthetic Outcome
Fresh (<24 hours)	Octahedral	1:0.1	High/Fast	Convex core@shell Au@Pd Nanocrystals (Figure 2.3A-C)
Fresh (<24 hours)	Octahedral	1:1	Low/Slow	Concave core@shell Au@Pd nanocrystals (Figure 2.3D-H)
Aged (3 ⁺ days)	Branched	1:0.1	High/Fast	Au/Pd Octopods (Figure 2.1A-C)
Aged (3 ⁺ days)	Branched	1:1	Low/Slow	Concave core@shell Au@Pd nanocrystals (Figure 2.1D1-H)

a. Seed age corresponds to how long the prepared seeds were allowed to sit before being used to prepare Au cores.

Table S2.2. pH of overgrowth solution after addition of various overgrowth reagents.

	HCl aliquot concentration					
	0.0	12.5	25.0	37.5	50.0	62.5
	pH of overgrowth solution					
Au core solution	3.21	3.22	3.21	3.20	3.19	3.19
+ HCl	3.25	2.91	2.79	2.54	2.35	2.24
+ metal precursors	3.04	2.76	2.57	2.42	2.29	2.21
+ ascorbic acid	3.03	2.76	2.58	2.45	2.35	2.26
decanted supernatant	2.78	2.64	2.44	2.33	2.23	2.15

Chapter 3: Elucidating the Role of Seed Structure in the Synthesis of Symmetrically Branched Nanocrystals

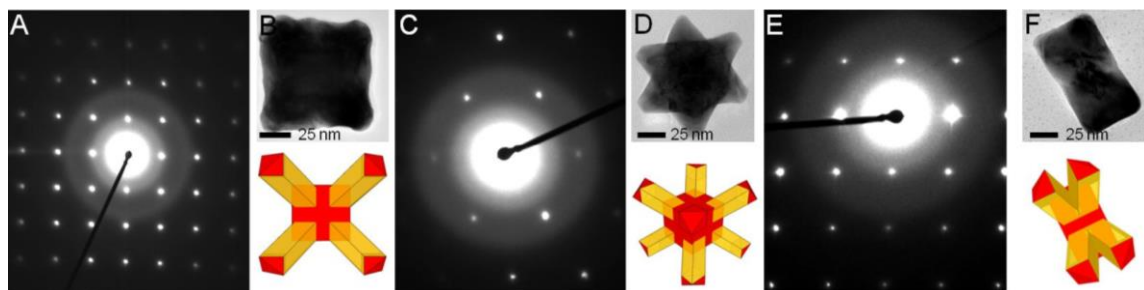


Figure S3.1. (A, C) Electron diffraction of individual Au/Pd octopods in two different orientations as revealed by (B, D) TEM (structural models included). (E) Electron diffraction of an individual Au/Pd bowtie in the orientation revealed by (F) TEM (structural model included).

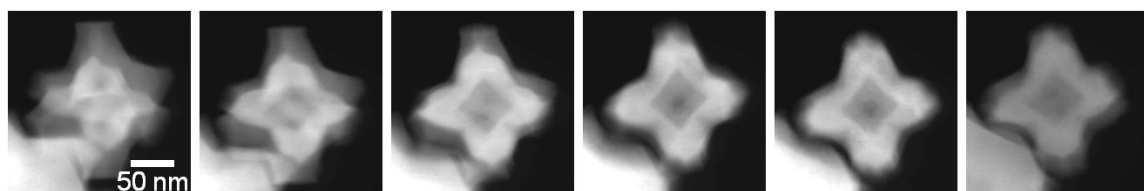


Figure S3.2. STEM images of an individual Au/Pd octopod through a series of tilts to reveal the structural relationship between the nanocube vertices and nanocrystal branches. See **Video 3.1**.

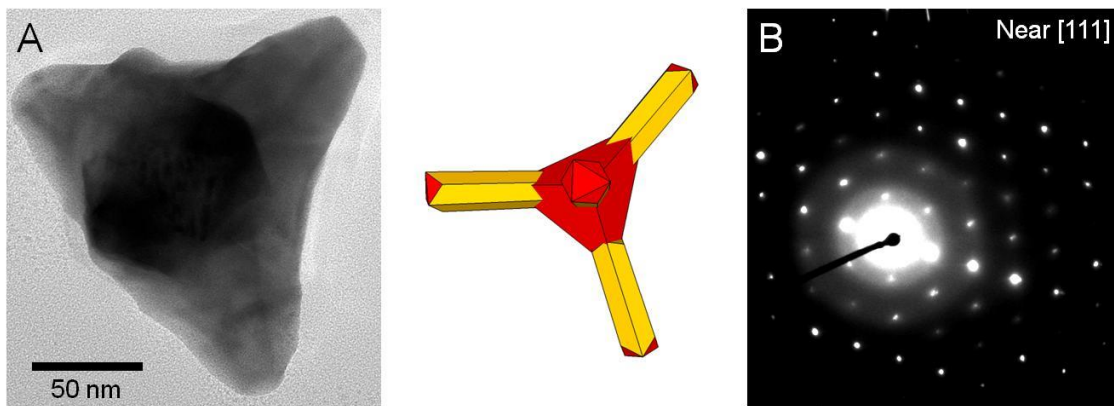


Figure S3.3. (A) A TEM image (structural model, right) and (B) electron diffraction of an individual Au/Pd pentapod oriented near the [111] zone axis.

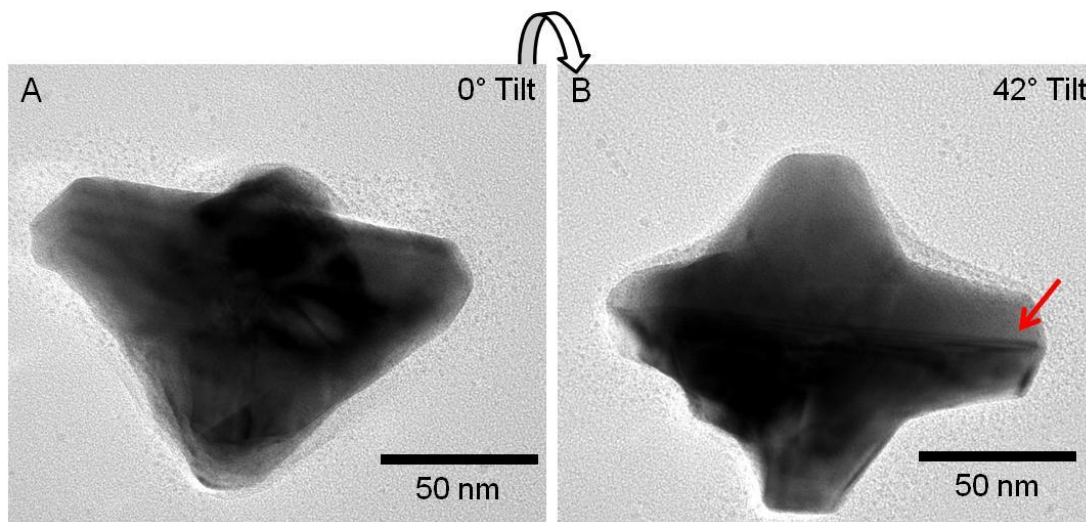


Figure S3.4. TEM images of an individual Au/Pd pentapod that is tilted by 0° then 42° to reveal a twin plane that extends the entire length of the structure, as indicated by the red arrow.

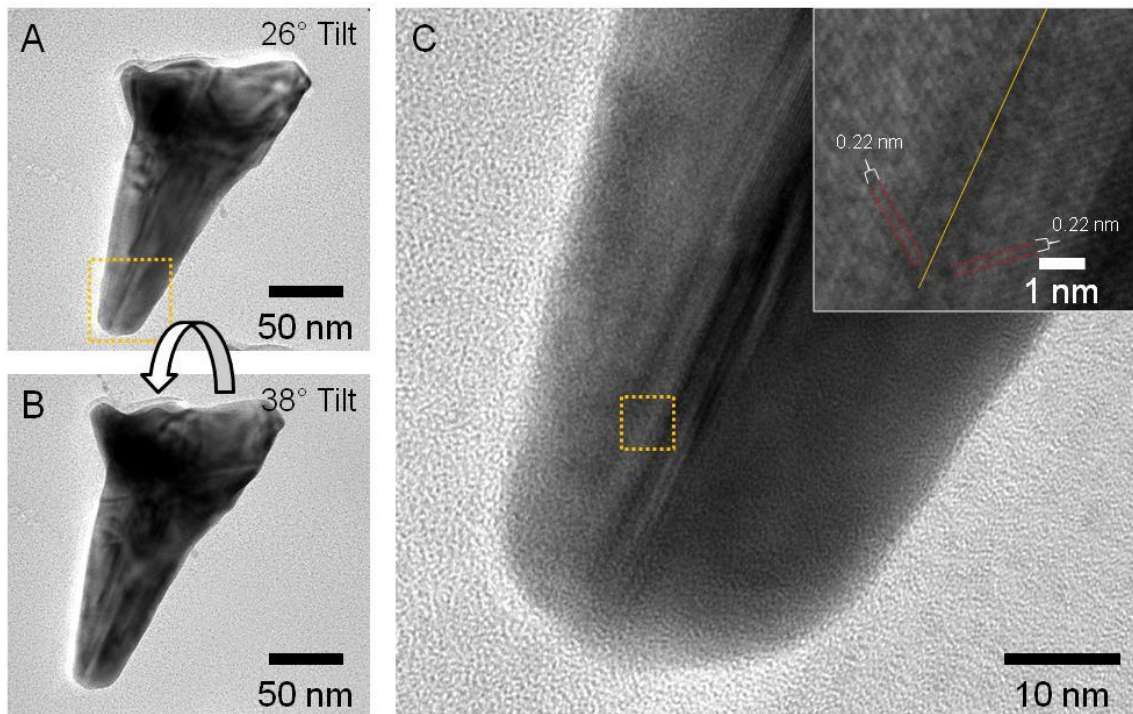


Figure S3.5. (A, B) TEM images of an individual Au/Pd pentapod that is tilted by 26° then 33°. (C) Higher magnification image of the region denoted in (A), with an enhancement of the denoted region in the inset.

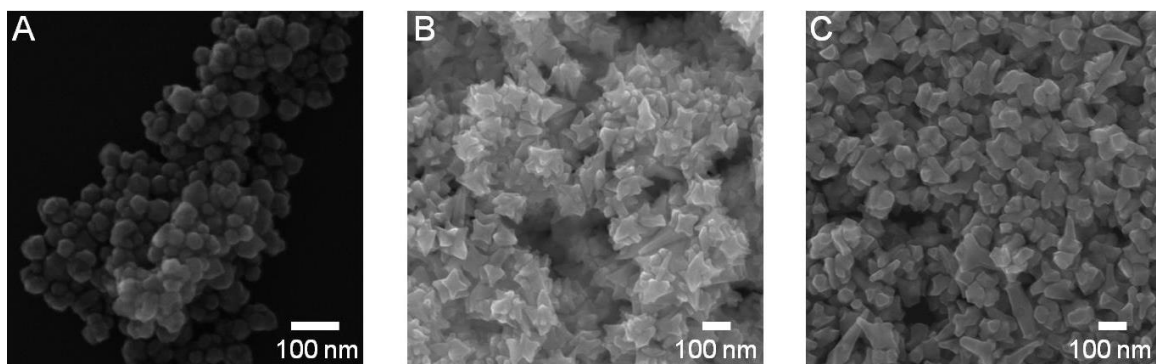


Figure S3.6. SEM images of nanostructures from Au/Pd overgrowth on Pd octahedra with varying concentrations of Br^- and CTAB/CTAC. The concentrations of surfactant/additives for each sample are: (A) 200 mM CTAB, (B) 200 mM CTAC and 100 mM NaBr, and (C) 200 mM CTAB and 200 mM NaBr.

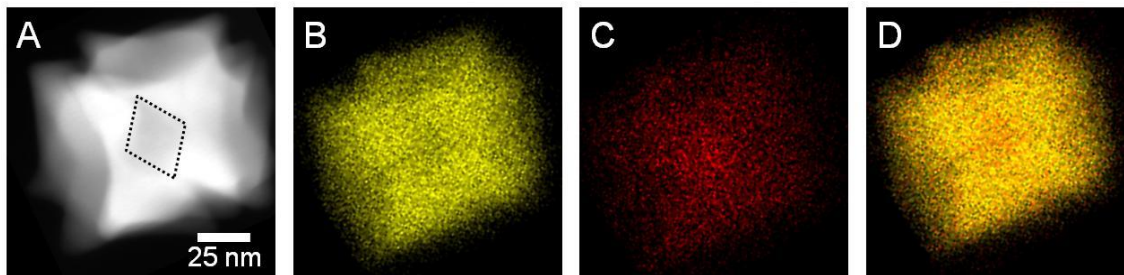


Figure S3.7. (A) A STEM image of an individual 24-branched Au/Pd nanocrystal and (B-D) elemental mapping by STEM/EDX analysis where yellow indicates Au and red indicates Pd.

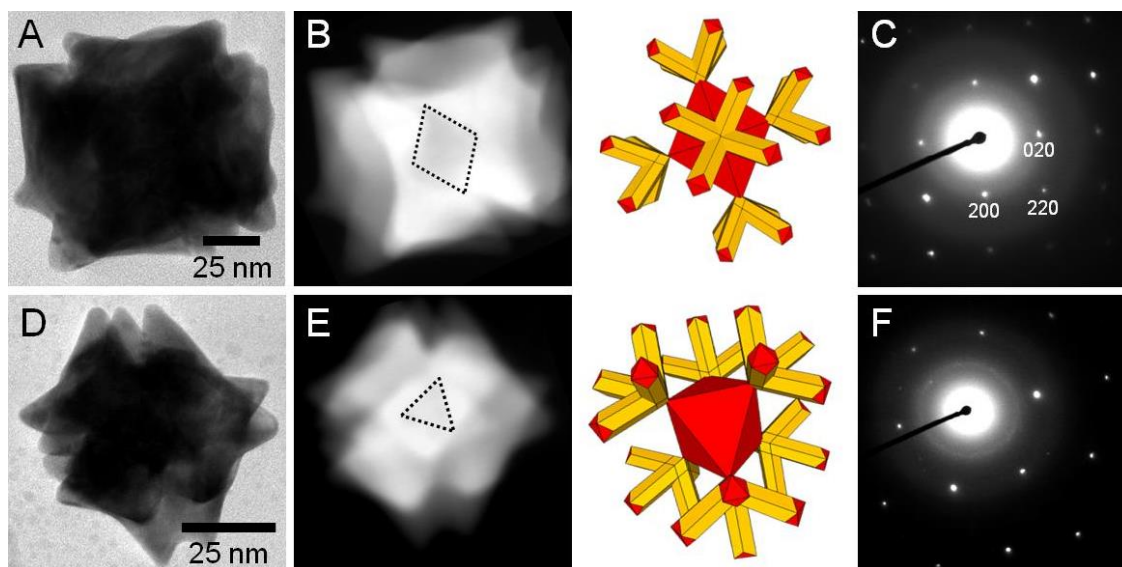


Figure S3.8. (A, D) TEM and (B, E) STEM images of individual 24-branched Au/Pd nanocrystals at two orientations (structural models included) and their corresponding (C, F) electron diffraction, which are near the $[100]$ and $[111]$ zone axes, respectively.

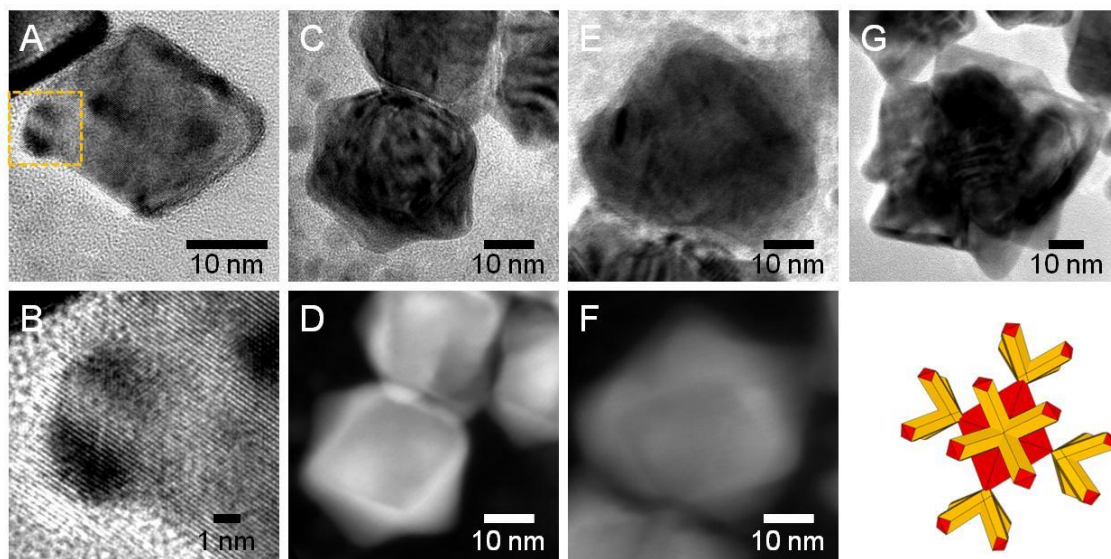


Figure S3.9. TEM (A-C, E, G) and corresponding STEM (D, F) images of product obtained by quenching the synthesis of 24-branched nanocrystals at (A, B) 1 minute, (C, D) 3 minutes, (E, F) 5 minutes, and (G) 10 minutes. (B) Higher magnification TEM of region indicated in (A). Model for (G) is provided.

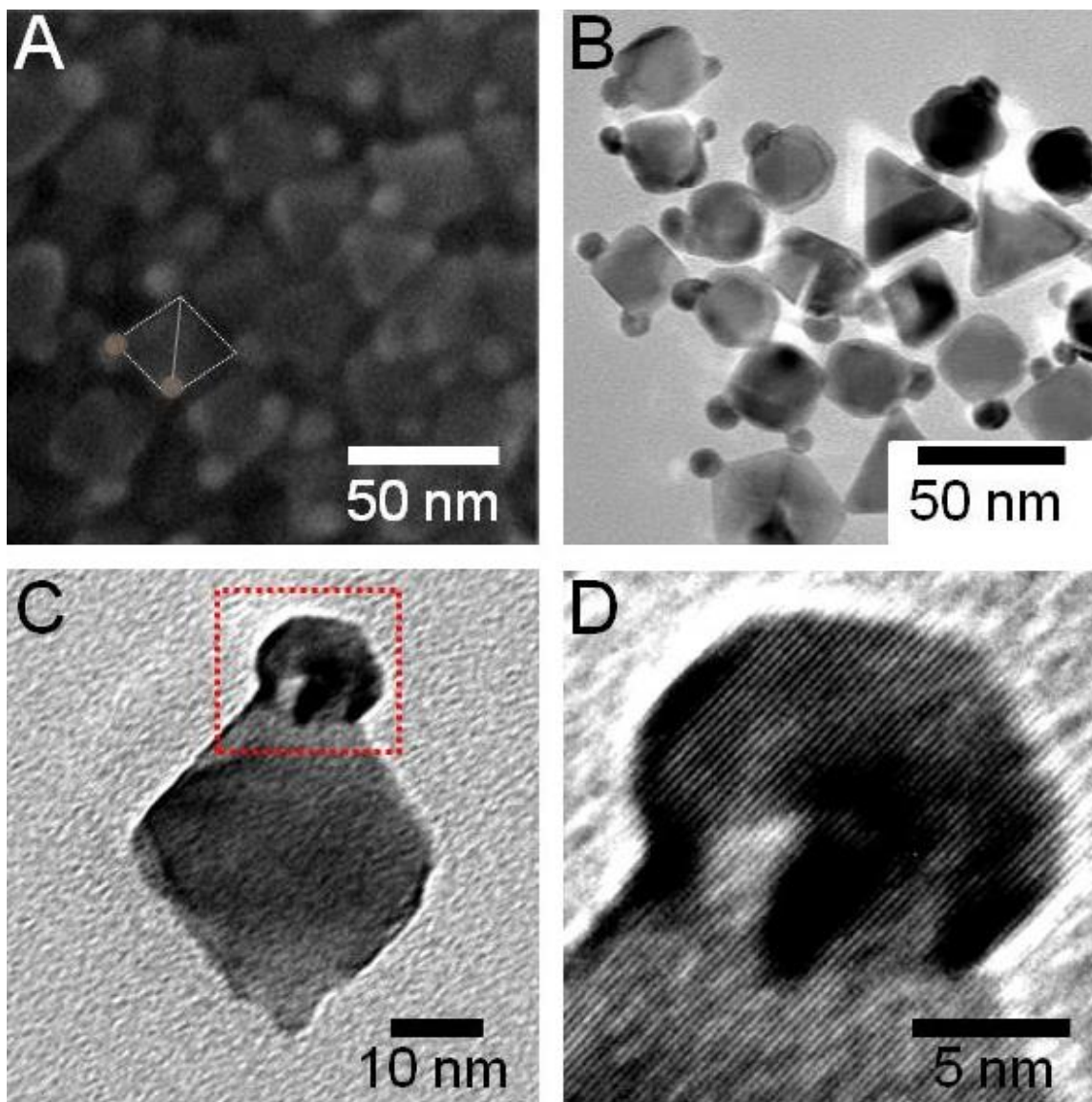


Figure S3.10. (A) SEM and (B) TEM images of octahedral Pd seeds with a small amount of Au/Pd overgrowth localized at the vertices. (C) A TEM image of an individual particle from this sample and (D) a TEM image at higher magnification corresponding to the region outlined in (C).

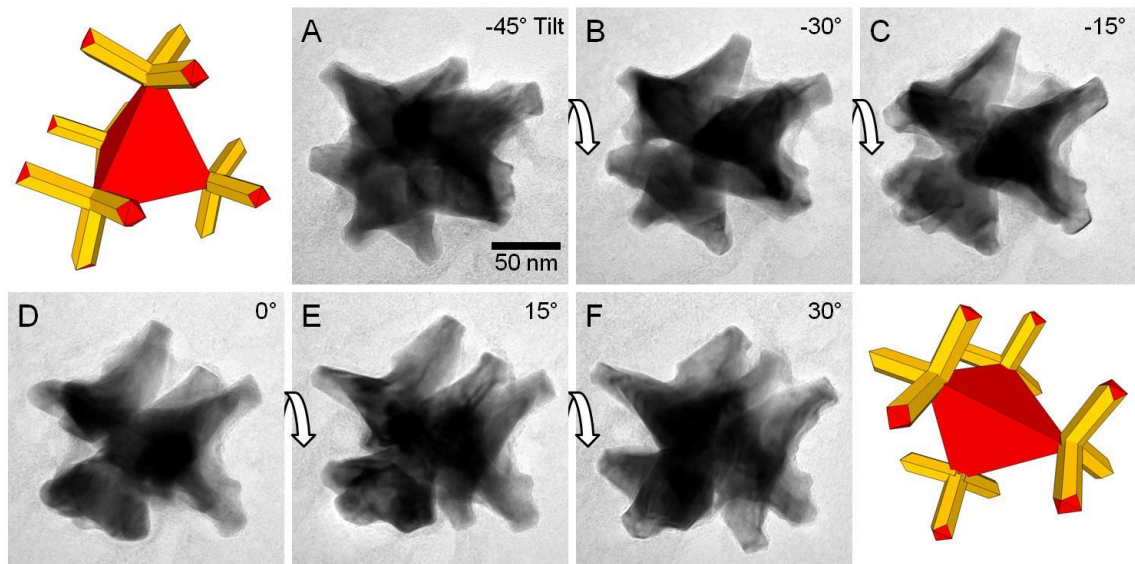


Figure S3.11. TEM images of an individual 12-branched Au/Pd nanocrystal tilted at 15° increments. Representative models for A and F are located to their left and right, respectively.

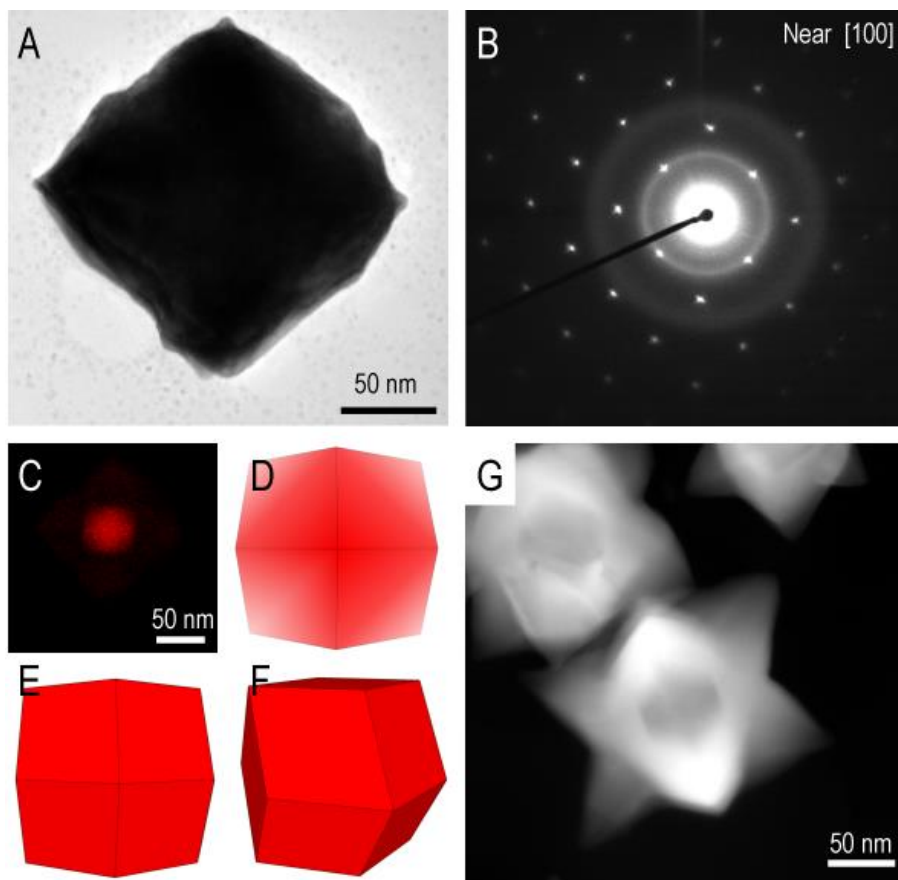


Figure S3.12. (A) TEM image of a Au/Pd octopod prepared from Pd rhombic dodecahedral seed and (B) its corresponding electron diffraction pattern. (C) Pd-only STEM-EDX map of the same particle. (D-F) Structural models of the rhombic dodecahedral seed where (D) indicates areas of the most Pd content with the brightest intensity. (G) STEM image of Au/Pd octopods prepared from Pd rhombic dodecahedral seeds.

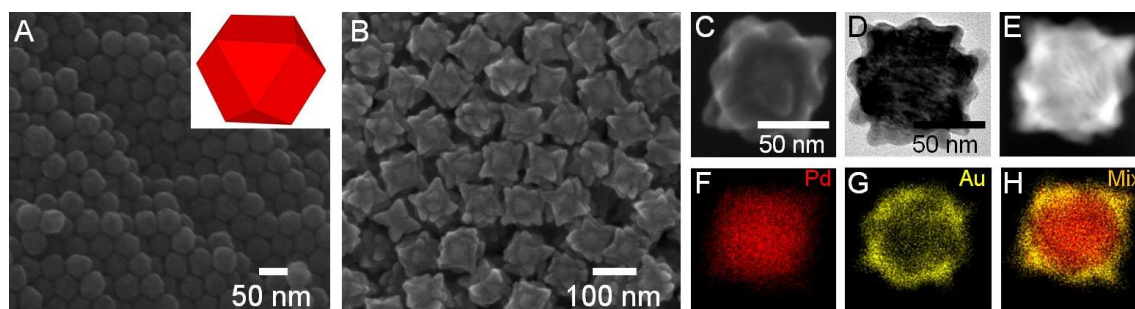


Figure S3.13. SEM images of (A) Pd cubooctahedra (inset: structural model) and (B) multi-branched Au/Pd nanocrystals. (C) A higher magnification SEM image of an individual multi-branched Au/Pd nanocrystal. (D) TEM and (E) STEM images of an individual multi-branched Au/Pd nanocrystal and corresponding (F-H) elemental mapping by STEM/EDX analysis where yellow is Au and red is Pd.

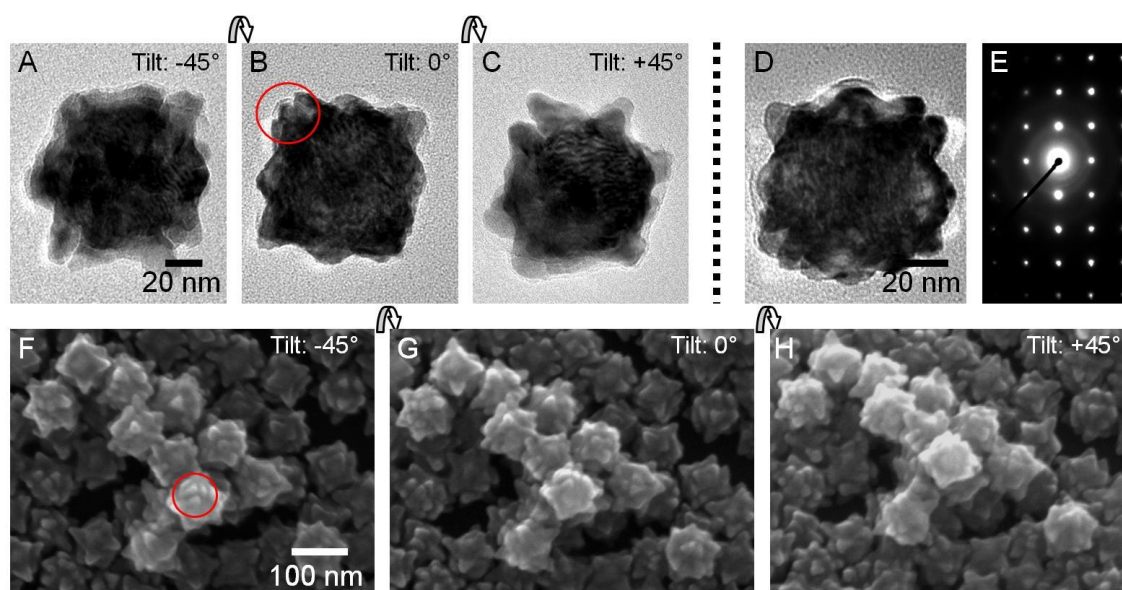


Figure S3.14. (A-C) TEM images of an individual multi-branched Au/Pd nanocrystal at various tilts. (D) A TEM image and corresponding (E) electron diffraction. (F-H) SEM images of many multi-branched Au/Pd nanocrystals at various tilts. Circled in red are branching patterns that are commonly observed.

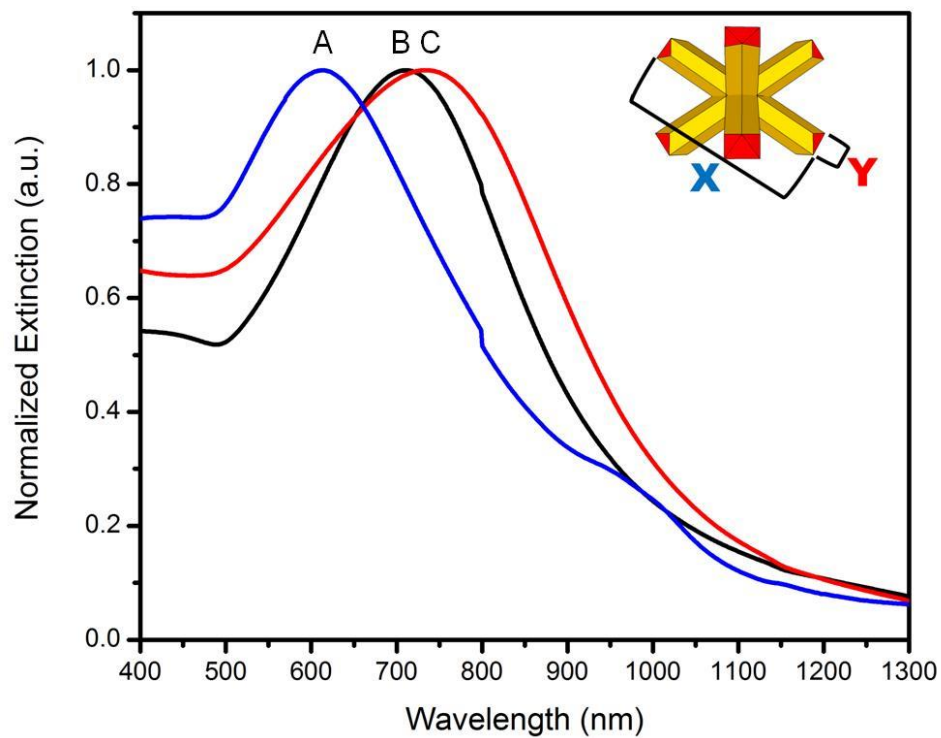


Figure S3.15. UV-visible spectra of (A) Au/Pd octopods prepared from Pd nanocube seeds, (B) Au/Pd octopods prepared from Au seeds, and (C) 24-branched Au/Pd nanocrystals prepared from Pd octahedral seeds. X = branch length and Y = branch width. Sample B was prepared according to established literature protocol (see **Figure S3.16**).¹

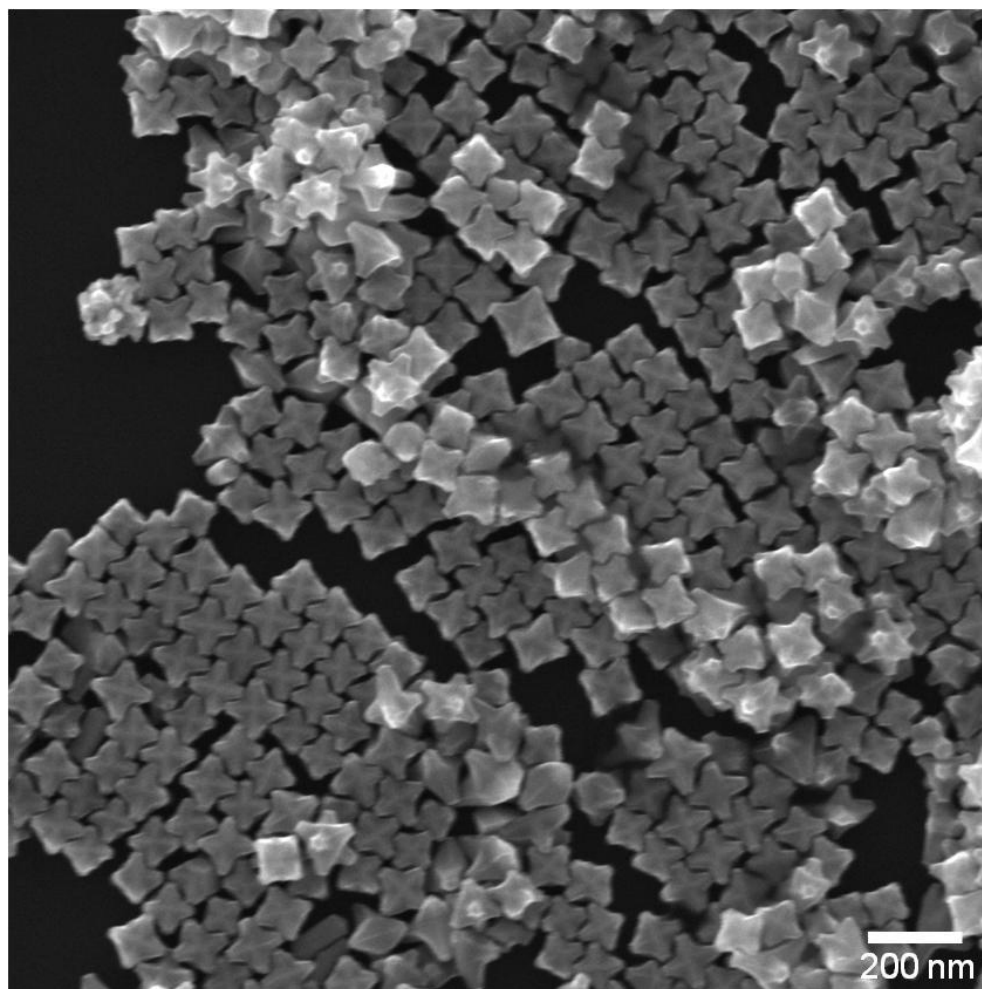
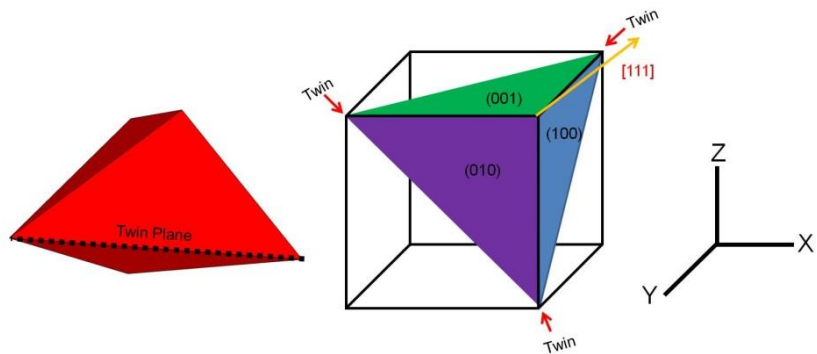
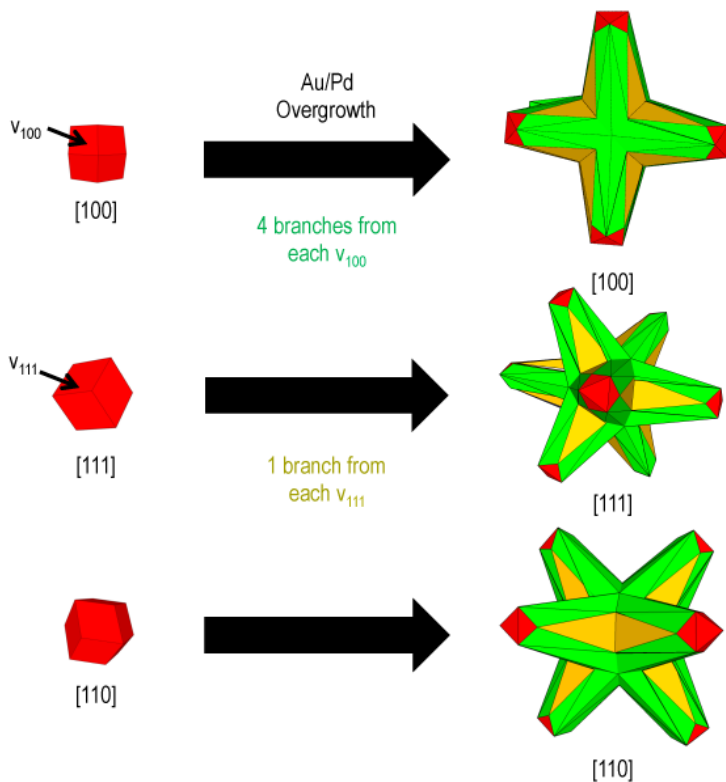


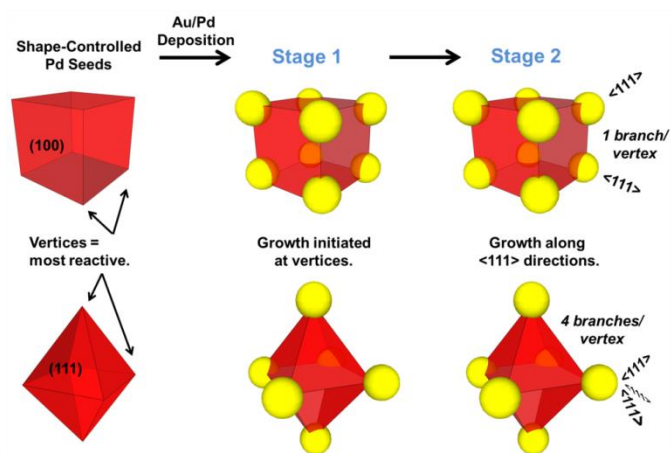
Figure S3.16. SEM image of Au/Pd octopods prepared from Au seeds (Sample B in **Figure S3.15**) They are prepared by a previously described literature protocol.²



Scheme S3.1. Left, model of a right bipyramid with the location of the twin plane denoted. Right, one single-crystalline domain of a right bipyramid positioned with a coordinate system and relevant crystallographic features denoted.



Scheme 3.2. Summary of branched growth directions from $\{110\}$ -terminated Pd rhombic dodecahedra seeds.



Scheme S3.3. Summary of synthetic results from single-crystalline $\{100\}$ - and $\{111\}$ -terminated nanocrystal seeds.

Chapter 4

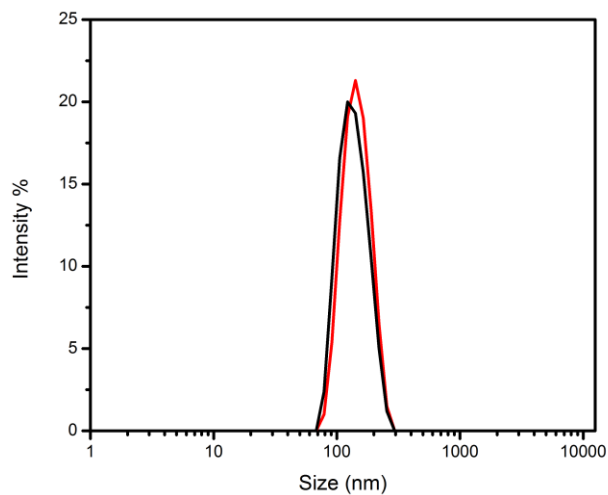


Figure S4.1. Dynamic light scattering of Na-PSS-modified Au/Pd octopods (Sample G) in water (black) and a 50/50 DMSO/water solution by volume (red). As there is no change in average size, the Na-PSS-modified Au/Pd octopods maintain colloidal stability. This experiment was run in triplicate to verify the result.

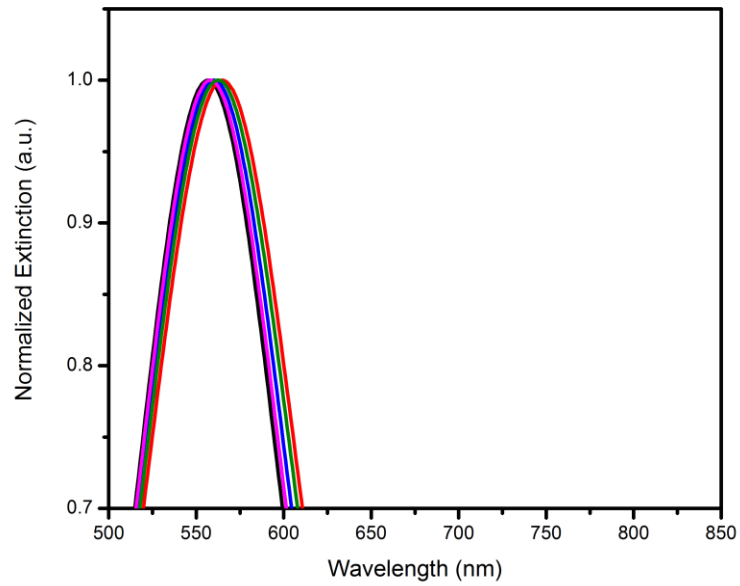


Figure S4.2A. Extinction spectra of Sample A in solvents with different RIs (denoted in Figure). Inset: a plot of SPR shift versus RI.

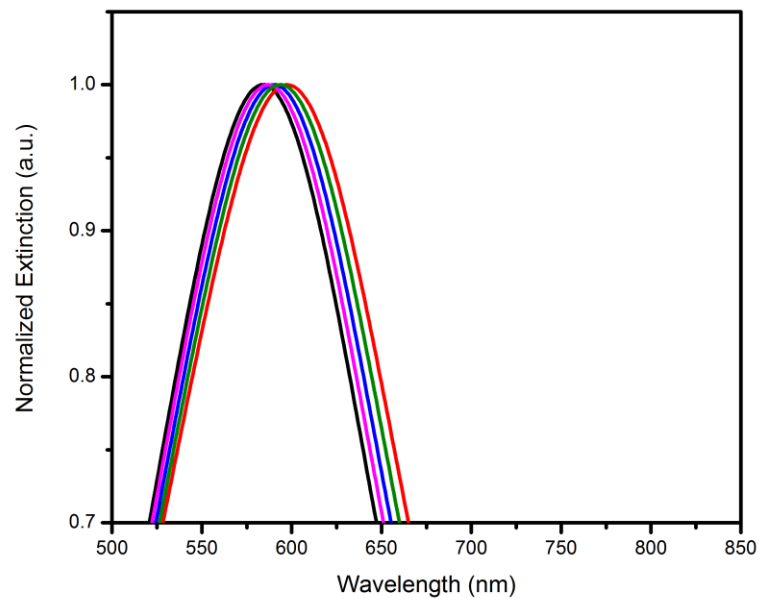


Figure S4.2B. Extinction spectra of Sample B in solvents with different RIs (denoted in Figure). Inset: a plot of SPR shift versus RI.

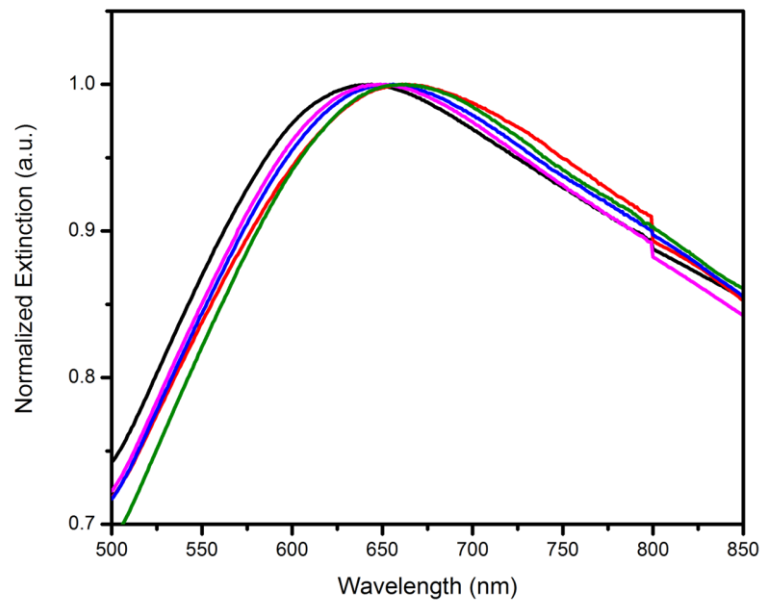


Figure S4.2C. Extinction spectra of Sample C in solvents with different RIs (denoted in Figure). Inset: a plot of SPR shift versus RI.

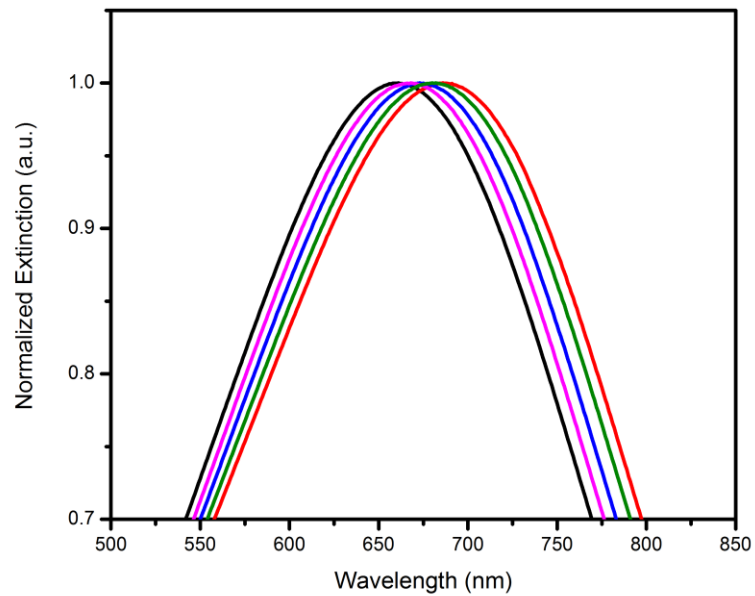


Figure S4.2D. Extinction spectra of Sample D in solvents with different RIs (denoted in Figure). Inset: a plot of SPR shift versus RI.

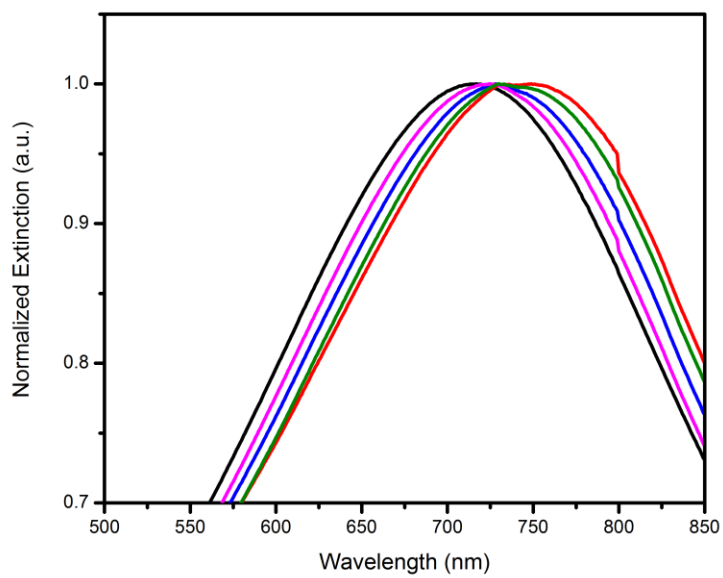


Figure S4.2E. Extinction spectra of Sample E in solvents with different RIs (denoted in Figure). Inset: a plot of SPR shift versus RI.

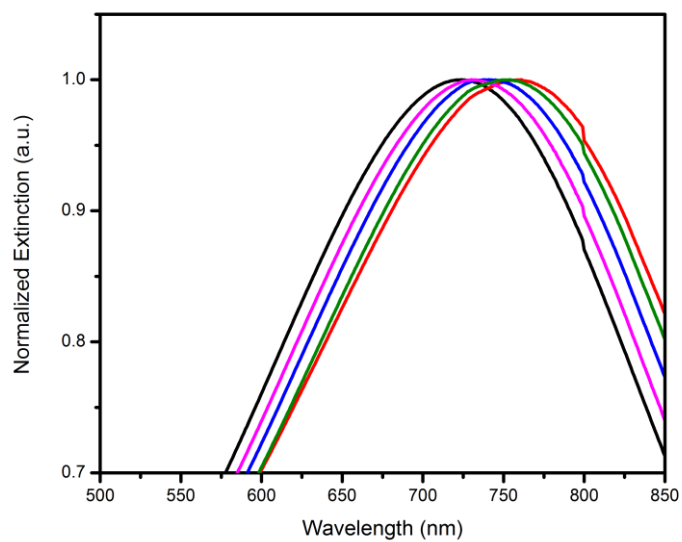


Figure S4.2F. Extinction spectra of Sample F in solvents with different RIs (denoted in Figure). Inset: a plot of SPR shift versus RI.

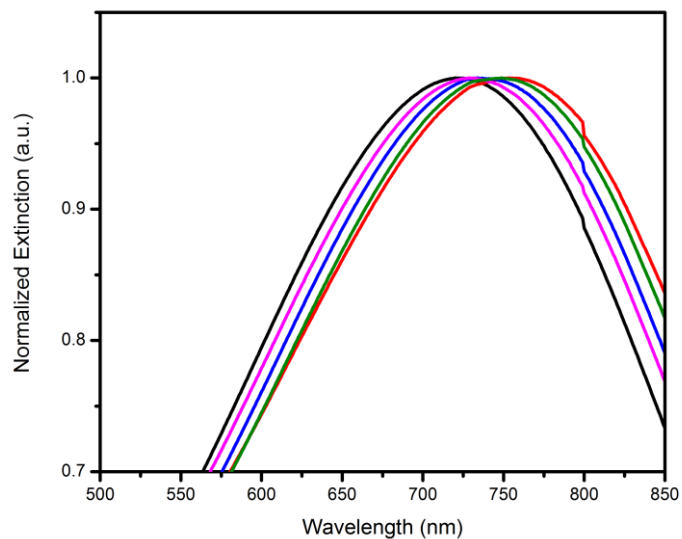


Figure S4.2G. Extinction spectra of Sample G in solvents with different RIs (denoted in Figure). Inset: a plot of SPR shift versus RI.

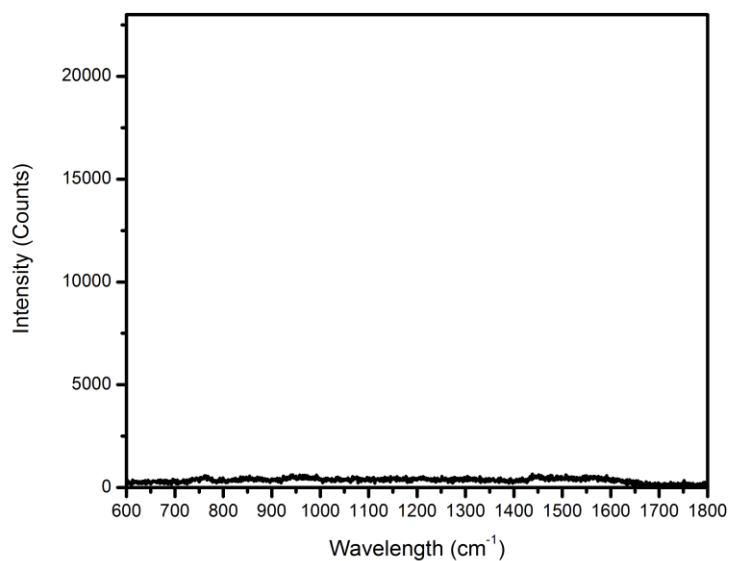


Figure S4.3. Raman spectrum from drop-casted Sample A (no derivitization with 4-MPy).

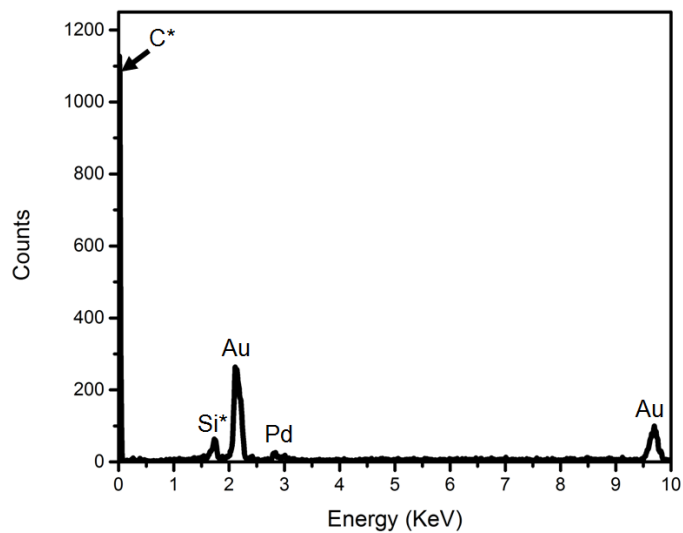


Figure S4.4. SEM/EDX spectrum of hollow Au/Pd octopods, indicating that Fe is not measurably present in the structures. The C and Si peaks observed originate from the sample substrate.

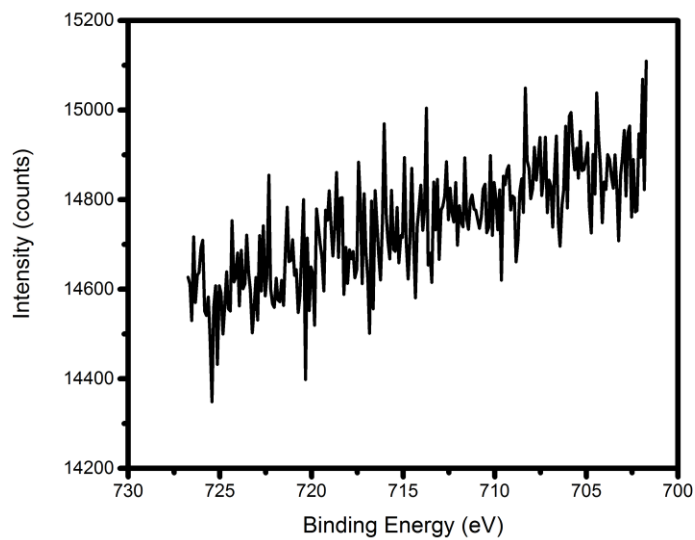


Figure S4.5. XPS analysis of hollow Au/Pd octopods in the Fe $2p_{1/2}$ and $2p_{3/2}$ region, indicating that Fe is not present in the sample.

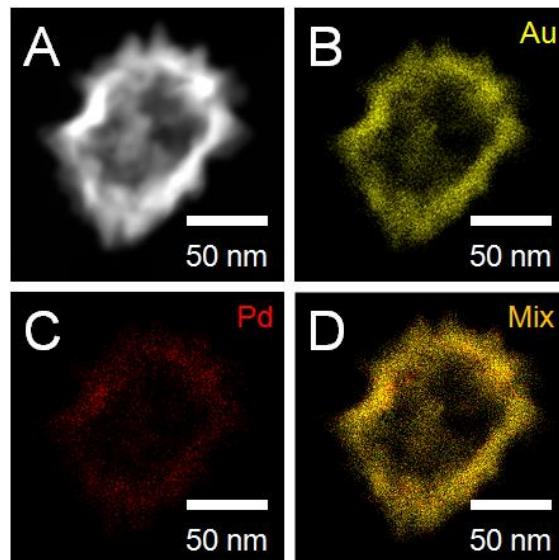


Figure S4.6. (A) A STEM image of one of the highly branched impurity structures after the etching procedure and (B-D) elemental mapping by STEM/EDX, where yellow indicates Au and red indicates Pd.

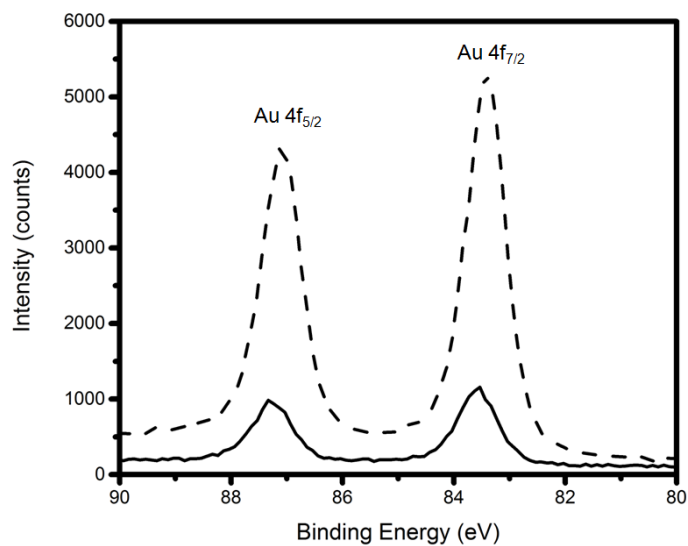


Figure S4.7. XPS analysis of Pd@Au/Pd octopods before etching (solid) and hollow Au/Pd octopods after etching (dashed) in the Au 4f_{7/2} and 4f_{5/2} region.

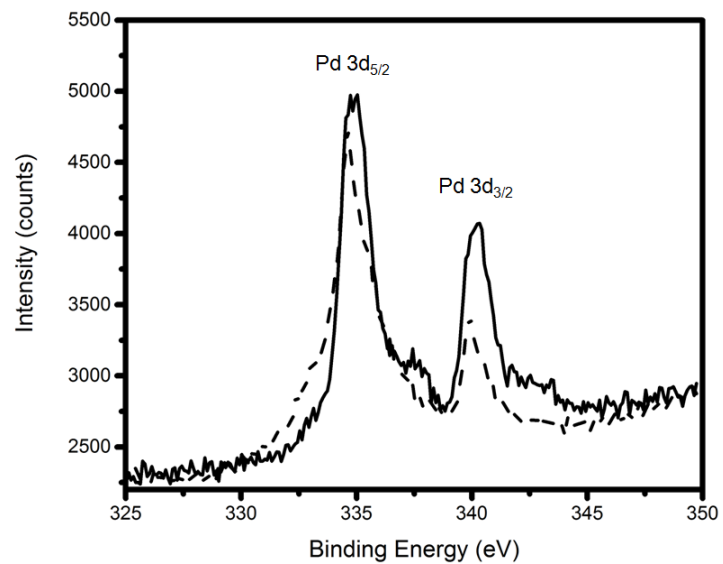


Figure S4.8. XPS analysis of hollow Pd@Au/Pd octopods before etching (solid) and hollow Au/Pd octopods after etching (dashed) in the Pd 3d_{5/2} and 3d_{3/2} region. The shoulder near 337 eV is likely attributed to Au 4d_{5/2}

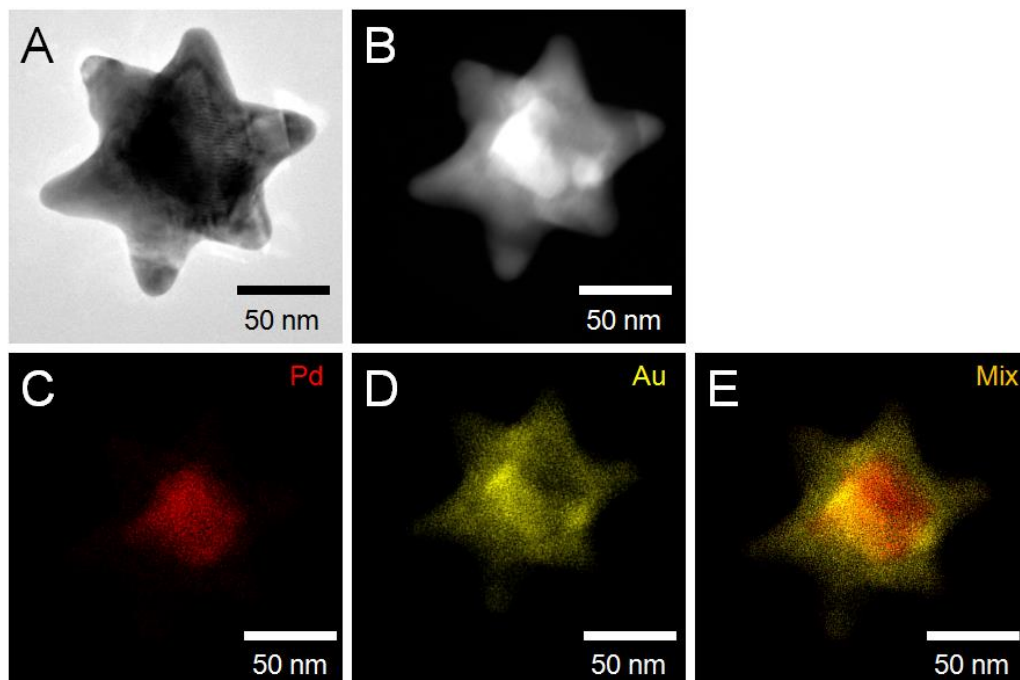


Figure S4.9. (A) A TEM image an etched particle, (B) its corresponding STEM image, and (C-E) elemental mapping by STEM/EDX where yellow indicates Au and red indicates Pd. Due to complete coverage of the Pd nanocube interior with overgrowth metal, the Pd seed cannot be removed by chemical etching.

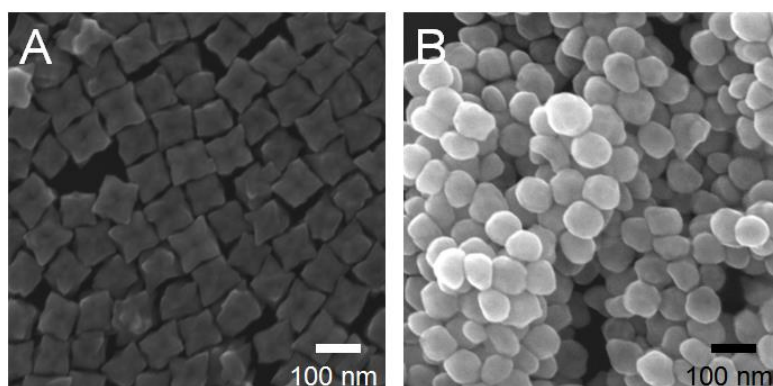


Figure S4.10. (A) An SEM image of Pd@Au/Pd octopods before etching and (B) an SEM image of the same sample after etching for 48 hours.

Chapter 5

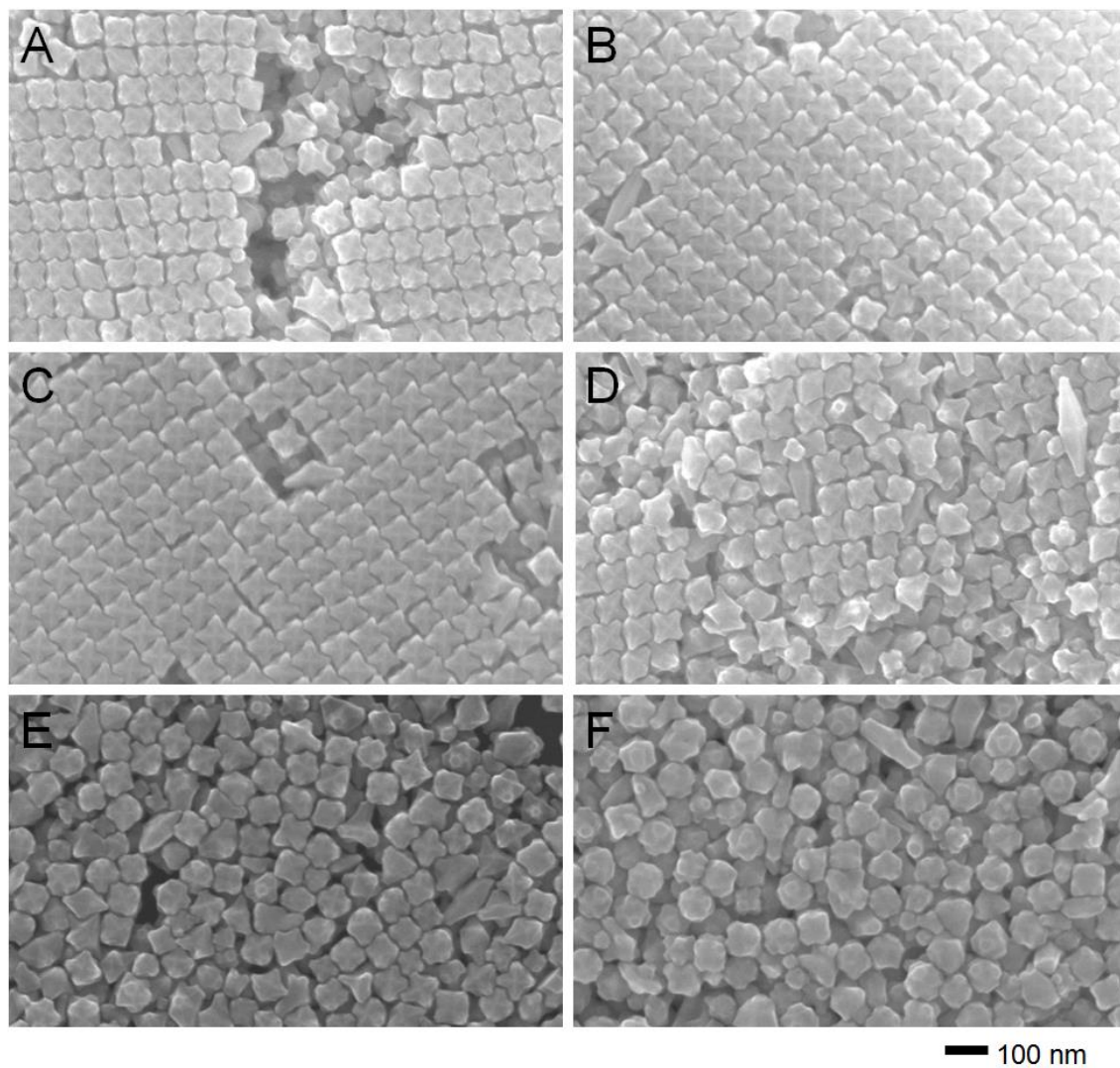


Figure S5.1. SEM images of Au/Pd octopods prepared with 2.0 mL of 3-methylsalicylic acid at the following concentrations: (A) 0 mM, (B) 2 mM, (C) 4 mM, (D) 6 mM, (E) 8 mM, and (F) 10 mM.

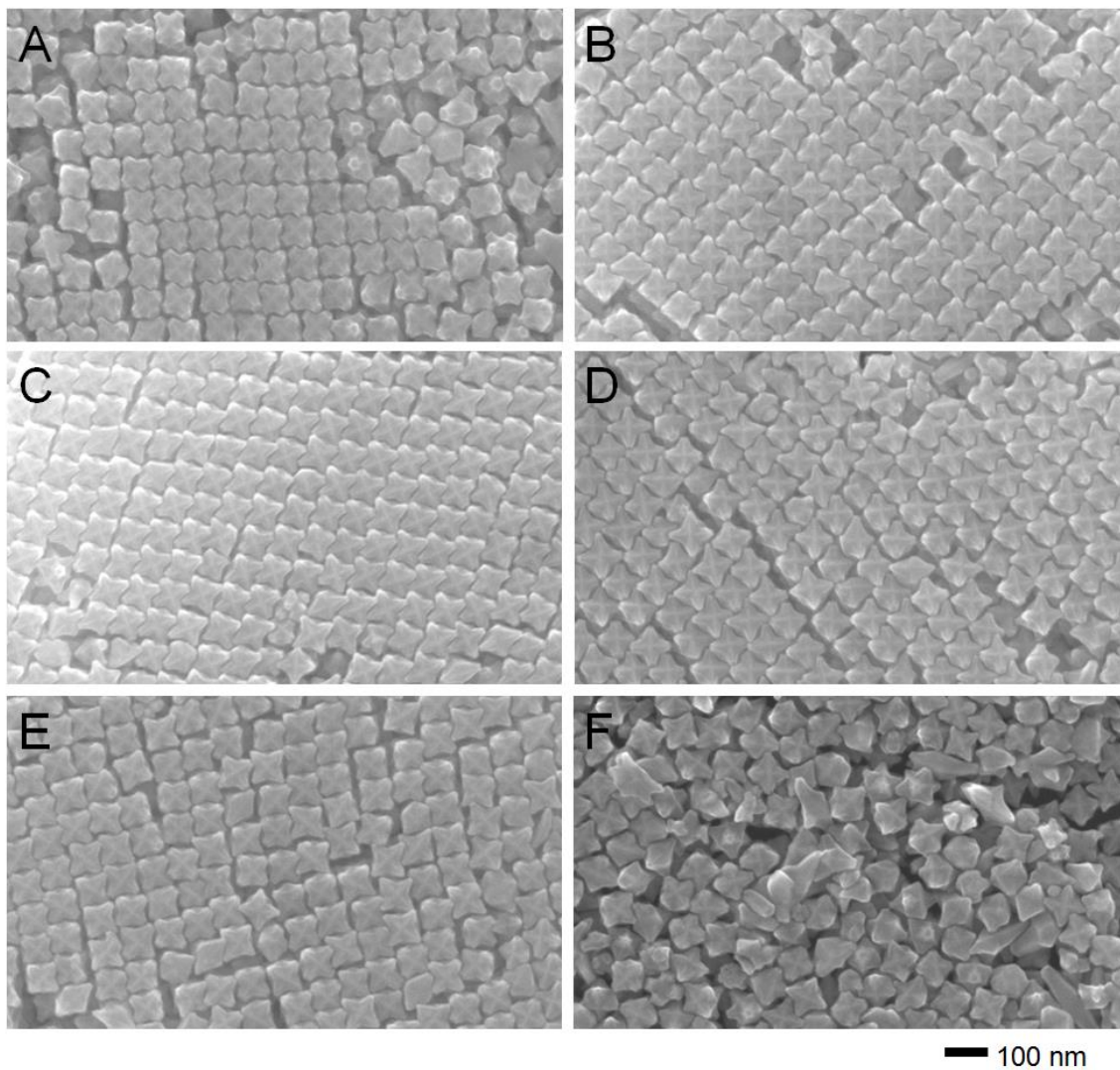


Figure S5.2. SEM images of Au/Pd octopods prepared with 2.0 mL of sodium salicylate at the following concentrations: (A) 0 M, (B) 0.02 M, (C) 0.04 M, (D) 0.06 M, (E) 0.08 M, and (F) 0.1 M.

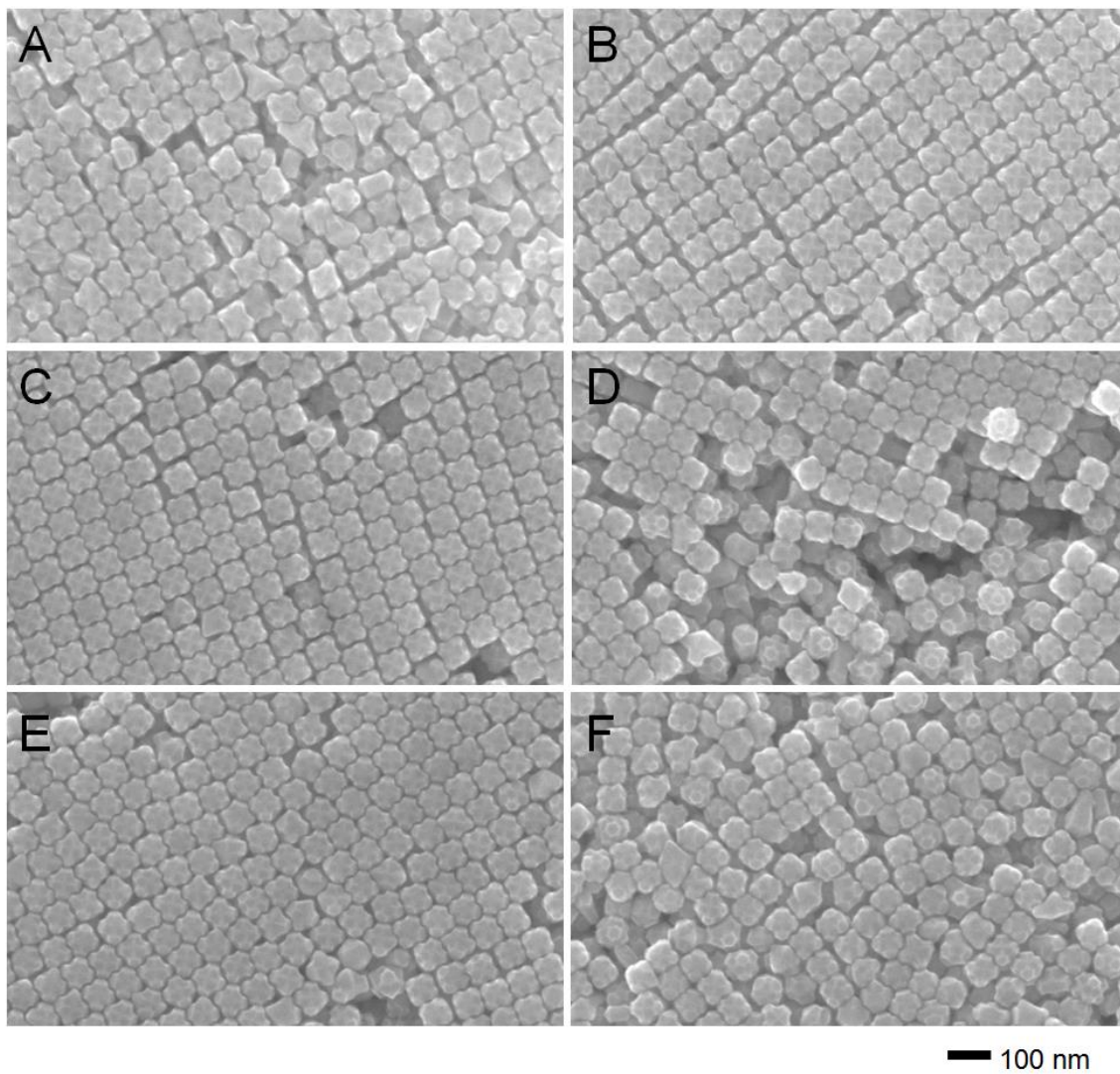


Figure S5.3. SEM images of Au/Pd octopods prepared with 2.0 mL of 6-dihydroxybenzoic acid at the following concentrations: (A) 0 mM, (B) 4 mM, (C) 8 mM, (D) 12 mM, (E) 16 mM, and (F) 20 mM.

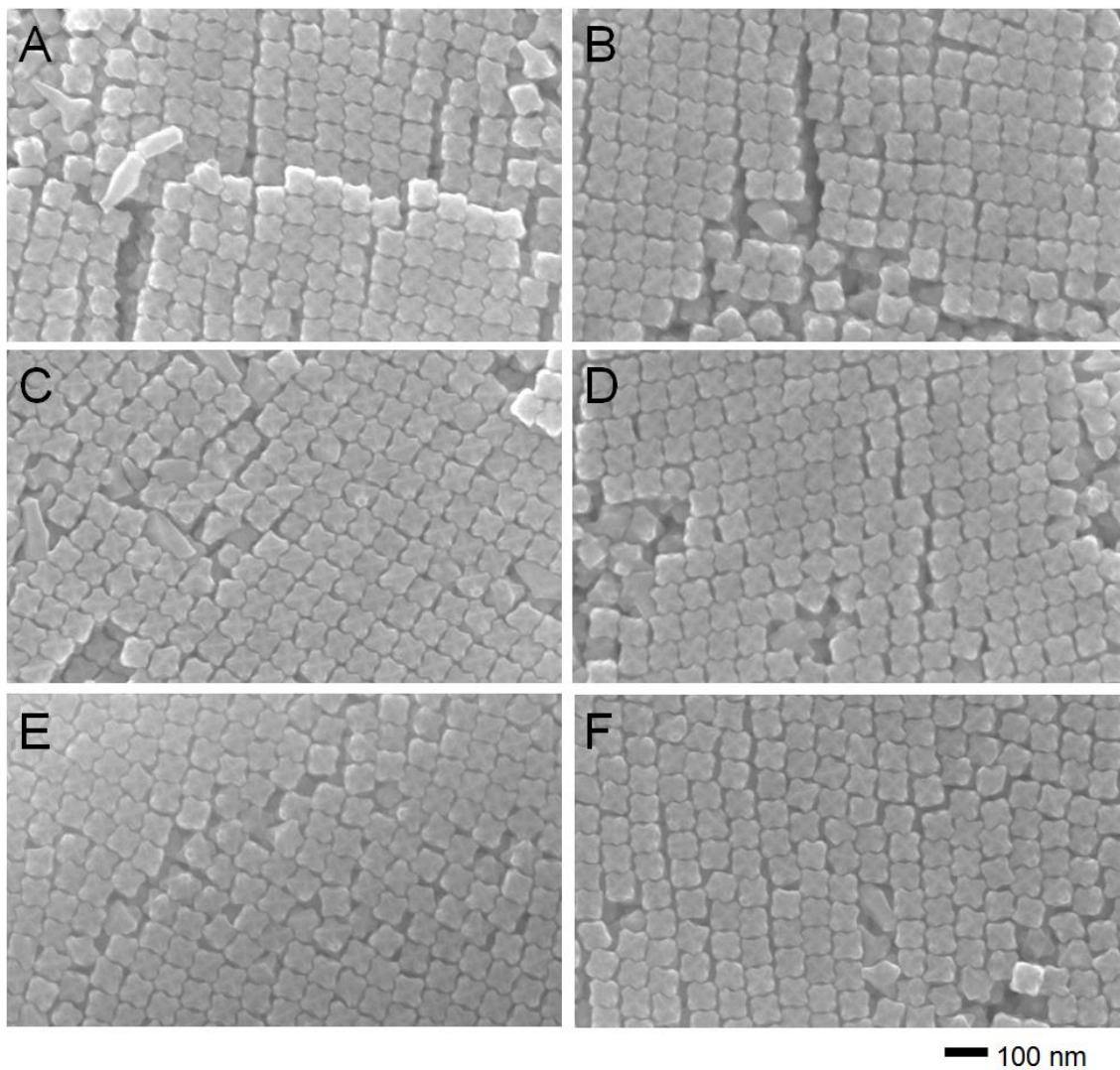


Figure S5.4. SEM images of Au/Pd octopods prepared with 2.0 mL of 5-bromosalicylic acid at the following concentrations: (A) 0 mM, (B) 2 mM, (C) 4 mM, (D) 6 mM, (E) 8 mM, and (F) 10 mM.

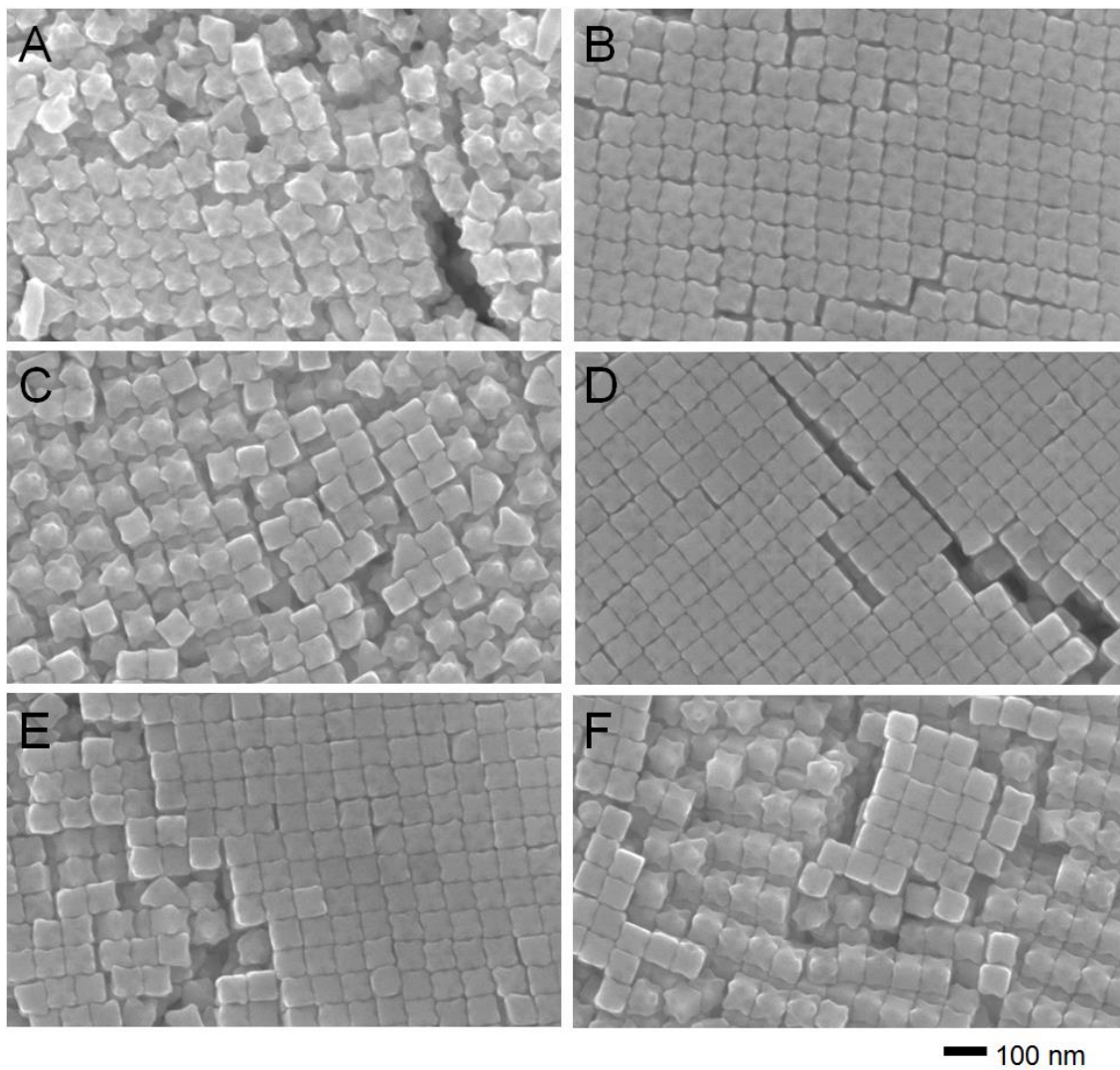


Figure S5.5. SEM images of Au/Pd octopods prepared with 2.0 mL of 5-aminosalicylic acid at the following concentrations: (A) 0 mM, (B) 2 mM, (C) 4 mM, (D) 6 mM, (E) 8 mM, and (F) 10 mM.

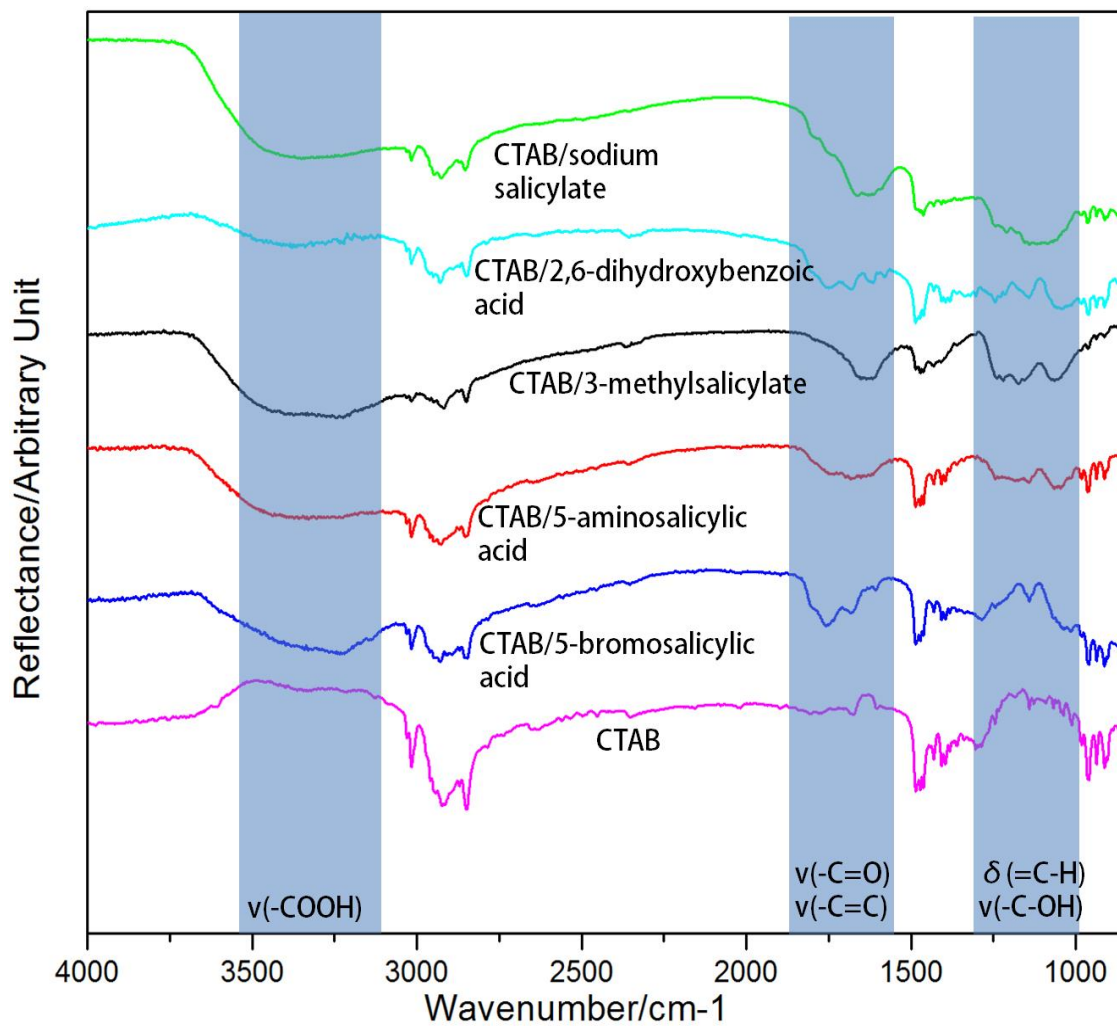


Figure S5.6. IR spectra of dried samples of Au/Pd octopods mixed with CTAB and an aromatic additive as well as a spectrum of Au/Pd octopods with only CTAB.

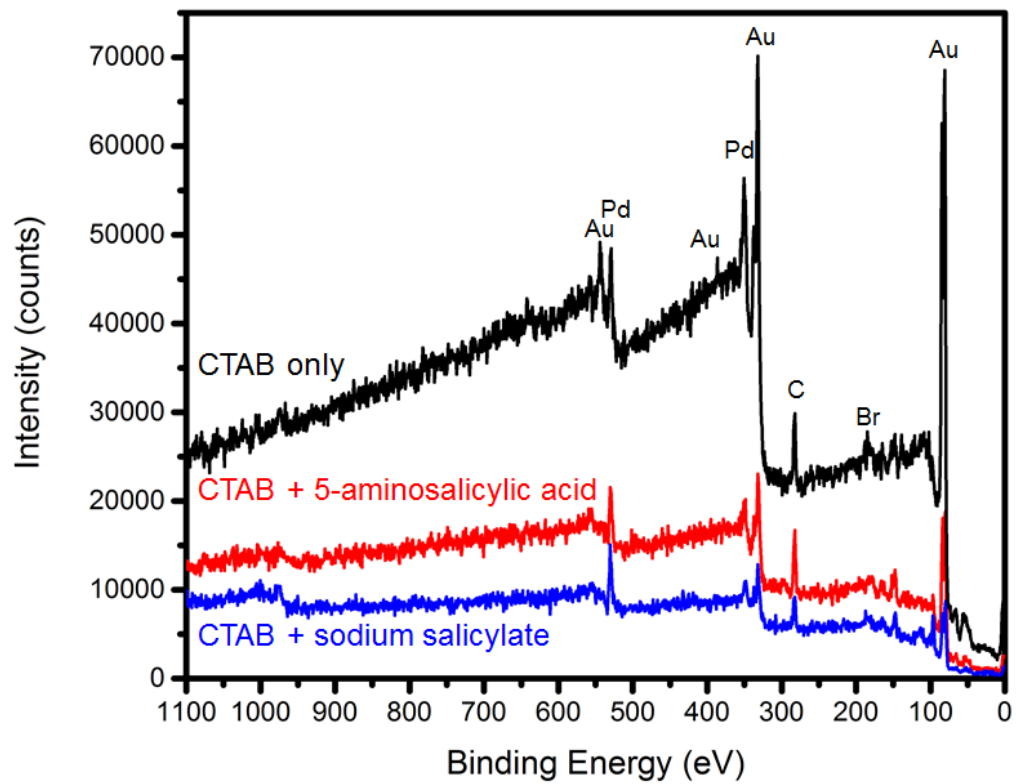


Figure S5.7. XPS long-range spectra for octopods prepared without additives (black), with 5-aminosalicylic acid (red), and with sodium salicylate (blue).

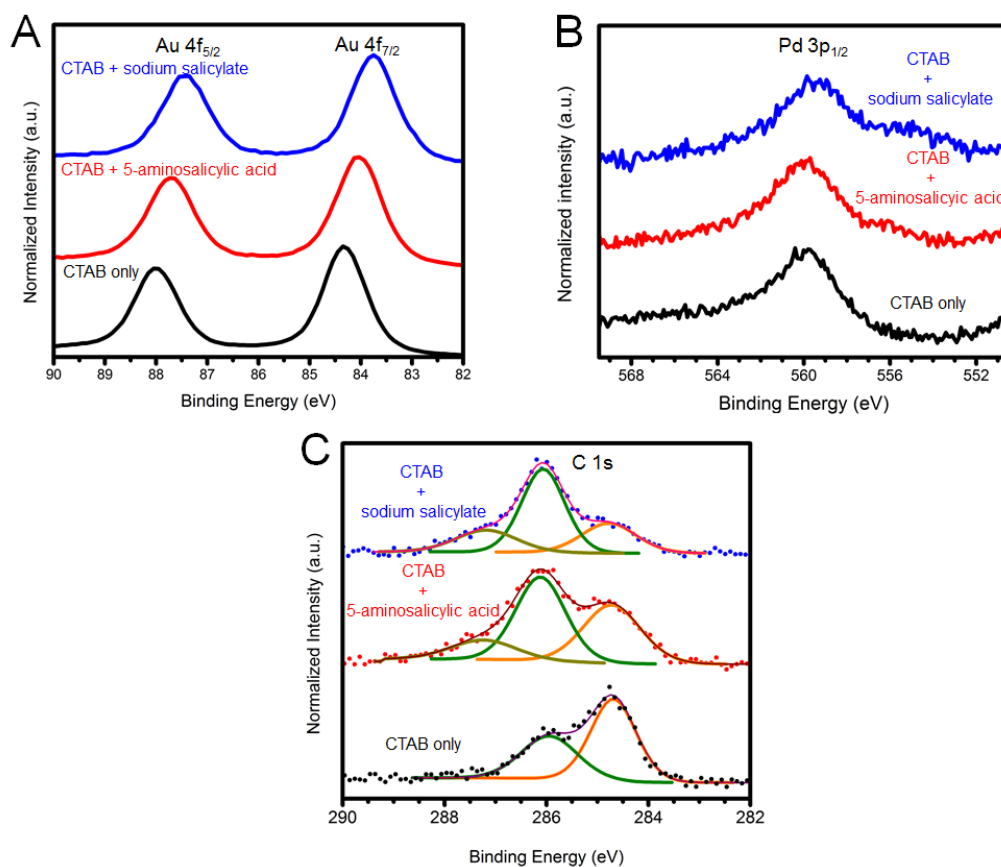


Figure S5.8. XPS spectra of octopods without aromatic additives (black), with 2 mL 0.006 M 5-aminosalicylic acid (red), and with 2 mL 0.04 M sodium salicylate (blue). In A) the Au 4f_{5/2} and Au 4f_{7/2} region, in B) the Pd p_{1/2} region, and in C) the C 1s region, where the solid lines underneath spectra correspond to deconvoluted peaks. For C) the orange peaks correspond to the adventitious hydrocarbon peak which was used for spectral calibrations, while assignments of the green and olive peaks cannot be made with certainty.

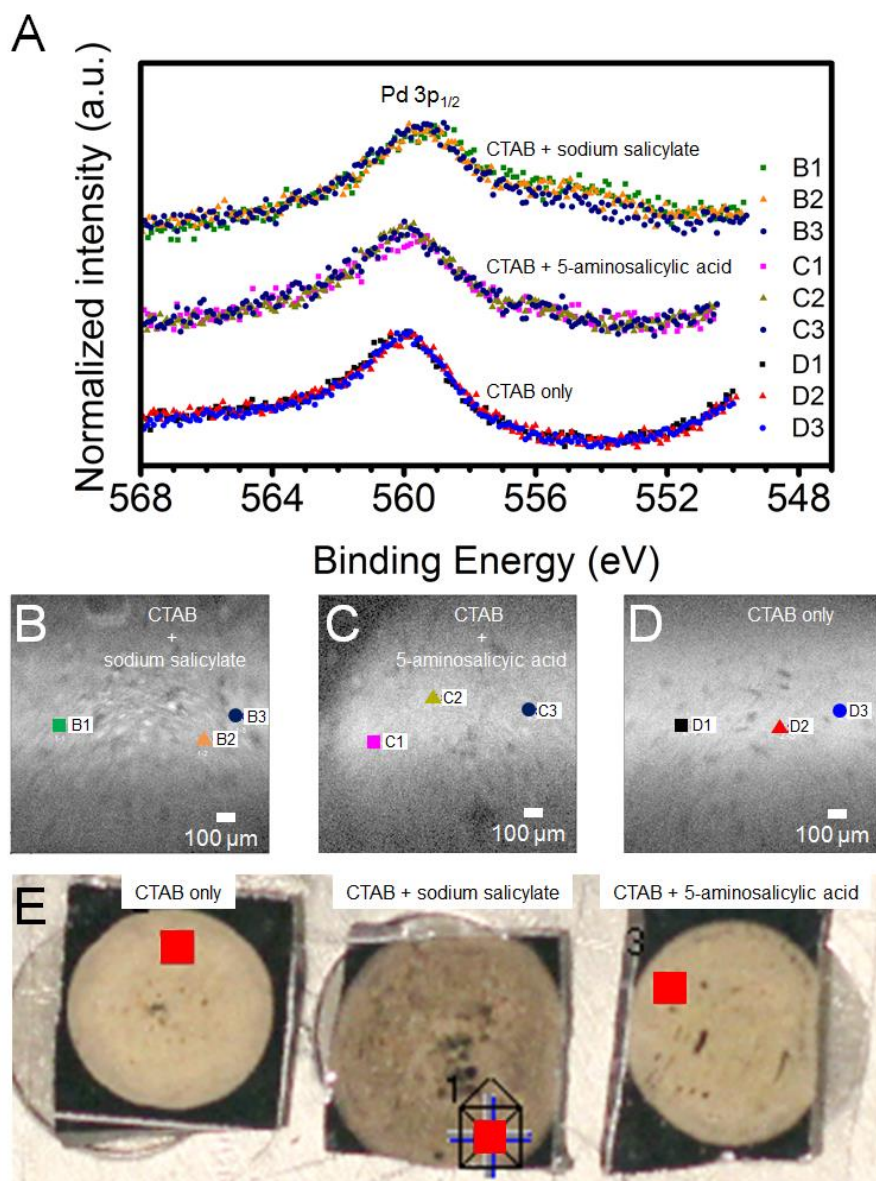


Figure S5.9. A) XPS spectra in the Pd p_{1/2} region of three separate scans of samples prepared with 2 mL 0.04 M sodium salicylate (top three), 2 mL 0.006 M 5-aminosalicylic acid (middle three), and without aromatic additives (bottom three). B-D) Corresponding SXI images indicating where on each sample spectra was acquired. E) Image of the samples dropcasted onto Si wafers indicating by the red squares where XPS was acquired.

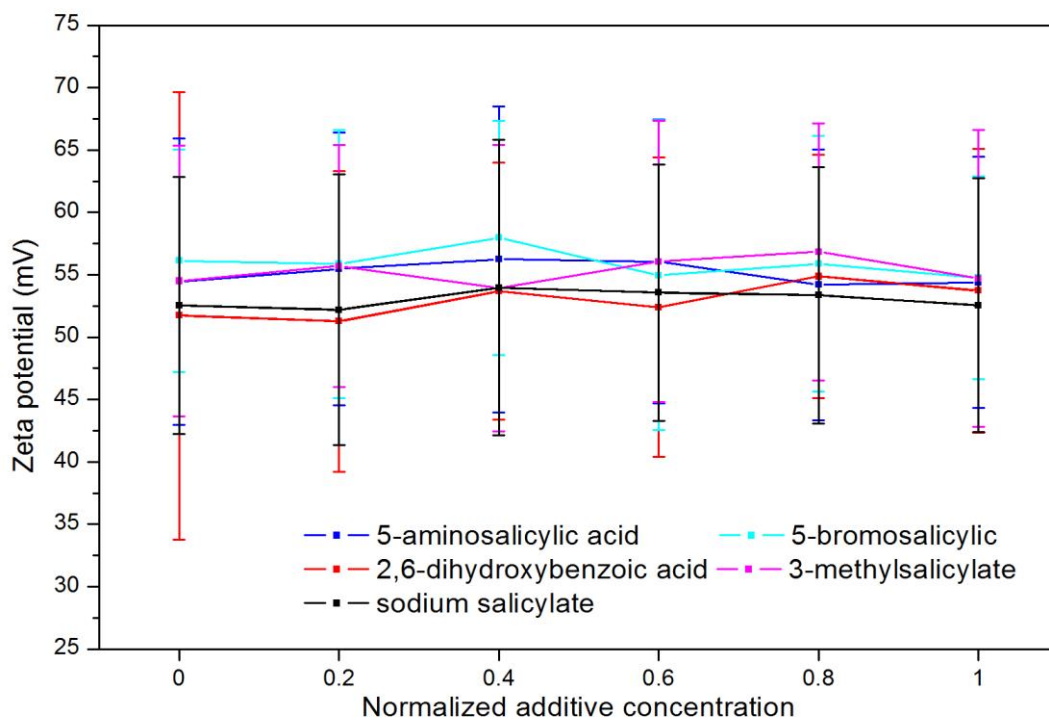


Figure S5.10. Plot of normalized additive concentration versus zeta potential. Normalization was done by taking the concentration of the additive divided by the maximum concentration of that additive in the study. Error bars represent standard deviation.

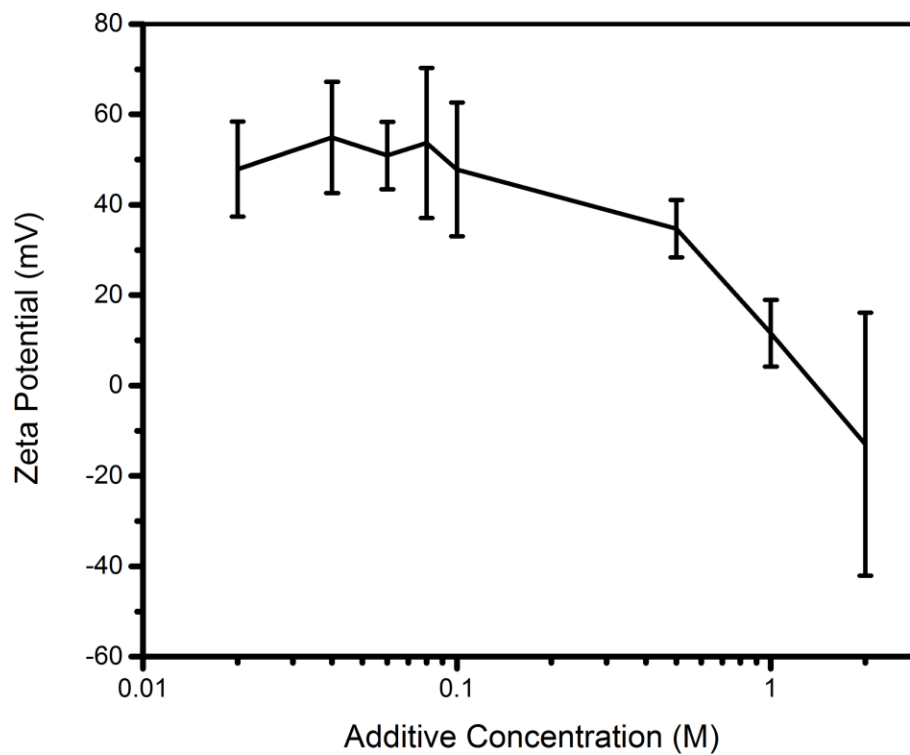


Figure S5.11. Plot of zeta potential measurements for nanoparticle solutions with varying concentrations of sodium salicylate. A difference in zeta potential can be observed, but only after adding considerably more organic additives than used in the study to generate homogeneous octopod samples.

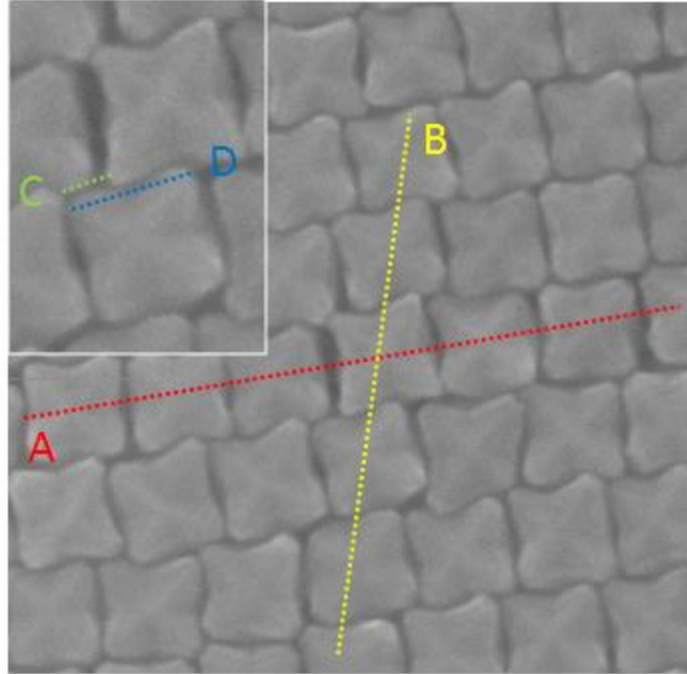


Figure S5.12. SEM image of assembled octopods with labels showing how % offset was measured. Line A shows the direction where octopods pack tip-to-tip with little offset. Line B shows the direction where the octopods pack tip-to-tip with some offset. Direction B is used for the offset measurements. Line C (top left inset) shows the distance between tips of two neighbor octopods along the direction indicated in Line B. Line D (top left inset) shows the tip-to-tip measurement of one octopod. The % offset is therefore calculated through the use of the following equation: $\% \text{ lattice offset} = \frac{C}{D} \times 100$.

Table S5.1. pH measurements of the growth solution that forms Au/Pd octopods during synthesis for each aromatic additive.

Sample	pK _a	Measurement	A	B	C	D	E	F
3-Methyl salicylic acid	3.06	Conc. (M)	0	0.02	0.04	0.06	0.08	0.1
		pH	2.48	2.46	2.48	2.50	2.54	2.58
Sodium salicylate	2.97	Conc. (M)	0	0.02	0.04	0.06	0.08	0.1
		pH	2.49	2.49	2.50	2.52	2.60	2.68
2, 6-Dihydroxybenzoic acid	1.23	Conc. (M)	0	0.004	0.008	0.012	0.016	0.02
		pH	2.43	2.36	2.34	2.29	2.27	2.25
5-Bromosalicylic acid	2.78	Conc. (M)	0	0.002	0.004	0.006	0.008	0.01
		pH	2.36	2.34	2.32	2.33	2.34	2.31
5-Aminosalicylic acid	2.41	Conc. (M)	0	0.002	0.004	0.006	0.008	0.01
		pH	2.55	2.54	2.55	2.56	2.58	2.55

References

1. Fang, P.-P.; Jutand, A.; Tian, Z.-Q.; Amatore, C., Au–Pd Core–Shell Nanoparticles Catalyze Suzuki–Miyaura Reactions in Water through Pd Leaching. *Angew. Chem. Int. Ed.* **2011**, *50*, 12184-12188.
2. DeSantis, C. J.; Skrabalak, S. E., Size-Controlled Synthesis of Au/Pd Octopods with High Refractive Index Sensitivity. *Langmuir* **2012**, *28*, 9055-9062.

Appendix C: Octopod Volume Proof

The volume of eight-pointed structures has been calculated before; however, no equation has been derived to take into account the unique structural features of octopods that include their hexagonal tips and tapered branches. Here, an equation is derived to account for these structural features and provide information about the octopod.

In deriving a method for calculating the volume of an octopod from scanning electron microscopy (SEM) images, the three-dimensional configuration of an octopod and its connection to the two-dimensional measurements that can be obtained from SEM imaging must be considered. For convenience and ease, the fewest parameters possible should be used and all parameters should be able to be measured facilely, with little to no ambiguity from the measurement of one particle to another.

Octopods are eight-branched nanostructures with O_h symmetry. They can be thought of as structures with one branch protruding from each of the eight vertices of a cube. As shown in **Figure C1**, particles typically lay with four branches toward and four away from the substrate.

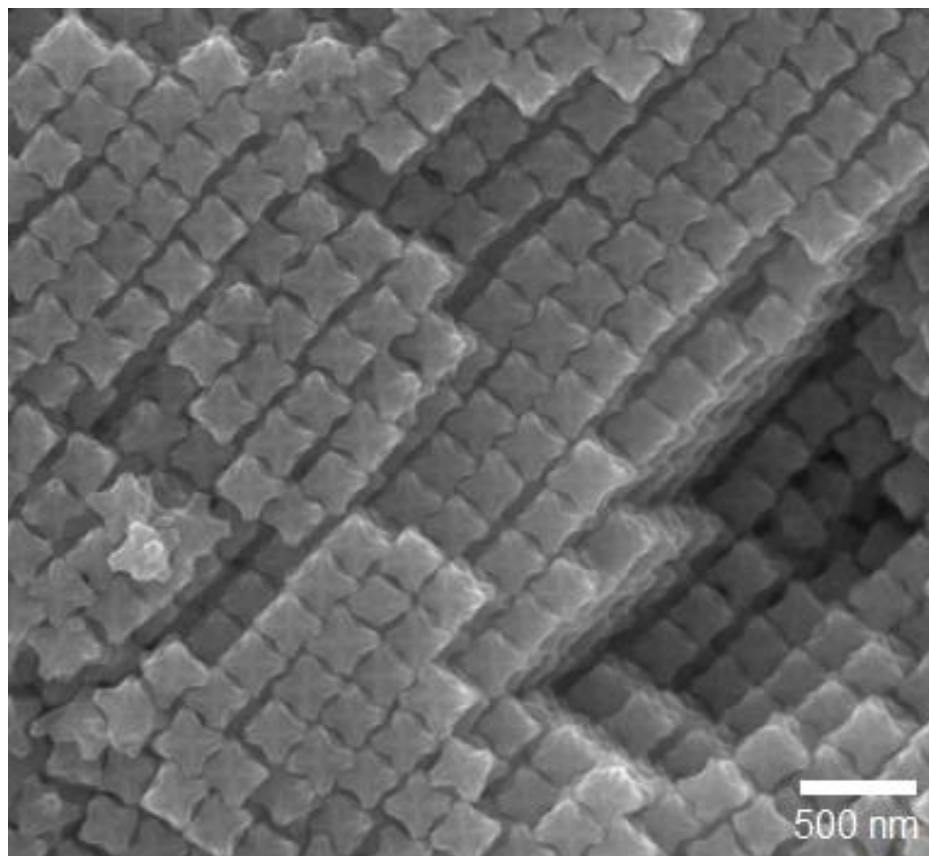


Figure C1

From SEM images of particles with this orientation, three parameters are easily measurable: tip-to-tip branch length (hereby denoted as x), tip thickness (hereby denoted as y), and branch base thickness (hereby denoted as q). These parameters are shown in **Figure C2**.

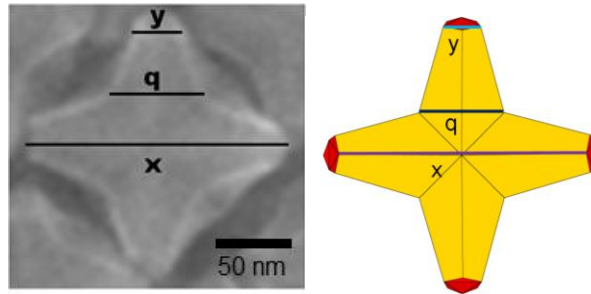


Figure C2

It should be noted that, while parameters y and q are directly relatable to the structure from measurements of two-dimensional SEM images, x is not. As indicated in **Figure C3**, parameter x shows the true tip-to-tip distance between two branches but does not account for the ascending and descending slope of the branches. So, for this proof, volume and surface area formulae will be derived in terms of z , which is the true length of a branch that accounts for its change in slope in all three dimensions. Afterward, z will be substituted for x , which is the measurable parameter.

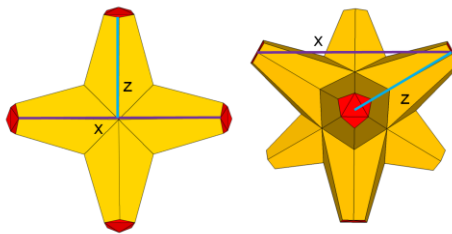


Figure C3

For the following proof, each branch will be approximated as a truncated hexagonal pyramid. This approximation simplifies the model so that the slopes of each of the edges of the hexagonal pyramid are the same. The truncated hexagonal pyramid design is based upon **Figure C4**, which shows an SEM image of an octopod so that one tip is facing

away from the substrate. In this image, the tip is truncated so that a hexagon forms (outlined in red for clarity). Each edge along the hexagonal pyramid is tapered (shown in yellow dashes for clarity).

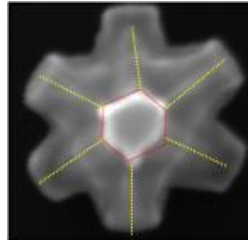


Figure C4

To mitigate the overlap of one branch with its neighbor, the truncated hexagonal pyramid will be separated into an additional section, as shown in **Figure C5**. For clarity, a is denoted as the center point of the base of the hexagonal pyramid that has overlap with its neighbors, b is denoted as the center point of the base of the hexagonal pyramid that has no overlap with its neighbors, and c is the center point of the truncated tip of the hexagonal pyramid.

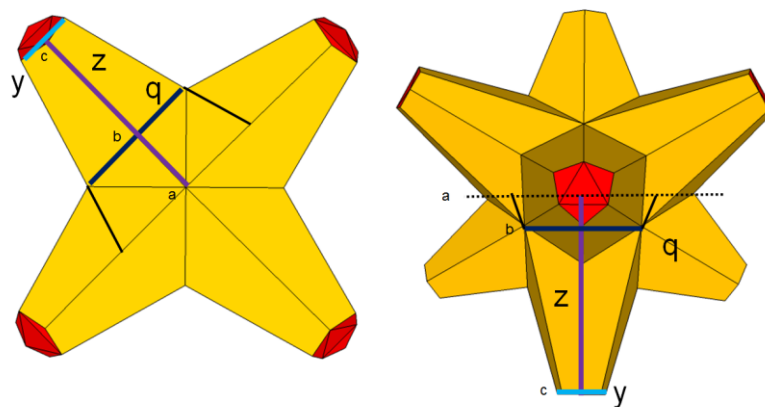


Figure C5

Truncating the branch at point b creates the surface shown in **Figure C6**.

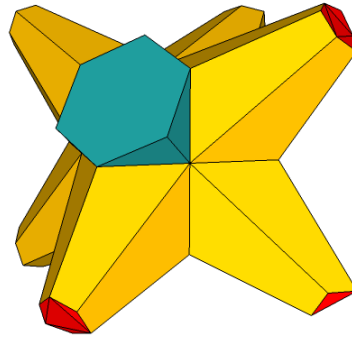


Figure S6

Figure C7 shows the abstracted portion of this interior region of the branch that does not overlap with its neighbors. It is an irregular polyhedron.

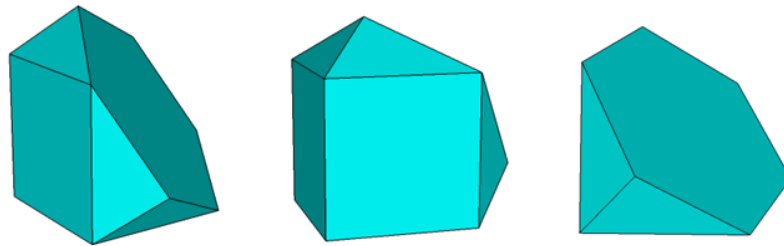


Figure C7

Therefore, we can generalize an equation that takes into account the two pieces that make up each branch: the truncated hexagonal pyramid and the irregular polyhedron.

$$Volume = 8(V_{irregular\ polyhedron} + V_{hexagonal\ pyramid})$$

For the irregular polyhedron portion, the square top could be completed by adding a triangular pyramid to the base of the hexagon, as shown in **Figure C8**. In doing so, the shape can now be thought of as three irregular tetrahedra attached to a cube.

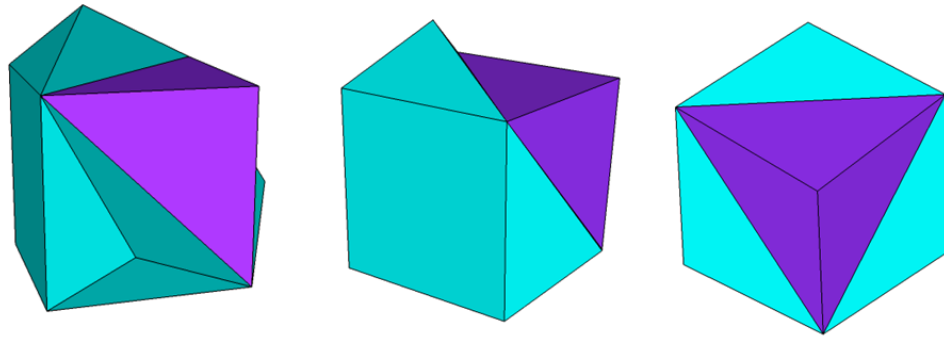


Figure C8

In **Figure C9**, the triangular pyramid is cut into one third. This irregular tetrahedron can be compared with one of the irregular tetrahedra on the exterior of the cube, painted green. Here, line *e* bisects the parallelogram formed from one third of the hexagon face of the irregular polyhedron. Thus, the interior angles of the tetrahedra must match. In addition, lines *f* and *g* intersect, thereby showing that the internal angles θ_1 and θ_2 are the same. Therefore, these two tetrahedra are the same size and volume. The irregular polyhedron portion can be modeled as the volume of a cube of size s_a , where s_a is the side of one of the vertices of the cube.

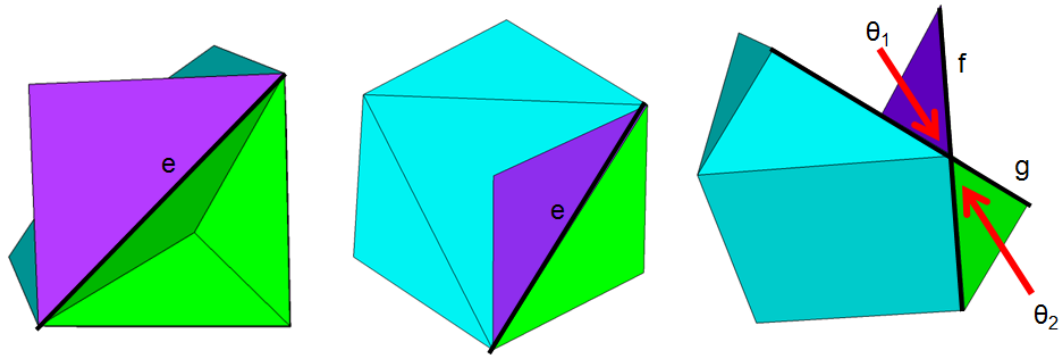


Figure C9

As shown in **Figure C10** there is a relationship between s_a and q . Looking in the direction where four branches face away from the substrate, a right triangle forms where s_a forms both bases and q forms the hypotenuse. Therefore, $s_a = \frac{q}{\sqrt{2}}$.

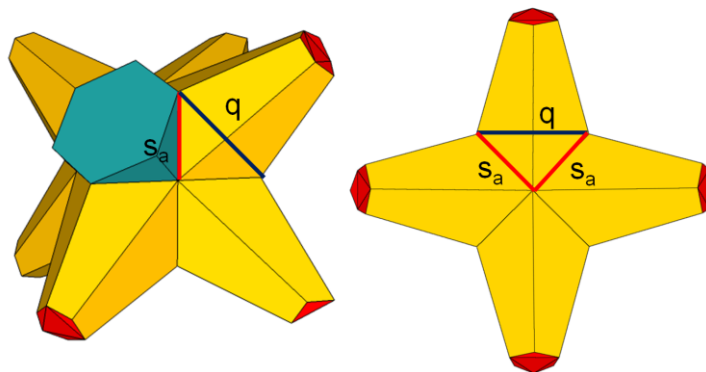


Figure C10

The volume of the irregular polyhedron can now be given in terms of q .

$$V_{irregular\ polyhedron} = \frac{\sqrt{2}q^3}{4}$$

The total volume of the octopod can be expressed with this defined term. In addition, the truncated hexagonal pyramid can be broken down into the two terms: one with a base at point b and one with a base at point c.

$$Volume = 8 \left(V_b - V_c + \frac{\sqrt{2}q^3}{4} \right)$$

The volume of a hexagonal pyramid can be derived from the following equation where n is the number of sides of the regular polyhedron, h is the height of the polyhedron, and s is one side of the polyhedron:

$$V_{Pyramid} = \frac{n}{12} h s^2 \cot \frac{\pi}{n}$$

Therefore, for a hexagonal pyramid (HP), where $n = 6$:

$$V_{HP} = \frac{\sqrt{3}}{2} h s^2$$

The entire volume can then be rewritten in terms of h and s at points b and c.

$$Volume = 4\sqrt{3}(h_b s_b^2 - h_c s_c^2) + 2\sqrt{2}q^3$$

For clarity, **Figure C11** shows the volume of an octopod with the branches not truncated.

The length from the truncated base c to the nontruncated tip will be defined as z_0 .

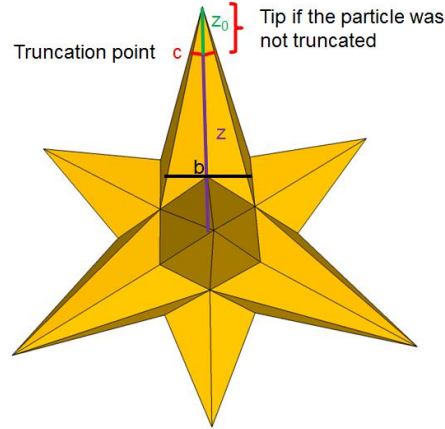


Figure C11

From this figure, it can be determined that $h_b = z + z_0 - \frac{q}{\sqrt{2}}$, $s_b = \frac{q}{2}$, $h_c = z_0$, and $s_c = \frac{y}{2}$. The entire volume can now be expressed in terms of z , z_0 , q , and y .

$$Volume = 4\sqrt{3} \left(\left(z + z_0 - \frac{q}{\sqrt{2}} \right) \frac{q^2}{4} - \frac{z_0 y^2}{4} \right) + 2\sqrt{2}q^3$$

This equation can be simplified and re-arranged.

$$Volume = \sqrt{3} \left(z_0(q^2 - y^2) + zq^2 - \frac{\sqrt{2}q^3}{2} \right) + 2\sqrt{2}q^3$$

However, z_0 is not a measurable parameter. Fortunately, it can be substituted with already defined variables.

Cutting the branch in half from the perspective shown in **Figure C11** in half results in a right triangle with angle $\frac{\theta}{2}$, which is opposite to bases $\frac{y}{2}$ and $\frac{q}{2}$. The height of the right triangle is $z + z_0$. See **Figure C12** for details.

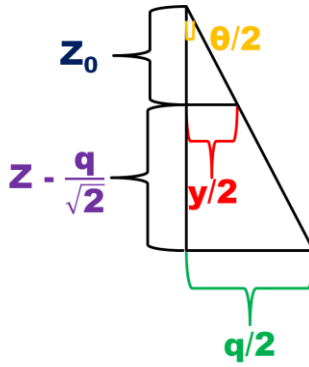


Figure C12

From this right triangle:

$$\tan \frac{\theta}{2} = \frac{\frac{q}{2}}{z + z_0 - \frac{q}{\sqrt{2}}} = \frac{\frac{y}{2}}{z_0}$$

This equation can then be solved for z_0 .

$$z_0 = \frac{yz - \frac{\sqrt{2}yq}{2}}{q - y}$$

Therefore, the equation for the volume of an octopod can be rewritten in terms of q , y , and z .

$$Volume = \sqrt{3} \left(\left(\frac{yz - \frac{\sqrt{2}yq}{2}}{q - y} \right) (q^2 - y^2) + zq^2 - \frac{\sqrt{2}q^3}{2} \right) + 2\sqrt{2}q^3$$

This equation can be simplified.

$$Volume = \sqrt{3} \left(\left(yz - \frac{\sqrt{2}yq}{2} \right) (q + y) + zq^2 - \frac{\sqrt{2}q^3}{2} \right) + 2\sqrt{2}q^3$$

Finally, z needs to be transformed into an expression in terms of x, y, and q. First, considering the octahedral symmetry of the branches, if the planar distance measured between two branches is x then the distance between each branch is $\frac{x}{\sqrt{2}}$. This proof is summarized in **Figure C13**.

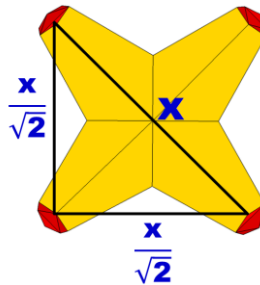


Figure C13

The relationship between x and z can be simplified to the shape of a cube where each vertex of a cube represents the tip of one of the branches of an octopod. In this model, x is a diagonal of one side of the cube, equivalent to the branch tip-to-tip measurement shown in **Figure C13**. As already noted, the side of the cube would be $\frac{x}{\sqrt{2}}$. Parameter z would be the measurement from the interior of the particle to one branch tip. A summary of this model is shown in **Figure C14**.

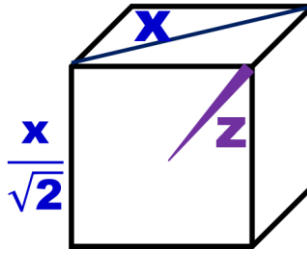


Figure C14

Therefore, it is possible to set z in terms of x and using the Pythagorean theorem.

$$z = \frac{\sqrt{6}}{4}x$$

Finally, this expression for z can be substituted into the main equation for volume to yield the master equation for the volume of an octopod.

$$Volume = \sqrt{3} \left(\left(\frac{\sqrt{6}}{4}xy - \frac{\sqrt{2}yq}{2} \right) (q + y) + \frac{\sqrt{6}}{4}xq^2 - \frac{\sqrt{2}q^3}{2} \right) + 2\sqrt{2}q^3$$

Octopod Surface Area Estimation Proof

The surface of an octopod is composed of 6 hexagonal faces located where the hexagonal pyramid is truncated and 48 quadrilateral faces along the sides of the branches. Like in the volume proof, for the surface area approximation will assume that the branches are truncated hexagonal pyramids. **Figure C15** shows one face of a branch normal to the viewer. The blue dashed line cuts the face into two pieces: a trapezoid and a right triangle with hypotenuse $\frac{q}{\sqrt{2}}$. The sides of that right triangle would be approximately equal to $\frac{q}{2}$ (the parameter q would go “through” the branch and therefore the on-face edge would be a close approximation).

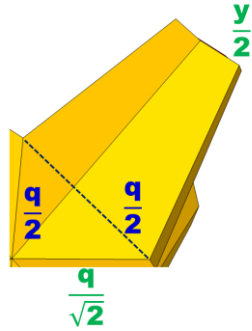


Figure C15

Recalling **Figure C13**, it is possible to define one of the sides of the branch in terms of x and q . **Figure C16** shows that this side is equal to $\frac{1}{2}\sqrt{x^2 - xq + 2q^2}$.

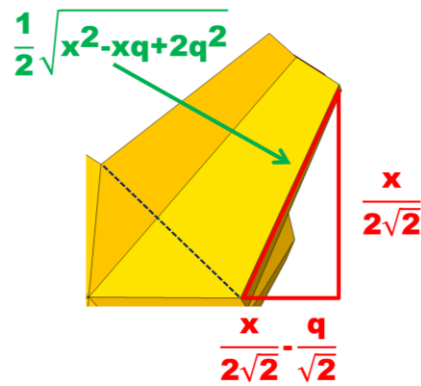


Figure C16

For the surface area approximation, both long sides of the trapezoid will be assumed to be equivalent. **Figure C17** summarizes the calculated and estimated values for each of the sides of the quadrilateral.

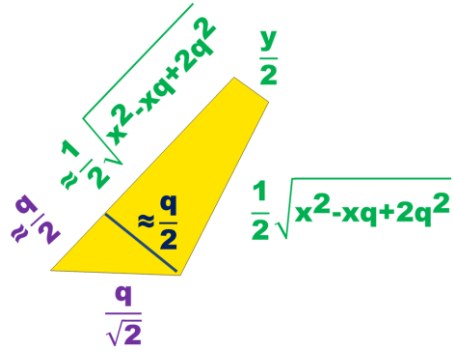


Figure C17

The area of the quadrilateral is the sum of the right triangle and the trapezoid with height

$$\frac{1}{2}\sqrt{x^2 - xq + 2q^2}.$$

$$\text{Area of quadrilateral} \approx \frac{1}{8}q^2 + \frac{1}{8}qy\sqrt{x^2 - xq + 2q^2}$$

The area of the hexagon region can be expressed in terms of y , where y is the diameter of the hexagon.

$$\text{Area of hexagon} = \frac{3\sqrt{3}}{8}y^2$$

Adding together the 48 quadrilateral faces and 8 hexagons gives the master equation that approximates the surface area of an octopod.

$$\text{Surface area} \approx 6q^2 + 6qy\sqrt{x^2 - xq + 2q^2} + 3\sqrt{3}y^2$$

Christopher DeSantis

Indiana University
E-mail: cdesanti@indiana.edu
Department of Chemistry
Phone: (812) 855-1721
800 E Kirkwood Ave.
Bloomington, IN 47405

Education:

2009 – 2014	Ph. D.	Chemistry, Indiana University
2005 – 2009	B. S.	Pennsylvania State University, Schreyer Honors College
		Major: Chemistry
		Minor: Philosophy

Research

2014 – Present	Postdoctoral Researcher, Rice University – Houston (N. J. Halas)
2009 – 2014	Research Assistant, Indiana University – Bloomington (S. E. Skrabalak)
2007 – 2009	Research Assistant, Pennsylvania State University – University Park (R. E. Schaak)

Awards

2013	Raymond Siedle Fellowship in Materials Chemistry, Indiana University
2013	John H. and Dorothy McKenzie Fellowship, Indiana University
2012 – 2013	Chester Davis Fellowship in Inorganic Chemistry, Indiana University
2012	Chemstry GRC Travel Award, Indiana University
2007 – 2008	John and Elizabeth Holmes Teas Scholarship, Pennsylvania State University

Publications

- (12) Ringe, E.; **DeSantis, C. J.**; Collins, S. M.; Skrabalak, S. E.; Midgley, P. A., Composition, Crystallography, and Plasmonic Response of Single Au/Pd Octopods. Submitted.
- (11) Bower, M. M.; **DeSantis, C. J.** Skrabalak, S. E. A Quantitative Analysis of Anions and pH on the Growth of Bimetallic Nanostructures. *J. Phys. Chem. C* **2014**, 118 (32), 18762–18770.
- (10) Weiner, R.G.; **DeSantis, C. J.**; Cardoso, M.B.T.; Skrabalak, S.E., Diffusion and Seed Shape: Intertwined Parameters in the Synthesis of Branched Metal Nanostructures. *ACS Nano* **2014**, 8 (8), 8625–8635.
- (9) **DeSantis, C. J.**; Sue, A. C.; Radmilovic, A.; Liu, H.; Skrabalak, S.E. Shaping the Synthesis and Assembly of Symmetrically Stellated Au/Pd Nanocrystals with Aromatic Additives. *Nano Lett.* **2014**, 14 (7), 4145–4150.
- (8) Motl, N. E.; Smith, A. F.; **DeSantis, C. J.**; Skrabalak, S. E. Engineering Plasmonic Metal Colloids through Composition and Structural Design. *Chem. Soc. Rev.* **2014**, 43, 3823–3834.
- (7) **DeSantis, C. J.**; Skrabalak, S. E. Manipulating the Optical Properties of Branched Au/Pd Nanocrystals through Interior Design. *Chem. Commun.* **2014**, 50 (40), 5367–5369. [Invited article for an Emerging Investigators issue]

- (6) **DeSantis, C. J.**; Weiner, R. G.; Bower, M. M.; Radmilovic, A.; Skrabalak, S. E. Seeding Bimetallic Nanostructures as a New Class of Plasmonic Colloids. *J. Phys. Chem. Lett.* **2013**, *4* (18), 3072–3082. [Highlighted in an editorial: Future Plasmonic Materials *J. Phys. Chem. Lett.*, **2013**, *4* (18), 3152–3152]
- (5) Mann, A. P. K.; Fu, J.; **DeSantis, C. J.**; Skrabalak, S. E. Spatial and Temporal Confinement of Salt Fluxes for the Shape-Controlled Synthesis of Fe₂O₃ Nanocrystals. *Chem. Mater.* **2013**, *25* (9), 1549–1555.
- (4) **DeSantis, C. J.**; Skrabalak, S. E. Core Values: Elucidating the Role of Seed Structure in the Synthesis of Symmetrically Branched Nanocrystals. *J. Am. Chem. Soc.* **2013**, *135* (1), 10-13.
- (3) **DeSantis, C. J.**; Skrabalak, S. E. Size-Controlled Synthesis of Au/Pd Octopods with High Refractive Index Sensitivity. *Langmuir* **2012**, *28* (24), 9055-9062. [Invited article for the special issue in colloidal nanoplasmonics]
- (2) **DeSantis, C. J.**; Sue, A. C.; Bower, M. M.; Skrabalak, S. E. Seed-Mediated Co-reduction: A Versatile Route to Architecturally Controlled Bimetallic Nanostructures. *ACS Nano* **2012**, *6*, (3), 2617-2628.
- (1) **DeSantis, C. J.**; Peverly, A. A.; Peters, D. G.; Skrabalak, S. E. Octopods versus Concave Nanocrystals: Control of Morphology by Manipulating the Kinetics of Seeded Growth via Co-Reduction. *Nano Lett.* **2011**, *11*, (5), 2164-2168.

Presentations

2014

Noble Metal Nanoparticle Gordon Research Seminar and Conference, Mount Holyoke College,
MA

2013

ACS National Meeting, Indianapolis, IN

2012

Noble Metal Nanoparticle Gordon Research Seminar and Conference, Mount Holyoke College,
MA

ACS National Meeting, Philadelphia, PA

2011

PINDU Inorganic Conference, Indiana University, Bloomington, IN

Central Regional Meeting of the ACS, Indianapolis, IN

MRS National Spring Conference, San Francisco, CA

Teaching and Mentoring Experience

Assistant Instructor, Indiana University

Chem M502 Solid-State Materials Chemistry, Spring 2011

Chem 100 The World of Chemistry, Fall 2010

Chem N330 Inorganic Chemistry Laboratory, Spring 2010, Fall 2009

Mentoring Experience, Indiana University

- Trained four undergraduate students in nanomaterial synthesis and characterization; two are co-authors on the *ACS Nano* publication, two are co-authors on the *J. Phys. Chem. Lett.* publication, and three will be co-authors on a submitted manuscript.
- Assisted in the graduate school application and selection process of undergraduate mentee; the student is currently attending Northwestern University.
- Trained undergraduate and graduate students throughout Indiana University for independent use of scanning electron microscope (SEM).
- Collaborated with graduate students in the Flood and Peters laboratory at Indiana University.

Technical Skills

- Colloidal nanomaterial design and synthesis, with an emphasis on multi-metal nanostructures.
- Proficient at analytical instruments that include: TEM (including STEM, EDX mapping, electron diffraction, and HR-TEM), SEM, cyclic voltammetry, and Raman spectroscopy
- Proficient in Origin and SketchUp 3D modeling software
- Calibration, routine maintenance, and user management (~50 users) of SEM

Appointed Positions

2012 – Present	Chair of the Gordon Research Seminar on Noble Metal Nanoparticles
2012 – 2014	Nanoscale Characterization Facility (NCF) SEM administrator, Indiana University, Department of Chemistry